Tectono-geomorphological evolution of the Northern Red Sea margins

Saleh Abood M Alqahtani

Submitted in accordance with the requirements for the degree of

Doctor of Philosophy

The University of Leeds

School of Earth and Environment

June, 2019

Intellectual Property and Publication Statements

The candidate confirms that the work submitted is his own and that appropriate credit has been given where reference has been made to the work of others.

Acknowledgements

I thank Allah for giving me the strength and making this possible.

I would like to thank my supervisors at the University of Leeds Dr. Richard Collier, Prof. Douglas Paton and Dr. Estelle Mortimer for their support and guidance throughout this project.

I thank my employer Saudi Aramco for sponsoring my postgraduate studies. I am particularly grateful to Maher Marhoon (GTT Chief Technologist), and my mentor Mahdi Abu-Ali for their continued support and encouragement and previous mentor Paul Nicholson for his guidance prior to the PhD journey. I would like to express my gratitude to the Red Sea Exploration Department (RSED) for supporting this PhD, particularly Saleh Alsaleh (RSED Manager). I am grateful to Prof. Abdulkader Afifi for his insightful scientific ideas and logistic support. Thanks also to Aramco Overseas (London) particularly my advisors Mr. Ben Williamson and Mrs. Aggie Cooper. Special thanks to my colleague and friend Abdullah Almusaeed for his company in the field, logistic support and insightful discussions. I am also grateful to Fahd Almalki, Hussain A. Qattan, Hussain S. Qattan and Obai Shaikh for sparing their time and effort and volunteering to accompany me to the field.

Special thanks go to Dr. Gareth Roberts (Imperial College London) for performing the drainage inverse modelling and his great comments and feedback. Thanks to Prof. Finlay Stuart (SUERC and the University of Glasgow) for facilitating the thermochronological analyses and his insightful discussions. Thanks also go to SUERC laboratory personnel for their time and effort and to Dr. Cristina Persano (University of Glasgow) for her insightful discussions.

Thanks to my dear friend Ibrahim Almakrami for his discussions and coffee breaks.

To my mother, my father and my sister, who, despite their illness and hard lives, gave me support and endeavored to make my life better. I will always be in their debt. I hope they are in a better place.

… to my aunt, brothers, nephews, nieces and their families for believing in me.

… to Hajar for the love she gave and the sacrifices she made. This difficult journey wouldn't be possible to complete without her.

… to Norah, the light that shone upon our lives when all of this just started, for the joy she brought along.

… to family and friends.

Abstract

The geodynamic evolution of continental rifts and rifted margins influences petroleum prospectivity. Rift studies have tended to focus on offshore domains, whilst a more holistic approach would also consider sub-aerial data, providing information on rift flank uplift, drainage evolution and sediment routing.

The Neogene northern Red Sea rift allows examination of the interaction between geodynamics, tectonics and geomorphology. Here, its tectono-geomorphic evolution is assessed by integrating drainage inverse modelling, drainage analysis, low-temperature thermochronology and structural mapping.

On the margin scale, inverse modelling shows an early uplift (~22-15 Ma) in the southern part of the northeastern Red Sea and northern Gulf of Suez margins, and a later uplift (~14-0 Ma) along the northeastern Red Sea/Gulf of Aqaba, Sinai and northern Egyptian Red Sea margins. A smaller scale (20-30 km) study using low-temperature thermochronology and structural mapping reveals that pre-existing structures of suitable orientation do not all show resolvable reactivation during Red Sea rifting.

The present-day drainage records the interplay of basement heterogeneities, rift-related uplift and later uplift. North-directed pre-rift drainage was modified forming transfer, hangingwall and footwall catchments. Later uplift reorganised drainage by reversal and capture, changing catchment sizes and relocating catchment outlets.

The early uplift is interpreted to have been driven by rifting with possible mantle support and the later uplift was driven largely by transform tectonics and dynamic support by mantle flow. The catchment distribution indicates that early northern Red Sea rifting was accommodated by SW-dipping faults, with polarity changing further north into, and within, the Gulf of Suez.

This study benefits from the integration of several datasets, and highlights rift geodynamic complexity and the necessity to integrate surface and subsurface data to constrain sediment pathways for petroleum exploration.

Contents

Acknowledgements ii

Abstract iii

List of Tables ix

List of Figures x

List of Abbreviations xxix

Chapter 1 Introduction 2

1.1 Rationale 2

1.2 Aims and objectives 4

1.2.1 Research questions and implications 5

1.2.2 Study area 5

1.3 Thesis layout 7

Chapter 2 Generic and regional background 9

2.1 Introduction 9

2.2 Landscape evolution at rifts and rifted margins 9

2.2.1 Continental extension 10

2.2.2 Uplift, erosion and exhumation 14

2.2.3 Drainage reorganisation 16

2.2.4 Quantifying continental uplift 22

2.2.5 Quantifying exhumation 25

2.3 Geologic setting of the Red Sea 27

2.3.1 Pre-rift setting 27

2.3.2 Afar Plume 30

2.3.3 Rift-normal extension 33

2.3.4 Oblique extension and initiation of Aqaba-Levant transform 34

2.3.5 Aqaba-Levant transform strain localisation in the north and sea-floor spreading in the south 36
2.3.6 Geodynamic models....37
2.3.7 Cenozoic geomorphic evolution 38
Chapter 3 Uplift evolution of continental rifts from drainage analysis: observations from the northern Red Sea and Gulf of Aqaba....46
3.1 Introduction....46
3.2 Methodology 48
3.2.1 Data....49
3.2.2 Methods 49
3.3 Results....60
3.3.1 Geomorphic characterisation 60
3.3.2 Uplift estimation....72
3.3.3 Minimum erosion and local relief estimation....79
3.4 Discussion 82
3.4.1 Morphotectonic evolution of the NE Red Sea and eastern Gulf of Aqaba margins....82
3.4.2 Geodynamic implications 86
3.4.3 Implications for sediment entry points 88
3.5 Conclusions 89
Chapter 4 Structural mapping of the faults southeast of the Midyan Peninsula, northeastern Red Sea margin 91
4.1 Introduction....91
4.2 Stress history and structures around the northern Red Sea 95
4.3 Methodology 98
4.3.1 Field mapping approach....98

4.3.2 Stereographic analyses 99
4.4 Results 104
4.4.1 Structural mapping results 104
4.4.2 Principal paleo-stress orientations 124
4.5 Discussion and conclusions 128
Chapter 5 Tectono-geomorphic evolution of the northeastern Red Sea margin during and after rifting: insights from low-temperature thermochronology 132
5.1 Introduction 132
5.2 Low-temperature thermochronology 136
5.2.1 Apatite fission track analysis (AFTA) 139
5.2.2 Apatite (U-Th)/He analysis (AHe) 141
5.3 Cenozoic exhumation history of the northern Red Sea margins 142
5.4 Methodology 146
5.4.1 Sample transect: The Sharma-Tabuk Road Transect 146
5.4.2 Sample selection 150
5.4.3 Laboratory procedure 150
5.4.4 Inverse thermal modelling 153
5.5 Results 157
5.5.1 AFT analysis 157
5.5.2 AHe analysis 165
5.5.3 Thermal modelling results 167
5.6 Discussion 172
5.6.1 Tectono-geomorphic evolution at the fault block scale 172
5.6.2 Tectono-geomorphic evolution at the margin scale 177
5.7 Conclusions 181

Chapter 6 Drainage evolution across rifts and rifted margins: Implications on the sediment pathways into the northern Red Sea and nearby basins 183
6.1 Introduction 183
6.2 Paleo-drainage around the northern Red Sea: current understanding ... 186
6.3 Methodology 189
6.3.1 Data 189
6.3.2 Methods 189
6.4 Results 191
6.4.1 Uplift estimation 191
6.4.2 Drainage analysis 202
6.4.3 Drainage evolution 220
6.5 Discussion 228
6.5.1 Assessment of uplift estimates 228
6.5.2 Controls on drainage evolution in rifts and rifted margins 230
6.5.3 Implications for sedimentation 233
6.6 Conclusions 234
Chapter 7 Summary and Concluding Remarks 237
7.1 Review of research focus 237
7.2 Synopsis of results 237
7.2.1 Uplift history 237
7.2.2 Exhumation history 238
7.2.3 Drainage evolution 239
7.3 Implications 241
7.3.1 Implications for the geodynamics 241
7.3.2 Implications for hydrocarbon prospectivity in rifts and rifted margins 244

7.4 Recommendations for future work 246

List of References 247

Appendix I 269

List of Tables

Table 5.1: Samples collected along the Sharma-Tabuk Road Transect, southeastern Midyan Peninsula. The light blue shading highlights the samples for which the analyses were performed. The asterisk * samples were dismissed at the visual inspection stage as unsuitable for analysis before preparation; the double asterisk ** samples did not yield apatites after laboratory separation was conducted. AFT = AFT dating; AHe = AHe dating; AFTL = AFT length measurements. Note the correlation between different granitic rocks and the apatite yield. 149

Table 5.2: AFT ages and mean track lengths of the Sharma-Tabuk Road transect samples. ρs is the ratio of the number of tracks per area. 160

Table 5.3: Mean AHe ages from the transect samples averaging selected single grain ages marked by red dots in Figure 5.13. 167

Table 5.4: Summary of the models that were run and the data used as input. Where the modelling resulted in GOF values >50 the corresponding cell is marked with a tick (✓). * In this run only AFT ages and AHe ages were used as input data (i.e. no FT length measurements). ** In this run one single grain AHe age (19.5±3.9 Ma) yielded GOF value of 0.92 and the other (25.3±5.1 Ma) yielded a value of 0.23.The light blue cells indicate the best models that are considered in the discussion later. 168

List of Figures

Figure 1.1: A Google Earth map showing the extent of the study areas. Yellow polygon: Chapter 3; Light blue polygon: Chapter 4 and 5; Red polygon: Chapter 6. Regional tectonic elements and Gulf of Suez faults are from Bosworth et al. (2005). Al Wajh (AWB) and Yanbu (YB) Basins faults are from Szymanski et al. (2016). Midyan Basin (MB) faults are from Tubbs et al. (2014). Purple lines: Precambrian basement structures; red lines: faults (Bosworth, 2015). RS: Red Sea; GA: Gulf of Aqaba; GS: Gulf of Suez; MS: Mediterranean Sea; MMN: Makkah-Madinah-Nafud volcanic trend; WAB: Wadi Azlam Basin; GD: Gebel Duwi. 6

Figure 2.1: Schematic diagrams showing (a-b) the two-end member modes of rifting with respect to the involvement of mantle (Modified from Bott (2006)), and the original models of (c) pure-shear (McKenzie, 1978) and (d) simple shear (Modified from Wernicke (1985)). The spatial and temporal relationship between uplift and onset of rifting can be deduced. 11

Figure 2.2: Schematic evolutionary diagrams depicting the stages of rifting: (a) Initiation of faulting; (b) Interaction and development of linkages between individual faults through transfer faults; (c) Development of through-going faults that localise deformation (Modified from Gawthorpe and Leeder (2000)). The thick black arrows indicate the direction of extension. 13

Figure 2.3: Processes of drainage reorganisation. Particular emphasis is put on the effect of uplift that could lead to drainage reversal or diversion. Diagrams of diversion, beheading and capture are modified from Bishop (1995). 18

Figure 2.4: Typical drainage domains in continental rift settings: footwall drainage, hangingwall drainage, transfer zone drainage and axial drainage (Modified from Gawthorpe et al. (1994)). 20

Figure 2.5: Development of drainage catchments during continental rifting leading to marine incursion (Modified from Gawthorpe and Leeder (2000)). (a) pre-rift drainage; (b) early rift depocentres and fragmentation of the drainage into small catchments; (c) integration of catchments as depocentres on the rift flanks are

abandoned and left as relict basins; (d) possible modification of the drainage by drainage reversal. 21

Figure 2.6: A schematic cross-section showing stream profiles in steady state (i.e. uplift rate (U) = erosion rate (E); blue) and transient state (green) (Modified from Whipple and Tucker, 1999). Upon uplift, erosion works to return the landscape to the pre-uplift state (dashed green line) and the wave of erosion is active below a knickpoint that migrates upstream. Note that the profile becomes steeper upon uplift. 24

Figure 2.7: A Google Earth map showing the tectonic setting around the Red Sea. Regional tectonic features and Gulf of Suez faults are from Bosworth et al. (2005). Hamd-Jizl (HJB), Al Wajh (AWB) and Yanbu (YB) Basins faults are from Szymanski et al. (2016). Midyan Basin (MB) faults are from Tubbs et al. (2014). Purple lines: Precambrian structures (Modified from Dixon et al. (1987) and Johnson et al. (2011)); red lines: Red Sea rift faults; light blue lines: Gulf of Aqaba strike-slip faults; dashed white line: Arabian and Ethiopian escarpments (Bosworth, 2015; and this study). RS: Red Sea; GA: Gulf of Aqaba; GS: Gulf of Suez; AG: Arabian Gulf; MS: Mediterranean Sea; MMN: Makkah-Madinah-Nafud volcanic trend; WAB: Wadi Azlam Basin, GD: Gebel Duwi. 28

Figure 2.8: Generalised stratigraphic columns of the Gulf of Suez and the northern and southern Red Sea margins (Modified from Bosworth and Burke (2005)). The earliest Miocene Qattar Formation in the N. Red Sea column is incorporated into the stratigraphy after Szymanski (2013), the Mid-Clysmic unconformity is after Tubbs et al. (2014) and the volcanics are added after Bosworth et al. (2005). The late-rift stage represents the oblique extension and Aqaba-Levant transform initiation. 30

Figure 2.9: Plate-scale evolution of the Red Sea and the adjacent plates and gulfs, showing the plate motion directions (Modified from Bosworth et al. (2005)). 31

Figure 2.10: A map of the Red Sea margins showing the extent of the Nubian (African) and Arabian Shields, and the distribution of the volcanism (Modified from Stern and Johnson (2010)). 32

Figure 2.11: Topography and bathymetry of the Red Sea and surrounding areas. Topographic data (above sea-level) are from GLOBE Task Team et al. (1999). The bathymetry (below sea-level) was constructed using depth points downloaded from https://topex.ucsd.edu/cgi-bin/get_data.cgi (Smith and Sandwell, 1997). The two datasets were combined using Esri ArcMap. The dashed lines are the locations of the cross sections in Figure 2.12. Note the topographic asymmetry where the Arabia surface is mostly higher than the African surface. 39

Figure 2.12: Topographic-bathymetric cross-sections across the northern (top), central (middle) and southern (bottom) Red Sea extending to Arabia and Africa. The locations of the sections are shown in Figure 2.11. The sections show the topographic asymmetry, which is clearest in the north. VE is approximately 300:1. 40

Figure 3.1: A geological map of the study area showing the major lithological units, rift basins, major rift faults and basement Precambrian structures (Modified from Brown et al. (1989), Clark (1987) and Powell et al. (2014)). The location of the geological map with respect to the Red Sea, Arabia and Africa is shown in the inset map (red polygon). Pal.: Paleozoic strata; Mes.: Mesozoic strata.....48

Figure 3.2: A chart showing the workflow followed in this chapter to a) extract drainage catchments and estimate minimum erosion volume, b) extract data for use in the drainage inverse modelling, and c) estimate the local relief. 50

Figure 3.3: A frequency plot, in logarithmic scales, of areas of all catchments extracted from the northeastern Red Sea (NERS) and eastern Gulf of Aqaba (EGA) margins DEM (WGS84, UTM zone 37°N). Note the large number of small catchments that were not analysed in terms of their tectonic settings. 51

Figure 3.4: (a) Selected extracted longitudinal profiles (grey solid lines) shown along with modelled profiles (black dotted lines) generated by calculating the uplift history that minimises the misfit between the two sets of profiles. The catchments that the streams were extracted from are indicated (NERS19 and NERS20; refer to Figure 3.7 for catchments numbers). (b) The locations of the extracted streams. .55

Figure 3.5: An example of the extracted drainage data used in the inverse modelling. (a) A catchment draining to the Red Sea showing the drainage network (blue lines) overlaid on the topography. The inset map shows the catchment location with respect to the NERS catchments (red-filled polygon). (b) Data extracted from the selected red star locations shown along the thick blue stream line in (a). Along the stream, extracted points are 30 to 43 m apart. The XY locations are with reference to GCS_Ain_el_Abd_1970 (Lambert Conformal Conic projection). 56

Figure 3.6: A catchment example showing the approach used to estimate the minimum erosion maps: minimum height, minimum volume for each catchment and the ratio of minimum volume to catchment area. (a) Present-day topography (DEM) surface. (b) Pre-incision theoretical elevation surface constructed by interpolation between interfluve heights. (c) A cross-section showing the concept behind the construction of the pre-incision surface. Note that the red line drawing is a schematic and does not represent how the surface is practically produced and is included here for an explanatory purpose. In practice, interpolating between the interfluves heights is performed in 3D rather than across a 2D cross-section. (d) The minimum erosion height map generated by subtracting the present-day topography (a) from the pre-incision map (b). (e) The minimum eroded volume map generated by summing up all of the eroded height values (d) within a single catchment. (f) The minimum eroded volume:catchment area ratio map. 59

Figure 3.7: Topography and drainage of the study area (WGS1984 UTM Zone 37°N). (a) A DEM topographic map showing the drainage network, valley knickpoints and main onshore basins. Faults are compiled from Brown et al. (1989), Tubbs et al (2014) (northern zone), and Szymanski et al. (2016) (southern zone). The numbers inside the white circles are those of NERS catchments refer to in the text in section 3.3.1. (b) Areas of northeastern Red Sea (NERS#; >200 km^2) and eastern Gulf of Aqaba (inset map; EGA#; >20 km^2) drainage catchments. NZ: northern zone; SZ: southern zone (see text for explanation). 61

Figure 3.8: The mean (black line), maximum and minimum (grey lines) elevations along swath profiles of the escarpments: (a) The northern zone; (b) The southern

zone. Locations of swaths are shown on the map (thin black outlines) and the escarpments are shown as thick black lines. 63

Figure 3.9: Drainage network and faults at (a) Midyan Basin and E Gulf of Aqaba margin, (b) Wadi Azlam, and (c) Al Wajh, Hamd-Jizl and Yanbu Basins. NMF: Northern Midyan Fault, IEF: Ifal East Fault, JT: Jabal Tayran, JL: Jabal al Lawz, HU: Harrat Uwayridh and HR: Harrat ar Rahah. (d) DEM map of the study area showing the locations of (a-c). 64

Figure 3.10: (a-b) Northeastern Red Sea valley elevation-vs-distance profiles. Note that, overall, the profiles are characterised by concave-up shapes that get steeper both nearer to the escarpment and towards the north. The numbers refer to the NERS# numbers. The knickpoint along the orange profile (catchment NERS4) corresponds to the location of the erosional escarpment. The Gulf of Aqaba profiles are plotted using the same scale as the Red Sea profiles for easier comparison (thin black profiles in the yellow box in (a)). (c-d) Eastern Gulf of Aqaba valley profiles. The numbers refer to the EGA# numbers. Note the convex-up shapes of the profiles, and the steeper valleys along the middle of the gulf (pink, orange and green profiles) and the existence of a clear knickpoint separating a very steep section and a shallower section along the red profile.....69

Figure 3.11: Drainage reorganisation as deduced from planform analysis. (a) Interpreted misfit streams across the boundaries of catchments NERS1 and EGA1, indicating WNW to NW direction of the paleo-drainage. (b) Interpreted paleo-drainage directed to the northwest across NERS13, 17 and 19. (c) A close-up of an example of misfit streams where the valley is much wider than the streams. (d) Drainage network (blue lines) and catchment boundaries (green lines) overlaid on satellite imagery from Esri Global Imagery showing the locations of (a) and (b). Red dashed arrows: interpreted paleo-drainage. Yellow arrows: stream course change during drainage reorganisation.....71

Figure 3.12: (a-c) Extracted profiles (grey solid lines) shown along with modelled profiles (black dotted lines) generated by calculating the uplift history that minimises the misfit between the two sets for the northern part of the study area. The catchments from which the streams were extracted are indicated. Note that

the horizontal distances along the three panels are different. Misfit is observed at upstream sections at (c). (d-f): Corresponding locations of extracted streams (blue drainage lines). 74

Figure 3.13: (a-c) Extracted profiles (grey solid lines) shown along with modelled profiles (black dotted lines) generated by calculating the uplift history that minimises the misfit between the two sets for the southern part of the study area. The catchments from which the streams were extracted are indicated. Note that the horizontal distances along the three panels are different. (d-f): Corresponding locations of extracted streams (blue drainage lines). 75

Figure 3.14: Representative streams selected along the whole study area showing their extracted (grey solid lines) and modelled profiles (black dotted lines) plotted using the same horizontal scale. The catchments from which the streams were extracted are indicated. The corresponding locations of extracted streams are shown on the right (blue drainage lines). 76

Figure 3.15: Maps of the study area showing the coverage (i.e. the number of data points used to extract the uplift rate value in a given cell) of the inverse modelling method through time. The dots at time 0 Ma show the locations of the vertices that were used to insert the uplift rates estimated from the inverse modelling. 77

Figure 3.16: Results of the inverse modelling showing the uplift evolution of the study area. (a) Cumulative uplift magnitude at present-day. (b) Spatial and temporal evolution of the uplift rates (21 Ma to present). The faults are shown in black lines and the basins are indicated at the 21 Ma uplift rate map. The volcanic fields (harrats) are shown in purple starting at the approximate time at which they erupted (see cumulative uplift map for their names). 78

Figure 3.17: Erosion volume across the study area. (a) A minimum erosion map produced using interfluves elevations to construct per-erosion topography. (b) A map of the catchments draining to the Red Sea (NERS#) and Gulf of Aqaba (EGA#) with areas >200 km^2 showing the contribution of eroded volume from each catchment. (c) A map of the ratio of minimum eroded volume divided by catchment area.....80

Figure 3.18: A local relief (10 x 10 km) map of the study area showing the two areas of high relief values. 81

Figure 3.19: A multi-stage tectono-geomorphic model of the northeastern Red Sea and eastern Gulf of Aqaba utilising results from the inverse model and observations from the geomorphic and drainage analyses. Ages of volcanics are from Camp et al. (1991) and Bosworth et al. (2005). The drainage network in d is the present-day network and the streams are modified in a-c according to the interpretation of the large-scale drainage paleo-direction and how it may have been affected by the different uplift events. 83

Figure 4.1: A simplified geological map of the Midyan Peninsula (note location with respect to the Red Sea in the inset map) overlaid on a hillshaded DEM (Modified from Clark (1987)). Note that the mappable Cretaceous unit occurs only in the AyG and AdG. The black box outlines Figure 4.4. NMF: Northern Midyan Fault; IEF: Ifal East Fault; JZF: Jabal az Zuhd Fault; JZ: Jabal az Zuhd Mountain; SEF: South-Eastern Fault; JSh: Jabal ash Shati mountain; JD: Jabal Dabbagh Mountain; ShF: Sharma Fault; AdG: Adaffa Graben; AyG: Aynunah Graben. 93

Figure 4.2: (a) A DEM map of the eastern side of the Midyan Peninsula. Note the sediment-basement contact (thin dotted line) and the escarpment (dash-dotted line). (b) A composite topographic profile along JZF and SEF as observed from the southwest (from the blue star) composed of 20 profiles covering the blue polygon in (a) and are parallel to its NE and SW boundaries. Profiles close to the observer have dark shading, and vice-versa. (c) A photograph showing the topographic profile of the JZF. Black boxes on (a) and (b): the mapping area; Red star on (a): location where photograph (c) was taken. RS: Red Sea; JZ: Jabal az Zuhd; JZF: Jabal az Zuhd Fault; SEF: South-Eastern Fault; IEF: Ifal East Fault; JSh: Jabal ash Shati.....94

Figure 4.3: Summary map of the different stress orientations that have affected the area surrounding the northern Red Sea since the Late Cretaceous as well as the late evolution during the Neoproterozoic (see legend for references). The coloured arrows represent the extension direction (and the compression direction at Wadi Araba (WA)). The coloured structural symbols represent the dominant structural

response to the stress orientation. The translucent purple square indicates this chapter study area. MB: Midyan Basin; AWB: Al Wajh Basin; GD: Gebel Duwi; WA: Wadi Araba; NFS: Najd Fault System. 97

Figure 4.4: A geological map of the southeastern part of the Midyan Peninsula (Modified from Clark (1987)). Location of map is shown in Figure 4.1 and the white box outlines the location of Figure 4.5a. JZ: Jabal az Zuhd; JZF: Jabal az Zuhd Fault; SEF: South-Eastern Fault; IEF: Ifal East Fault; JSh: Jabal ash Shati; ShF: Sharma Fault; AdG: Adaffa Graben; AyG: Aynunah Graben. 101

Figure 4.5: (a) A close-up on the SEF (South-Eastern Fault) and JZF (Jabal az Zuhd Fault) showing the locations of systematic transect measurements of structural features (white stars). The white box outlines the location of Figure 4.5b. (b) Locations of the panels (outcrops along the Wadi Aynunah Valley) that were used to map part of the structural features of the SEF. Note locations of systematic transect measurements (white circles) that are close to the panels. 102

Figure 4.6: Examples of the metre-scale transect lines along which all fracture orientations were measured. The black and white arrows define the start and end of each line. The circle in Line 15 photo encloses a GPS device for scale. Locations of these lines (6, 7, 10 and 15) are also shown in Figure 4.5a. 103

Figure 4.7: (a) A structural geology map of the study area with detailed mapping of SEF structures (Lithology modified from Clark (1987)). JZ: Jabal az Zuhd mountain; JZF: Jabal az Zuhd Fault; IEF: Ifal East Fault; WA: Wadi Aynunah Valley; SEF: South-Eastern Fault; AyG: Aynunah Graben; AdG: Adaffa Graben; ShF: Sharma Fault. (b) The same map in (a) showing lower hemisphere equal-area projected stereonets of joints and shear fractures generated using Stereonet 10.0 (Allmendinger et al., 2011; Cardozo and Allmendinger, 2013). The slip directions were plotted using FaultKin 8.0 (Marrett and Allmendinger, 1990; Allmendinger et al., 2011) then added to the stereonets. The number next to each stereonet plot is the number of data points (i.e. joint/shear fracture plane orientation). The rainbow contours are plotted for the density of the poles to planes. The slip direction arrows in the stereonet plot marked by the asterisks (*) were coloured in red only for clarity given the dark background. The double-headed

coloured arrows to the bottom-left corner of the map represent the regional horizontal extension direction from the literature: red: Late Neoproterozoic (Johnson et al., 2012); blue: Late Cretaceous (Bojar et al., 2002; Bosworth et al., 2005); black: Miocene (Bojar et al., 2002; Bosworth et al., 2005); green: Plio-Pleistocene (Bosworth and Strecker, 1997); grey: Present-day (ArRajehi et al., 2010). The stratigraphy and structure key is as shown in (a).....105

Figure 4.8: Spacing and frequency of fractures with respect to their orientation (bottom frequency graphs), measured at a selected line transects that are perpendicular to local structural orientation along the SEF and JZF (top map). The lithology code is as per Figure 4.7. The black dots in the graphs represent the spacing between the fractures, whereas the blue columns represent the number of fractures corresponding to each zone of strike angles (horizontal axis). The grey angle band represents the general Red Sea trend. 107

Figure 4.9: (a) An overview photograph of the JZF showing basement rock to the left (NE) and conglomerate to the right (SW) (28°14'13.99"N, 35°16'20.62"E). The fault zone is about 10 m in this view. (b) Fracturing at a basement granitic outcrop associated with the JZF (28°16'11.44"N, 35°11'13.71"E). (c) A close-up of the fractured basement shown in (b). (d-e) An example of fault gouge with orientation semi-parallel to the JZF (28°16'15.61"N, 35°11'16.69"E).....110

Figure 4.10: An example of striations indicating local left-lateral strike-slip deformation at the southeastern end of JZF (28°13'55.73"N, 35°17'22.50"E). Displacement direction (i.e. movement of the removed rock) is indicated by the white arrow and number. 111

Figure 4.11: Panel 1 interpretation. Note the lens-shaped blocks over different scales. The deformation is concentrated at a number of faults bounding blocks that are less deformed. The orientations of the structural features are plotted on the stereonet at the bottom right. 113

Figure 4.12: Panel 2 interpretation showing complex brittle deformation. The foreground of the view is ~850 m-wide. Note the fracture distribution with respect to distance along lines 11 and 12 (a bin size of 10 cm was used to produce the

histograms). The fracture density varies along the metre-transect lines within the basement blocks. For fracture spacing and frequency distribution with respect to fracture strike see Figure 4.8. Complex brittle and some ductile deformations over a number of scales are shown in a-e (next page). The orientations of the structural features along the panel are plotted on the stereonets at the bottom. 114

Figure 4.13: Panel 3 interpretation showing faults of various orientations separating zones of less deformation. This outcrop features less fracturing compared to other panels, which is related to its position within a less deformed, low strain, host basement rock (see Figure 4.18). The orientations of the slip surfaces and faults are plotted on the stereonet at the bottom right. 116

Figure 4.14: Panel 4 interpretation showing two zones of relatively high brittle deformation bounding a lower strain basement block. Note the fracture distribution with respect to distance along lines 1 and 2 (top left; a bin size of 10 cm was used to produce the histograms). Notice the general increase in fracture number at the southern sides of the metre-transect lines towards the fault. For fracture spacing and frequency distribution with respect to fracture strike see Figure 4.8. The two stereonets at the bottom show the structural orientations. 117

Figure 4.15: Panel 5 interpretation showing lenses of fractured basement between zones of higher brittle strain/faulting. Note the relationship between foliation and brittle deformation. Note the fracture distribution with respect to distance along line 10 (bottom right; a bin size of 10 cm was used to produce the histogram), where the fracture density increases towards the fault. For fracture spacing and frequency distribution with respect to fracture strike see Figure 4.8. The stereonet at the bottom right shows the structural orientations. 118

Figure 4.16: Panel 6 interpretation showing a 3-4 metre thick south-dipping fault. Note the existence of metre-scale lens-shaped blocks (a), fault rock (b) and slip surfaces (yellow arrows in c-d). The stereonet at the bottom right shows the structural orientations. 119

Figure 4.17: Examples of slip surfaces from the southeastern part of the SEF (28°11'24.12"N, 35°25'49.90"E). The white arrows and bearings represent the direction of slip of the removed rock. 120

Figure 4.18: (a) A detailed structural map of the SEF at Wadi Aynunah, showing the complexity of this zone (solid lines are mapped faults and dashed lines are inferred and uncertain faults). (b) A simplified cross-section along the purple line in (a). (c) A 3D view of the fault zone constructed to show its complexity. The red stars denote the two zones of brittle deformation bounding the granitic block. Note the interpretations of panels 2 (Figure 4.11), 4 (Figure 4.14) and 5 (Figure 4.15). 121

Figure 4.19: Overview outcrop photograph of the slip surfaces at the footwall of Sharma Fault (ShF; 28° 3'0.40"N, 35°15'50.22"E). The white arrows and bearings represent the direction of slip of the downthrown rock. 123

Figure 4.20: Examples of a fault surface approximately ~1 km northeast of Adaffa Graben (AdG; 28° 4'19.30"N, 35°18'51.05"E). (Left) A fault surface dipping to the north. (Right) Striations along the surface indicate normal sense of slip of footwall rock towards the north. General slip direction is indicated by the white arrow. 123

Figure 4.21: Examples of faulting along the eastern boundary of Aynunah Graben (AyG; 28° 6'34.40"N, 35°16'5.02"E). General slip directions are indicated by the white arrows. (Left) Fractures and slip surfaces dipping mostly to the west. (Right) Striations that indicate highly oblique to normal sense of displacement. 124

Figure 4.22: Paleo-stress analysis of shear fractures using SG2PS (Sasvári and Baharev, 2014). σ1, σ2 and σ3 orientations are indicated below each stereonet, respectively. The mean vectors of the shear fractures are shown in the rectangles below each stereonet. The number of data points is indicated at the top left of each stereonet. The asterisks * indicates where the joints were used for the stress inversion assuming perfectly normal slip as no slip indicators were measured (joint poles plotted and contoured using Stereonet 10.0 (Allmendinger et al., 2011; Cardozo and Allmendinger, 2013)). The double-headed coloured arrows (top right of map) indicate the regional horizontal extension: red: Late Neoproterozoic

(Johnson et al., 2012); blue: Late Cretaceous (Bojar et al., 2002; Bosworth et al., 2005); black: Miocene (Bojar et al., 2002; Bosworth et al., 2005); green: Plio-Pleistocene (Bosworth and Strecker, 1997); grey: Present-day (ArRajehi et al., 2010). JZ: Jabal az Zuhd mountain; JZF: Jabal az Zuhd Fault; SEF: South-Eastern Fault; JSh: Jabal ash Shati; AyG: Aynunah Graben; AdG: Adaffa Graben; ShF: Sharma Fault. 126

Figure 4.23: A simplified 3D view of the SEF and JZF highlighting the along-strike variation in structural styles from localised Oligo-Miocene normal faulting at the JZF to more distributed deformation (localisation at smaller faults) at the SEF. ..130

Figure 5.1: (a) A simplified geological map of the Midyan Peninsula overlaid on a hill shaded DEM (Modified from Clark (1987)). The white line is the position of (b). The two yellow lines are approximate positions of the apatite and zircon (U-Th)/He transects presented in Stockli and Bosworth (2019). NMF: Northern Midyan Fault; IEF: Ifal East Fault; JZF: Jabal az Zuhd Fault; JZ: Jabal az Zuhd mountain; SEF: South-Eastern Fault; JSh: Jabal ash Shati mountain; JD: Jabal Dabbagh mountain; ShF: Sharma Fault; AdG: Adaffa Graben; AyG: Aynunah Graben. (b) A topographic cross-section showing the main geomorphic elements of southeastern Midyan (see line of section on (a). 135

Figure 5.2: Nominal temperature ranges for different thermochronometric systems (Modified from Gallagher and Brown (1999) and Peyton and Carrapa (2013)). The apatite FT and (U-Th)/He (purple and pink boxes, respectively) represent the most suitable of these systems for quantifying thermal evolution of the uppermost continental crust. PAZ: apatite FT partial annealing zone; PRZ: apatite (U-Th)/He partial retention zone (see text for explanation). 136

Figure 5.3: (a-c) Cartoon cross-sectional view of the end-member models of passive margin escarpment evolution (Modified from Gallagher et al. (1998)). (d) The low-temperature thermochronological age-vs-distance plots corresponding to the end-member models. Note that even for the same topography, the expected behaviour of the FT ages across the margin for each model is different.....139

Figure 5.4: A compilation of northern Red Sea and nearby margins AFT and AHe data from existing studies (citations in figure) and the current study. Yellow lines: approximate locations transects presented in Stockli and Bosworth (2019) and discussed in text. MB: Midyan Basin; WAB: Wadi Azlam Basin; AWB: Al Wajh Basin; HJB: Hamd-Jizl Basin; YB: Yanbu Basin; JZ: Jabal az Zuhd; JD: Jabal Dabbagh; GD: Gebel Duwi. 144

Figure 5.5: A geological map of the southeastern part of the Midyan Peninsula (Modified from Clark (1987)) showing the locations of samples collected for thermochronological analysis along the Sharma-Tabuk Road Transect (black circles: apatite grains extracted; white circles: no apatite grains extracted). 148

Figure 5.6: An example of the HeFTy data input interface and parameters (sample 16-T1-11a). (a) Input of AFT data. Note: only 30 (out of 153) length measurements are shown in this figure. (b) Input and parameters of a single grain AHe age. 156

Figure 5.7: A cross-section along the Sharma-Tabuk Road transect, showing samples 16-T1-3a, 5a, 6a, 10a and 11a. Between the brackets, the pooled AFT age and AHe age are shown in Ma (rounded to the nearest Ma), respectively. The SEF is plotted as one fault rather than a zone of faults for simplicity. The simplified geological map (top right) shows the position of the transect line (yellow line) and the locations of the samples with respect to the main structures. 159

Figure 5.8: A radial plot showing single grain age dispersion and whole sample central age for sample 16-T1-3a. The axes are: age (Ma; right), single-grain precision increasing to the right (bottom) and single grain age deviation from the mean (i.e. deviation from a line connecting the origin (0,0) and the central mean to the right (left). The points are coloured according to the D_{par} value. n is the number of grains for which ages were calculated. 161

Figure 5.9: (a-b) Radial plots showing single grain age dispersion and whole sample central age for sample 16-T1-5a, using all of the analysed grains (a) and a selected number of the highest quality grains (b). Note that there are two age peaks that can be deciphered from the point distribution. The axes are: age (Ma; right), single-grain precision increasing to the right (bottom) and single grain age

deviation from the mean (i.e. deviation from a line connecting the origin (0,0) and the central mean to the right (left). The points are coloured according to the D_{par} value. n is the number of grains for which ages were calculated. (c) Distribution of track lengths measured from sample 16-T1-5a. TL= track length. 162

Figure 5.10: (a) and (b) Radial plots showing single grain age dispersion and whole sample central age for sample 16-T1-6a, using all of the analysed grains (a) and a selected number of the highest quality grains (b). Note that there are two age peaks that can be deciphered from the point distribution. The axes are: age (Ma; right), single-grain precision increasing to the right (bottom) and single grain age deviation from the mean (i.e. deviation from a line connecting the origin (0,0) and the central mean to the right (left). The points are coloured according to the D_{par} value. n is the number of grains for which ages were calculated. (c) Distribution of track lengths measured from sample 16-T1-6a. TL= track length. 163

Figure 5.11: (a) and (b) Radial plots showing single grain age dispersion and whole sample central age for sample 16-T1-10a, using all of the analysed grains (a) and a selected number of the highest quality grains (b). The axes are: age (Ma; right), single-grain precision increasing to the right (bottom) and single grain age deviation from the mean (i.e. deviation from a line connecting the origin (0,0) and the central mean to the right (left). The points are coloured according to the D_{par} value. n is the number of grains for which ages were calculated. (c) Distribution of track lengths measured from sample 16-T1-10a. TL= track length. 164

Figure 5.12: (a) A radial plot showing single grain age dispersion and whole sample central age for sample 16-T1-11a. The axes are: age (Ma; right), single-grain precision increasing to the right (bottom) and single grain age deviation from the mean (i.e. deviation from a line connecting the origin (0,0) and the central mean to the right (left). The points are coloured according to the D_{par} value. n is the number of grains for which ages were calculated. (b) Distribution of track lengths measured from sample 16-T1-11a. TL= track length. 165

Figure 5.13: Dispersion of single grain AHe ages from the transect samples. Note the over-dispersion in samples 16-T1-3a, 10 and 11a and to some extent 5a. The

red dots represent the single grain ages used in the calculation of the mean ages of the samples in Table 5.3. 167

Figure 5.14: HeFTy models showing t-T paths, measured and modelled c-axis projected FT length distributions. Green lines: acceptable fit; pink: good; black: best. The model starting age is always older than double the AFT central age (see constraining boxes (blue rectangles)). 16-T1-3a was modelled with (right) and without (left) an imposed constraint at the onset of rifting (~23 Ma). Only AFT data were used in the modelling of 16-T1-5a and 11a. The vertical line with the star at the top represents the time of the onset of the Red Sea rifting. 171

Figure 5.15: (a) A cross-section along transect 16-T1 showing the range of depths of erosion using a range of paleo-geothermal gradients (20-60 °C/km), where the maximum possible depth of erosion corresponds to the 20 °C/km gradient, and vice versa. Erosion depth estimation is based on the cooling magnitudes since the onset of rifting (~23 Ma) deduced from the HeFTy models. (b) Diagrammatic calculation of the maximum possible displacement across SEF, where end-member geothermal gradients are assigned to 16-T1-5a and 6a as shown. Note that, even with this extreme scenario, the maximum possible displacement across the SEF would not be detectable using the low-temperature thermochronology techniques employed here. (c) Simplified geological map showing the cross-section line. 175

Figure 5.16: A proposed model for the tectono-geomorphic evolution of the NE Red Sea margin along the transect of the samples used for the thermochronological study (location of transect is the same as that of Figure 5.15). ShF: Sharma Fault; SEF: South-eastern Fault; JSh: Jabal ash Shati. The depth of erosion at each sample location is calculated using 50-55°C/km paleo-geothermal gradients. The dashed line does not exactly represent a paleo-surface, but is constructed based on depth of erosion from each sample. The thin black lines are schematic demonstrating how erosion evolved. Note that ShF could have initiated a fault scarp that retreat to form the present-day escarpment but the along-strike (NW-directed) drainage would have played a more major role. Note also that SEF did not have a measureable effect on the paleo-topography prior to the erosion and

that the paleo-geothermal gradient at 16-T1-5a was possibly extremely high and local. The red lines represent dykes without reference to their age. 179

Figure 5.17: A schematic 3D model showing the interpretation deduced for the tectono-geomorphic history of the study area, proposing that the area represented a relay ramp between two SW/SWW-dipping normal faults. JZF: Jabal az Zuhd Fault; SEF: South-Eastern Fault; ShF: Sharma Fault; JD: Jabal Dabbagh. JD is shown to relate to the exhumation estimate by Stockli and Bosworth (2019). 181

Figure 6.1: A satellite imagery map showing the study area (dashed white polygon). Also shown are the major rift basins and faults (black lines; Modified from Bosworth (1995), Tubbs et al. (2014), Bosworth (2015) and Szymanski et al. (2016)), the pre-rift Precambrian structures (Red lines: Modified from Bosworth et al. (2005) and Johnson et al. (2011)). Wadi Araba thrust and anticline (light blue) to the west of the Gulf of Suez are Late Cretaceous (Bosworth et al., 2005).....185

Figure 6.2: Simplified geological map of the study area, showing the pre-existing Proterozoic basement structures and rift faults. The Arabian geology is modified from Clark (1987), Brown et al. (1989) and Powell et al. (2014). The Egyptian and Sinai geology is modified from Egyptian Geological Survey and Mining Authority (1981). Midyan Basin (MB) faults are from Tubbs et al. (2014). Wadi Azlam Basin (WAB) and Gebel Duwi (GD) faults are from Bosworth (2015). Hamd-Jizl (HJB), Al Wajh (AWB) and Yanbu (YB) Basins faults are from Szymanski et al. (2016). Najd Fault System (NFS) and Hanabiq Shear Zone (HSZ) are from Johnson et al. (2011). DSb: Darag Sub-basin; CSb: Central Sub-basin; SSb: Southern Sub-basin. GoA: Gulf of Aqaba.....188

Figure 6.3: Cross-sectional and map views of the streams that were used to invert for uplift. On the cross-sections, the solid grey lines are the extracted stream profiles and the dotted black lines are the modelled profiles. Streams in (a), (c), (e), (g), (i) and (k) were extracted and conditioned by myself. The rest were provided by Dr. Gareth Roberts (Appendix I), who also performed the inverse modelling and generated the figure.....193

Figure 6.4: Maps of the study area showing the coverage (i.e. the unit-less number of data points used to extract the uplift rate value in a given cell) of the inverse modelling method through time. AR: Arabia, AF: Africa, and SN: Sinai. Maps in figure were generated by Dr. Gareth Roberts. 194

Figure 6.5: Uplift rate estimates of the study area during the early rift (22 Ma), the main rift (20 and 14 Ma) and the early strike-slip tectonics and oblique rifting (14 and 12 Ma). Rift and strike slip faults are shown as black lines. 198

Figure 6.6: Cumulative uplift estimates of the study area during the early rift (22 Ma), the main rift (20 and 14 Ma) and the early strike-slip tectonics and oblique rifting (14 and 12 Ma). Rift and strike slip faults are shown as black lines. 199

Figure 6.7: Uplift rate estimates of the study area during strike-slip tectonics and oblique rifting (8, 6 and 4 Ma) and the present day (0 Ma). Rift and strike slip faults are shown as black lines. 200

Figure 6.8: Cumulative uplift estimates of the study area during strike-slip tectonics and oblique rifting (8, 6 and 4 Ma) and the present day (0 Ma). Rift and strike slip faults are shown as black lines. 201

Figure 6.9: Catchments with outlets at the Red Sea, Gulf of Aqaba and Gulf of Suez showing their areas (WGS84, UTM zone 37°N). Numbers in black: NE Red Sea margin catchments (NERS); Yellow: SW Red Sea margin catchments (SWRS); Green: E Gulf of Suez catchments (EGS); Red: W Gulf of Suez catchments (WGS). Black box outlines Figure 6.10. 203

Figure 6.10: A close up of catchments with outlets at the Gulf of Aqaba coastline. Numbers in blue: E Gulf of Aqaba margin catchments (EGA); White: W Gulf of Aqaba margin catchments (WGA). Catchment 1 on the eastern Gulf of Aqaba margin (i.e. EGA1) extends beyond the figure view and is shown wholly in Figure 6.9. 204

Figure 6.11: A frequency plot (logarithmic horizontal scale) of areas of all catchments extracted from the northern Red Sea, Gulf of Suez and Gulf of Aqaba margins (WGS84, UTM zone 37°N). Note that catchment larger than 10,000 km^2 exist on both Red Sea margins and the eastern Gulf of Aqaba margins. 205

Figure 6.12: A DEM map showing the catchments, drainage and knickpoints along the northern Red Sea and the nearby gulfs. The map shows other streams outside the area of focus, including tributaries to the Nile. The white arrows show examples of data deterioration where extracted streams cross the catchments boundaries. The black boxes show the locations of Figure 6.13a (Arabian margin) and Figure 6.13b (African margin). The positions Figure 6.14 profiles are traced in red. 206

Figure 6.13: Satellite imagery showing examples of the interpretation of paleo-drainage directions that are incorporated into the present-day drainage from the Red Sea (a) Arabian and (b) African margins. Orange arrows represent the paleo-drainage direction interpreted here; yellow stars are locations of drainage capture; yellow diamond (top left of (a)) denotes approximate location of drainage reversal; blue arrows represent the direction of drainage after it has been modified. Red lines are Precambrian basement structures and black lines are Oligo-Miocene faults. 213

Figure 6.14: Selected stream profiles showing the overall shallower gradients of northward-flowing streams compared to southward-flowing streams within the large catchments in the study area as well as profiles of two Nile tributaries (Top three plots). The zero point along the Length axis is the point at which the streams join. Also shown is the incorporation of paleo-drainage into coastline-perpendicular rift-related drainage at NERS4 (Bottom). Locations are shown in Figure 6.12.....215

Figure 6.15: Present-day catchments along the northern Red Sea and nearby gulfs presented on restored plates to ~20 Ma. Note the relationship between the catchments and structures. Red lines: Precambrian structures; black lines: Cenozoic faults; blue polygons: catchments. FD: footwall drainage; HD: hangingwall drainage; AZD: accommodation zone drainage. Plate reconstruction was performed using Schettino et al. (2016) and Schettino et al. (2019) poles and angles or rotation. 219

Figure 6.16: A proposed drainage evolution model around the northern Red Sea during the early rift stage (Early Miocene) devised by combining the uplift

estimates, the structural evolution and the drainage interpretation. The blue lines are the inferred major rivers. AZ: Accommodation zone. 223

Figure 6.17: A proposed drainage evolution model around the northern Red Sea during the main rift stage and early strike-slip tectonics (Middle Miocene). Ages of volcanics are from Camp et al. (1991) and Bosworth (2005). The blue lines are the inferred major rivers. 225

Figure 6.18: A proposed drainage evolution model around the northern Red Sea during the late rift stage and intense strike-slip tectonics (Pliocene). Ages of volcanic harrats are from Camp et al. (1991) and Bosworth et al. (2005). The blue lines are the inferred major rivers.....227

Figure 7.1: Proposed model for the geodynamic evolution of the northern Red Sea. Both stages feautured significant uplift on the Arabian margin (uplift denoted by vertical arrows).....243

List of Abbreviations

NERS: Northeastern Red Sea

SWRS: Southwestern Red Sea

EGA: Eastern Gulf of Aqaba

WGA: Western Gulf of Aqaba

EGS: Eastern Gulf of Suez

WGS: Western Gulf of Suez

U: Uplift rate

$\int Udt$: Cumulative uplift

E: Erosion rate

t: Time

x: Distance along a stream to the base-level

$\frac{\partial z}{\partial t}$: Rate of elevation change

$\frac{\partial z}{\partial x}$: Stream slope

$\frac{\partial^2 z}{\partial x^2}$: Stream concavity

A: Upstream drainage area

v: Advection parameter (stream incision)

κ: Diffusion parameter (lowering of the landscape)

m: Dimentionless exponent of the upstream drainage area

n: Dimentionless exponent of the stream slope

τ_G: Landscape response time

MD: Midyan Basin

WAB: Wadi Azlam Basin

AWB: Al Wajh Basin

YB: Yanbu Basin

HJB: Hamd-Jizl Basin

NFS: Najd Fault System

IEF: East Ifal Fault

JZF: Jabal az Zuhd Fault

SEF: South-Eastern Fault

ShF: Sharma Fault

NMF: Northern Midyan Fault

JZ: Jabal az Zuhd Mountain

JD: Jabal Dabbagh Mountain

JSh: Jabal ash Shati Mountain

GD: Gebel Duwi Mountain

WA: Wadi Araba

AdG: Adaffa Graben

AyG: Aynunah Graben

AFTA: Apatite fission track analysis

AHe: Apatite (Uranium-Thorium)/Helium

AFTL: Apatite fission track length

PAZ: Partial annealing zone of fission tracks

PRZ: Partial retention zone of helium

T_c: Thermochronometric system closure temperature

D_{par}: Mean long diameter of a chemically etched fission track parallel to crystal c-axis

CARF: Central Arabian Rift Flank

SUERC: Scottish Universities Environmental Research Centre

LA-ICP-MS: Laser Ablation-Inductively Coupled Plasma-Mass Spectrometry method

λ_d = 1.55125x10^{-10} a^{-1} (^{238}U total decay constant)

ζ = A calibration factor for using LA-ICP-MS

ρ_s: Number of spontaneous fission tracks per unit area

FD: Footwall drainage

HD: Hangingwall drainage

AZD: Accommodation zone drainage

Part I: Introduction and background

Chapter 1 Introduction

1.1 Rationale

Continental rifts and rifted margins are areas of active and intensive research driven by questions relevant to the wide geological community (e.g. Olsen and Morgan, 2006; Bradley, 2008). Chief among the reasons to study these tectonic environments is the need to understand the processes and properties that play major roles in the rifting and break-up of lithospheric plates and the formation of oceans. For instance, significant efforts have been put into studying the tectono-stratigraphy of rifts and rifted margins (e.g. Gregersen et al., 2019), and temporal and spatial relationships between structures, strata, magmatic bodies and uplift have been used to give insights into the mechanisms of rifting (e.g. Sengör and Burke, 1978).

A more holistic approach would also consider the acquisition and interpretation of data from the sub-aerial part of the margin. Although mostly characterised by erosion and/or non-deposition, these parts of the margin hold information that can elucidate aspects of the margin evolution relevant to uplift, erosion and exhumation (e.g. Summerfield, 1993). Tectono-geomorphic processes that result in uplift, erosion and drainage evolution play significant roles in the mass balance of sediments from erosion in drainage catchments to accumulation in basins (Castelltort et al., 2015 *and references therein*). Understanding these aspects, therefore, should help in the overall understanding of the margin evolution, complementing data from the basins and continental shelf. In particular, the temporal and spatial distribution of uplift with respect to the rift processes gives insights into the driving mechanisms of lithospheric extension.

Furthermore, questions relevant to petroleum exploration fuel the research in these tectonic domains (e.g. Levell et al., 2010). Economically, continental rifts, sag basins and passive margins associated with major oceanic basins collectively host approximately two thirds of the global giant hydrocarbon fields (i.e. ≥500 Million barrels of oil equivalent (BOE); Mann et al., 2003). Understandably, the focus of the petroleum-oriented research in these domains has been on geophysical and

drilling data collected from rift and sag basins, as well as the marine parts of passive margins.

However, from a petroleum exploration perspective, as described earlier, understanding the tectono-geomorphic (drainage) evolution of the sub-aerial margin serves as a predictive tool for sediment dispersal into the rift and sag basins when incorporated to other studies (e.g. sediment provenance; Smyth et al., 2014 *and references therein*). Understanding how drainage evolved along a rift/rifted margin provides a framework that can be eventually used to identify areas along the margin where thick clastic units that have the potential to form reservoir rocks may be deposited. Moreover, another important aspect of the tectono-geomorphic evolution is that uplift along the margin is associated with erosion that works to keep the topography in a steady state (uplift rate = erosion rate). An important aspect related to the enhancement or reduction of erosion is the effect of elevated topography that might be imposed on the climate (e.g. orographic effects (Sepulchre et al., 2006). A by-product of this uplift-erosion relationship is supplying even more eroded material as sediments to downstream (rift basins) areas. Research that eventually results in the reduction of the risk of exploration would need to integrate different disciplines leading to better definition of plays and drilling targets. That is, stratigraphic and structural relationships in the basins need to be understood within the same spatio-temporal frame as the uplift and drainage evolution.

The Red Sea represents a tectonic spectrum that encompasses a young passive margin in the south and continental extension in the north (Bosworth et al., 2005). The youth of the Red Sea and the spatial variation of lithospheric and sub-lithospheric processes (present continental extension in the north, sea-floor spreading in the south, strike-slip tectonics in the Gulf of Aqaba, failed rifting in the Gulf of Suez, and the prior existence of plume volcanism at Afar) make it a natural laboratory to test different models of continental rifting and break-up (e.g. Bosworth et al., 2005; Almalki et al., 2015; Bosworth, 2015; Stockli and Bosworth, 2019). In addition, high interests in hydrocarbon exploration encouraged geological and geophysical research within the basins of the Red Sea, the Gulf of Suez and the Gulf of Aqaba (Bosworth et al., 2005 *and references therein*).

Expanding the knowledge of the evolution of the margin to the presently sub-aerial and basement-dominated domains of the northern Red Sea, therefore, would be beneficial for both scientific and petroleum-related research. Unlike passive margins where the geomorphology can be significantly modified and become different to the geomorphology during the rifting (Summerfield, 1993), the young Red Sea margins represent early stages along the rifting-to-break-up spectrum. This sets the scene to better assess how the geomorphology develops as rifting gave way to break-up and highlight the implications it has on understanding the geodynamics and to petroleum prospectivity.

1.2 Aims and objectives

This research project focuses on extracting geomorphological pieces of information from the northern Red Sea margins that may be integrated with each other and with the geology to better understand how these margins evolved. The aims are to investigate the tectono-geomorphic evolution during the Cenozoic rifting utilising the geomorphic signature, and relate this evolution to uplift driving mechanisms in space and time. These aims are achieved by fulfilling the following objectives:

1. Uplift variation along the northeastern Red Sea margin throughout the Cenozoic rifting stages is estimated and linked to driving mechanisms. These driving mechanisms are investigated by integrating the temporal and spatial (wavelength and location) aspects of the uplift events with the geological features of the margin (e.g. volcanism indicative of high temperature mantle source).
2. Exhumation along a transect that crosses the northeastern Red Sea sub-aerial margin is evaluated in terms of timing and magnitude with respect to rift flank uplift and erosion. The exhumation study extends from the fault-block scale (tectonic exhumation) to the margin scale (formation of an erosional escarpment).
3. Drainage evolution is investigated on all margins of the northern Red Sea (Arabian, African and Sinai margins) in light of the uplift estimates and drainage network analysis. This investigation takes into account the opening of the Red Sea, Gulf of Suez and Gulf of Aqaba and the effects that these events would have imposed on the drainage evolution. The drainage evolution on the margins is used as a predictive tool for point-source sediment inputs to the basins.

1.2.1 Research questions and implications

The research questions that this thesis attempts to answer with respect to the tectono-geomorphic evolution are:

- How did uplift evolve along the northeastern Red Sea and eastern Gulf of Aqaba margins, and what are the likely processes that drove its evolution?
- What is the geomorphic signature of rifting on the northeastern Red Sea rift flank, and how did the geomorphology evolve after the onset of rifting?
- How did uplift affect drainage evolution of all of the northern Red Sea (and adjacent gulfs) margins?

In terms of the implications of this work, the following questions may be addressed:

- What are the implications of estimating the spatio-temporal distribution of uplift for the geodynamics of rifting?
- What are the implications of understanding the tectono-geomorphic evolution for hydrocarbon prospectivity in rifts and rifted margins?

1.2.2 Study area

The study area is divided into three sub-areas, each is investigated using a different approach (Figure 1.1).

- Study area 1: Estimating uplift using drainage profile inversion was conducted on an area straddling the northwestern Arabian margin that extends from the Yanbu Basin to southwest Jordan, and from the coastline to approximately 250-km inland (Chapter 3).
- Study area 2: A more focused study of structural characterisation of brittle structures (Chapter 4) and exhumation history based on low-temperature thermochronology (Chapter 5) was conducted over an area located just to the southeast of the Midyan Basin, northeastern Red Sea.
- Study area 3: The study of the drainage evolution covers, in addition to the study area of Chapter 3, the southern part of Sinai, and the drainage catchments that drain towards the northern Red Sea and Gulf of Suez from the west, extending from the Egypt-Sudan boundary to the northernmost part of the Gulf of Suez (Chapter 6).

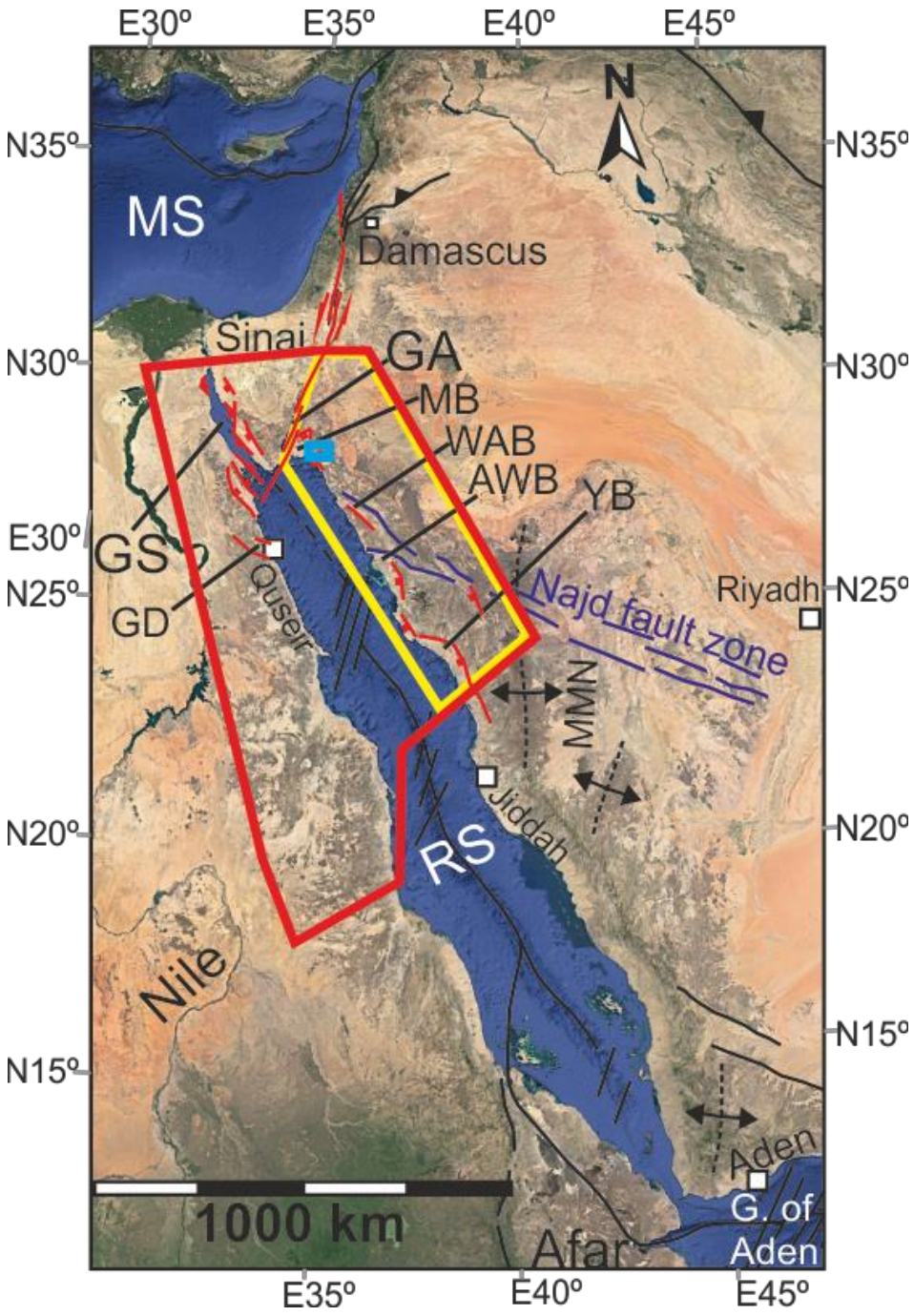

Figure 1.1: A Google Earth map showing the extent of the study areas. Yellow polygon: Chapter 3; Light blue polygon: Chapter 4 and 5; Red polygon: Chapter 6. Regional tectonic elements and Gulf of Suez faults are from Bosworth et al. (2005). Al Wajh (AWB) and Yanbu (YB) Basins faults are from Szymanski et al. (2016). Midyan Basin (MB) faults are from Tubbs et al. (2014). Purple lines: Precambrian basement structures; red lines: faults (Bosworth, 2015). RS: Red Sea; GA: Gulf of Aqaba; GS: Gulf of Suez; MS: Mediterranean Sea; MMN: Makkah-Madinah-Nafud volcanic trend; WAB: Wadi Azlam Basin; GD: Gebel Duwi.

1.3 Thesis layout

This thesis is divided into three parts, collectively containing seven chapters. Brief descriptions of these chapters (excluding this chapter) are provided below:

- ***Part I: Introduction and background***
  - **Chapter 2** is a review of the generic literature on the tectono-geomorphic evolution in response to continental extension (Section 2.2), and the regional literature on the evolution of the Red Sea and adjacent gulfs (Section 2.3).
- ***Part II: Results chapters***
  - **Chapter 3** presents a study of the uplift evolution of the northeastern Red Sea and eastern Gulf of Aqaba margins. The chapter focusses on estimating uplift history and assessing its influence on the geomorphology. Drainage data (stream elevation profiles), extracted from a Digital Elevation Model (DEM), are used as input in an inverse model that finds the uplift history that results in the least misfit between the actual and modelled stream profiles.
  - **Chapter 4** presents a smaller scale, field-based study of the structural geology of the faults that are located southeast of the Midyan Basin (northeastern Red Sea margin). The structural synthesis presented in this chapter is integrated later during the discussion of Chapter 5.
  - **Chapter 5** assesses the tectono-geomorphic evolution of the northeastern Red Sea margin. Here, low-temperature thermochronology is used to estimate the exhumation along a 2D line in the sub-aerial part of the margin. The estimates are integrated with field structural mapping data (presented in Chapter 4) to evaluate the structures activity in light of the exhumation.
  - **Chapter 6** presents an integrative study of the uplift history (using inverse modelling as in Chapter 3) and drainage network analysis from all margins of the northern Red Sea (Arabia, Africa and Sinai) in order to investigate the drainage evolution in space and time throughout the Neogene rifting stages.
- ***Part III: Summary and conclusions***
  - **Chapter 7** is a synopsis of the results and discussion points from Chapters 3-6. The results are discussed in light of their implications for the geodynamics

and the petroleum prospectivity. The chapter ends by presenting the possible routes from relevant future research.

Chapter 2 Generic and regional background

2.1 Introduction

This chapter provides a review of the literature that serves as a background to chapters 3-6. More specific literature reviews relevant to the aims and methodologies are presented later in each chapter.

This literature review is divided into two main sections. The first section (2.2) reviews the literature on the continental landscape evolution at rifts and rifted margins focussing on the geomorphic effects; particularly drainage reorganisation in response to syn-rift and post-rift uplift processes. The second section (2.3) reviews the existing literature on the geologic setting and evolution of the Red Sea, the Gulf of Suez and the Gulf of Aqaba.

2.2 Landscape evolution at rifts and rifted margins

In order to understand the basics of landscape evolution at rifts and rifted margins, the literature on the relevant tectonic evolution and the different possible causes of uplift is reviewed in this section. Furthermore, the changes in drainage network imposed by the rifting processes (and deeper mantle-related processes) are highlighted. These reviews serve as a basis for interpreting geomorphic observations from the study area and linking them to rift-related tectonic and mantle-related processes.

A section is dedicated towards reviewing the literature on recent developments on the use of drainage as a means to estimate uplift quantitatively, relevant to the methodology followed in Chapters 3 and 6. Finally, low-temperature thermochronology is reviewed briefly as a tool for assessing the landscape evolution, which is relevant to determining exhumation in Chapter 5 (a more detailed review is presented in Section 5.2).

2.2.1 Continental extension

Continental extension results in the formation of sedimentary rift depocentres bounded by normal faults (Allen and Allen, 2005; Olsen and Morgan, 2006). Thermal perturbation and the space deficit resulting from thinning are revealed by elevated surface heat flow, uplift and volcanism (Allen and Allen, 2005).

A number of models have been proposed to explain the evolution of continental extension (Figure 2.1). With respect to the driving forces of rifting, two end-member models that predict contrasting sequences of rifting, uplift and volcanism may be highlighted (Figure 2.1): 1) active rifting in which the mantle plays the main role by pushing vertically through the plate, causing uplift and volcanism followed by rifting; and 2) passive-mantle rifting, whereby rifting occurs in response to far-field stresses related to the movement of the plates, in which case volcanism and uplift post-date the onset of rifting (Sengör and Burke, 1978).

In terms of the mechanics of extension, two end-member models have been proposed to explain the observations at rifted margins, namely: the pure shear model (McKenzie, 1978) and simple shear model (Wernicke, 1985; Figure 2.1). The pure shear model explains extension by uniform stretching with a symmetric brittle deformation of the crust and a ductile deformation of the lithospheric mantle (McKenzie, 1978). This model can explain the formation of intracontinental rifts; however, its application to the processes leading to the formation of passive margins is difficult given the asymmetries that characterise the conjugate margins and the vertically non-uniform stretching (Buck et al., 1988). On the other hand, simple shear extension is accommodated by a plate-scale low-angle detachment fault whereby the lithosphere is broken into upper and lower plates with pronounced margin asymmetry (Wernicke, 1985).

It is not unlikely, however, that the formation of a single rift system could be explained by a combination of the two models (e.g. Chorowicz, 2005). Chorowicz (2005) reviewed the rifts along the EARS and showed that crustal extension may be accommodated along major listric normal faults that sole into lower crust detachments (simple-shear model) whereas the lithospheric mantle is extended more symmetrically with the ascent of asthenospheric material (pure shear).

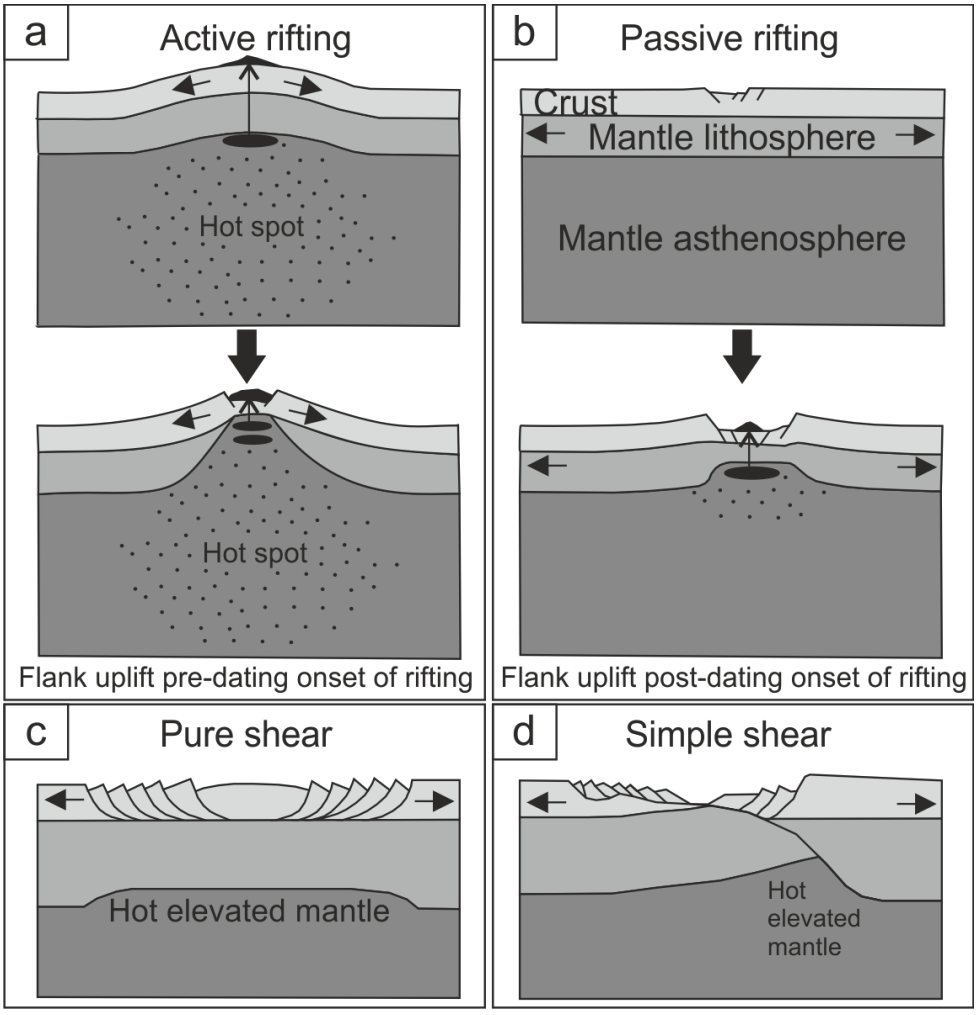

Figure 2.1: Schematic diagrams showing (a-b) the two-end member modes of rifting with respect to the involvement of mantle (Modified from Bott (2006)), and the original models of (c) pure-shear (McKenzie, 1978) and (d) simple shear (Modified from Wernicke (1985)). The spatial and temporal relationship between uplift and onset of rifting can be deduced.

The following is a review of the rifting stages and post-rift state of margins, which serves as a framework for the review of uplift and drainage evolution in subsequent sections.

2.2.1.1 Rifting

Upon the initiation of rifting, a large number of disconnected half-graben-bounding normal faults (rupturing the surface or forming topographic monoclines) are spread across a wide zone of deformation (Gawthorpe and Leeder, 2000; Figure 2.2). It has been documented that strain is usually accommodated through the reactivation

of pre-existing structures (e.g. Færseth et al., 1995; Younes and McClay, 2002). During this early stage of rifting, the subsidence of the individual half-grabens bounded by normal faults and the uplift of the associated footwall blocks have low rates influenced by how faults interact as extension progresses (Gupta et al., 1998). Sedimentation is often underlain by a regional or local unconformity surface that separates syn-rift sedimentary units on top from pre-rift sedimentary or basement below (syn-rift unconformity; Bosence, 1998).

Along strike and in between the fault segments, accommodation zones (relay ramps) develop, where some of the inter-fault displacement is accommodated (Fossen and Rotevatn, 2016), usually coinciding with pre-existing basement structures (Lambiase and Bosworth, 1995; Younes and McClay, 2002). These zones have typical widths of 15-30 km and are structurally complicated by folding as well as antithetic and synthetic faults (Younes and McClay, 2002). Syn-rift sedimentation is highly impeded by accommodation zones as they usually persist as structural highs, but they play a role in hosting drainage directed towards the basins (Lambiase and Bosworth, 1995; also see Section 2.2.3.1).

With continued extension, fault interaction promotes the linkage of individual segments across accommodation zones (where transfer faults are established) resulting in larger and fewer faults (Gupta et al., 1998; Figure 2.2). Eventually, the extension reaches the rift climax, which is characterised by the localisation of strain along fewer major normal faults, optimally oriented with respect to stress, resulting in increased lengths and displacements (Gupta et al., 1998; Cowie et al., 2000). Basinal subsidence during this stage increases substantially even if the same extension rate persists since rift initiation (Gupta et al., 1998). Strain localisation and migration towards the axis of the rift leaves relict basins straddling the shoulders of the rifts, which become areas of uplift and erosion (Gawthorpe and Leeder, 2000; Figure 2.2).

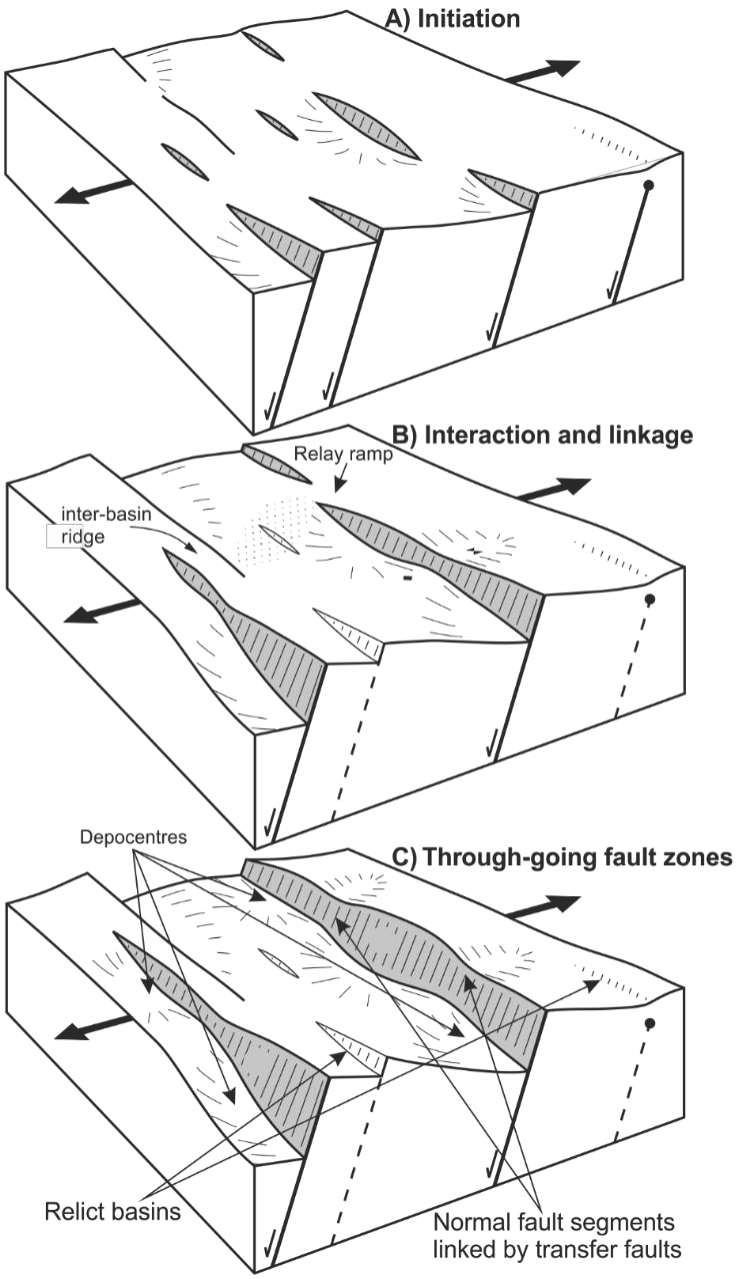

Figure 2.2: Schematic evolutionary diagrams depicting the stages of rifting: (a) Initiation of faulting; (b) Interaction and development of linkages between individual faults through transfer faults; (c) Development of through-going faults that localise deformation (Modified from Gawthorpe and Leeder (2000)). The thick black arrows indicate the direction of extension.

2.2.1.2 Post-rift

Rifts may proceed leading to continental break-up and the formation of rifted passive margins juxtaposing continental and oceanic lithospheres (Olsen and

Morgan, 2006; Merle, 2011). Alternatively, rifting may fail as extension rates dwindle resulting in failed rifts (e.g. the North Sea; Erratt et al., 1999). In either case, as the thermal state of the lithosphere returns to an equilibrium state, thermal cooling results in large-scale subsidence at the rift forming a sag basin, although isostatic uplift due to thick sedimentation in the basin could affect the rift flanks (Lambiase and Bosworth, 1995).

Post-rift sedimentary units are often underlain by an unconformity surface that separates them from the underlying syn-rift sedimentary units. This unconformity surface may be detected basin-wide or locally where elevated normal fault footwall blocks have been eroded, and is termed the post-rift unconformity (Bosence, 1998). However, this unconformity (and the syn-rift unconformity) would not always be easily correlated across the rift and its surroundings given that deformation (and uplift and erosion) are likely to migrate through time resulting in multiple unconformities.

2.2.2 Uplift, erosion and exhumation

There are different mechanisms that drive rift flank uplift and they differ in terms of their spatial scale and timing with respect to the rifting. The two-end member models that describe the evolution of continental rifts in terms of the driving force of extension (i.e. active and passive models) have different signatures with respect to the extent of and timing of uplift (Sengör and Burke, 1978; Figure 2.1).

Before proceeding to review uplift during extension, it is important to clarify some ambiguity related to the interchangeable use of exhumation and uplift in the literature by stating their definitions from the outset (Gallagher, 2012). The definitions used in this section are based on Molnar and England (1990). Defining these terms from the outset is important as uplift and exhumation are different outcomes of different methodologies used in this thesis (uplift is estimated using the inverse modelling of drainage profiles (Chapters 3 and 6) and exhumation is estimated using low-temperature thermochronology (Chapter 5)).

Uplift is a displacement vector against the direction of gravity relative to a reference level (Molnar and England, 1990). In details, *surface uplift* refers to the displacement of the surface of the earth relative to the geoid, whereas *rock uplift* is

defined as the displacement of rock relative to the geoid. These two terms of uplift are related by *exhumation*, which refers to the displacement of rock relative to the surface of the earth and, therefore, represents the difference between rock uplift and surface uplift (i.e. thickness of rock removed by erosion). Both surface and rock uplift can occur in response to tectonism, but rock uplift can also be driven isostatically by erosion and denudation (Summerfield, 1993).

2.2.2.1 Syn- and post-rift uplift and erosion

Variation in the timing and spatial distribution of uplift during continental extension has been attributed to different processes operating over variable spatial scales and at different stages with respect to rifting. In general, uplift may pre-date, coexist with or post-date the onset or rifting. The spatial and temporal aspects of uplift have generally been attributed to the presence or absence of an active role of the mantle.

As presented earlier, the mantle may play an active role in driving continental extension or it may play a passive role as far-field stresses drive rifting (Sengör and Burke, 1978; Figure 2.1a). The effect of the role of the mantle is both temporal and spatial. Active rifting driven by thermal asthenospheric upwelling results in a spatially large-scale (~1000 km) uplift that pre-dates the onset of rifting, leading eventually to an unconformity surface (i.e. the pre-rift unconformity; Bosence 1998).

On the other hand, passive rifting leads to uplift through faulting and flexure of fault-bounded blocks with much smaller spatial scale (~<100 km; Figure 2.1b). Although the mantle plays a passive role in such settings, induced small scale convection of the asthenosphere has been argued to explain flank uplift that does not pre-date the onset of rifting (e.g. Steckler, 1985). Furthermore, deeper flow linked to mantle plumes has been suggested to drive flank uplift with smaller wavelength than the uplift driven by mantle upwelling (e.g. Hosny and Nyblade, 2014). In the latter, the driving force is not a direct consequence of rifting and could operate several millions of years after the start of rifting.

In addition, the spatial variation of uplift across the rift axis can be attributed to whether the extension occurred through pure or simple shear. In the pure shear

model, uplift of the rift flank is symmetrical on both margins and is attributed to the thermal changes of the lithosphere (McKenzie, 1978; Figure 2.1c). Conversely, in the simple shear model, uplift is asymmetric across the rift axis and overlies the thinnest part of the lithosphere where the detachment reaches the asthenosphere (Wernicke, 1985; Figure 2.1d).

Erosion results in changes in the lithospheric thickness and thereby represents a mechanism that contributes to uplift not only of the rift shoulder but also of the basin margin (e.g. van Balen et al., 1995). That is, as erosional denudation operates by removing material from the earth surface, it effectively unloads the lithosphere, which can result in an isostatic disequilibrium and, depending on the effective elastic thickness of the lithosphere, long wavelength uplift may occur albeit with limited magnitude (Beaumont et al., 2000; Gallagher, 2012).

At passive margins, the topographic elevation and relief may become subdued as erosion and denudation dominate over uplift. Alternatively, erosional escarpments that are separated from the rift-bounding faults may develop. Three end-member models of high-escarpment passive margin evolution have been proposed: a downwarp model, a scarp retreat model, and a pinned divide model (Gallagher et al., 1998). The evolutionary paths for these different models involve different spatio-temporal distribution of uplift and exhumation, which may be deduced using the powerful tools of low-temperature thermochronology (see detailed review in Sections 2.2.5.1 and 5.2).

Uplift and erosion impact the geomorphic evolution of rifts and rifted margins. Specifically, these topography-shaping forces affect, and are affected by, the drainage evolution in these tectonic settings. The following section reviews how drainage reorganises when the forces of uplift and erosion are imposed.

2.2.3 Drainage reorganisation

The geomorphic response to rifting, in terms of faulting, uplift and subsidence, has implications on the sedimentary architecture of the basin (Lambiase and Bosworth, 1995; Gawthorpe and Leeder, 2000). Between the sedimentary basin and the rift flanks, drainage evolution plays a paramount role in sculpturing the landscape and delivering sediments to the basin.

Drainage catchments and stream profile gradients are affected by uplift and erosion (Willett et al., 2014). Uplift, either related to normal fault footwall block rebound or regional uplift due to thermal or density changes in the upper mantle, may modify the established courses of streams. In essence, drainage reorganisation takes place if surface uplift rate outpaces stream incisions (Figure 2.3). Conversely, if the erosional power and rate of streams outweigh rock strength and uplift rate then the stream course does not change forming antecedent drainage.

Drainage reorganisation occurs through stream capture, diversion, beheading and reversal and can result in: 1) the progressive subtraction of drainage area from one drainage catchment and its addition to another catchment with a retreating drainage divide, and/or 2) the incorporation of drainage streams into a growing drainage catchment (Bishop, 1995; Prince et al., 2011; Figure 2.3). Such mechanisms of reogranisation can affect draiange over large scales. For instance, reversal has been proposed to cause significant shifts in continent-scale drainage (e.g. Haworth and Ollier, 1992; Shephard et al., 2010).

Vestiges of drainage reorganisation may be observed in the present-day drainage network (Summerfield, 1993; Bishop, 1995). Indications of changes in the drainage take the form of anomalous features that may be identified on the drainage network map. These include elbows of capture (sharp turns along the stream course), wind gaps (valley sections where water flow had ceased), and stream misfits (streams that are larger or smaller than their valleys in terms of drainage power and upstream area; Bishop, 1995; Willett et al., 2014; Figure 2.3).

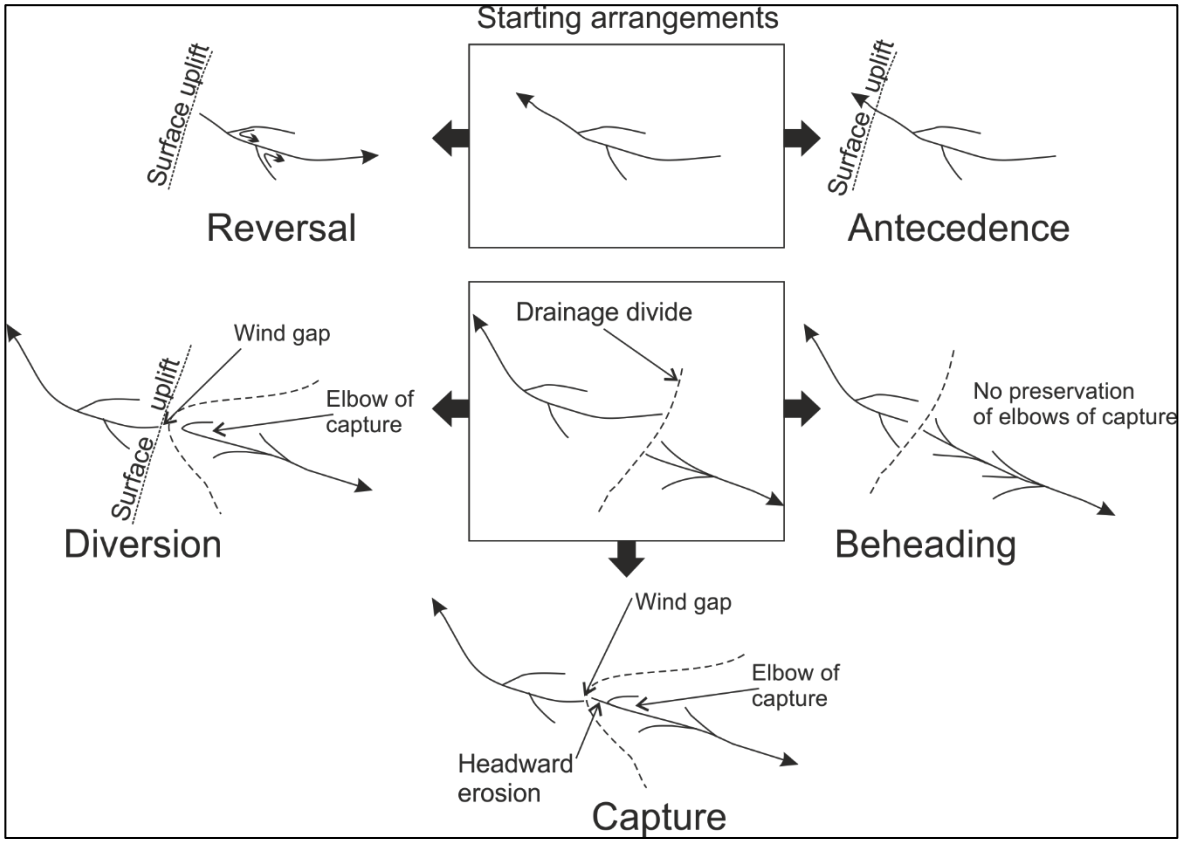

Figure 2.3: Processes of drainage reorganisation. Particular emphasis is put on the effect of uplift that could lead to drainage reversal or diversion. Diagrams of diversion, beheading and capture are modified from Bishop (1995).

Furthermore, the longitudinal profiles of individual streams (i.e. elevation vs distance from the coastline) may contain a record of drainage reorganisation. For instance, knickpoints, i.e. points where the slope of the stream bed decreases rapidly in the upstream direction, may signify drainage capture (e.g. Prince et al., 2011; Fan et al., 2018). Knickpoint retreat, i.e. the migration of a relatively short and high-slope stretch of the stream upslope, is an important implication of the relative drop of base-level, which can be achieved via uplift. Climate, particularly precipitation, represents another factor affecting the rate of knickpoint retreat and, hence, stream profiles shapes (Whittaker and Boulton, 2012).

2.2.3.1 Drainage evolution at rifts and rifted margins

This review addresses the causes and effects of drainage reorganisation at rifts and rifted margins, focussing on rift-related tectonic and mantle-related processes. During continental extension, the topographic changes imposed by rifting, uplift

and subsidence have fundamental impact on the evolution of drainage network (Jackson and Leeder, 1994; Eliet and Gawthorpe, 1995). As a result, the pre-rift drainage network is modified to some extent forming catchments that are characteristic of rift domains (e.g. Gawthorpe et al., 1994; Figure 2.4). In the case of active-mantle rifting, doming and structures may interact resulting in outward drainage directions (e.g. Moore and Blenkinsop, 2002).

Pre-existing antecedent drainage system may be maintained during the early phase of rifting as only slight modification of the slope occurs in response to the development of small faults and monoclines (Gawthorpe and Leeder, 2000). The maintenance of the stream course is due to the low rate of uplift during the rift initiation stage. However, if base-level is relatively high, drainage may become partitioned as the pre-rift drainage is captured by headward eroding streams established near the half-grabens resulting in catchment fragmentation (Gawthorpe and Leeder, 2000; Figure 2.5).

As rifting progresses, normal fault-related footwall and hangingwall dip-slope catchments are established as transverse drainage systems directed normal to the axis of the basin (Eliet and Gawthorpe, 1995; Gawthorpe and Leeder, 2000; Figures 2.4 and 2.5). Footwall catchments are characteristically small and their stream profiles are relatively steep and short. Fault blocks associated with footwall catchments may become subject to crestal erosion driven by the uplift, which leads to the deposition of locally sourced basal conglomeratic syn-rift units (e.g. Yielding, 1990). Hangingwall catchments are larger, with shallower and longer stream profiles (Gawthorpe and Leeder, 2000).

Given their spatial positions between faults and their relatively high elevation compared to the basins, accommodation zones are suitable locations for drainage (i.e. transfer zone drainage) into the basins (Lambiase and Bosworth, 1995; Figures 2.4 and 2.5). Because accommodation zones are usually aligned with pre-rift drainage (that utilises weaknesses at pre-rift basement structures) and away from the influence of rock uplift at the footwall block, transfer zone drainage is expected to inherit long-established pre-rift drainage that is not largely influenced by rift-related uplift. Therefore, transfer zone catchments are usually larger than the other catchments, delivering more far-sourced sediments to the basin (Figure 2.4).

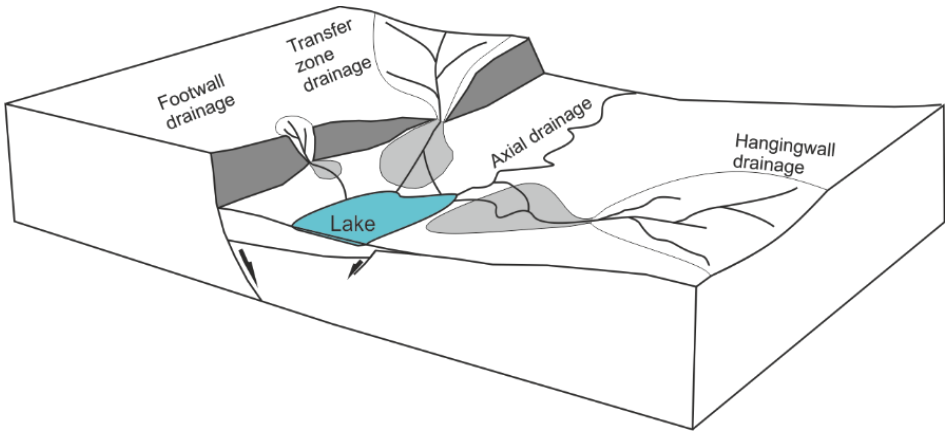

Figure 2.4: Typical drainage domains in continental rift settings: footwall drainage, hangingwall drainage, transfer zone drainage and axial drainage (Modified from Gawthorpe et al. (1994)).

During the rift climax, the different catchments around the rift become feeders into an axial drainage system or a lake/sea paralleling the bounding fault system depending on the established base-level (Leeder and Jackson 1993; Eliet and Gawthorpe 1995; Gawthorpe and Leeder, 2000; Figures 2.4-2.5). Furthermore, as strain becomes localised along a few normal faults, footwall uplift rates increase, which may result in the deflection or reversal of drainage away from the rift depocentres (Lambiase and Bosworth, 1995; Figure 2.5).

The topographic relief that results from rifting enhances erosion, which results in delivering more sediments into the depocentres. Depending on the generated accommodation space in these depocentres and the sedimentation rate, basinal overfilling or underfilling may develop. In the case of the overfilling, the base-level becomes low relative to the topographic surface and the drainage is connected to downstream drainage forming larger catchments (e.g. Geurts et al., 2018; Jackson and Leeder, 1994).

As displacements along the faults diminish, the landscape becomes modified mainly by erosion caused by drainage fluvial processes. However, uplift driven by processes unrelated to rifting can be imposed later than the onset of rifting, in which case drainage reorganisation may take place (e.g. Salles et al., 2017). Such an effect may result in significant modification of drainage catchments even in the continental scale, as suggested by Shephard et al. (2010) who proposed that

mantle convection in northwestern South American during the Cenozoic resulted in the establishment of the east-directed Amazonian catchment.

The processes of drainage capture and reversal affect the overall drainage organisation in that, during early rifting, catchments may become numerous and small in size as multiple sink areas are generated at the different rift basins, unless large pre-rift drainage is captured by the rift drainage (Figure 2.5). As rifting progresses and basins on the rift flank are abandoned (as sediment sink areas), the number of catchments decrease and their sizes increase (Duffy et al., 2015; Geurts et al., 2018; Figure 2.5).

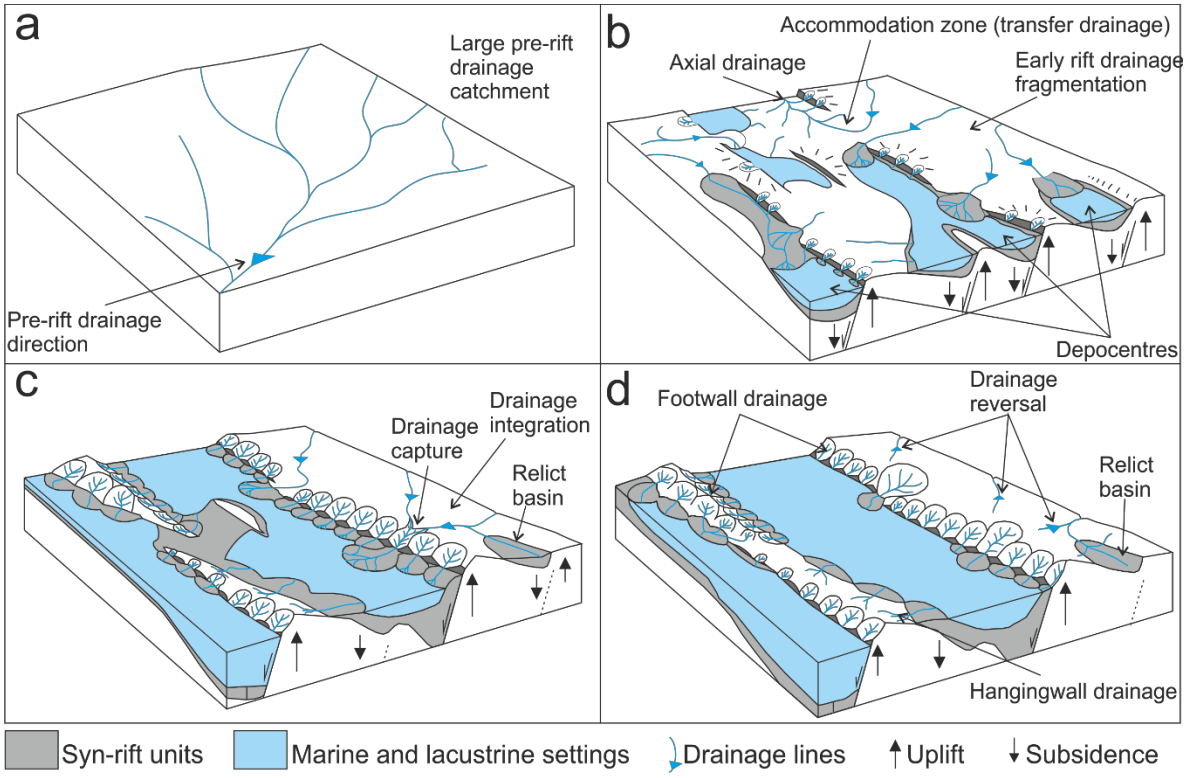

Figure 2.5: Development of drainage catchments during continental rifting leading to marine incursion (Modified from Gawthorpe and Leeder (2000)). (a) pre-rift drainage; (b) early rift depocentres and fragmentation of the drainage into small catchments; (c) integration of catchments as depocentres on the rift flanks are abandoned and left as relict basins; (d) possible modification of the drainage by drainage reversal.

In summary, along active rifts, catchment size and orientation may provide insights into the rift tectonics in terms of arrangement of rift structures, sub-basins and the influence of pre-existing structures on the rifting (e.g. Summerfield, 1993). That is,

footwall drainage catchments would be semi-perpendicular to the rift faults and small in size; hangingwall drainage catchments would be semi-perpendicular to the rift and larger in size; transfer zone catchments would utilise pre-existing basement structures and follow their orientation and might be larger than the hangingwall catchments (Summerfield, 1993; Gawthorpe et al. 1994).

At passive margins, drainage evolution has an impact on the escarpment evolution (e.g. Gunnell and Harbor, 2010; de Sordi et al., 2018). In particular, rift-related drainage controls the escarpment near the faults as footwall catchments work to erode through these early scarps. The drainage divide retreat can occur through headward erosion by streams (i.e. erosion at the stream source in a direction opposite to the flow). Pre-existing structures that might have hosted long-lasting drainage may be incorporated into the coastal catchments resulting in enlarging the catchment size and, therefore, increasing the volume of eroded and transported sediment load towards the margin (e.g. de Sordi et al., 2018).

This brief review of drainage evolution at rifts and rifted margins implies that heterogeneity is likely to characterise the stratigraphic and sedimentary architecture of basins, and highlights the importance of understanding drainage evolution.

2.2.4 Quantifying continental uplift

Estimating rock uplift geologically may be done by examining the ages and elevations of strata that are, environmentally, indicative of marine conditions or low-elevation and low-relief. Dated marine deposits may include beach or coral terraces that are preserved inland. Such terraces present a powerful tool for determining rock uplift rates during the Pleistocene (e.g. McNeill and Collier, 2004). These uplifted marine units, however, extend only a few kilometres inland and, therefore, the estimated uplift rates are limited both in space and time. Away from the coastline, deposits that indicate low-relief and low-elevation settings may be used to infer cumulative uplift given their current elevations (e.g. laterites; Wilson et al., 2014).

Furthermore, uplift rates have been quantified by utilising the topographic response as recorded by the drainage network. Different approaches have been pursued to

understand uplift from drainage inventories. These approaches range from using topographic metrics along rivers and across catchments to performing inverse modelling to solve for the uplift rates by minimising the misfit between modelled and actual stream profile (elevation vs distance) shapes (e.g. Pritchard et al., 2009). The latter approach is pursued in this thesis and the section below presents the methods used to estimate uplift using drainage data.

2.2.4.1 Estimating uplift from drainage

Drainage analysis shows that there exists a power-law relationship between the slope and the upstream area along fluvial streams (Wobus et al., 2006 *and references therein*). In this relationship, the slope and upstream area are related by the steepness of the stream profile and its concavity, such that:

$$S = k_s A^{-\theta} \qquad \text{(Equation 2.1)}$$

where S is the slope, A is the upstream area, k_s is the steepness index and θ is the concavity index (Wobus et al., 2006 *and references therein*).

Wobus et al. (2006) described a stream profile analysis method using these topographic indices, which can be derived from the topographic data, to highlight where the slope-vs-area relationship does not hold, thereby delineating possible uplift events. In this case, the knickpoints along the profiles (i.e. the stretch of the profile that is associated with higher gradient than the rest of the profile) separates segments that have distinct concavity and steepness values (Figure 2.6). Therefore, topographic indices (e.g. channel steepness) may provide a way to highlight variation of rock uplift between different catchments (e.g. Cyr et al., 2010).

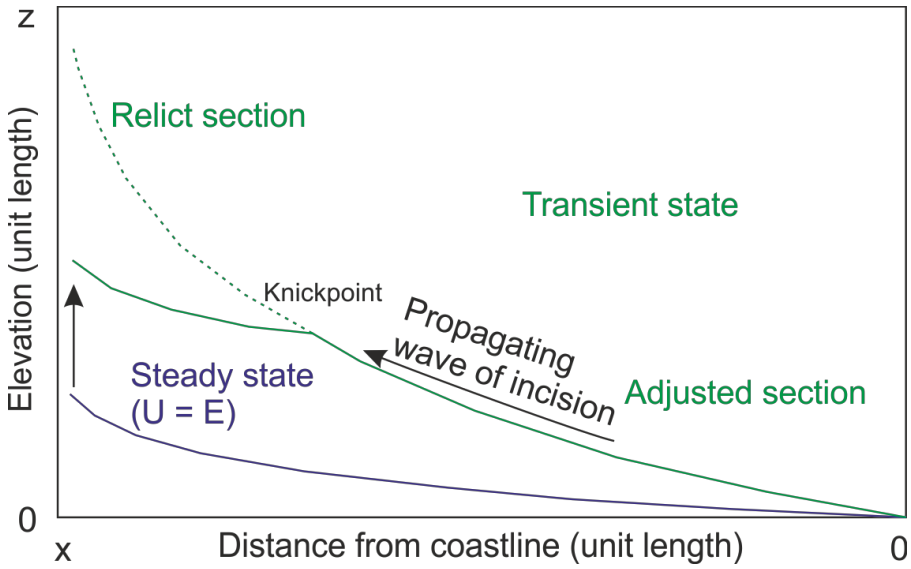

Figure 2.6: A schematic cross-section showing stream profiles in steady state (i.e. uplift rate (U) = erosion rate (E); blue) and transient state (green) (Modified from Whipple and Tucker, 1999). Upon uplift, erosion works to return the landscape to the pre-uplift state (dashed green line) and the wave of erosion is active below a knickpoint that migrates upstream. Note that the profile becomes steeper upon uplift.

A more inclusive approach has been devised to utilise the whole river profile, rather than the breaks in the slope-vs-area relationship, to decipher information about the topographic state. Over the past decade, much research has focussed on the development of inverse algorithms that utilise drainage profile shapes and solve for uplift rate in space and time (e.g. Pritchard et al., 2009; Roberts and White, 2010; Roberts et al., 2012a; Roberts et al., 2012b; Czarnota et al., 2014). These inverse algorithms have proved reliable in determining uplift variation in space and time when compared to independent geological estimates (e.g. spot measurements of uplift from elevated marine terraces; Wilson et al., 2014; Rudge et al., 2015).

The advantage these inverse models hold over spot measurements is the larger spatial extent that depends on the ubiquitous drainage data. However, data coverage deteriorates away from the extracted streams that are used in the modelling and back in time (e.g. Rudge et al., 2015). Therefore, quality-checking the modelling results against, and integrating them with, independent geological evidence is important.

Furthermore, estimations of exhumation using low-temperature thermochronology (next section) have been used to validate inverse modelling results. As clearly stated earlier in Section 2.2.2, exhumation does not necessarily equate uplift, and, therefore, low-temperature thermochronology-deduced exhumation events can only be used to interpret the uplift results, e.g. within a tectonic framework, but cannot be used to validate the rate and magnitude of uplift quantitatively.

2.2.5 Quantifying exhumation

2.2.5.1 Estimating exhumation using low-temperature thermochronology

In this section, an overview of the usage of low-temperature thermochronology in assessing the evolution of the landscape is presented. This literature review briefly describes the theory and application of low-temperature thermochronology. A more thorough and detailed description of the techniques used in this study and their application to rift and rifted margins is presented in Chapter 5 (Section 5.2).

Thermochronology is a field of geochronology that deals with the use of time and temperature-dependent dating techniques, which depend on the radioactivity of certain isotopes, to estimate the geological thermal history of the rocks (Lisker et al., 2009). Theoretically, dating a grain thermochronologically is the determination of the age at which it passed across a particular isotherm, which is pertinent to the thermochronometric system in use.

Thermochronological analyses involve processing minerals that host radioactive isotopes (e.g. apatite, zircon, titanite and biotite), which are of particular interest to the history of rocks in the crustal levels as their ranges of temperature-sensitivity span temperatures from 40 to 800°C (Gallagher and Brown, 1999; Peyton and Carrapa, 2013). The focus in this study is on the two thermochronometric systems of apatite as they are relevant to the thermal state of the uppermost part of the continental crust (~40-125°C); namely, apatite fission tracks (AFT) and apatite uranium-thorium/helium ((U-Th)/He) or AHe; Lisker et al., 2009).

The use of AFT and AHe to analyse the thermal evolution of the rocks rests on the physics of radioactive decay of ^{238}U that is hosted in apatite grains; a process that

occurs most frequently via the release of He nuclei and significantly less frequently by nuclear fission that creates fission tracks (FTs) in the grain (Vermeesch, 2019 *and references therein*). Like other geochronological dating techniques, estimating the dates using low-temperature thermochronology is conducted by determining the amounts (concentrations) of radioactive parent isotopes (^{238}U) and radiogenic daughter products (He and FTs). However, unlike other geochronological techniques that measure the absolute age of rock grains, low-temperature thermochronology utilises the concept of closure temperature (T_c) lower than which the grain, theoretically, retains radiogenic daughters.

As will be described more thoroughly in Chapter 5, rift-related uplift and displacement and landscape evolution at passive margins can be studied by assessing the rock thermal history. Combining more than one thermochronological dating technique can ultimately be used to constrain not only the cooling ages, but also the rates of cooling, even if the cooling is not monotonic. In turn, these ages and rates of cooling can be used to estimate rock exhumation timing and rate, which may be interpreted in the context of normal fault displacement, uplift and denudation (e.g. Gallagher and Brown, 1999; Stockli, 2005; Mortimer et al., 2016). As the techniques are temperature-dependent, constraints (or assumptions) on the paleo-geothermal gradients need to be made to convert the magnitude of cooling (in C°) to exhumation (in km).

2.3 Geologic setting of the Red Sea

In this section, I review the different tectonic stages that the Red Sea has undergone since the Oligo-Miocene. The review serves to highlight the different models that describe the formation of the Red Sea, which have an impact on the variation of uplift and exhumation. Furthermore, a final section (2.3.7) is dedicated to the current understanding of the geomorphic evolution of the Red Sea margins.

The 330° NW-trending Oligo-Miocene Red Sea rift is part of a greater rift system that also includes the Gulf of Aden, Gulf of Suez and Gulf of Aqaba/Dead Sea, with Afar forming a tectonic link between this system and the East African Rift (Bosworth et al., 2005; Bosworth, 2015; Figure 2.7). The rift system captures different stages from continental rifting to breakup (Almalki et al., 2015; Bosworth, 2015). Oceanic spreading developed in the southern Red Sea, whereas the northern Red Sea is still experiencing continental extension (Bosworth et al., 2005).

2.3.1 Pre-rift setting

The lithology of the Nubian and Arabian shields is dominated by basement-forming Proterozoic metamorphosed volcanics, clastics, volcaniclastics and intrusions (Clark, 1985; Ramsay et al., 1986). Basement heterogeneity is caused by sutures and metamorphic lineaments that resulted from Precambrian Pan-African Orogeny (Abdelsalam and Stern, 1996). Dominating the Precambrian structures at the northern Arabian Shield are the NW-SE sinistral strike-slip shear zones of the Najd Fault System, which extend also to Africa and Sinai (Johnson et al., 2011; Figures 2.7-2.9). Furthermore, NE-SW Precambrian structures exist both on the Arabian and African margins, which may be aligned with each other when plates are restored to pre-rift stage (e.g. Onib-Hamisana and Baraka sutures on the African margin and Hanabiq shear zone (N-S basement structure to the east of the Al Wajh Basin) on the Arabian margin (Johnson et al., 2011; Figure 2.7)).

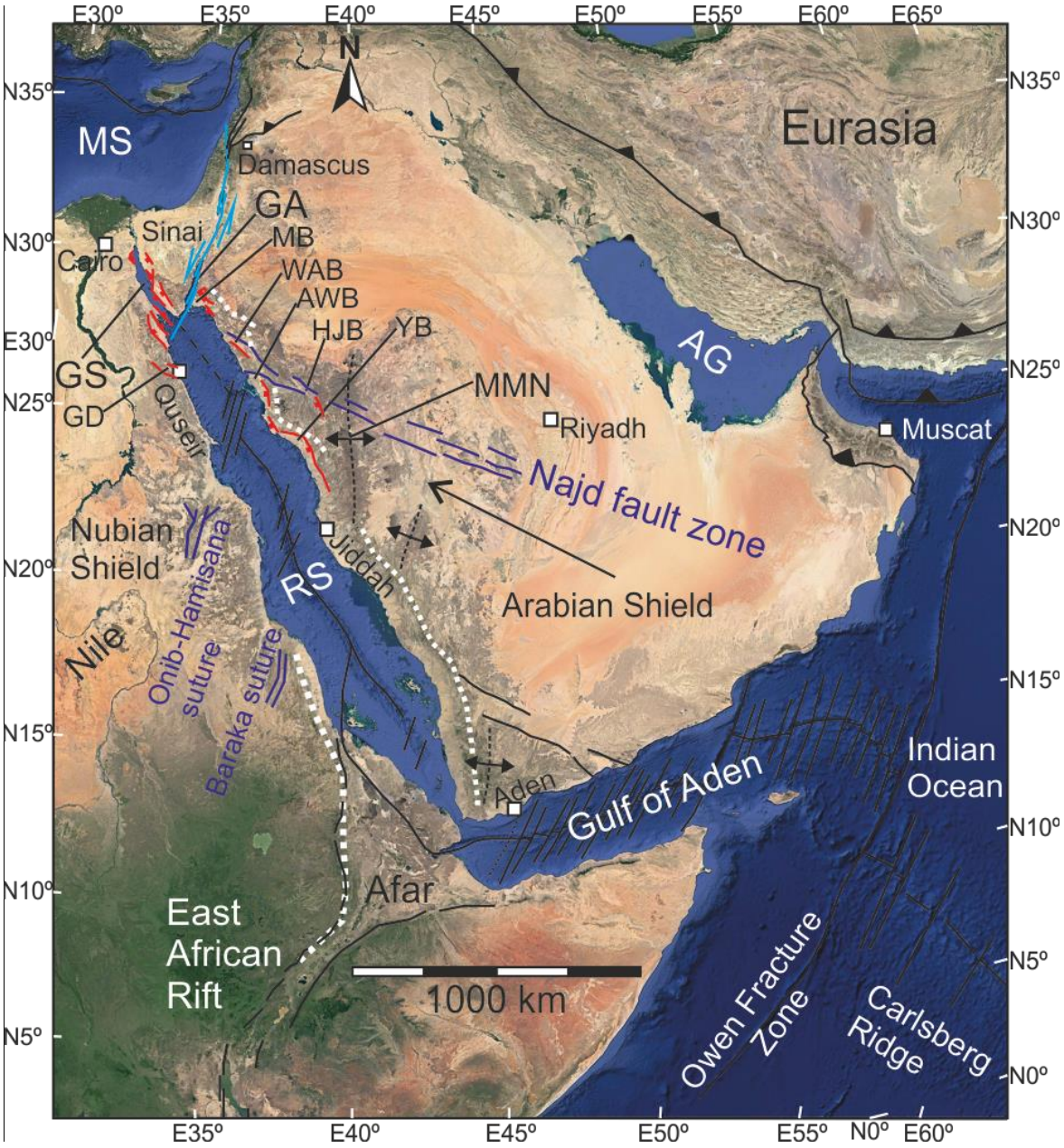

Figure 2.7: A Google Earth map showing the tectonic setting around the Red Sea. Regional tectonic features and Gulf of Suez faults are from Bosworth et al. (2005). Hamd-Jizl (HJB), Al Wajh (AWB) and Yanbu (YB) Basins faults are from Szymanski et al. (2016). Midyan Basin (MB) faults are from Tubbs et al. (2014). Purple lines: Precambrian structures (Modified from Dixon et al. (1987) and Johnson et al. (2011)); red lines: Red Sea rift faults; light blue lines: Gulf of Aqaba strike-slip faults; dashed white line: Arabian and Ethiopian escarpments (Bosworth, 2015; and this study). RS: Red Sea; GA: Gulf of Aqaba; GS: Gulf of Suez; AG: Arabian Gulf; MS: Mediterranean Sea; MMN: Makkah-Madinah-Nafud volcanic trend; WAB: Wadi Azlam Basin, GD: Gebel Duwi.

Thorough peneplanation of basement rocks preceded the deposition of Paleozoic clastic sedimentary units that now trace the boundaries of the Nubian and Arabian Shields (Bosworth et al., 2005; Feinstein et al., 2013). In the Central Arabian Rift Flank (CARF), Szymanski et al. (2016) suggested a large-scale Carboniferous tectonic event (~350 Ma) that is deduced from zircon and apatite (U-Th)/He analyses. This age falls within the range of ages of the Hercynian Orogeny, which has been linked to unconformity surfaces interpreted on seismic sections from eastern Arabia (e.g. Stewart, 2016).

The basement and Paleozoic strata are unconformably overlain by Mesozoic units that largely signify marine influence of the Tethys Ocean (Bosworth et al., 2005). The Paleozoic and Mesozoic pre-rift stratigraphy is generally thickest in the north (towards the Tethys domain) and south (Indian Ocean) and thinnest around the middle (Omar et al., 1989; Bosworth et al., 2005). During the early Mesozoic, Szymanski et al. (2016) argue that western Arabia remained stable without significant tectonics that may be indicated by exhumation signals from the inverse modelling of their (U-Th)/He data. Their ages, however, show clustering at 200-260 Ma and 120-160 Ma. Further north, in southwestern Jordan, Feinstein et al. (2013) presented Late Triassic to Early Jurassic apatite FT cooling ages. These ages are correlatable with Permo-Triassic rift-related block uplift in eastern Arabia (e.g. Faqira et al., 2009), which suggests that the western Arabia signals were caused by uplift driven by far-field stresses.

Early Cretaceous rifting oriented NW-SE in northeastern Africa (central Red Sea) was associated with spatially short-wavelength uplift of rift flanks (Bosworth et al., 1996). Strike-slip tectonics were recorded during the Late Cretaceous and utilised pre-existing basement structures with NNW-SSE orientation of trans-tension (Bojar et al., 2002; Figure 2.9). Nonetheless, low relief characterised the aerially exposed Arabia, with most of it shallowly submerged between the Late Cretaceous and Oligocene (Bohannon et al., 1989). This low relief and elevation is indicated by Oligocene erosional surfaces, a landscape state characteristic of the Afro-Arabian Plate prior to 30 Ma (Burke and Gunnell, 2008).

These trans-tensional tectonics were coeval and post-dated by the compressional tectonics that led to the closure of the Neo-Tethys Ocean during the Late

Cretaceous-?Eocene (Bosworth et al., 1999). These resulted in the formation of the E-W to NE-SW Syrian arc fold belt (Bosworth et al., 1999) as well as the folds and thrusts in the northernmost parts of the present-day Red Sea and Gulf of Suez (e.g. Wadi Araba Anticline; Moustafa and Khalil, 1995).

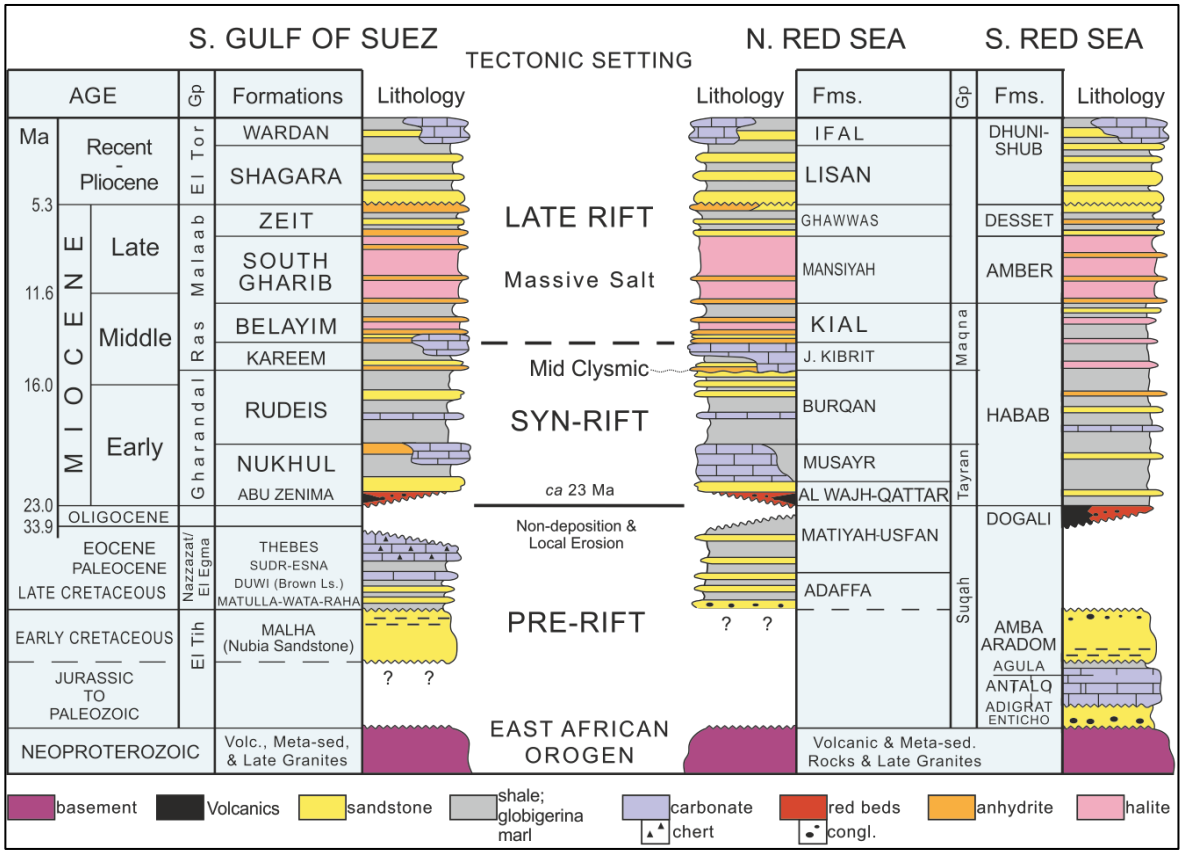

Figure 2.8: Generalised stratigraphic columns of the Gulf of Suez and the northern and southern Red Sea margins (Modified from Bosworth and Burke (2005)). The earliest Miocene Qattar Formation in the N. Red Sea column is incorporated into the stratigraphy after Szymanski (2013), the Mid-Clysmic unconformity is after Tubbs et al. (2014) and the volcanics are added after Bosworth et al. (2005). The late-rift stage represents the oblique extension and Aqaba-Levant transform initiation.

2.3.2 Afar Plume

Plume-related volcanics were extruded over much of the Oligocene around the southern Red Sea (Coleman et al., 1983; Bohannon et al., 1989; Davison et al., 1994; Bosence, 1998; Bosworth et al., 2005) prior to initial continental rifting (Lazar et al., 2012; Tubbs et al., 2014; Figures 2.8 and 2.9). These volcanics are equivalent to the Older Harrats and Jizan Volcanics in Saudi Arabia and the

Yemeni Volcanic Group in Yemen (Figure 2.10). Note that the term harrats, which will be encountered again in the thesis, refers to sub-aerial volcanic lava fields.

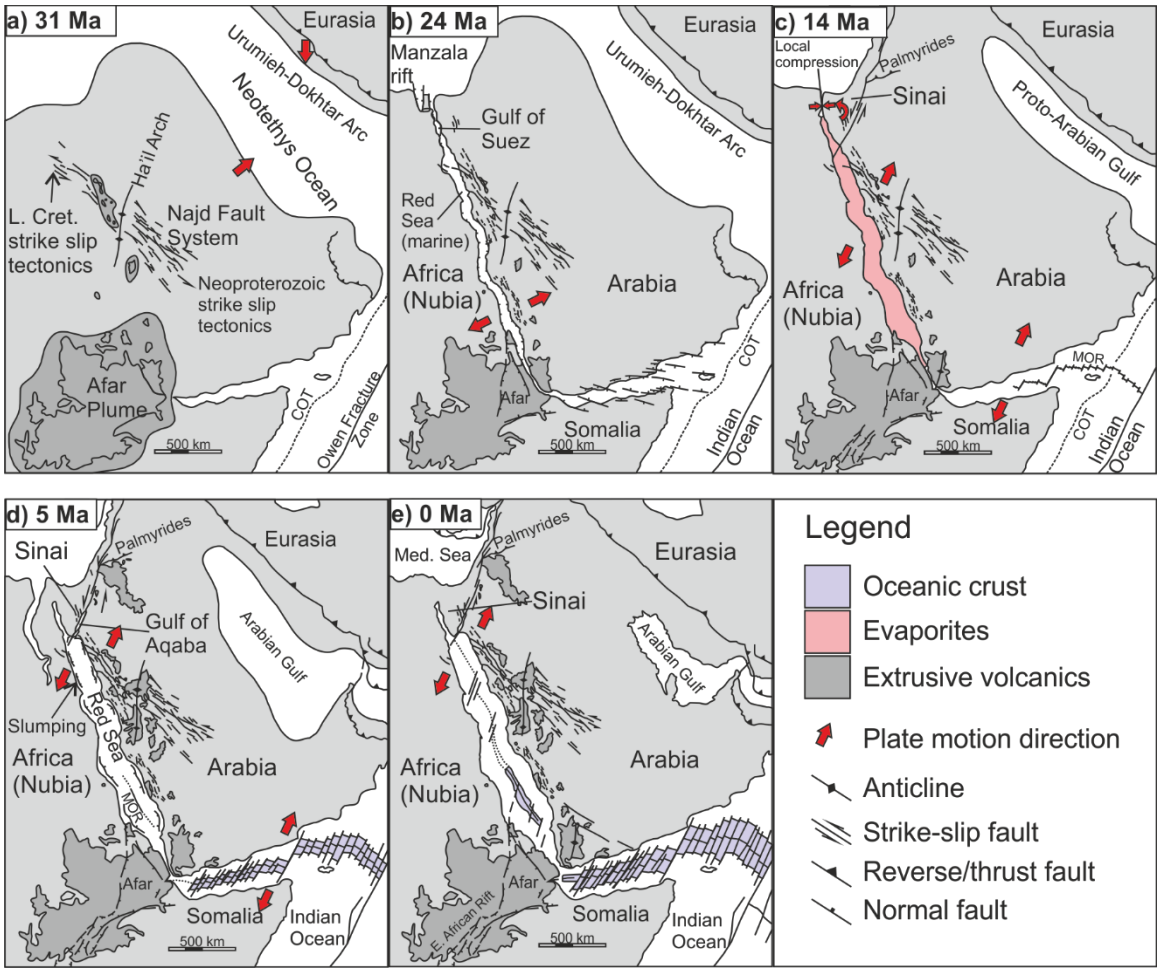

Figure 2.9: Plate-scale evolution of the Red Sea and the adjacent plates and gulfs, showing the plate motion directions (Modified from Bosworth et al. (2005)).

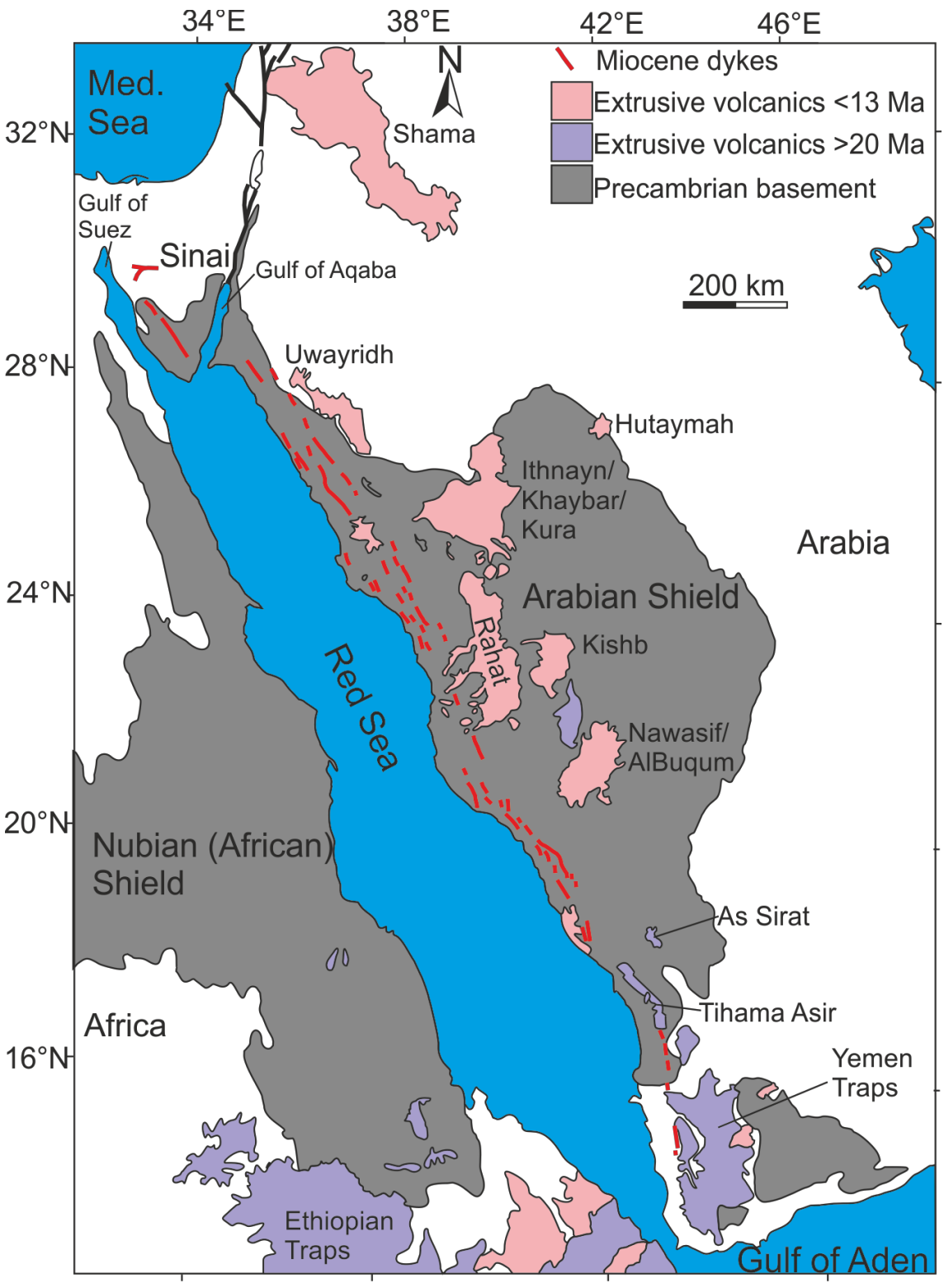

Figure 2.10: A map of the Red Sea margins showing the extent of the Nubian (African) and Arabian Shields, and the distribution of the volcanism (Modified from Stern and Johnson (2010)).

2.3.3 Rift-normal extension

Early rifting in the Red Sea and Gulf of Suez was characterised by short normal faults with marked block rotation and local uplift during the Oligocene-Early Miocene (Bosworth et al., 1998; Figure 2.9). Far-field stresses oriented ~060° NE governed the Red Sea orientation (330° NW), and pre-rift Precambrian basement structures played a role in the local (<100 km) orientations of rift faults, depocentres, and accommodation zones (Bosworth, 1994; Younes and McClay, 2002; Bosworth et al., 2005; Figure 2.9). The result is a wide zone of extension that possibly extended over 1,200 km at the northern Red Sea and Gulf of Suez, narrowing down towards the south (Stockli and Bosworth, 2019 *and references therein*). This early extension formed rift basins that now straddle the Arabian flank including Midyan, Wadi Azlam, Al Wajh, Yanbu and Hamd-Jizl Basins, across an approximately ~150 km-wide zone (Bosworth et al., 2005; Szymanski et al., 2016).

The role of pre-existing basement heterogeneity is particularly clear in the northern and Central Red Sea and the Gulf of Suez. WNW-NW (Najd Fault System) and NE (Onib-Hamisana and Baraka sutures) were reactivated and often linked by other N-S structures along the Red Sea (Dixon et al., 1987; Kenea et al., 2001; Figure 2.7). The early rift basins were characterised by rhomboidal geometries as in the Gulf of Suez, which indicates the influence of the pre-rift structures (Khalil and McClay, 2001). Evidence of such linkage is, however, absent along the southern Arabian margin possibly due to the lack of such pre-existing structures (Davison et al., 1994; Bosworth et al., 2005; Figure 2.9).

In the created accommodation spaces, red clastic beds and granitic cobbles (Abu Zenima and Tayran Group [Al Wajh Formation]) and carbonates (Nukhul Formation) were deposited in the Gulf of Suez and northern Red Sea. These units signify variable depositional settings from lacustrine and alluvial plain to shallow marine environments (Hughes et al., 1999; Bosworth et al., 2005; Hughes and Johnson, 2005; Tubbs et al., 2014; Figure 2.8). In the Hamd-Jizl Basin, the early rift is represented by the Qattar Formation, which largely signifies fluvial environmental conditions (Szymanski, 2013).

Variations in the early syn-rift facies suggest a topographic response to the formation of the earliest depocentres of the Red Sea (Hughes and Johnson, 2005). For instance, Hughes and Johnson (2005) concluded that the early rift Tayran Group includes carbonates on structural highs, deep water shales, marginal marine sands and restricted basin evaporites.

Concomitant with the syn-rift sedimentation, magmatism resulted in the emplacement of tholeiitic basaltic dykes at approximately 23-24 Ma along much of the Red Sea (Bosworth et al., 2005; Figure 2.10). These dykes follow an overall orientation of 330° NW, which parallels the Red Sea, and are mostly confined to the Arabian side (Figure 2.10).

Towards the end of the Aquitanian, fault segments started linking and the rift basins entered a phase of accelerated subsidence (Bosence, 1998; Bosworth and McClay, 2001). This phase was characterised by widespread marine sedimentation and deposition of Globigerina shales and limestones in basinal settings (e.g. Rudeis and Burqan Formations; Steckler et al., 1988; Tubbs et al., 2014). On the African side, flank uplift is argued to have occurred during the Early Miocene (~22 Ma) coeval with the basinal subsidence (Omar et al., 1989; Steckler et al., 1998).

Post-dating the accelerated subsidence, an unconformity termed the Mid-Clysmic event developed in the central Gulf of Suez (Mid-Rudeis Formation; Jarrige et al., 1990) and the Midyan Basin (overlying the Burqan Formation; Tubbs et al., 2014). Bosworth et al. (2005) suggested the possibility that this unconformity signified the effect of far-field stresses that preceded collision with Eurasia. On top of the Mid-Clysmic unconformity surface, Jabal Kibrit Formation (Midyan Basin in NE Red Sea), and Kareem Formation (Gulf of Suez) were deposited with lithologies encompassing clastics, carbonates and evaporites (Bosworth et al., 2005; Tubbs et al., 2014). During the Burdigalian (~19 Ma), igneous activity started to diminish (Coleman et al., 1983; Bosworth, 1994).

2.3.4 Oblique extension and initiation of Aqaba-Levant transform

During the Middle Miocene (14-12 Ma), left-lateral strike-slip tectonics commenced between the northern Red Sea and Gulf of Suez, leading to the formation of the Gulf of Aqaba (Bosworth et al., 2005; Figure 2.9). Regional tectonic reorganisation

occurred as the minimum horizontal stress became oblique to the Red Sea and semi-parallel to the Gulf of Aqaba (~N-S/NNE-SSW; Bosworth et al., 2005).

The initiation of the Aqaba-Levant strike-slip tectonics caused marked reduction in the rate of extension, block rotation and subsidence in the Gulf of Suez, leading to an unconformity surface overlying the Kareem Formation (Steckler et al., 1988; Bosworth, 1995). In the Red Sea, rift shoulder uplift and linkage of individual faults continued (Bosworth et al., 1998; Bosworth and McClay, 2001) as strain migrated towards the axis of the rift away from uplifted early rift basins (e.g. Al Wajh, Yanbu, and Hamd-Jizl Basins (Saudi Arabia; Szymanski et al., 2016; Figure 2.7). In the northernmost Red Sea, deformation continued along faults bounding the Early Miocene basins as evidenced, for example, by the hard linkage of the Ifal East Fault segments to the east of the Midyan Basin (Koeshidayatullah et al., 2016).

The Aqaba-Levant tectonics were coeval with volcanism in the north as is the case at the Harrat ash Shama (13 Ma) and Harrat Uwayridth/ar Rahah (~12 Ma; Ilani et al., 2001; Bosworth et al., 2005). Furthermore, the harrats of Saudi Arabia (MMN-volcanic line) that intersect the central Red Sea erupted along a N-S trend (Szymanski, 2013; Figures 2.7 and 2.10).

As the plate-scale minimum horizontal stress became semi-parallel to the Gulf of Aqaba during the Middle Miocene, the Sinai Plate reacted by rotating anticlockwise around a semi-vertical axis (Bosworth et al., 2005; Figure 2.9). Earlier estimates of the stress state during the Miocene at the Gulf of Suez, however, indicate continued rift-normal extension with the rotation of the stress vectors happening much later during the Pleistocene (Bosworth and Strecker, 1997). The Middle Miocene estimate of the rotation of the Sinai Plate is supported by the argument that this rotation resulted in compression tectonics at the northern Gulf of Suez that caused partial closure of the waterway from Mediterranean Sea leading to the precipitation of widespread evaporites (the Middle Miocene Kial and Belayim Formation in the northern and central Red Sea; Bosworth et al., 2005; Figure 2.8). Conversely, the northern Gulf of Suez and southern Red Sea featured marine sedimentation suggesting continued link to the Mediterranean Sea and the Indian Ocean, respectively (Bosworth et al., 2005). During the Late Miocene evaporation and halite precipitation prevailed throughout the Red Sea due to dramatic eustatic

sea-level drop (South Gharib and Mansiyah Formations; Bosworth et al., 2005; Tubbs et al., 2014; Figure 2.8).

The change in tectonic settings and the existence of the evaporites had implications on the deposition of the succeeding units; mainly, the Upper Miocene clastic Ghawwas Formation (Hughes and Johnson, 2005; Tubbs et al., 2014; Figure 2.8). The Ghawwas Formation was deposited in accommodation spaces created by salt diapirsm, possibly induced by tectonism and displacement along a basal salt detachment. In the Midyan Basin, the depositional environment for these clastics changed from a brief marine environment to later lacustrine settings (Tubbs et al., 2014). This environmental change reflects the relative base-level drop in the northern Red Sea that could be related to either basin overfilling or uplift.

2.3.5 Aqaba-Levant transform strain localisation in the north and sea-floor spreading in the south

During the Pliocene, the left-lateral strike-slip tectonics became localised along the Aqaba-Levant transform, creating pull-apart basins and uplift of western Midyan Peninsula (Tubbs et al., 2014; Figure 2.9). Contemporaneously, seafloor spreading started to develop in the southern Red Sea at 5 Ma, evidenced by the existence of striping on magnetic maps (Bosworth et al., 2005).

In the northern Red Sea, seismic imaging displays extended continental lithosphere and deeps in the centre of the basin that have been interpreted as nucleation of oceanic crustal material (Cochran, 2005). Oceanic accretion was interpreted, based on crustal thickness variation, magnetic intensity and basalt composition, to have started in disconnected axial deeps in the northern-central Red Sea since 2.2 Ma (Ligi et al., 2012). This reflects the localisation of deformation at the axis of the Red Sea.

Sedimentation during the Pliocene was trapped at onshore and offshore basins causing sediment starvation at the Red Sea axial trough (Bosworth et al., 2005). For instance, clastic sedimentation dominated the uplifted Midyan Basin (Lisan and Ifal Formations; Figure 2.8).

Quaternary to Present seismic activity continues in the southern Gulf of Suez and Gulf of Aqaba (Bosworth et al., 2005). Furthermore, volcanism is still active along the Saudi Arabian Red Sea margin, including recent and Quaternary eruptions at Harrats Kishb, Khaybar and Rahat and Quaternary lava at Harrats al Birk, Ishara, Kura and Ithnayn (Bosworth et al., 2005; Figure 2.10).

2.3.6 Geodynamic models

Different models have been put forward to explain the dynamics of the Red Sea rifting utilising knowledge about rifting, uplift and volcanism (e.g. Bohannon et al., 1989; Omar et al., 1989; Menzies et al., 1992; Davison et al., 1994; Bosence, 1998; Bosworth et al., 2005; Almalki et al., 2015). Although there are disagreements on the applicability of such models, it is noted that causes and effects change along the Red Sea. Modification of an ideal normal-to-extension rifting was imposed by pre-existing basement structures, the collision of Arabia and Eurasia and the effect of the Afar plume (Bosworth et al., 2005), which suggests that no one model should be applicable to the whole Red Sea rifting.

Along the central Arabian Red Sea margin, Bohannon et al. (1989) argued for a model of passive mantle rifting supported by a sequence of volcanism and rifting that pre-date uplift. Davison et al. (1994) argued that the role of the Afar plume in determining the different sequence of events was to attenuate the lithosphere, guiding far field stresses rather than to drive rifting actively. Compatible with these views, Bosence (1998) favoured the pure shear passive model (McKenzie, 1978) as it explains the conformable relationships between pre-rift sediments and plume volcanics (Figure 2.1c). Conversely, with respect to the geometry of extension, the topographic and volcanics asymmetry were used to suggest that the simple shear model is applicable to the Red Sea extension (Wernicke, 1985; Voggenreiter et al., 1988; Figure 2.1d).

Advocates of mantle-active rifting supported their argument by observations of high thermal flow and elevated shoulders along the Gulf of Suez (Steckler, 1985) and large quantities of continental flood basalts at the southernmost Red Sea and Afar (e.g. White and McKenzie, 1989). For instance, at the western Gulf of Suez margin, uplift was interpreted to have occurred after, yet relatively close to, the

onset of rifting and was explained by a geodynamic model of small-scale mantle convection as a driving force complementing the effect of thermally-induced uplift via passive mantle extension (Steckler, 1985; Omar et al., 1989).

Alternatively, other workers favoured hybrid models (e.g. Almalki et al., 2015). Through imaging the lithospheric thickness, Hansen et al. (2007) proposed a two-phase history with a passive rifting mechanism giving way to dynamically supported active processes. Additionally, classic models of extension (active and passive) were argued to not be applicable in the Yemeni Red Sea (Menzies et al., 1992; Davison et al., 1994). Hosny and Nyblade (2014) concluded that uplift and topographic and volcanic asymmetry were driven by deep flow linked to mantle plumes that significantly post-dated the onset of rifting, rather than the extension itself.

2.3.7 Cenozoic geomorphic evolution

2.3.7.1 Uplift, erosion and exhumation

A great escarpment with elevations over 3 kms in some areas flanks the southern Arabian coastal plain of the Red Sea extending from 21°30’N to the southwestern corner of the Arabian Peninsula (Figures 2.7, 2.11 and 2.12). North of 21°30’N, the escarpment gradually diminishes in elevation and becomes laterally discontinuous, before resuming its continuity north of 26°6'N with an average elevation of ~1-2 kms. Szymanski et al. (2016) suggested that, spatially, the area between the high elevation in the south and the lower elevation in the north, which coincides with the Makkah-Madinah-Nafud (MMN) volcanic trend, defines a point of changing rift styles between the southern and northern Red Sea.

On the African side, the southern counterpart escarpment bounds the Ethiopian plateau and reaches heights of over 2 km but retains lower elevations at the Red Sea Hills and further north at the Gulf of Suez margin (Figures 2.7, 2.11 and 2.12). However, basement blocks locally reach >2 km in elevation. High elevations are also noted in the Sinai Peninsula exceeding 2 km (Bosworth, 2015).

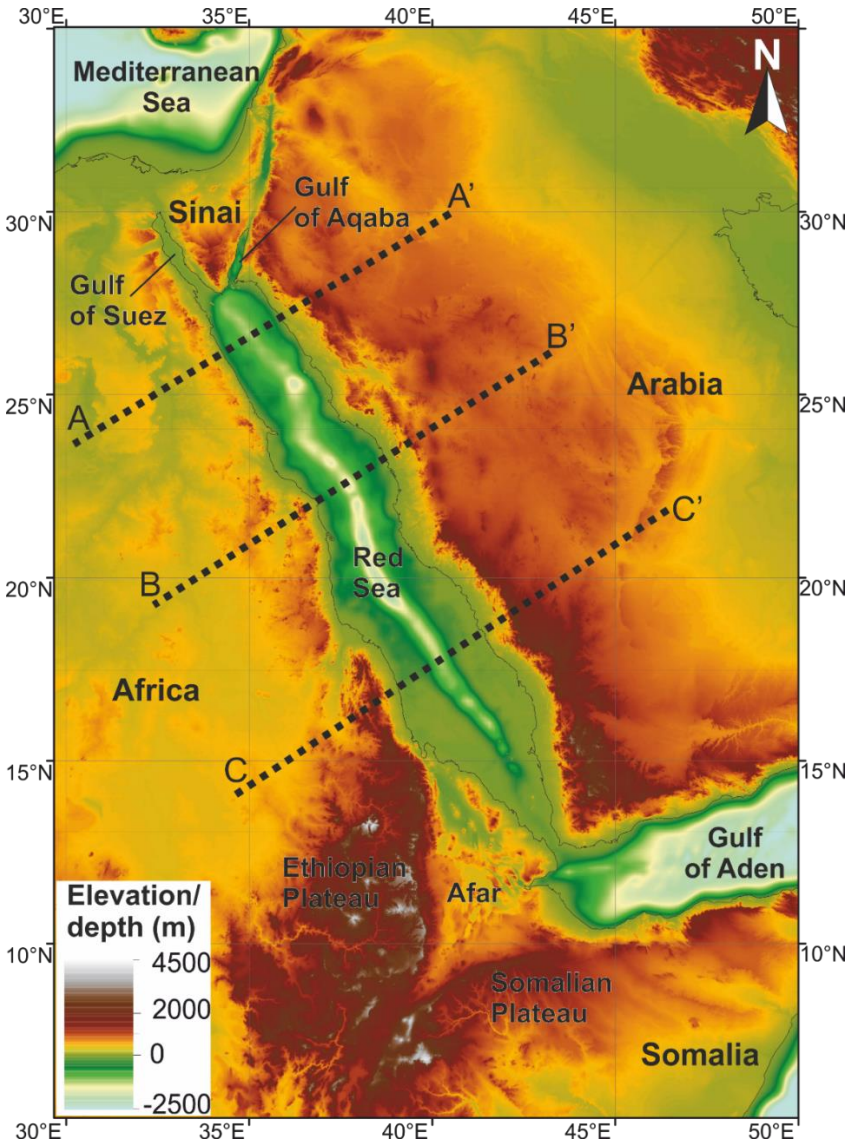

Figure 2.11: Topography and bathymetry of the Red Sea and surrounding areas. Topographic data (above sea-level) are from GLOBE Task Team et al. (1999). The bathymetry (below sea-level) was constructed using depth points downloaded from https://topex.ucsd.edu/cgi-bin/get_data.cgi (Smith and Sandwell, 1997). The two datasets were combined using Esri ArcMap. The dashed lines are the locations of the cross sections in Figure 2.12. Note the topographic asymmetry where the Arabia surface is mostly higher than the African surface.

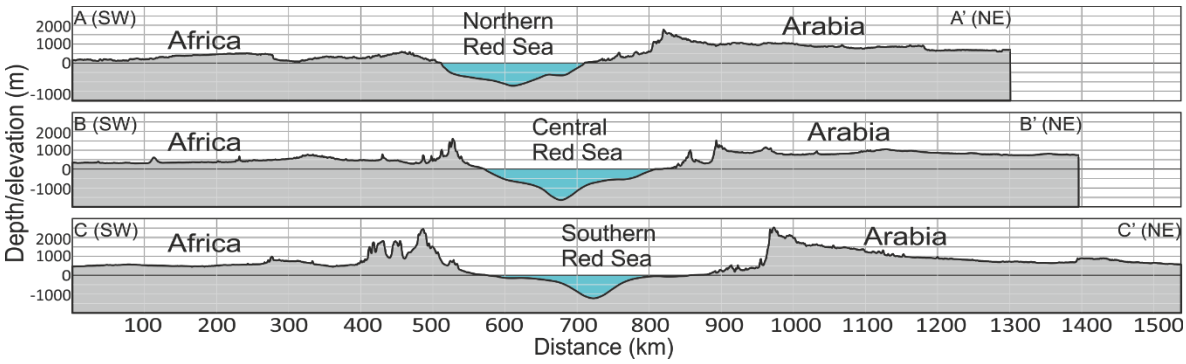

Figure 2.12: Topographic-bathymetric cross-sections across the northern (top), central (middle) and southern (bottom) Red Sea extending to Arabia and Africa. The locations of the sections are shown in Figure 2.11. The sections show the topographic asymmetry, which is clearest in the north. VE is approximately 300:1.

The high elevations described above have provided an impetus to assess the dynamics of the uplift spatially and temporally (Bosworth, 2015). Several studies have attempted to explain this surface uplift by considering the lithospheric structure (Hansen et al., 2007), shear wave velocity (Hansen et al., 2008; Park et al., 2008; Yao et al., 2017), mantle flow (Daradich et al., 2003; Japsen et al., 2012) and geomorphic state in terms of drainage profiles (Wilson et al., 2014). Furthermore, estimates of the exhumation history along the Red Sea margins have been produced using low-temperature thermochronology and assuming different paleo-geothermal gradients (e.g. Bohannon et al., 1989; Omar et al., 1989; Menzies et al., 1992; Steckler and Omar, 1994; Omar and Steckler, 1995; Ghebreab et al., 2002; Feinstein et al., 2013; Szymanski, 2013; Szymanski et al., 2016).

Low-temperature thermochronology data around the Red Sea indicate that denudation commenced at 24-23 Ma before regional rift shoulders developed at 22-20 Ma (Bosworth, 2015 *and references therein*). Erosion of the uplifted shoulders was coeval with the early Red Sea rifting and the regional dyking at 24–23 Ma (Bosworth et al., 2005).

Numerical modelling of AHe and ZHe ages showed that exhumation driven by normal faulting characterised the tectono-geomorphic state of the central Arabian rift flank (CARF), rather than a more extensive uplift of the whole rift flank (Szymanski et al., 2016). In detail, these modelling results indicated exhumation

from ~1.7±0.8 km depths along Red Sea parallel faults across ~150-km wide area at ~23 Ma (8-Myr-long phase of broad extension), before faulting migrated towards the Red Sea basin at ~15 Ma during the rift-oblique extension (Szymanski et al., 2016).

Older AFT cooling ages (~34 Ma) from the Egyptian sides of the Red Sea and Gulf of Suez were reported by Steckler and Omar (1994) and Omar and Steckler (1995) who suggested that they were related to an earlier phase of Red Sea rifting. Omar and Steckler (1995) reanalysed samples presented in Bohannon et al. (1989) from southwestern Saudi Arabia and concluded that these two cooling (hence, uplift and erosion) events in Egypt (Early Oligocene (34 Ma) and Early Miocene (21-25 Ma)) characterised the whole Red Sea. Bosworth and McClay (2001), however, proposed that the older cooling was possibly associated with an earlier (Late Eocene) Syrian arc-related compression, limiting the influence of the Red Sea rifting to the Early Miocene cooling event.

S-wave receiver function model of the lithosphere shows that the high elevations of western Arabia are not accounted for isostatically but are rather supported by lithospheric flexure or asthenospheric convection (Hansen et al., 2007). The dynamic support of the Arabian Plate has also been demonstrated through the inversion of drainage profiles to estimate the history of uplift (Wilson et al., 2014) and seismic tomography (Daradich et al., 2003). Daradich et al. (2003) concluded that mantle convection drove the tilt of the Arabian plate over a scale that is much larger than the rift. Red Sea uplift and tilt of Arabia were suggested to be of a late stage (post-dating 12 Ma) and, therefore, not related to the rifting process (Camp and Roobol, 1992; Daradich et al., 2003; Japsen et al., 2012).

In the Gulf of Aqaba domain, Clark (1987) reported in the accompanying report to his map a minimum of 500 m of uplift in the northwestern part of the Midyan Basin, associated with the Gulf of Aqaba opening. Carbonate Pleistocene terraces along the eastern margin of the Gulf of Aqaba have experienced uplift of up to 19 m, interpreted to have been driven by transform-normal extension (Bosworth et al., 2017; Taviani et al., 2019). The uplift profile along the gulf margin shows an increase from the northeast to the centre before decreasing towards the southwest, and the uplift rates were calculated to be approximately 0.12-0.16 mm/a (Bosworth

et al., 2017). The uplift resulted in the exposure of the syn-rift Miocene strata at the Midyan Basin (Tubbs et al., 2014).

Red Sea terraces that are time-equivalent to those along the Gulf of Aqaba, however, have not been similarly uplifted (Plaziat et al., 1998; Bosworth et al., 2005). Along the Arabian Red Sea, such paleo-sea-level indicators are now 4-7 m above sea-level (Manaa et al., 2016; Bosworth et al., 2019). Considering that the last interglacial stage sea-level was ~7 m higher than present-day level, these elevation values demonstrate more tectonic stability than the Gulf of Aqaba.

Further north, AFT analysis (AFTA) of samples collected from southwestern Jordan (within 30 km northeast of the city of Aqaba) suggests a Cenozoic uplift of 3.8 km, which started in the Oligocene (Feinstein et al., 2013). This age is much older than the Middle Miocene age of the Dead Sea transform, where their study area is located, and was interpreted to be related to the plate modifications heralding the advent of the Red Sea rifting (Feinstein et al., 2013).

In the Sinai Peninsula, AFTA of basement rocks collected from the western margin of the Gulf of Aqaba shows very old ages that suggest that minimal uplift has occurred in this part of the margin (Kohn and Eyal, 1981). This corroborates the conclusion made by Bosworth et al. (2017) that the Gulf of Aqaba transform is associated with significant dip-slip component that resulted in the uplift of its eastern margin.

2.3.7.2 Drainage evolution

Paleo-drainage since the Oligocene in Arabian and Northeast Africa was generally directed towards the north (varying from NE to NW; Goudie, 2005; Feinstein et al., 2013 *and references therein*) and may be attributed to the regional slope towards the north of Arabia-Nubia due to Afar doming (Avni et al., 2012). This is supported by sedimentological indications that eastern Sinai, the Dead Sea Rift and the western Jordanian Plateau received Early Miocene fluvial sediments that were partly sourced from the Precambrian Arabian-Nubian Shield basement (Zilberman and Calvo, 2013).

The general northward direction has been suggested to characterise major drainage in the Central Arabian Rift Flank (CARF) prior to capture by rift-related

drainage (Brown et al., 1989). Furthermore, this direction is indicated by sedimentary structures within the Lower Miocene Burqan Formation in the Midyan Basin that suggest that the sediments were delivered from the southeast (Hughes and Johnson, 2005). Although the Burqan Formation was deposited in marine conditions, the paleo-current indicators suggest that clastic sediment input into the basin was largely fed by northward flowing drainage from the southeast of the basin.

On the African margin, the catchment of the River Nile has existed since the Oligocene (Fielding et al., 2018) but it evolved during several stages to its current state (Goudie, 2005). The tributaries from the proto-Red Sea margin flowed towards the west and northwest to join the main Nile channel, which was interpreted to have been approximately 700 km west of its present-day course (Macgregor, 2012). The north-directed drainage is also indicated by Late Miocene to Recent thick sedimentary units deposited over the Middle Miocene halite and sourced by the large N-S oriented Halaib catchment (60,000 km^2) that is located in southeastern Egypt and northeastern Sudan (Macgregor, 2012).

Further north, Macgregor (2012) proposed that close to Gulf of Suez margin, drainage during the Early Miocene first flowed southward before turning westward towards the paleo-position of the Nile main channel. However, early rift clastics in the Gulf of Suez were interpreted to have been sourced from the south, prior to ~19-15 Ma (Evans, 1990). The southern extent of the catchment that sourced these sediments is not known but, given the present-day topographic highs south of the western Gulf of Suez margin, it is likely that this catchment extended further south than the present-day extent. Such north-directed drainage had probably characterised the Wadi Qena (presently a large watershed with drainage flowing southward as part of the Nile catchment) prior to Red Sea tectonics (Goudie, 2005).

In general, drainage is affected by the prevailing climate, which is presently arid across most areas surrounding the Red Sea basins except the southern areas where orographic precipitation results in a wetter climate (Bosworth, 2015). However, it is likely that early during the Cenozoic, the climate was wetter and, therefore, the presently arid valleys were flowing rivers (Goudie, 2005). During the

Late Miocene two distinct climate states have been distinguished in the African Northeast from sedimentary strata; an arid Tortonian and a wet Messinian (Griffin, 1999). Established during the Pleistocene, the present-day aridity resulted in a lack of permanent rivers on the Arabian side that would have formed deltas in wetter paleo-climates similar to the Tokar Delta in Sudan (Bosworth, 2015).

Part II: Results chapters

Chapter 3 Uplift evolution of continental rifts from drainage analysis: observations from the northern Red Sea and Gulf of Aqaba

This chapter evaluates the uplift of the northeastern Red Sea and eastern Gulf of Aqaba margins during the Cenozoic rifting stages. The chapter forms a framework for the spatially smaller study area of brittle deformation and exhumation closer to rift basins (Chapter 4 and 5) and the spatially larger study area of the drainage evolution in light of uplift estimates across the northern Red Sea and the nearby gulfs (Chapter 6).

3.1 Introduction

Elevated passive margins and relict rift basins preserved on rift flanks beg the question of what syn- and/or post-rift processes resulted in their uplifted positions, a subject of several studies given its importance for understanding the evolution of continental margins (e.g. Weissel and Karner, 1989; Japsen et al., 2012). Several authors have attributed these processes to rifting (e.g. Osmundsen and Redfield, 2011), which can include normal fault footwall block tilting and strike-slip deformation (e.g. Bosworth et al., 2017). Others have demonstrated the youth of such uplifts, suggesting post-onset-rifting processes (e.g. Doglioni et al., 2003; Walford and White, 2005; Japsen et al., 2012).

Uplift has a great impact on drainage evolution, and landscape characterisation, therefore, can provide an insight into its spatio-temporal evolution (e.g. Twidale, 2004). In particular, the use of drainage profiles (i.e. elevation vs distance to base-level) has recently received considerable attention to reconstruct epeirogeny-related uplift histories (e.g. Roberts and White, 2010; Paul et al., 2014; Wilson et al., 2014).

The Red Sea is flanked by continental rift basins (close to the point of break-up in the north (Cochran, 2005)), young passive margins in the south, and an active transform margins bounding the Gulf of Aqaba (Bosworth et al., 2005). The

northeastern Red Sea margin is dominated by basement units with Cenozoic rift basins straddling the rift flank (Hughes and Johnson, 2005; Szymanski et al., 2016; Figure 3.1).

Topographically, the Arabian margin is characterised by a prominent escarpment in the south that, in general, diminishes in elevation towards the north (Bosworth, 2015). The plate-scale drainage divide coincides with the escarpment in the south but deviates from it towards the north where it becomes generally oriented N-S (Wilson et al., 2014). Moreover, the Arabian margin is higher than the conjugate African margin (Japsen et al., 2012).

Understanding the spatial and temporal distribution of uplift in an area that has undergone two phases of extension (rift-normal and rift-oblique/strike-slip) with indications of sub-lithospheric active upwelling helps decipher the relative effect of the causal processes of the uplift. In this respect, little work has been undertaken to constrain the uplift during the Cenozoic along the northeastern Red Sea and the eastern Gulf of Aqaba.

Here, the morphotectonic evolution of the northeastern Red Sea and eastern Gulf of Aqaba margins is investigated in order to address the question of how uplift varied spatially and temporally. Firstly, the present-day drainage is analysed to investigate the relationship between rift structures, uplift and drainage evolution. Secondly, uplift history is estimated through an inverse model that relates uplift to the erosional signal recorded by the drainage streams (e.g. Pritchard et al., 2009). The uplift model is correlated with geomorphological metrics, namely an estimate of the minimum erosion volume and the local relief. Finally, a morphotectonic evolutionary model integrating uplift, structural observations and the drainage analysis interpretation is proposed. This workflow benefits from its dependency on ubiquitous drainage pathways and simple geomorphic metrics, and has applicability in quantifying the evolution of margins worldwide, particularly where uplift measurement data are limited.

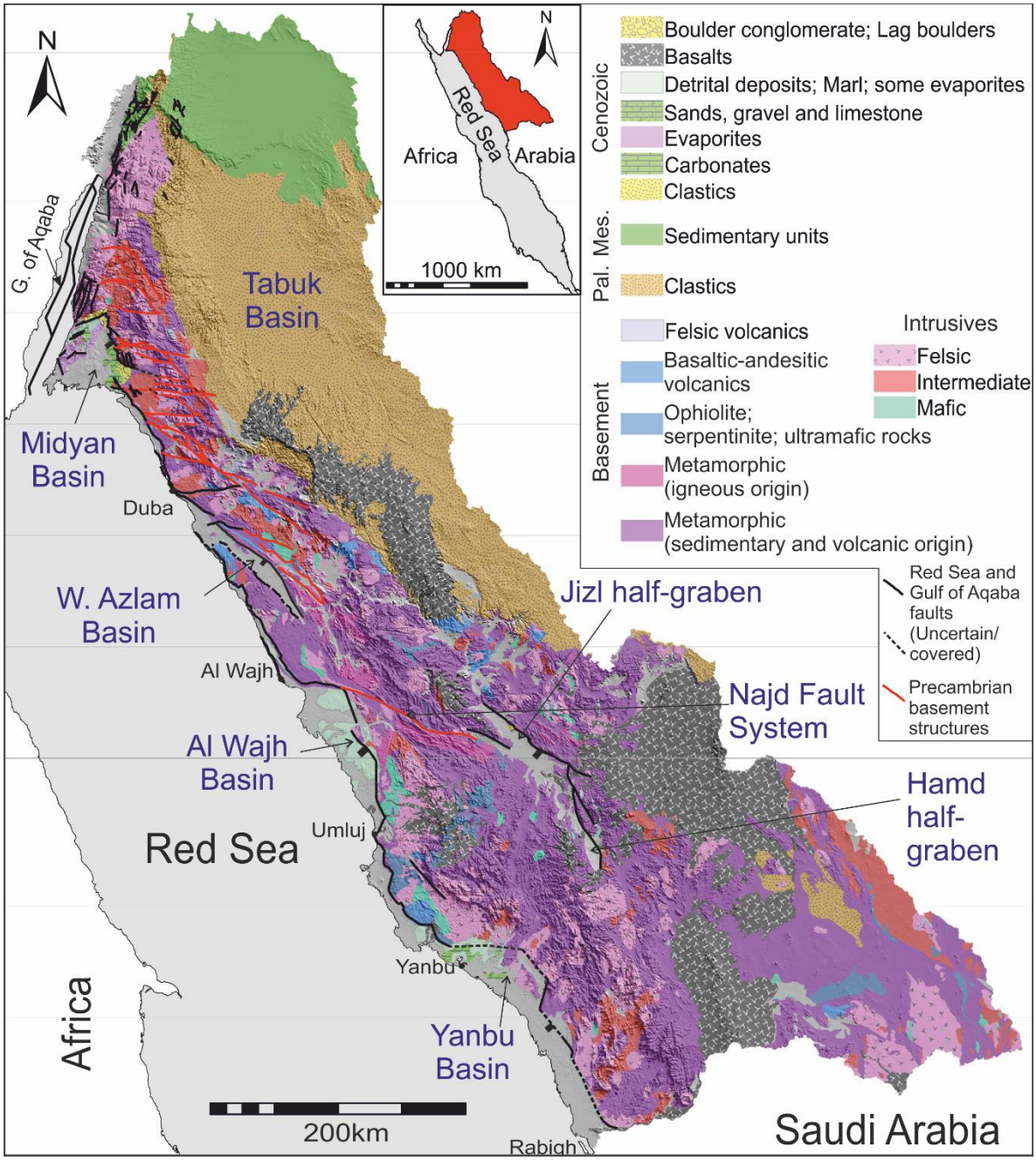

Figure 3.1: A geological map of the study area showing the major lithological units, rift basins, major rift faults and basement Precambrian structures (Modified from Brown et al. (1989), Clark (1987) and Powell et al. (2014)). The location of the geological map with respect to the Red Sea, Arabia and Africa is shown in the inset map (red polygon). Pal.: Paleozoic strata; Mes.: Mesozoic strata.

3.2 Methodology

The methodology aims to constrain the morphotectonic evolution of the northeastern Red Sea and the eastern Gulf of Aqaba during rifting, focusing on the

spatio-temporal variation of the uplift. To that end, a workflow utilising drainage network analysis and geomorphic features is implemented to establish a morphotectonic evolutionary model for this portion of the rift flank.

3.2.1 Data

This study utilises topography data extracted from the Advanced Spaceborne Thermal Emission and Reflection Radiometer global digital elevation model (ASTER GDEM; ~30x30 m). The data were downloaded from https://gdex.cr.usgs.gov/gdex/ (ASTER GDEM is a product of NASA and METI).

In addition, Esri Global Imagery data were used to validate DEM interpretations. The data cover the northeastern Red Sea and eastern Gulf of Aqaba drainage catchments that have outlets between the town of Rabigh and the northern tip of the Gulf of Aqaba (Figure 3.1).

3.2.2 Methods

3.2.2.1 Data preparation

ArcMap was used to process and analyse the DEM following an established procedure (O'Callaghan and Mark, 1984; Tarboton et al., 1991) to extract the drainage network and catchments (Figure 3.2). The workflow makes use of predefined tools that can be found in the ArcToolbox. The ArcMap workflow started with conditioning the DEM (filling data gaps and removing spikes) before calculating the drainage flow direction. The flow direction was used to calculate the drainage accumulation. The drainage accumulation at a particular raster cell is basically the number of raster cells that contribute flow towards this cell (Tarboton et al., 1991).

Raster cells with accumulation values greater than 100 cells (equivalent to ~90 km^2) were extracted and the resultant raster network was converted into drainage network vector format. Furthermore, flow direction was used to extract the boundaries of the catchments (as raster before being converted to vector format). This process of extraction yields catchments that vary in size from ~105,000 km^2 to less than 1 km^2 (Figure 3.3).

Catchments along the northeastern Red Sea margin that are less than 200 km^2 cover mostly loose sediments substrate and are associated with low reliefs and slopes. Due to the possible deterioration in the data (e.g. catchment boundary definition), the analysis is confined to those catchments that are larger than 200 km^2. In contrast, mostly-bed rock catchments draining to the Gulf of Aqaba have areas as low as 20 km^2. A total of 45 catchments along the Red Sea (NERS; larger than 200 km^2) and 24 catchments along the Gulf of Aqaba (EGA; larger than 20 km^2) have been selected for geomorphic analysis and drainage characterisation. For each of these catchments, the area was calculated, which is to be used in further calculations (see Section 3.2.2.3).

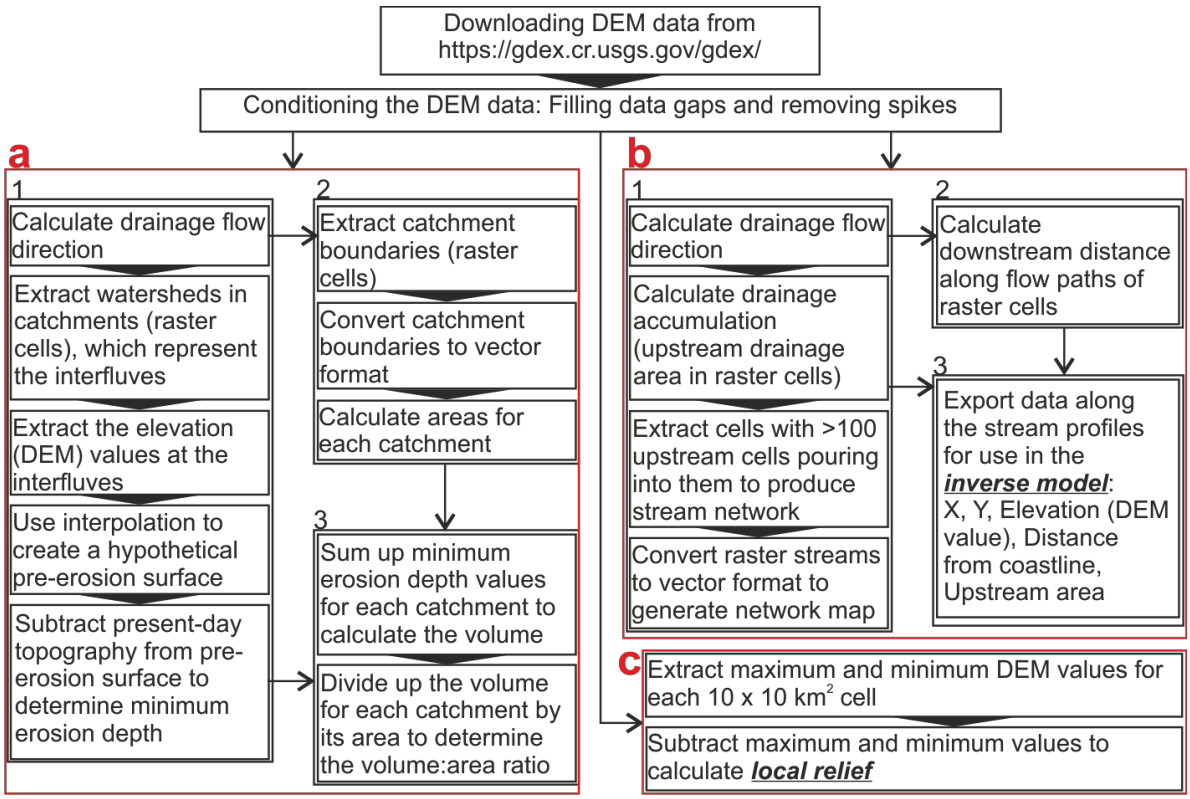

Figure 3.2: A chart showing the workflow followed in this chapter to a) extract drainage catchments and estimate minimum erosion volume, b) extract data for use in the drainage inverse modelling, and c) estimate the local relief.

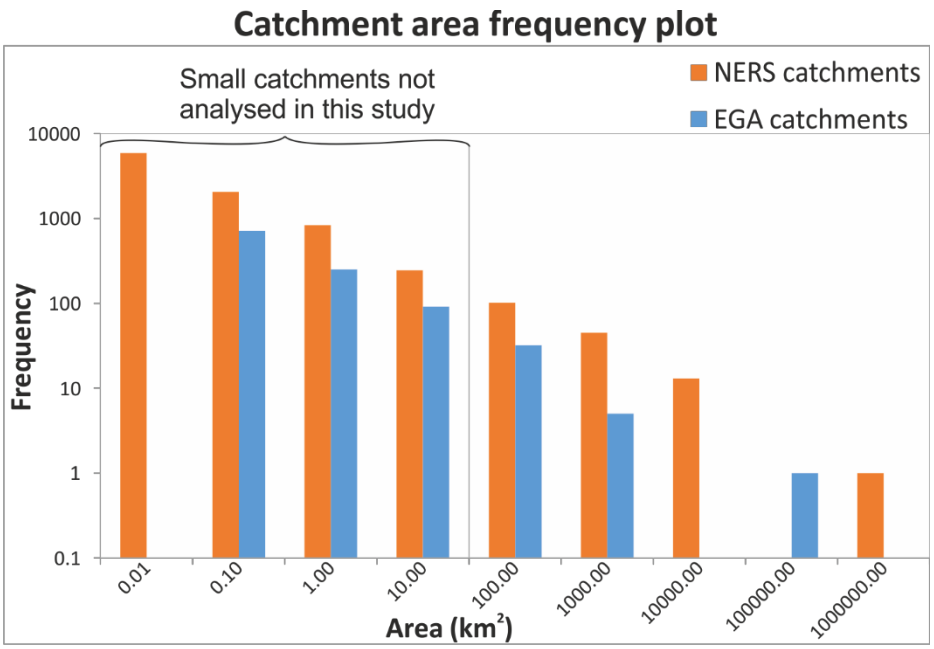

Figure 3.3: A frequency plot, in logarithmic scales, of areas of all catchments extracted from the northeastern Red Sea (NERS) and eastern Gulf of Aqaba (EGA) margins DEM (WGS84, UTM zone 37°N). Note the large number of small catchments that were not analysed in terms of their tectonic settings.

3.2.2.2 Uplift history from drainage inverse modelling

River profiles (i.e. elevation vs distance from the coastline) are shaped by the forces of uplift and erosion (Pritchard et al., 2009; Roberts and White, 2010; Wilson et al., 2014). The equation describing the relationship between uplift, erosion and profile shape is given by:

$$\frac{\partial z}{\partial t} = U(x,t) + E(x,t) \qquad \text{(Equation 3.1)}$$

where *U* and *E* are the rates of uplift and erosion, respectively, $\frac{\partial z}{\partial t}$ is the change in elevation with time (i.e. surface uplift) and x is the distance along the stream to the base-level. An increase in the gradient of the valley bed at the drainage mouth in response to uplift, for example, will migrate upstream but will be moderated by an erosional rate.

It is generally accepted that the stream power erosional model provides a way of modelling longitudinal river profile evolution on long length (10s-100s kms) and time (Myrs) scales (e.g. Rosenbloom and Anderson, 1994; Whipple and Tucker, 1999; Roberts et al., 2019). The model builds upon the following formulation

describing erosion as nonlinearly resulting from a combination of advective (stream incision) and diffusive (topographic lowering) processes (e.g. Rosenbloom and Anderson, 1994; Whipple and Tucker, 1999):

$$E(x,t) = -vA^m \left(\frac{\partial z}{\partial x}\right)^n + \kappa\left(\frac{\partial^2 z}{\partial x^2}\right) \qquad \text{(Equation 3.2)}$$

where *n* and *m* are dimensionless exponents of the stream gradient (∂z/∂x) and the upstream area (*A*), respectively, *v* represents the advection parameter related to the lateral migration of incision along the stream, and κ represents a diffusion parameter related to the lowering of the landscape. The incision rate is controlled by the discharge, and the upstream drainage area value at each point along the stream is assumed to be a proxy to the discharge. Substituting the right-hand side in Equation 3.2 for *E* in Equation 3.1 yields:

$$\frac{\partial z}{\partial t} = U(x,t) - vA^m \left(\frac{\partial z}{\partial x}\right)^n + \kappa\left(\frac{\partial^2 z}{\partial x^2}\right) \qquad \text{(Equation 3.3)}$$

Over the past decade, much research has focussed on the development of inverse algorithms that build upon the above relationships and utilise drainage profile shapes to solve for uplift rate in space and time (e.g. Pritchard et al., 2009; Roberts and White, 2010; Roberts et al., 2012a; Roberts et al., 2012b; Czarnota et al., 2014). That is, given the shapes of the stream profiles, which can be extracted from DEM data, solving for uplift rate (*U*) can only be accomplished by parameterising the erosional rate (*E*).

Here, an inverse model is used to solve for uplift rates and magnitudes and the following sections illustrate its setup. Furthermore, the parameters used for calibrating the erosional component are defined, along with the input data and assumptions made.

3.2.2.2.1 Inverse modelling setup

Wilson et al. (2014) determined the incision of basalts at Harrat Rahat, which is located partly within this study area (southernmost volcanic field in Figure 3.1), for their study of the Cenozoic epeirogeny of Arabia and used the incision rate to determine the values of *v* and *m* (*v* = 120, *m* = 0.2). κ can vary by many orders of magnitude without significantly affecting the calculated uplift histories (e.g. Roberts

and White, 2010). Finally, the value of *n* influences the propagation of the incisional signal. If n >1, the steep parts of the stream migrate upstream in a rate that is higher than that of the shallower stream (shock wave behaviour; Pritchard et al., 2009; Wilson et al., 2014). In the case of a shock wave behaviour, the recent uplift events might result in the modification of the stream profile such that records of earlier events are omitted. On the basis of the lack of evidence of this behaviour both in Arabia and other continents (e.g. Africa and Australia; Roberts et al., 2012a; Czarnota et al., 2013), a value of 1 was assigned for *n*. The aforementioned, therefore, justifies the use of the following values to calibrate the erosional component of Equation 3.3:

$$v = 120;\ m = 0.2;\ n = 1;\ \kappa = 0$$

These values simplify the stream power model and result in the following linear equation:

$$\frac{\partial \mathrm{z}}{\partial \mathrm{t}} = vA^m\left(\frac{\partial \mathrm{z}}{\partial x}\right) - \mathrm{U}(x,t) \qquad \text{(Equation 3.4)}$$

Using the method of characteristics, Rudge et al. (2015) rewrote Equation 3.4 as:

$$\frac{\mathrm{dx}}{\mathrm{dt}} = -vA^m \qquad \text{(Equation 3.5)}$$

and

$$\frac{\mathrm{dz}}{\mathrm{dt}} = -U(x(t),t) \qquad \text{(Equation 3.6)}$$

where $U(x(t),t) = U(x,t)$. Equation 3.5 may be rearranged so that, when integrated, the value of *t* is solved for.

$$\frac{\mathrm{dt}}{\mathrm{dx}} = -\frac{1}{vA^m} \qquad \text{(Equation 3.7)}$$

Using the present day values of x and z as boundary conditions at t = 0, and using the values of x = 0 and z = 0 as boundary conditions at a time in the past (landscape response time: τ_G) when the stream was established at the coastline, Equations 3.6 and 3.7 are integrated to yield (Rudge et al., 2015):

$$z^* = \int_0^{\tau_G} U(x(t),t)dt \qquad \text{(Equation 3.8)}$$

$$\tau_G = \int_0^{x^*} \frac{dx}{vA^m} \qquad \text{(Equation 3.9)}$$

and

$$\tau_G - t = \int_0^{x(t)} \frac{dx}{vA^m} \qquad \text{(Equation 3.10)}$$

Here, z^* and x^* are the values of z and x at the present day, and τ_G is the response time of the landscape to an erosional signal that is initiated at the coastline (Wilson et al., 2014).

The relationship in Equation 3.8 can be inverted to for uplift rates that vary in space and time and satisfy the present day values of the elevation (z^*) and distance from the coastline (x^*; incorporated into the equation through τ_G (see Equation 3.9)). These uplift rate values are inserted at vertices that are 10 to 15-km apart at time steps of 3 Myrs. At each time step, linear interpolation is performed to estimate the uplift rates in between the vertices. Integrating the uplift histories over time ($\int Udt$) yields cumulative uplift, which is used to produce fitting theoretical profiles that can be compared to the input, actual, profiles (Roberts and White, 2010; Figure 3.4).

During the inverse modelling, the actual shapes of these profiles were compared iteratively with modelled profiles based on different uplift histories until the history that minimises the difference was achieved (Rudge et al., 2015; Figure 3.4). The data were extracted and conditioned by myself, and the code that was used to perform the inverse modelling was developed by Rudge et al. (2015) and was performed using the dataset in this chapter by Dr Gareth Roberts, Imperial College London (Appendix I).

It is important to point that the data coverage of the model (number of nonzero data points used to extract the uplift value in a given cell) deteriorates both away from the streams (i.e. input data) and back in time. As will be shown in the results section (3.3.2), coverage maps are constructed through time. Given the coverage reduction back in time, the time scale of the model is controlled by the chosen erosional parameters and, therefore, would not capture uplift events earlier than the Cenozoic. However, over the regional scale, geological observations indicate that the Northeastern Africa-Arabia landscape was characterised by low topography and relief and was, in parts, shallowly submerged during the latest Mesozoic and the early Cenozoic times (e.g. see Bohannon et al., 1989; Burke and Gunnell, 2008).

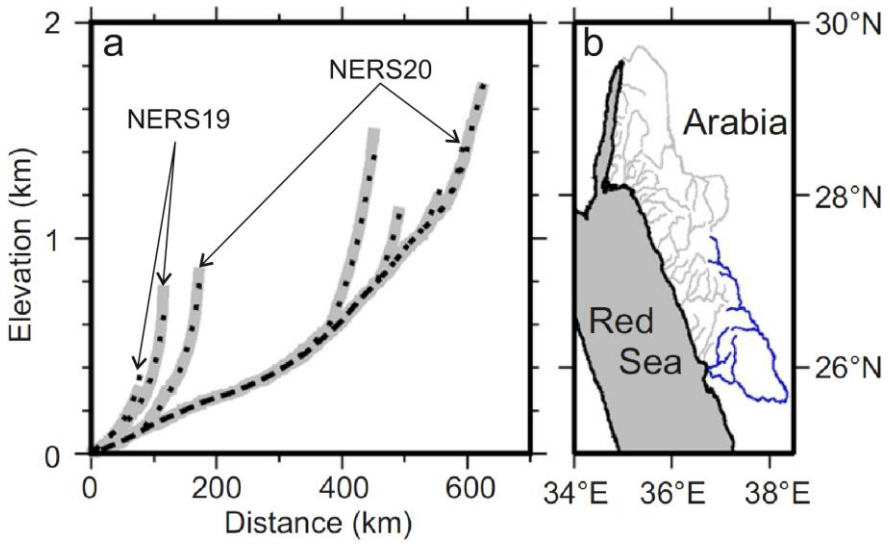

Figure 3.4: (a) Selected extracted longitudinal profiles (grey solid lines) shown along with modelled profiles (black dotted lines) generated by calculating the uplift history that minimises the misfit between the two sets of profiles. The catchments that the streams were extracted from are indicated (NERS19 and NERS20; refer to Figure 3.7 for catchments numbers). (b) The locations of the extracted streams.

3.2.2.2.2 Input data for modelling

The inverse modelling approach described above was followed to determine uplift rates and magnitudes over an area that extends from Yanbu to the northeastern Gulf of Aqaba, and from the coastline to a distance of approximately 200 km inland (Figure 3.1). Using this model, the uplift history that would most likely result in the present-day shapes of the stream profiles was estimated (Pritchard et al., 2009; Roberts and White, 2010; Rudge et al., 2015).

A total of 463 longitudinal profiles (elevation vs distance) draining to the Red Sea and the Gulf of Aqaba were extracted from the DEM for use in the uplift modelling. The streams for which the profiles were extracted represent a sub-set of all of the streams that drain the sub-aerial parts of the margin. For each stream, its position (longitude and latitude), distance from the coastline, elevation, and drainage area have been extracted at a spacing governed by the horizontal raster resolution of the input Digital Elevation Model (DEM; ~30 to 43 m; Figure 3.5; Appendix I).

The lateral stream density increases at the coastal side of the escarpments (see Uplift estimation results (Section 3.3.2)). The high density and the choice of fine

spacing for the vertices at which the uplift rates are inserted makes possible the delineation of short wavelength uplift that might result from, for example, normal faulting.

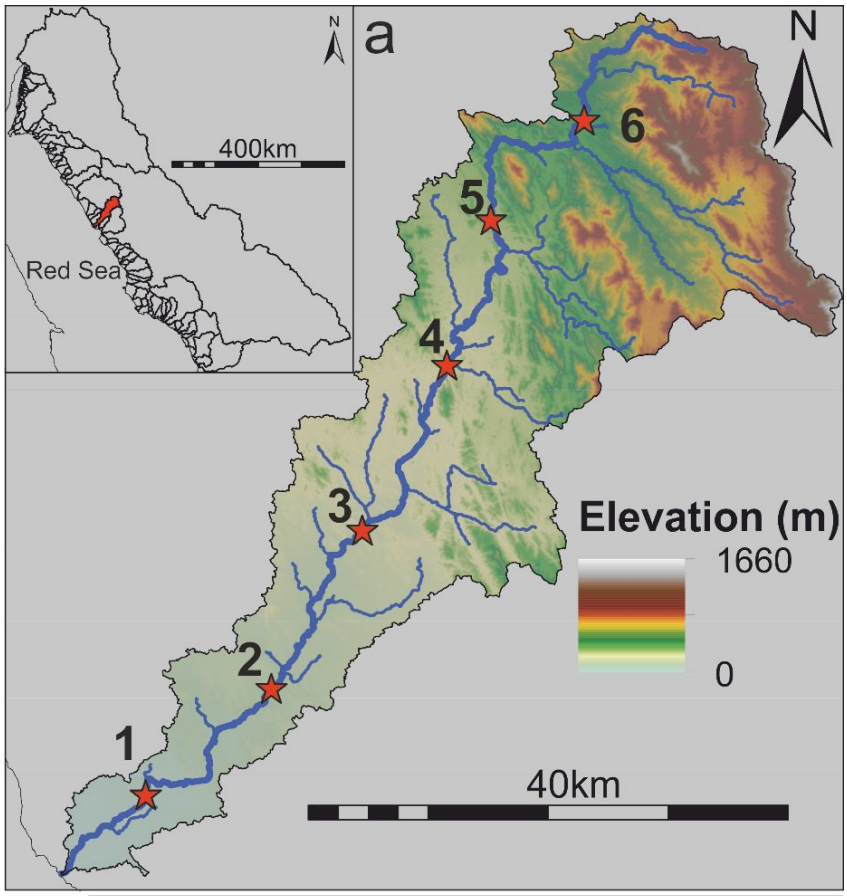

b

Point	X (long.) (m)	Y (lat.) (m)	Z (elevation) (m)	x (distance from divide) (m)	A (upstream drainage area) (m^2)
1	-1128732	165174	34	120038	1277613562
2	-1117442	172752	103	100002	1178018800
3	-1108522	184884	176	80003	991023182
4	-1100039	197640	242	60038	699123195
5	-1095112	209148	305	40024	429141506
6	-1086535	216477	431	20023	127177679

Figure 3.5: An example of the extracted drainage data used in the inverse modelling. (a) A catchment draining to the Red Sea showing the drainage network (blue lines) overlaid on the topography. The inset map shows the catchment location with respect to the NERS catchments (red-filled polygon). (b) Data extracted from the selected red star locations shown along the thick blue stream line in (a). Along the stream, extracted points are 30 to 43 m apart. The XY locations are with reference to GCS_Ain_el_Abd_1970 (Lambert Conformal Conic projection).

A few assumptions were made prior to the implementation of the inverse modelling. First, it is clear that climate can affect the profile shape by enhancing or reducing the erosional rate. As discharge is approximated by the upstream drainage area, it is assumed that climatic information is embedded in the equation. Independent observations on the variation of the climate during the modelled time-span are hard to obtain and the upstream drainage area represents a valid approximation.

Second, the base-level is assumed to be constant over the temporal and spatial scale of the study. It has been shown previously that varying the length of the stream profile and, therefore, changes in sea-level do not affect the calculated uplift rate (Rudge et al., 2015 *and references therein*). Furthermore, an erosional signal that is caused by a significant lowering of the base-level would be characterised by a regional scale given that the base-level for all the streams was lowered. Therefore, if spatial variation in the calculated signal exists, it is unlikely to be caused by a change in the base-level and would rather reflect a spatial distribution in uplift rate. Finally, eustatic sea-level fluctuations occur at higher rate than the investigated scale in this study and during the Cenozoic sea-level drop did not exceed 100 metres (Miller et al., 2005).

3.2.2.3 Other geomorphic analyses

Other geomorphic analyses were performed to be compared with the results of the uplift estimation. Four maps were generated to define topographic variation along the margin, which can be compared to the uplift maps; local relief, minimum bulk erosion (in terms of eroded heights), minimum bulk erosion volume in each catchment, and ratio of the eroded volume estimate to the catchment area. The production of these maps was done using ArcMap.

The local relief was estimated by calculating the difference between the maximum and minimum elevation values over an area. For the purpose of comparing the relief with estimates of uplift, a cell size of 10 x 10 km was used for the calculation of the relief.

The minimum bulk erosion was estimated by subtracting the present-day topography from a surface connecting the interfluve elevations (Figure 3.6a-d).

Similar approach has been used to evaluate the topographic response and correlation with uplift in tectonically active area (e.g. Giaconia et al., 2012; Bellin et al., 2014). The surface connecting the interfluve elevations is assumed to be representative of the pre-rift (pre-incision) topography. The produced map does not show a distribution of the actual erosion heights but represents a device to show the relative variation of erosion given the pre-rift surface assumption. The interfluve elevations were determined by sampling elevations of watersheds within each catchment. The difference between this surface and the present-day topography provides a rough estimate of the minimum height of eroded material.

The estimated minimum erosion values were summed up for each catchment. The summation effectively yields the volume of eroded material for each catchment (Figure 3.6e). This minimum erosion volume was divided by the catchment areas in order to find the ratio of eroded volume to area, which gives an indication of the relative difference of erosion between different catchments (Figure 3.6f). It is important to emphasise that no age constraint is assigned to the pre-erosion surface and, therefore, the resultant maps can only be used to view the relative spatial differences.

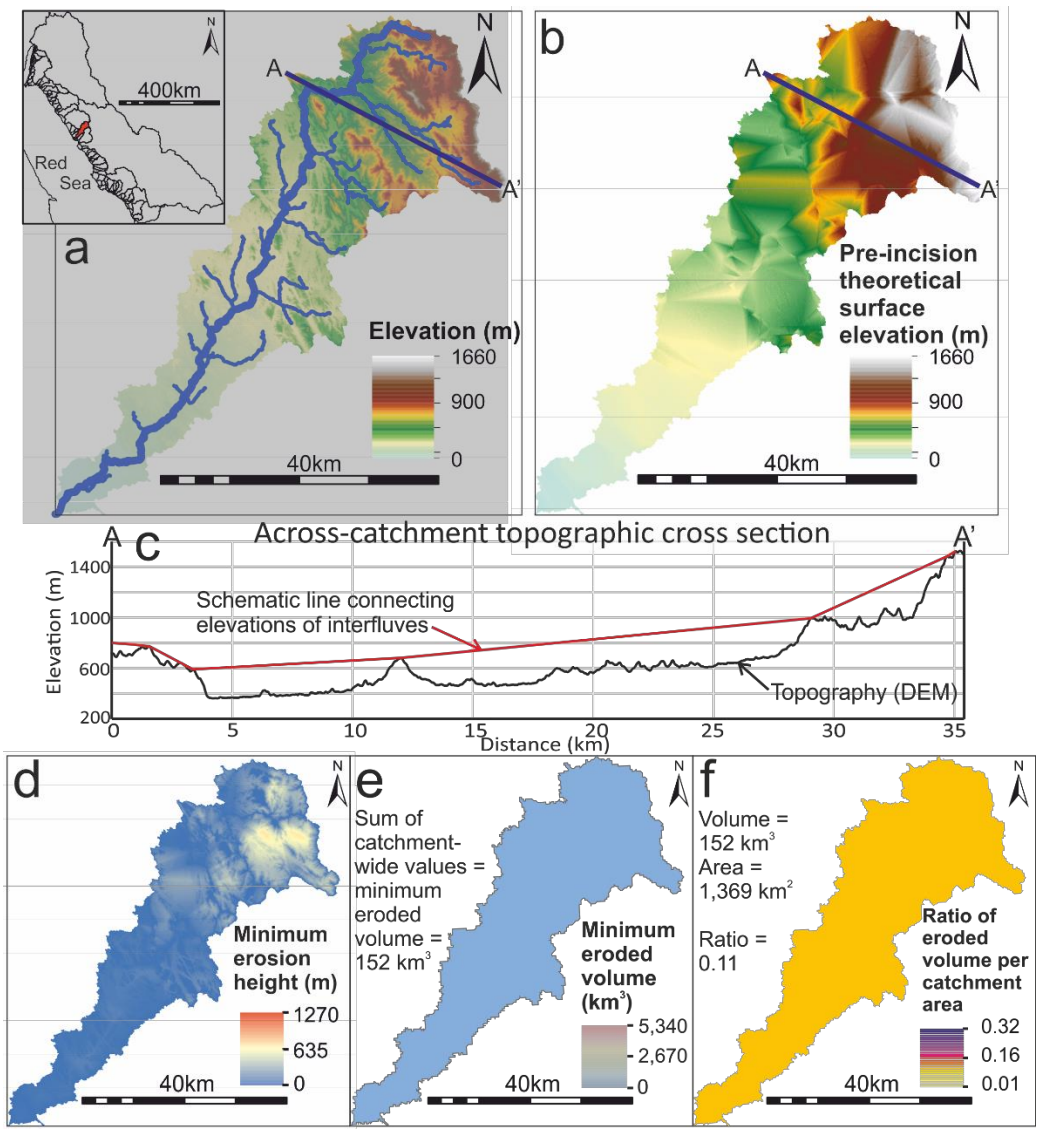

Figure 3.6: A catchment example showing the approach used to estimate the minimum erosion maps: minimum height, minimum volume for each catchment and the ratio of minimum volume to catchment area. (a) Present-day topography (DEM) surface. (b) Pre-incision theoretical elevation surface constructed by interpolation between interfluve heights. (c) A cross-section showing the concept behind the construction of the pre-incision surface. Note that the red line drawing is a schematic and does not represent how the surface is practically produced and is included here for an explanatory purpose. In practice, interpolating between the interfluves heights is performed in 3D rather than across a 2D cross-section. (d) The minimum erosion height map generated by subtracting the present-day topography (a) from the pre-incision map (b). (e) The minimum eroded volume map generated by summing up all of the eroded height values (d) within a single catchment. (f) The minimum eroded volume:catchment area ratio map.

3.3 Results

3.3.1 Geomorphic characterisation

3.3.1.1 NE Red Sea margin

The NE Red Sea margin can be spatially divided into a southern and a northern zones of relatively high escarpments separated by an area of lower elevation (Figures 3.7a and 3.8). The low elevation coincides with the largest drainage catchment (northeastern Red Sea catchment no. 20 (NERS20); around 105,000 km^2 (Figure 3.7)). The distance from the coastline to the escarpments varies between 100 and 45 km (Figure 3.7). Using 200 km^2 as a lower catchment size limit (as those smaller are prone to errors in terms of the delineation of their boundaries due to the low relief and loose sediments they cover (see Section 3.2.2.1)), the mean catchment areas corresponding to the northern and southern zones are ~1,400 and 1,100 km^2, respectively (Figure 3.7b).

3.3.1.1.1 Catchment NERS20

Catchment NERS20 covers several tectonic and geomorphic elements in-board, outboard and in between the two escarpments. These include the Hamd-Jizl Basin, the northern part of the Al Wajh Basin and the plateau areas behind the southern escarpment (Figure 3.7). Close to the coast where NERS20 covers the northern part of the Al Wajh Basin, the width of this catchment (~40 km) is comparable to those of the nearby catchments (e.g. NERS19 and NERS26; Figure 3.9c). Approximately 100 km from the coast, the width of NERS20 increases significantly from ~40 km to >700 km, where its shape becomes elongated in a NW-SE orientation, semi-parallel to the coastline (Figure 3.7a).

Notable within NERS20 are two main channel orientations; a NW-SE and a WNW-ESE (Figure 3.7a). The NW-SE channel is semi-parallel to the Red Sea trend and coincides with an axial valley within the early rift Hamd and Jizl half-grabens. Further east of these half-grabens, drainage off their footwall blocks forms watershed limits within the catchment with pour points into the half-grabens close to where the bounding faults intersect (Figure 3.9c). The lateral arrangement of

these watersheds resembles footwall drainage that would have characterised these early rift half-grabens.

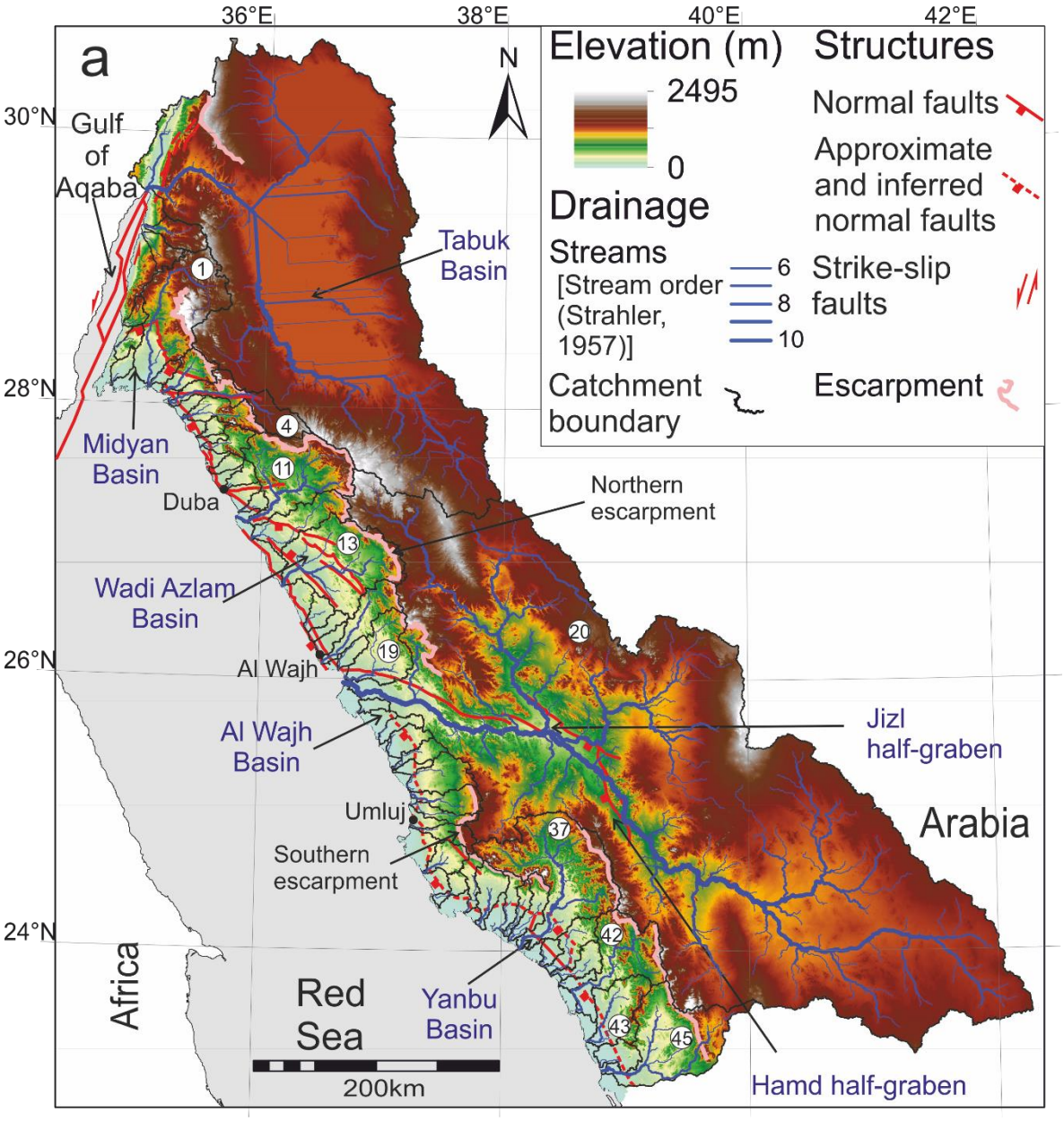

Figure 3.7: Topography and drainage of the study area (WGS1984 UTM Zone 37°N). (a) A DEM topographic map showing the drainage network, valley knickpoints and main onshore basins. Faults are compiled from Brown et al. (1989), Tubbs et al (2014) (northern zone), and Szymanski et al. (2016) (southern zone). The numbers inside the white circles are those of NERS catchments refer to in the text in section 3.3.1. (b) Areas of northeastern Red Sea (NERS#; >200 km^2) and eastern Gulf of Aqaba (inset map; EGA#; >20 km^2) drainage catchments. NZ: northern zone; SZ: southern zone (see text for explanation).

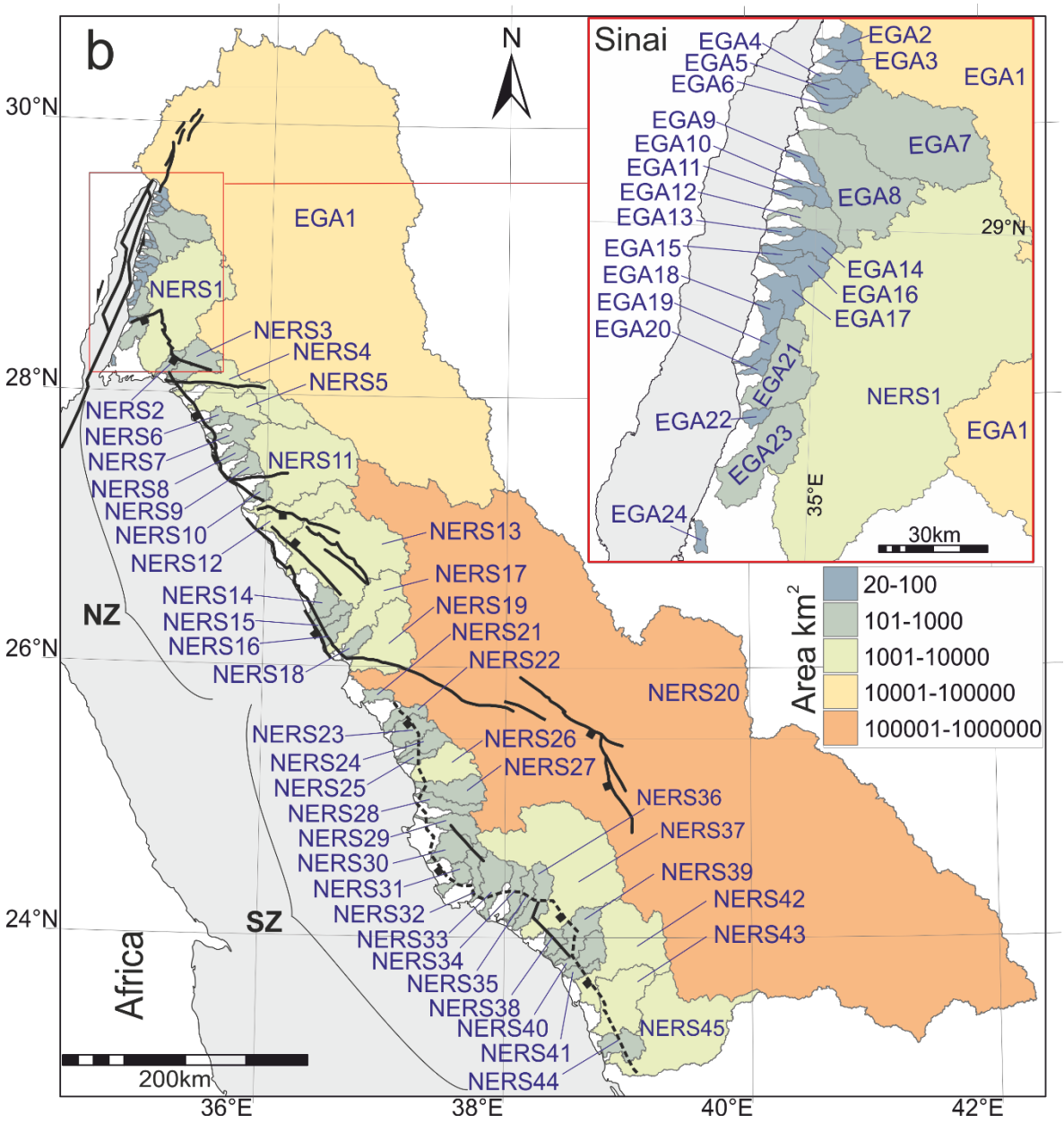

Figure 3.7 (continued).

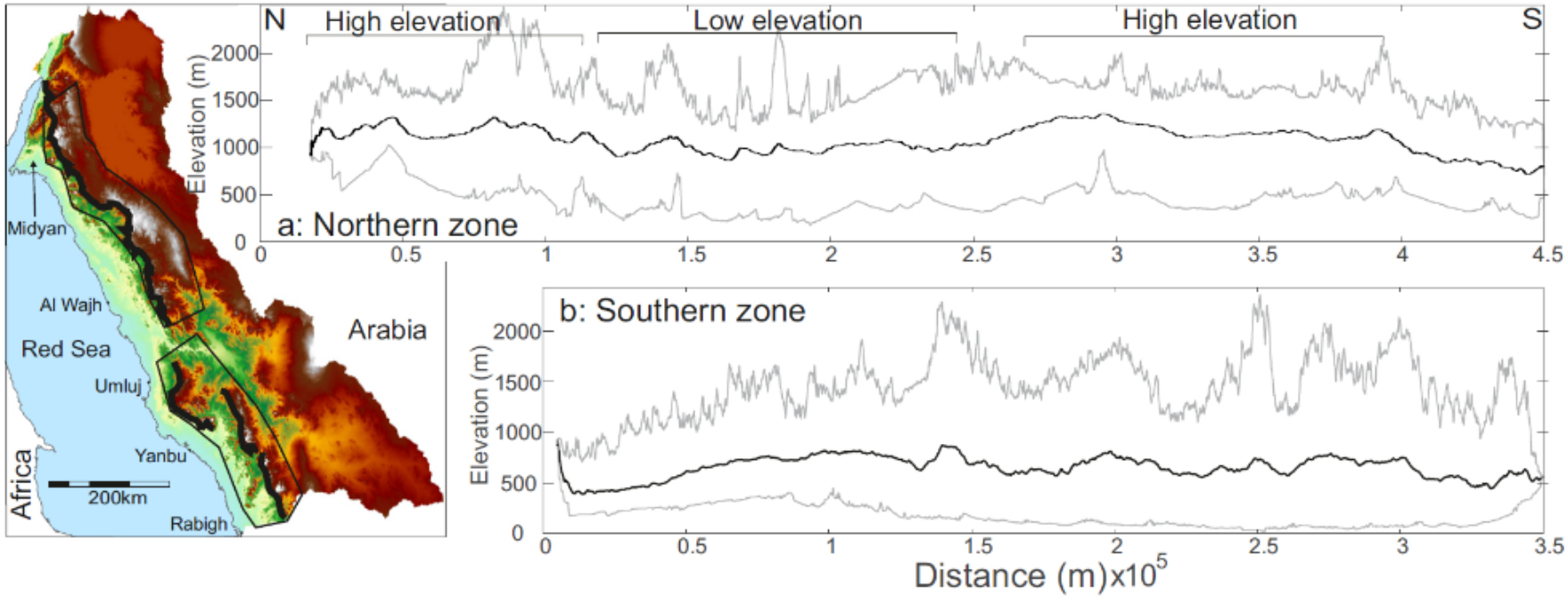

Figure 3.8: The mean (black line), maximum and minimum (grey lines) elevations along swath profiles of the escarpments: (a) The northern zone; (b) The southern zone. Locations of swaths are shown on the map (thin black outlines) and the escarpments are shown as thick black lines.

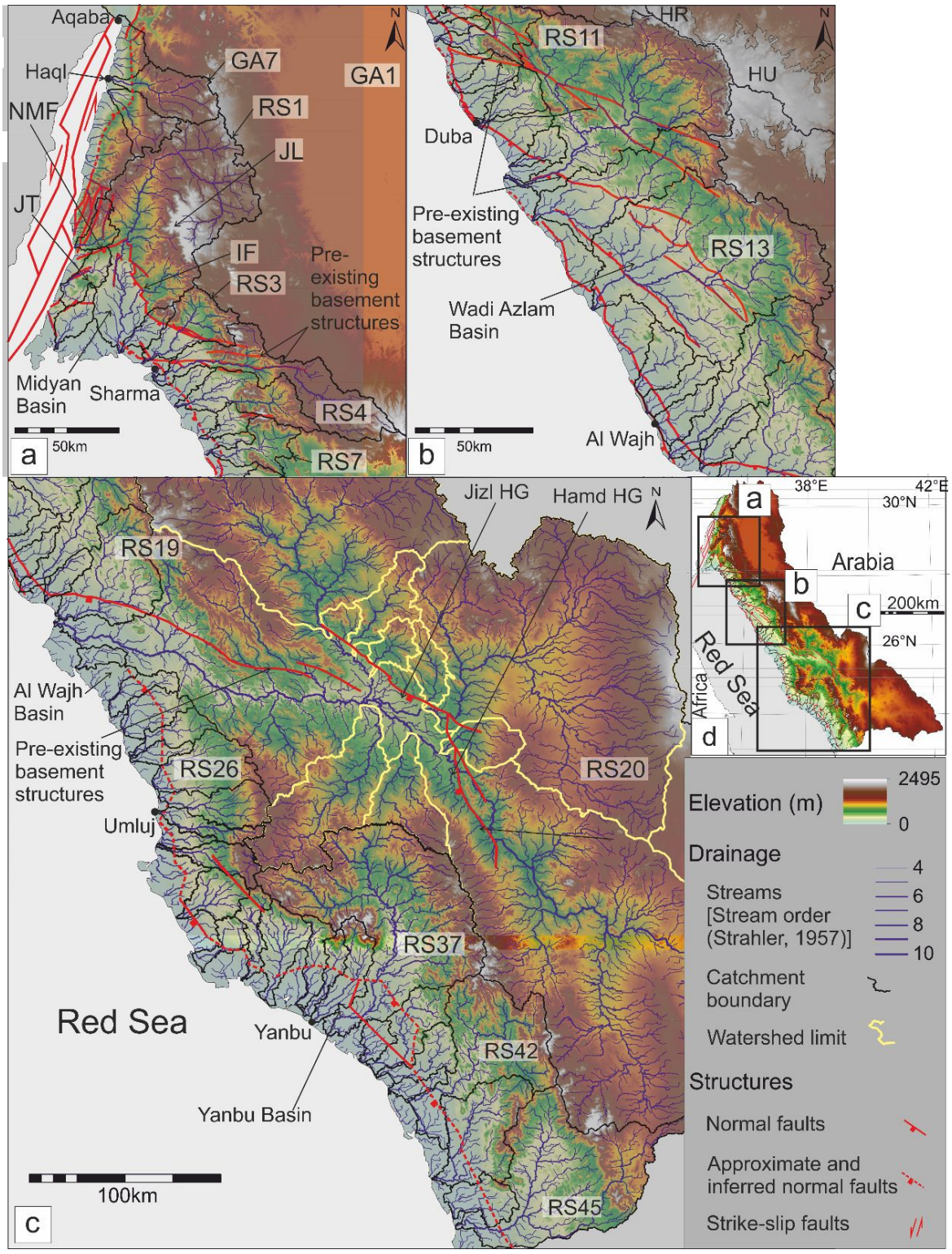

Figure 3.9: Drainage network and faults at (a) Midyan Basin and E Gulf of Aqaba margin, (b) Wadi Azlam, and (c) Al Wajh, Hamd-Jizl and Yanbu Basins. NMF: Northern Midyan Fault, IEF: Ifal East Fault, JT: Jabal Tayran, JL: Jabal al Lawz, HU: Harrat Uwayridh and HR: Harrat ar Rahah. (d) DEM map of the study area showing the locations of (a-c).

3.3.1.1.2 Southern zone

The southern zone is semi-parallel to the coastline from Rabigh to Umluj and features a discontinuous mountain range, with an average elevation of ~650 m (Figure 3.8b). The drainage divide between NERS20 and the catchments in the southern zone coincides with the escarpment where clearly defined. The exceptions are catchments NERS21-26 and NERS45 (Figure 3.7).

Within the southern zone, clear distinction can be made between large (>1000 km^2) catchments in the southern part of the zone (along the Yanbu Basin) and small (<1000 km^2) catchments in the northern part (along the Al Wajh Basin and off the footwall block between the two basins; Figure 3.7). The catchments at the Yanbu Basin latitude are longer with a drainage divide that is approximately 100 km away from the coastline, compared to ~40 km in the northern part.

Overall, smaller catchments have shapes that are elongate and perpendicular to the coastline (Figure 3.7b). These catchments have transverse streams across the basin bounding faults and are considered to be footwall drainages (~40 km). These catchments have outlets spaced at ~20-40 km intervals, with relatively short streams (generally <70 km) semi-perpendicular to the coastline (e.g. NERS26-36; Figure 3.9c).

On the other hand, larger catchments (>1000 km^2 and <7000 km^2) including NERS37, 42 and 45, which are still significantly smaller than EGA1 and NERS20, have more irregular shapes that are narrow close to the coastline but wider away from it. Drainage within these catchments is characterised by various trends as is the case at catchment NERS37, where upstream drainage is directed towards the south and southeast before turning towards the southwest at the main downstream channel (Figure 3.9c). These catchments are likely to have formed at early rift relay zones as indicated by their positions with respect to bounding faults (Figures 3.9c). It is, however, observed that catchments NERS42 and 43, which are larger than 1000 km^2 in size, are positioned such that they cross the normal fault bounding the Yanbu Basin (i.e. footwall drainage; Figure 3.9c). Therefore, footwall drainage catchments become smaller in size towards the north of the zone.

3.3.1.1.3 Northern zone

The northern zone, paralleling the coastline from Al Wajh to the Midyan Peninsula, is characterised by a relatively continuous escarpment with an average elevation of ~1100 m (Figure 3.8a), although higher elevations are recorded at Jabal al Lawz northeast of the Midyan Basin (Figure 3.9a). The top of the escarpment coincides with a major drainage divide along most of its length, with the exceptions of catchment NERS1 and 4 and parts of NERS11 where the divide is located on the plateau east of the escarpment (Figure 3.7). The swath profile covering the escarpment shows two distinguishable high elevation areas (~1200 m) separated by an area of lower elevation (~1000 m; Figure 3.8a).

Catchments with sizes <1000 km^2 are positioned mostly on the footwall blocks of the coastal faults north of the Al Wajh and north of Duba and, therefore, represent footwall drainage (e.g. NERS6-10 and 14-16; Figure 3.7). In contrast to the southern zone, all of the catchments that represent footwall drainage in the northern zone are smaller than 1000 km^2, which indicates that the trend of northward decreasing footwall catchment sizes characterises all of the NE Red Sea margin (Figure 3.7b). In the northern zone, the footwall catchments have outlets spaced at ~10-25 km intervals, with relatively short streams (generally 20-40 km) semi-perpendicular to the coastline (Figure 3.9). These catchments have shapes that are elongate and perpendicular to the coastline (Figure 3.7b).

Conversely, larger catchments (>1000 km^2 and <7000 km^2) including NERS1, 4, 11, have more irregular shapes that are narrow close to the coastline but wider away from it. Drainage within these catchments is characterised by various trends. For example, the upstream tributaries of the main Midyan Basin axial drainage (catchment NERS1), located east and northeast of Jabal al Lawz, flow towards the northwest before joining the southwest- and south-directed drainage within the basin (Figure 3.9a). These catchments are likely to have formed at early rift relay zones (e.g. NERS1, 4, and 11) as indicated by their positions with respect to bounding faults (Figures 3.9a, b and d). An exception is NERS13, which is dominated by axial drainage paralleling Wadi Azlam Basin western fault (Figures 3.7 and 3.9b). This axial drainage is diverted to the west-southwest where it incises the basement block towards the sea, suggesting that the Wadi Azlam axial

drainage has been captured by headward erosion of the coastal fault footwall block drainage to the west.

3.3.1.2 E Gulf of Aqaba margin

Along the eastern Gulf of Aqaba margin, the elevation increases substantially north of Midyan to more than 1800 m, in contrast to the elevations within the Midyan Basin (a maximum of ~730 m; Figures 3.7 and 3.9). The coastal plain is absent to very narrow (~3 km) within the first 30 km north of the Northern Midyan Fault (Figure 3.9a). Further north than this, the plain widens gradually reaching a maximum width of ~15 km before narrowing again (Figure 3.9a).

Draining off into the Gulf of Aqaba is the regional catchment EGA1, which has an area of ~59,000 km^2 (Figure 3.7b). This catchment is elongated in a NNW-SSE trend and has a common catchment boundary with NERS20 in the south. East of the escarpment, EGA1 covers a large flat area (Tabuk Basin) where the drainage is generally directed towards the NNW (Figure 3.7a). The drainage is redirected at downstream positions towards the west and southwest (after passing through remnants of the escarpment), reaching the Gulf of Aqaba at its northern tip (Figure 3.7a).

Excluding the regional catchment EGA1, catchments draining to the Gulf of Aqaba with areas larger than 20 km^2 have a mean area value of ~130 km^2; remarkably smaller than the catchments draining to the Red Sea (Figure 3.7b, inset box). The Gulf of Aqaba catchments are mostly elongate, with axes perpendicular to the gulf axis. The exceptions are the catchments within the Midyan Basin (and just to its north), which have more oblique shapes with their long axes approximately 35° from the gulf axis (e.g. EGA21 and 23; Figure 3.7b). The catchments' long axes increase gradually from just north of the Midyan Basin to a maximum value of ~55 km east of Haql (EGA7) before rapidly decreasing further north (Figure 3.9a).

3.3.1.3 Drainage profiles

The stream profiles (elevation vs distance from the coastline) of the valleys draining to the NE Red Sea and the E Gulf of Aqaba coasts show remarkable differences. The NE Red Sea valleys are generally characterised by concave-up

profiles (Figure 3.10a and b). The exact shapes, however, are variable in terms of steepness and concavity as can be noted when comparing the profiles corresponding to NERS13, 17 and 37 with those of NERS1 and 20. Furthermore, excluding the NERS20 profile, it is observed that the concavity decreases towards the north (compare NERS37 and NERS1; Figure 3.10a).

One valley (catchment NERS4) hosts a clear knickpoint that separates steep downstream section from a shallower upstream section (Figure 3.10a). This knickpoint corresponds to the position of the escarpment and defines a change in the direction of the stream flow from NW to WNW/W (Figure 3.10b).

Conversely, along the eastern Gulf of Aqaba margin, plotting the elevation of valley beds as a function of distance from the coastline shows convex-up profiles that are much steeper that the NE Red Sea profiles (Figure 3.10a-d). The steepness of these profiles are highest at the middle of the eastern Gulf of Aqaba margin (profiles corresponding to EGA16, 17 and 19; Figure 3.10c).

At this middle part of the margin, a prominent knickpoint exists along the EGA21 profile within 2 km of the coastline. Comparatively, towards the northern and southern parts of the margin, the steepness is lower. Wide knickzones are noted at the most northern profiles (EGA1, 7 and 8), which are longer than the southern counterparts (Figure 3.10c and d).

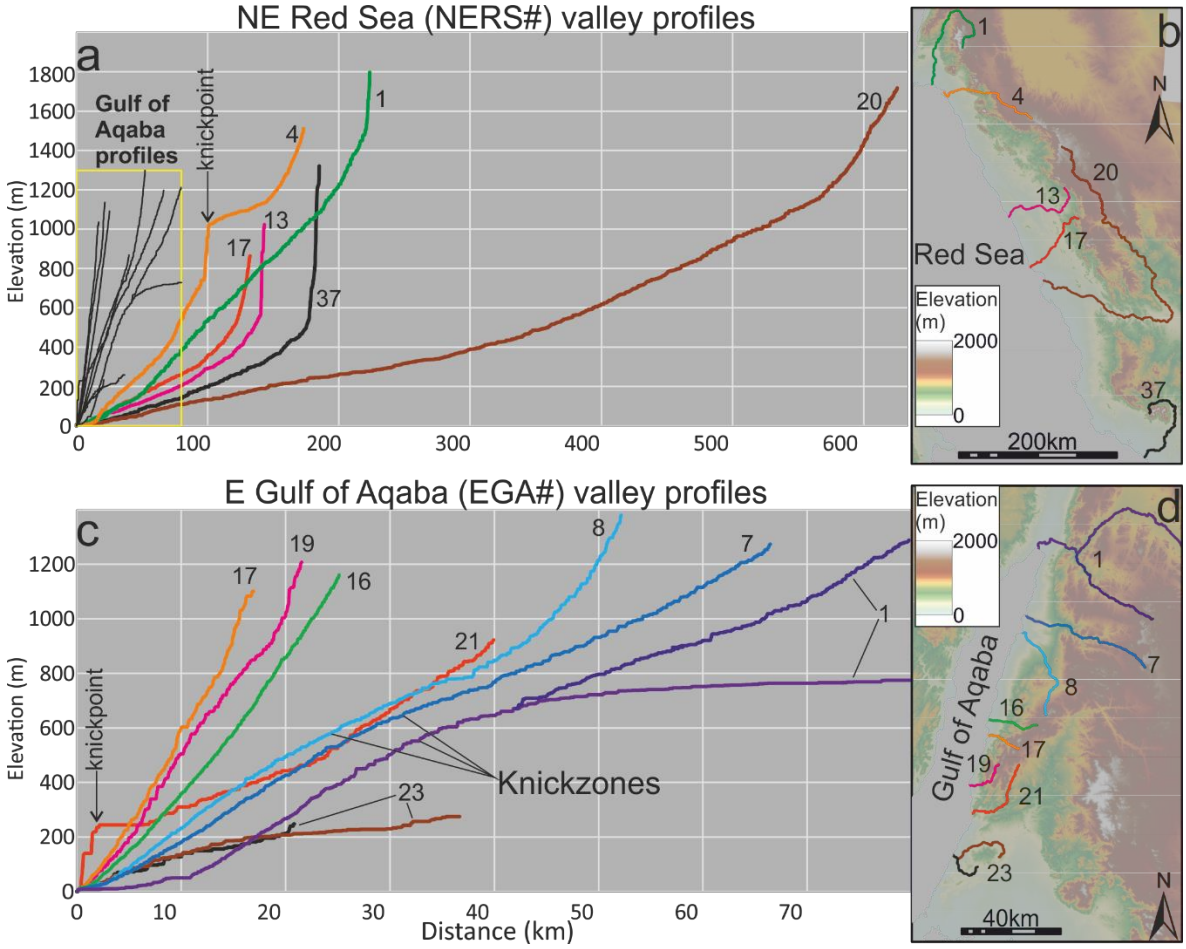

Figure 3.10: (a-b) Northeastern Red Sea valley elevation-vs-distance profiles. Note that, overall, the profiles are characterised by concave-up shapes that get steeper both nearer to the escarpment and towards the north. The numbers refer to the NERS# numbers. The knickpoint along the orange profile (catchment NERS4) corresponds to the location of the erosional escarpment. The Gulf of Aqaba profiles are plotted using the same scale as the Red Sea profiles for easier comparison (thin black profiles in the yellow box in (a)). (c-d) Eastern Gulf of Aqaba valley profiles. The numbers refer to the EGA# numbers. Note the convex-up shapes of the profiles, and the steeper valleys along the middle of the gulf (pink, orange and green profiles) and the existence of a clear knickpoint separating a very steep section and a shallower section along the red profile.

3.3.1.4 Drainage anomalies

Drainage anomalies that signify events of reorganisation are recognised in some parts of the study area (Figure 3.11). Misfit streams, which are significantly smaller than the hosting valleys, are noted east of the escarpment with mostly NW-NNW and NE orientations in the Paleozoic sandstones in catchment NERS11 (Figure 3.9b) and at the boundary between catchments EGA1 and NERS1 (Figures 3.11a, c and d). These streams are located in the upstream parts of the catchments (near the catchment boundary) and are, therefore, of low stream order (Strahler, 1957). The sizes of these streams, however, are not compatible with the much wider valleys that host them (e.g. Figure 3.11a and c). That is, it is interpreted that these wider valleys corresponded in the past to higher order (i.e. larger and associated with larger upstream area) that the present-day streams. This interpretation means that the drainage on either side of the catchment boundary (e.g. boundary between catchments EGA1 and NERS1) was connected within a larger catchment.

Moreover, semi-linear and contiguous trends of drainage streams across catchment boundaries are noted between NERS19, 17 and 13 (Figures 3.11b and d). As indicated by the orientations of these streams, the overall drainage was likely to have been directed towards the NW and NNW. Drainage reorganisation that would resulted from topographic adjustment (e.g. during rifting) has likely caused the redirection of these streams to their present-day course.

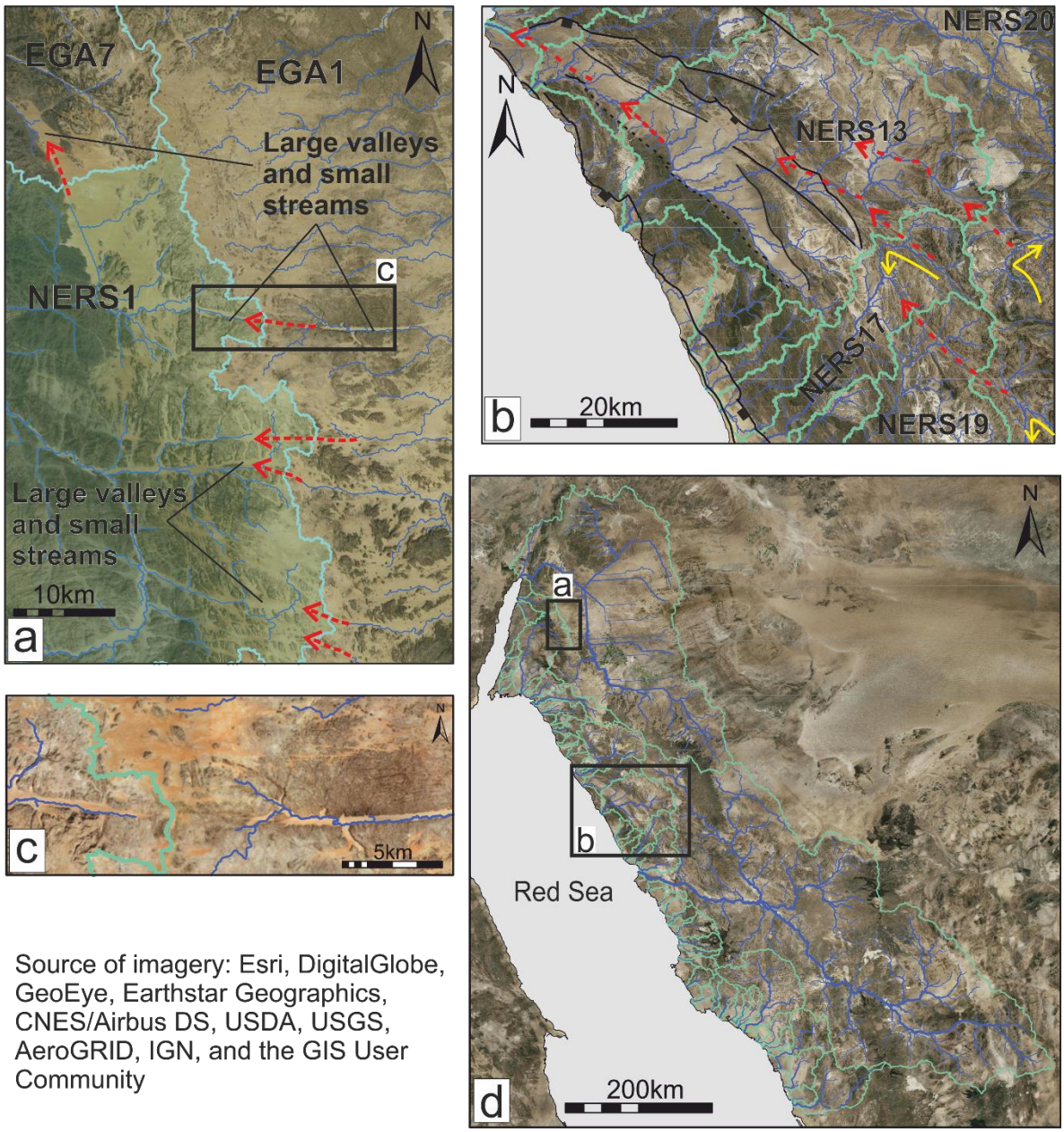

Figure 3.11: Drainage reorganisation as deduced from planform analysis. (a) Interpreted misfit streams across the boundaries of catchments NERS1 and EGA1, indicating WNW to NW direction of the paleo-drainage. (b) Interpreted paleo-drainage directed to the northwest across NERS13, 17 and 19. (c) A close-up of an example of misfit streams where the valley is much wider than the streams. (d) Drainage network (blue lines) and catchment boundaries (green lines) overlaid on satellite imagery from Esri Global Imagery showing the locations of (a) and (b). Red dashed arrows: interpreted paleo-drainage. Yellow arrows: stream course change during drainage reorganisation.

3.3.2 Uplift estimation

3.3.2.1 Inverse modelling of stream profiles

Overall, the modelled profiles provide a good fit when compared to the observed profiles, but misfit occurs at some upstream sections of some profiles (Figures 3.12-3.14). The data coverage increases towards the present-day and towards the extracted streams, which represent the input data (Figure 3.15). The high stream density used in this study increases the spatial coverage, particularly since the Late Miocene (6 Ma map in Figure 3.15).

Estimation of uplift using the drainage inverse model shows early rift uplift in the southern part of the study area that later shifted to the north (Figure 3.16). The stream profiles along the coast differ in that they become less concave, with slightly steeper slopes in downstream parts, towards the north (Figure 3.10). This observation gives an indication that more uplift occurred in the north in more recent times compared to the south, which agrees with the results of the inverse modelling (Figure 3.16). The central area, where minimal uplift is estimated, corresponds to catchment NERS20. The cumulative uplift at the present-day amounts to 2.2 km in the Yanbu region, 2.7 near Duba, 3.3 km at the mountainous blocks east of Midyan, and 2.4 km along the Gulf of Aqaba (Figure 3.16a).

In detail, modelling results show that uplift at 21-15 Ma was distributed over an area more than 150 km wide, north of the Yanbu Basin with an average rate of ~0.14 mm/a (Figure 3.16b). This uplifted area extended northeast to cover the Hamd-Jizl half-grabens. Moreover, particularly clear on the 21 Ma map, smaller uplift rates (~0.09 mm/a) are observed at the Wadi Azlam Basin and the block to its southwest that is bound by the Yanbu Basin eastern fault. During this period, the uplift wavelength perpendicular to the coastal border fault became narrower from approximately 200 km (21 Ma) to approximately 120 km (15 Ma; Figure 3.16b).

Starting at the 12 Ma time map, uplift shifted northward becoming focused (wavelengths of ~60 km) north of Duba, and east and southeast of Midyan, with an average rate of ~0.14 mm/a (Figure 3.16b). More diffuse uplift is also observed at the northwestern part of Harrat Uwayridh/ar Rahah, with a wavelength, clearly shown on the 9 Ma time map, of approximately 100-120 km and an average rate of

~0.1 mm/a. During this period, uplift initiated along the eastern Gulf of Aqaba starting over a wavelength of ~60 km (9 Ma) then narrowing down to ~20 km (6 Ma).

At the 3 Ma and Present time maps, zones of focused uplift (wavelength of ~20-60 km) became dominant at the normal fault footwall blocks east of the Midyan Basin (0.36 mm/a) and along the Gulf of Aqaba (0.29 mm/a; Figure 3.16b). These zones are flanked by an extensive zone of more diffuse uplift that extends towards the north and the northeast, with a wavelength of ~200 km and an average uplift rate of ~0.17 mm/a. Further south, to the southeast of the Wadi Azlam Basin, a ~60-100 km-across, semi-circular zone of uplift is observed, with uplift rate increasing from the 3 Ma time map (~0.05 mm/a) to the present (~0.08 mm/a).

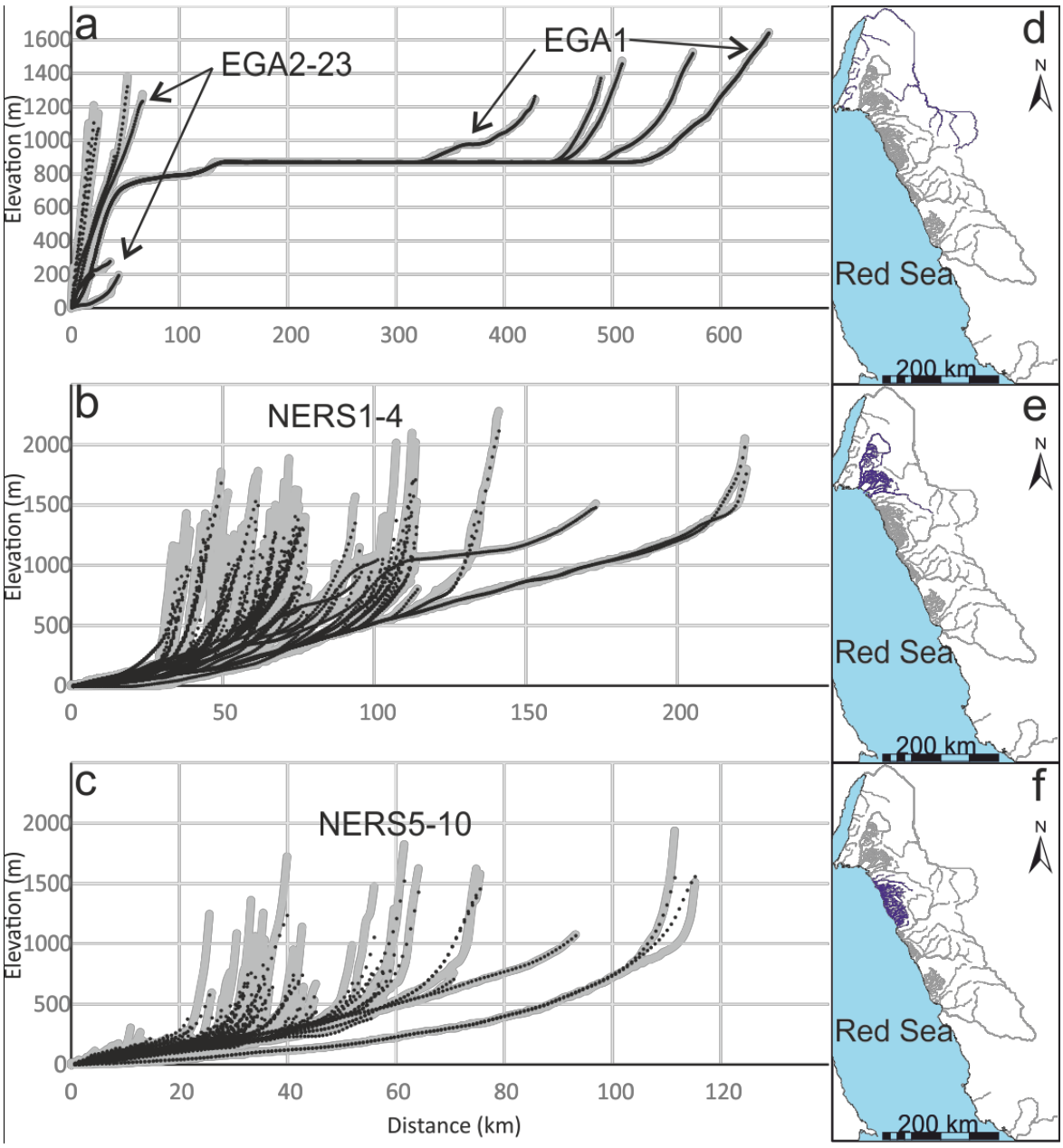

Figure 3.12: (a-c) Extracted profiles (grey solid lines) shown along with modelled profiles (black dotted lines) generated by calculating the uplift history that minimises the misfit between the two sets for the northern part of the study area. The catchments from which the streams were extracted are indicated. Note that the horizontal distances along the three panels are different. Misfit is observed at upstream sections at (c). (d-f): Corresponding locations of extracted streams (blue drainage lines).

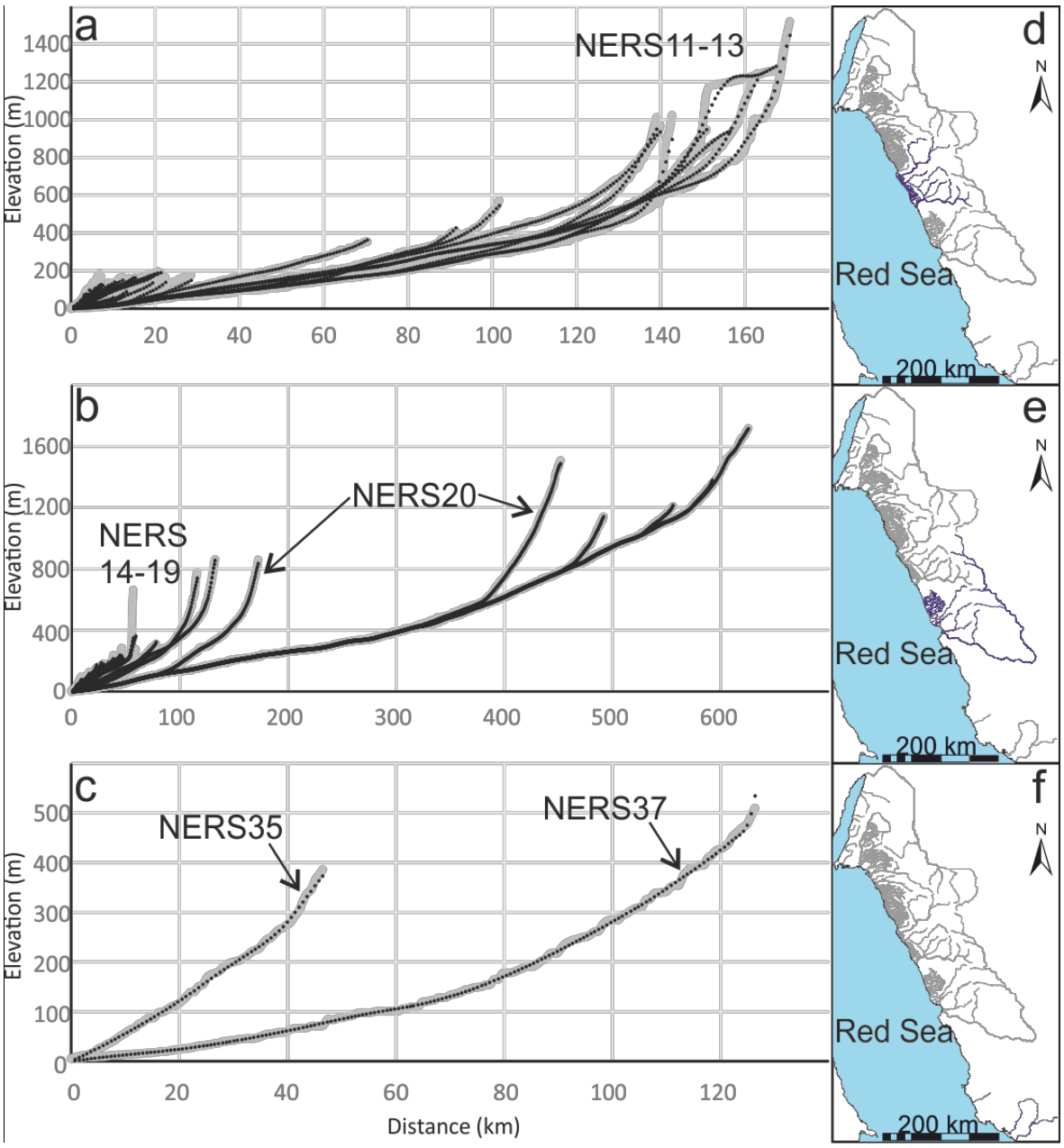

Figure 3.13: (a-c) Extracted profiles (grey solid lines) shown along with modelled profiles (black dotted lines) generated by calculating the uplift history that minimises the misfit between the two sets for the southern part of the study area. The catchments from which the streams were extracted are indicated. Note that the horizontal distances along the three panels are different. (d-f): Corresponding locations of extracted streams (blue drainage lines).

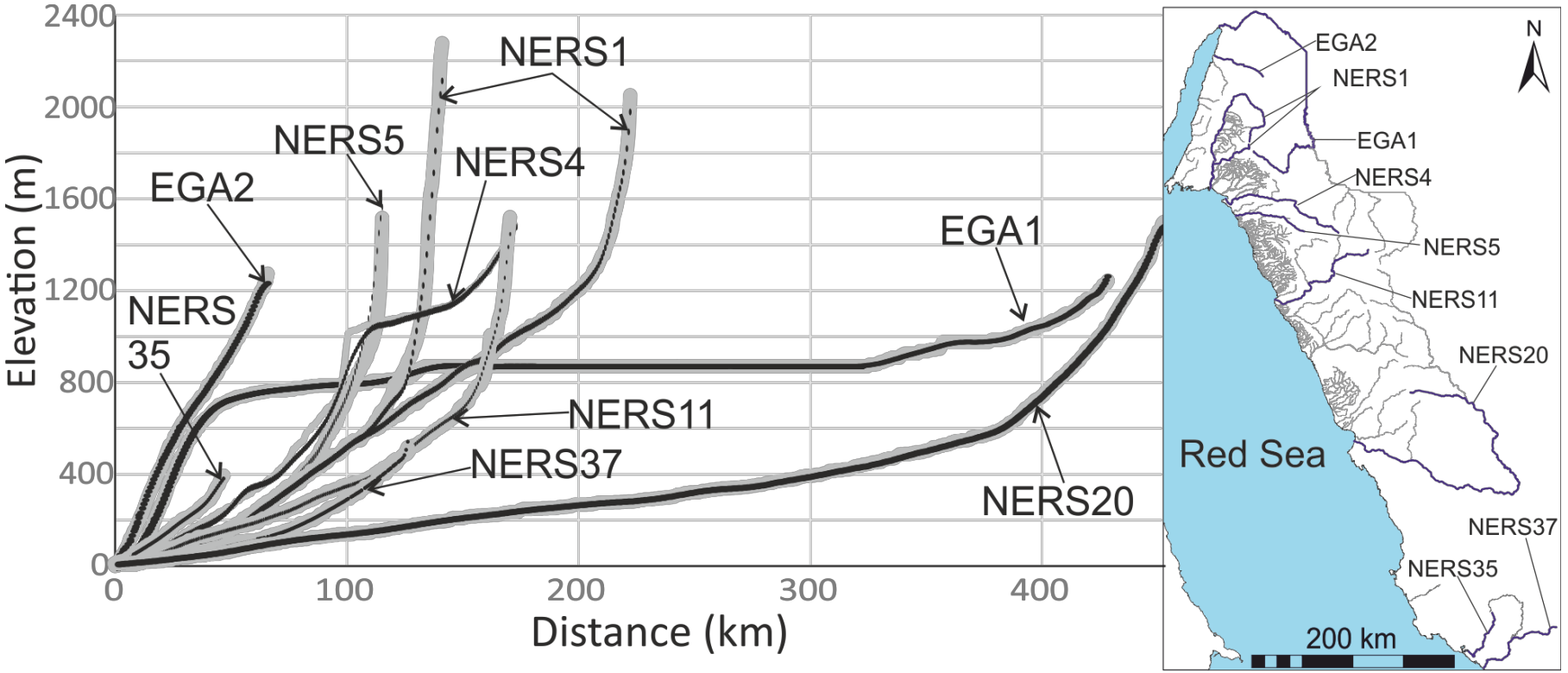

Figure 3.14: Representative streams selected along the whole study area showing their extracted (grey solid lines) and modelled profiles (black dotted lines) plotted using the same horizontal scale. The catchments from which the streams were extracted are indicated. The corresponding locations of extracted streams are shown on the right (blue drainage lines).

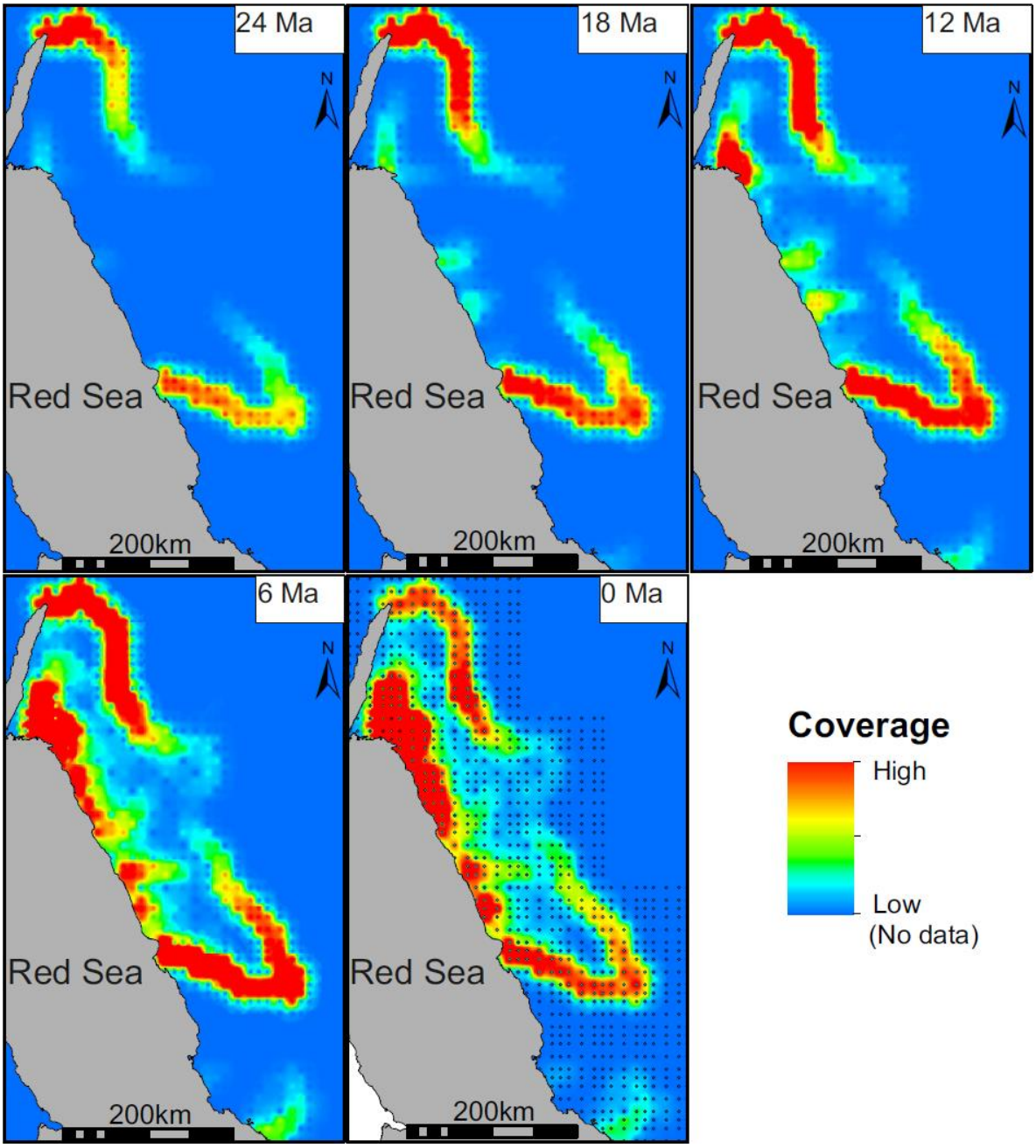

Figure 3.15: Maps of the study area showing the coverage (i.e. the number of data points used to extract the uplift rate value in a given cell) of the inverse modelling method through time. The dots at time 0 Ma show the locations of the vertices that were used to insert the uplift rates estimated from the inverse modelling.

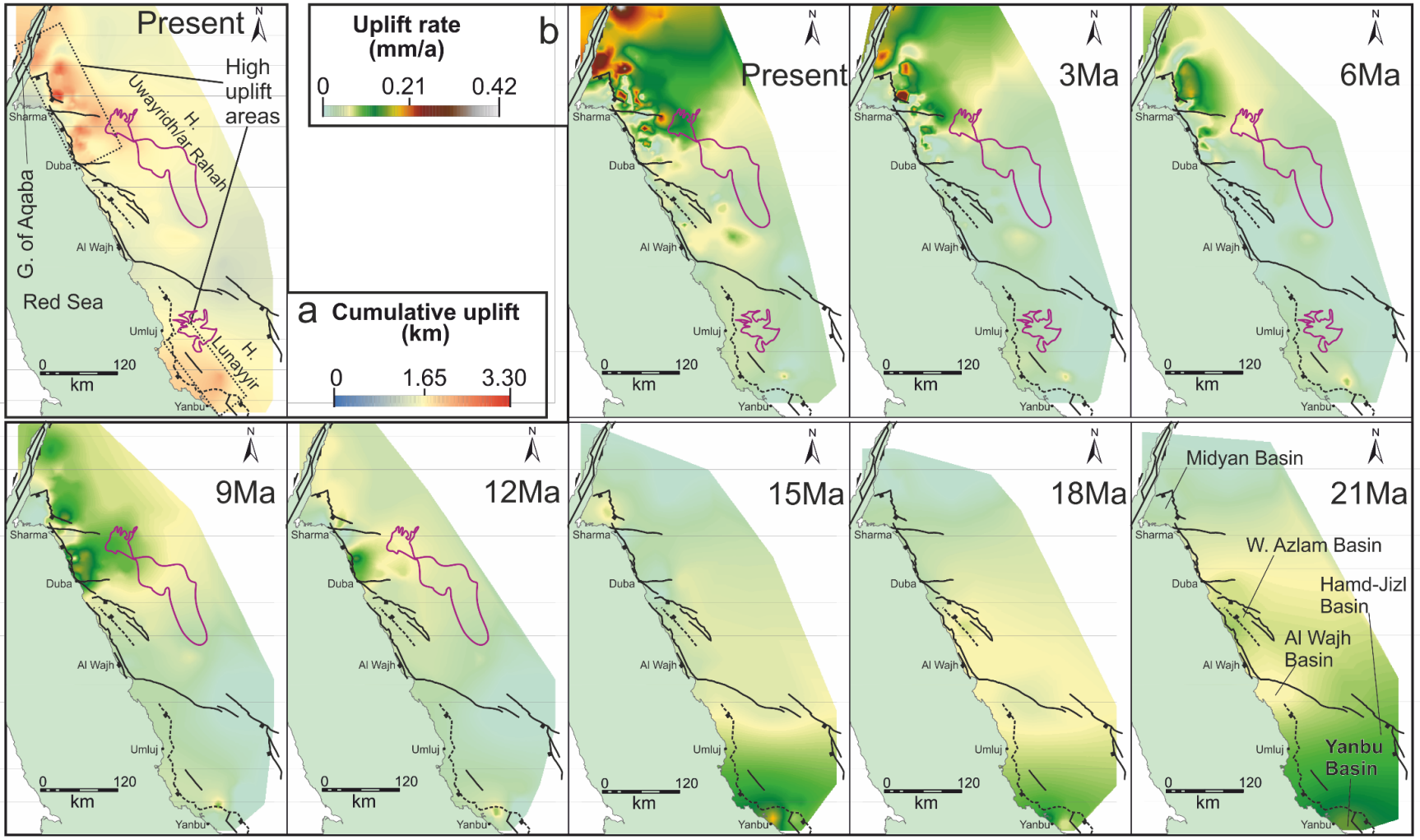

Figure 3.16: Results of the inverse modelling showing the uplift evolution of the study area. (a) Cumulative uplift magnitude at present-day. (b) Spatial and temporal evolution of the uplift rates (21 Ma to present). The faults are shown in black lines and the basins are indicated at the 21 Ma uplift rate map. The volcanic fields (harrats) are shown in purple starting at the approximate time at which they erupted (see cumulative uplift map for their names).

3.3.3 Minimum erosion and local relief estimation

The location of highest minimum erosion estimates varies spatially with respect to the coastline, becoming both more confined and closer to the coast towards the north (Figure 3.17). In the south, between Rabigh and Duba, minimum erosion is spread across a 60-80 km wide area that is, on average, ~60 km away from the coastline (Figure 3.17a). In contrast, from Duba to the mountainous area east of Midyan, minimum erosion is focused on a 20-40 km-wide area ~30 km away from the coastline. Further north, minimum erosion has occurred 0-10 km away from the coastline, distributed across 20-40 km. North of Midyan Basin, two areas of focused erosion are separated by less extensive erosion and merge further to the north.

Summing all of the erosion height estimates within each catchment shows that the largest catchment (i.e. NERS20) provides the largest minimum erosion volume (i.e. 5350 km^3; Figure 3.17b). This estimate is significantly larger than those from all of the other catchments. However, dividing the minimum eroded volume by the catchment area yields high ratio values in the northern (particularly at NERS5 and 7) and southern zones compared to NERS20 as well as catchments NERS13-35 (Figure 3.17c).

The local relief (10 x 10 km) map (Figure 3.18) shows a spatial variation that is comparable to the minimum eroded volume:catchment area ratio map (Figure 3.17). A 50-100 km wide belt of high local relief is observed paralleling the coastline throughout the study area (Figure 3.18). Between this belt and the coastline the local relief drops rapidly. In detail, this local relief belt features higher values in the south (near Yanbu) and the north (north of Duba), and along the central eastern Gulf of Aqaba margin. At the Hamd-Jizl half-grabens and east of Al Wajh, lower local relief values are observed. These variations in relief and minimum erosion are important as they show that the estimates of high cumulative uplift (Figure 3.16) are associated with high values of relief and high estimates of minimum eroded volume.

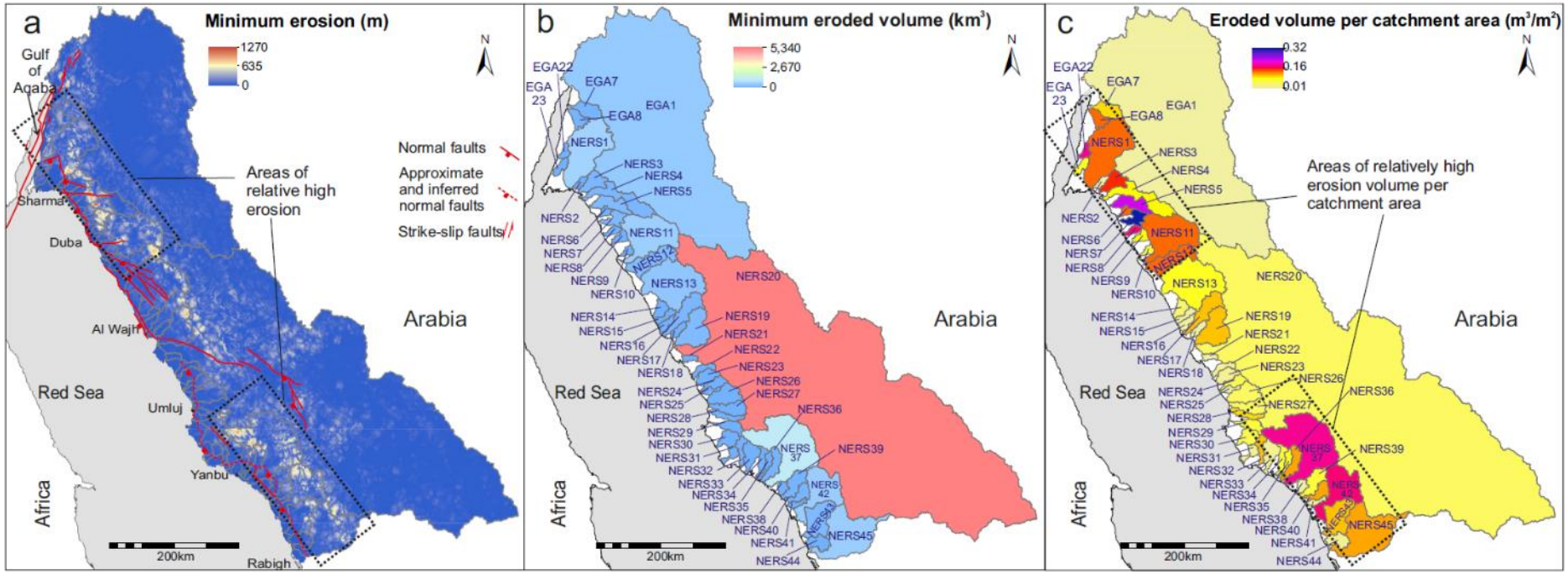

Figure 3.17: Erosion volume across the study area. (a) A minimum erosion map produced using interfluves elevations to construct per-erosion topography. (b) A map of the catchments draining to the Red Sea (NERS#) and Gulf of Aqaba (EGA#) with areas >200 km^2 showing the contribution of eroded volume from each catchment. (c) A map of the ratio of minimum eroded volume divided by catchment area.

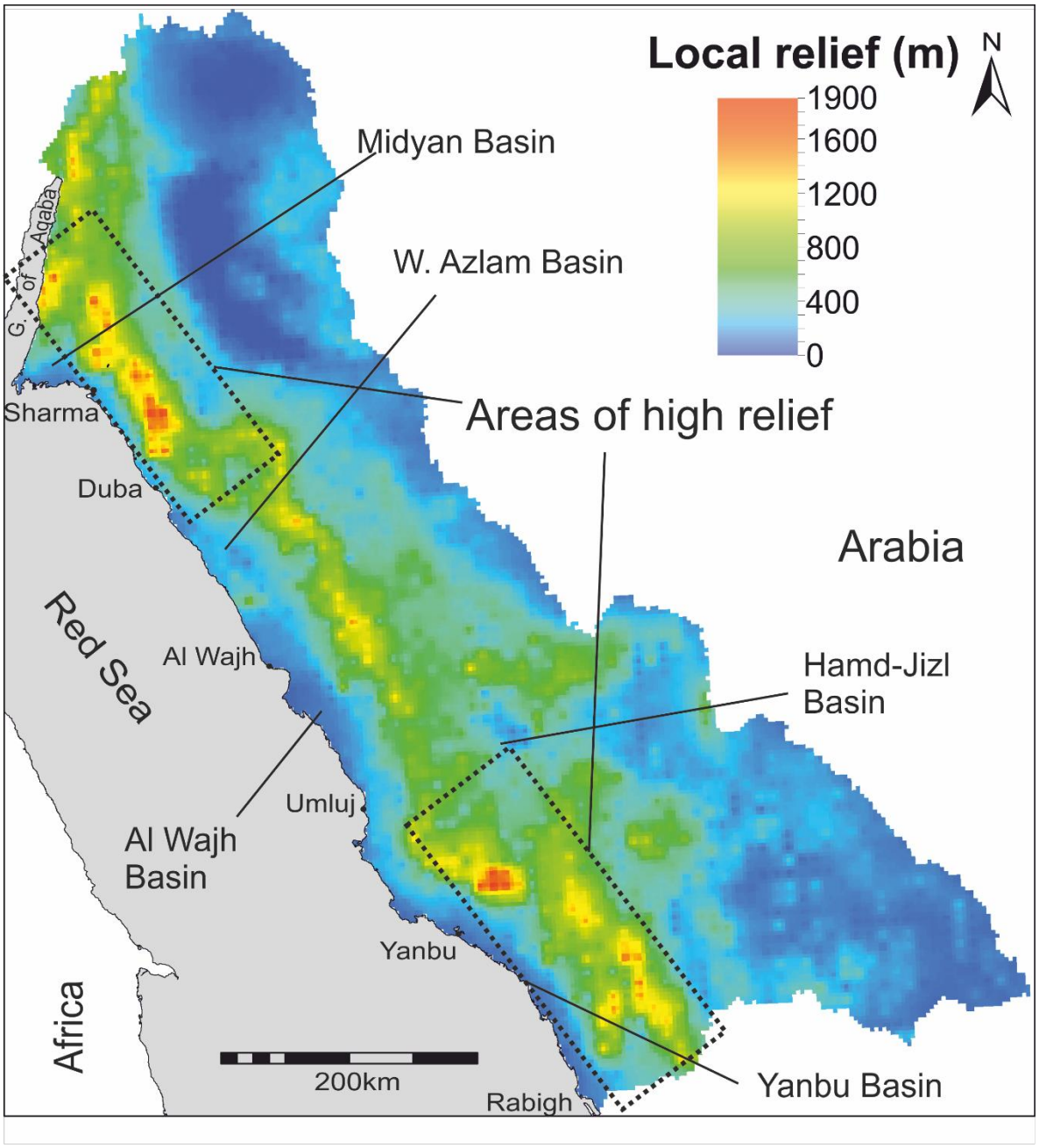

Figure 3.18: A local relief (10 x 10 km) map of the study area showing the two areas of high relief values.

3.4 Discussion

3.4.1 Morphotectonic evolution of the NE Red Sea and eastern Gulf of Aqaba margins

By integrating the results of the inverse model and the analyses of drainage and other geomorphic metrics, an evolutionary morphotectonic model along the NE Red Sea and eastern Gulf of Aqaba margins is proposed (Figure 3.19). This model depicts how the drainage has been affected by pre-existing structures and, more importantly, the Cenozoic rifting and uplift.

3.4.1.1 Pre-rift state

The original drainage, deduced from satellite imagery and drainage characterisation and complemented by highlights of paleo-drainage from the literature (e.g. Brown et al., 1989), exhibits a general north to northwest-directed pre-rift paleo-drainage (Figure 3.19a). This drainage is likely to have been directed towards basins in the Levant (e.g. Zilberman and Calvo, 2013) or further north to the Tethys domain by catchments that preceded the two largest catchments in the study area (NERS20 and EGA1).

Regional slope towards the north developed during the Oligocene in response to Afar doming (Avni et al., 2012), and drainage direction would have probably been modulated by the NW-SE (e.g. Najd Fault System) and NE-SW (Precambrian structures in the Nubian Shield) oriented heterogeneities in the basement (Johnson et al., 2011). It will be seen that the overall north-directed pre-rift drainage had generated atypical catchment areas (larger than expected from typical rift-related drainage) in the subsequent rift phases.

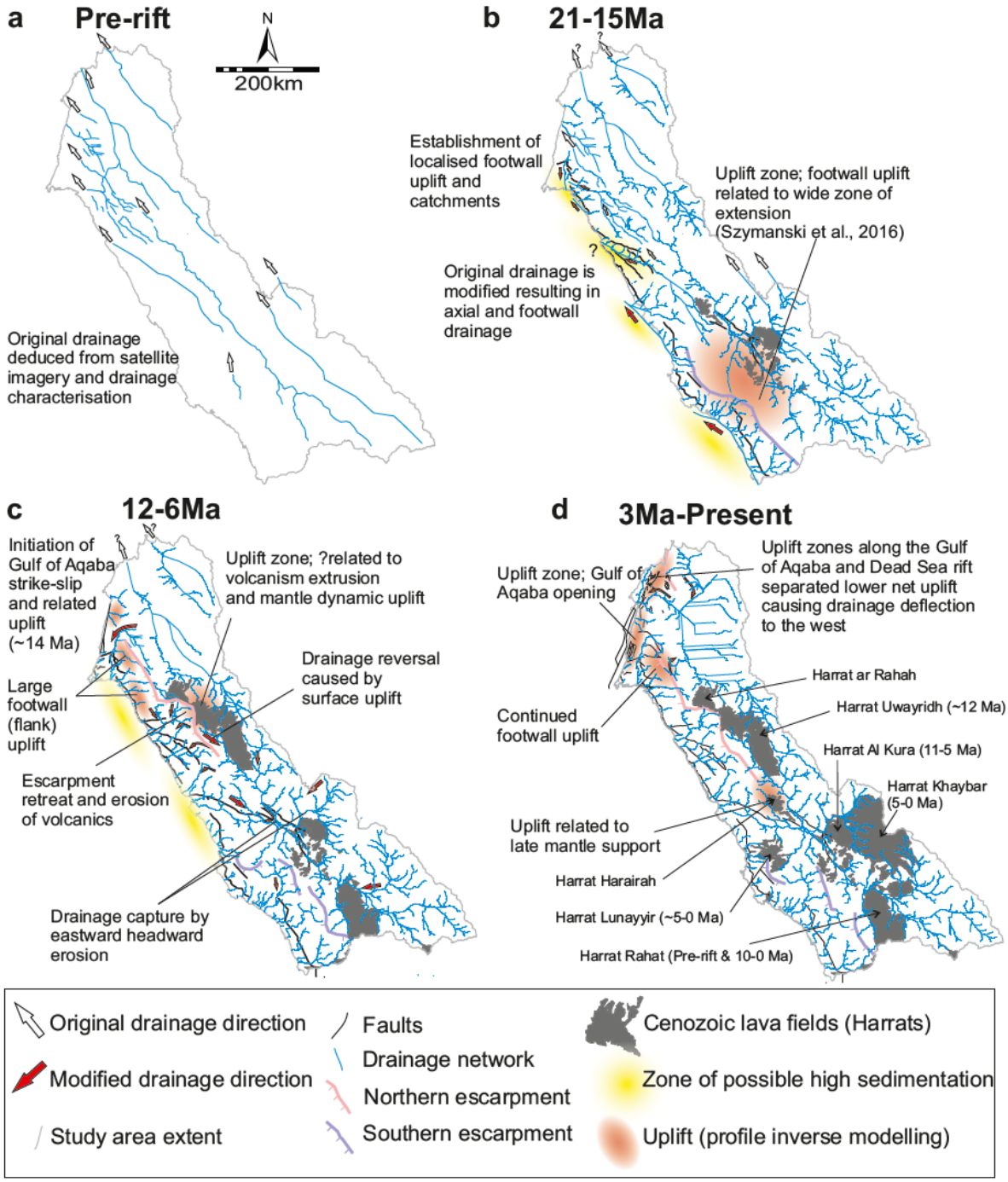

Figure 3.19: A multi-stage tectono-geomorphic model of the northeastern Red Sea and eastern Gulf of Aqaba utilising results from the inverse model and observations from the geomorphic and drainage analyses. Ages of volcanics are from Camp et al. (1991) and Bosworth et al. (2005). The drainage network in d is the present-day network and the streams are modified in a-c according to the interpretation of the large-scale drainage paleo-direction and how it may have been affected by the different uplift events.

3.4.1.2 Early to main rift-related uplift (21-15 Ma)

Uplift was associated with fault block rebound during the Late Oligocene to Early Miocene extension along the northeastern Red Sea across a 150 km wide zone of deformation (Szymanski et al., 2016), which falls within the same period of denduation around the whole Red Sea that commenced at 24-23 Ma leading to regional rift shoulder uplift by 22-20 Ma (Bosworth, 2015). Denudation does not necessarily equate to uplift but it is reasonable to assume that relative base-level drop driven by the tectonic uplift can result in denduation. Uplift timing of the fault block north of Yanbu based upon drainage inversion (Figure 3.16b) falls within published early rifting and denudation age estimates (Bosworth, 2015 *and references therein*), and is corroborated by high ratios of minimum eroded volume per catchment area for catchments NERS37 and 42 and local relief values (Figures 3.17 and 3.18). Furthermore, the end of the diffuse extension phase at ~13 Ma proposed by Szymanski et al. (2016) at the Central Arabian Rift Flank is reflected in the model whereby the uplift zone became narrower from 21 Ma to 15 Ma before disappearing at 12 Ma (Figure 3.16b).

The Early Miocene uplift is supported by the existence of early rift clastics in Midyan Basin, including conglomerates with granitic composition, which indicates crestal erosion of the uplifted basement (Hughes et al., 1999). However, uplift near the Midyan Basin is not resolved in this study until 15 Ma, implying that resolvable footwall uplift commenced between 18 and 15 Ma (Figure 3.16b). This might indicate that the initial fault segments bordering the Midyan Basin from the east did not coalesce until the early Middle Miocene. This is supported, for example, by the structural context and evolution of the Late Burdigalian Ad-Dubaybah carbonate platform interpreted in Koeshidayatullah et al. (2016) to have developed within a relay zone that became hard-linked during this rifting stage.

Over the regional scale, the spatial positions of rift basins had a profound effect on the drainage evolution (Figure 3.19b). The downstream channel of the largest catchment draining the rift flanks (i.e. NERS20) utilises major basement heterogeneities of the Neoproterozoic Najd Fault System (Johnson et al., 2011). Branches of this system were probably exploited during the Red Sea rifting (Bosworth et al., 2005) forming transfer draiange zones. However, the shape of the

NERS20 is suggestive of an earlier NW-SE pre-rift elongated catchment that had an outlet much further north than its current outlet, which supports the north-directed drainage interpretation (e.g. Brown et al., 1989).

3.4.1.3 Onset of strike-slip tectonics and oblique extension: northward shift of uplift (15-6 Ma)

The onset of the strike-slip tectonics along the Gulf of Aqaba was associated with oblique extension and localised deformation at the Red Sea (~14-12 Ma; Bosworth et al., 2005; Tubbs et al., 2014). The observed shift of the uplift locus from south to north during and after this period (Figure 3.16b) is likely due to coalescence of Red Sea fault segments at more proximal positions to the rift axis (i.e. near Duba and east of Midyan), and the initiation of the Gulf of Aqaba strike-slip tectonics. The relatively small wavelengths and high uplift rates during this period at these zones (~60 km and 0.14 mm/a, respectively) support the conclusion of uplift due to normal faulting. In more southern areas (e.g. south of Al Wajh Basin), the disappearance of the uplift signal is expected as the extensional deformation migrated to the axis of the Red Sea, as also suggested by low-temperature thermochronology (Szymanski et al., 2016).

Fault scarps that formed during the earlier phase of rifting (previous section) continued to retreat as, for instance, erosion continued of the Paleozoic clastics and overlying volcanics of Harrat Uwayridh/ar Rahah (lava flows dated at ~12 Ma; Bosworth et al., 2005; Figure 3.9b). This suggests a post-12 Ma period of enhanced denudation leading to the present-day erosional escarpment (Figure 3.19c). The diffuse uplift zone at the northwest of Harrat Uwayridh/ar Rahah (wavelength of ~100-120 km and uplift rate of ~0.1 mm/a [12-9 Ma time maps]; Figure 3.16b) is not likely to be directly caused by the faulting near Duba. This indicates that starting at approximately 12 Ma, another source of support contributed to the uplift. However, the wavelength of the uplift (~100-120 km) is not indicative of typical mantle plume upwelling that can cause doming of with ~1000-km diameter (e.g. East Africa; Chorowicz (2005)). Given that this uplift was coeval with the harrat volcanics, off-rift axis mantle-sourced hot material (rather than large-scale plume-driven doming) is interpreted as a likely candidate for lowering the density and causing the uplift. This interpretation partly supports earlier

propositions that the volcanics and high topography on the Arabian side of the Red Sea were the result of mantle flow rather than the rifting mechanics (Hosny and Nyblade, 2014).

3.4.1.4 Intensification of strike-slip tectonics (3-0 Ma)

The intensification of the Gulf of Aqaba deformation as well as the strain localisation along the fault bounding the Midyan Basin from the east were associated with increased uplift rates as revealed by the inverse model (Tubbs et al., 2014; Bosworth et al., 2017; Figures 3.16b and 3.19d). The short wavelength of this uplift near the gulf (~50-60 km) is compatible with the existence of a large dip-slip motion at the transform fault (Bosworth et al., 2017).

Along the Gulf of Aqaba eastern margin, the steam profiles convexities, knickzones, knickpoint (located within 2 km off the coastline), high elevation and relief all signify a transient state and net uplift. The knickpoints elevation trend correlates partly with that of Pleistocene uplift, which shows an increase from the south to the centre before decreasing to the north (Bosworth et al., 2017). Uplift rates along the gulf coastline were calculated to be 0.15 mm/a (125-0 Ka) based on elevation of Pleistocene marine terraces (Bosworth et al., 2017). Moreover, assuming a near sea-level topography prior to the Gulf of Aqaba tectonics, Bosworth et al. (2017) estimated a minimum value of 0.12-0.16 mm/a for the uplift rates from 14-11 Ma to the present. A similar rate is estimated by the inverse model (mean uplift rate ≈ 0.17 mm/a; cumulative uplift ≈ 1.66 km; 15-0 Ma; Figure 8b).

Misfit streams along the eastern boundary of NERS1 are possibly related to drainage reversal caused by the uplift of the Midyan eastern mountains during this or the previous stage (Figures 3.11a, c and 3.19c-d). This is supported by the fact that the Midyan Basin is dominated by a large alluvial plain that testifies to an earlier catchment that was larger than the present-day NERS1 area (Figure 3.7).

3.4.2 Geodynamic implications

Plate-scale uplift of the Arabian margin has been suggested to be caused by a long-wavelength plate tilt driven by mantle flow upwelling (Japsen et al., 2012); a

young uplift (~12 Ma; Daradich et al., 2003) compared with the early Red Sea rift-related uplift. This mantle support is also indicated by relatively thin lithosphere beneath the elevated flank (Hansen et al., 2007) and low shear velocity (Hansen et al., 2008; Park et al., 2008; Yao et al., 2017), and revealed using uplift estimation through inversion of river profiles (Wilson et al., 2014).

The estimated uplift near Yanbu lies north of the dynamically supported regional uplift zone in southwestern Arabia interpreted by Wilson et al. (2014). The timing of the uplift across the southern part of the study area vis-à-vis rifting is similar to that of the exhumation interpreted as a record of footwall rebound by normal faulting (Szymanski et al., 2016). Furthermore, the long uplift wavelength (~200 km; 21-15 Ma time maps in Figure 3.16b) may suggest an additional dynamic uplift possibly due to mantle upwelling during the early rift phase. The low coverage that affects the inverse model back in time, however, makes this suggestion uncertain as the long wavelength might have been the result of the smoothing during the interpolation of the uplift rate estimates.

During the Middle Miocene, the uplift of the area covered by the northwestern part of the Harrat Uwayridh/ar Rahah is interpreted to have resulted from mantle processes given that 1) it post-dated rifting by ~12-14 Myrs, and 2) it coincides with the ~12 Ma old volcanics (Bosworth et al., 2005) that are characterised by hot mantle-sourced basalts (Kaliwoda et al., 2007). Moreover, a relatively low-velocity zone exists in the mantle (65-85 km depth) beneath the fault block north of Yanbu and continues northward to just southwest of Harrat Uwayridh/ar Rahah (Yao et al., 2017). This zone coincides with an uplift zone southeast of the Wadi Azlam Basin with an uplift rate and a wavelength that have been increasing from 3 Ma to the present (Figure 3.16b). The aforementioned indicates that temporal and spatial dynamic support by mantle material beneath the rift flank played a role in the evolution of the margin.

In the northern part of the study area (Midyan area), the short period separating rifting from the uplift compared with mature passive margins (discussed in Japsen et al., 2012) and the lack of post-rift volcanism indicate that the bulk of the uplift is related to rifting processes and later Gulf of Aqaba transform tectonics. The uplift locus east of the Midyan Peninsula is underlain by higher-than-average shear

wave velocities (e.g. Yao et al., 2017) reducing the possibility of an asthenospheric dynamic support. The relatively short wavelength and large amount of cumulative uplift (~60 km and ~3 km, respectively; Figure 3.16a) in this area support this conclusion.

3.4.3 Implications for sediment entry points

The integration of uplift estimates and drainage evolution interpretation throughout the rifting stages leads to qualitatively predict how sediment entry points into the rift basins changed through time. Three main factors are suggested here to play a significant role in the positions of sediment entry points along rifts and passive margins that did not experience pre-rift doming; the direction of the pre-rift drainage, the geomorphic evolution in response to rifting and the geomorphic evolution in response to post-rift uplift.

During the Early Miocene early rifting, the formation of half-grabens led to generation of rift-related drainage as suggested by typical rift drainage models (i.e. footwall, hangingwall, transfer and axial drainage; e.g. Gawthorpe et al., 1994). However, given the pre-rift slope towards the north and the existence of basement weakness zones (Precambrian structures) intersecting the rift obliquely and hosting significant pre-rift drainage, a number of early rift basins would have received significant sediments from transfer catchments the previously were part of the pre-rift drainage (Lambiase and Bosworth, 1995). A possible example is the Midyan Basin that is located at the northern outlet of the interpreted predecessor to catchment NERS20 (Figure 11).

Later in the Middle Miocene, with uplift shifting to more northern locations, drainage reversal of the original drainage in NERS20 and its capture by headward eroding streams initiating at the Al Wajh Basin is interpreted to have resulted in shifting the major sediment sink area from the north to the Al Wajh Basin (Figure 11). This shift would have occurred during or after the evaporitic conditions in the basin and indicates that major post-salt sedimentation is likely thicker at and near Al Wajh Basin. Such a change in drainage direction highlights the significance of geodynamic processes that are not related to rifting in modifying the drainage, which has been highlighted even in continental-scale catchments elsewhere (e.g.

Salles et al., 2017; Shephard et al., 2010). More relevant to basin analysis and petroleum prospectivity is the effect such drainage modification has in dispersing sediments along the margin strike.

3.5 Conclusions

A workflow utilising a combination of drainage network analysis and inverse modelling of drainage profiles to estimate Cenozoic uplift was implemented to investigate the onshore tectono-geomorphic evolution of northeastern Red Sea and eastern Gulf of Aqaba margins. The workflow benefits from its dependency on ubiquitous surface drainage data and easily constructed geomorphic metrics, and therefore has applicability at other sub-aerial environments.

The northeastern Red Sea margin catchments and streams reflect the interplay of basement heterogeneities and geomorphic evolution in response to rift-related uplift and later uplift. Over the regional scale, geomorphic segmentation is highlighted by two zones of high escarpments, separated by an area of low topography, where the largest catchment (NERS20) is positioned. Small catchments are mostly associated with footwall drainage, separating larger catchments that developed between faults utilising accommodation zones.

Along-margin spatial geomorphic variation is associated with south-to-north spatial and temporal variation in uplift rate and magnitude. The inverse modelling shows that uplift evolved from an early (21-15 Ma) southern locus to a late (12-0 Ma) northern one. Both of these loci are associated with present-day high topographic relief, high ratios of minimum eroded volume per catchment area and relatively high escarpment elevation.

The current study agrees with the model in which the early-rift uplift in the southern part of the study area is a record of footwall uplift with a possible additional mantle dynamic support. In the north, uplift represents footwall uplift due to fault coalescence near the Midyan area, and transform tectonics at the Gulf of Aqaba domain, as well as mantle-driven uplift near Harrat Uwayridh.

This study has implications on understanding the complexity characterising rift geodynamics as depicted on the surrounding geomorphology that responds to the

spatio-temporal evolution of uplift. Furthermore, knowledge acquired by assessing uplift variation and drainage evolution from the onshore parts of rifts and passive margins can be integrated with basinal subsurface data to better constrain paleo-drainage/sediment pathways during the past.

Chapter 4 Structural mapping of the faults southeast of the Midyan Peninsula, northeastern Red Sea margin

This chapter investigates the brittle deformation southeast of the Midyan Basin (northeastern Red Sea) addressing the extent of the Oligo-Miocene rifting. The chapter compares the deformation style in the basement to that of known nearby Oligo-Miocene normal faults. The conclusions made here are linked later to the exhumation presented in Chapter 5.

4.1 Introduction

Continental stretching occurs via brittle deformation in the form of normal faulting and fracturing in the brittle upper crust and ductile strain in the lower crust (Pagli et al., 2015). It is theoretically possible to acquire an insight into the direction of the extensional forces that led to the deformation by measuring the orientations of the normal faults given that the overall trend of these structures is perpendicular to the maximum extension direction (Fossen, 2010). However, complications arise from the existence of pre-rift structures that could date back to 100s of millions of years, possibly to the Precambrian.

Orientations of fractures and kinematic slip indicators provide information vital to the understanding of the integrated tectonic history of areas that have undergone a complicated history of deformation. Given these field data, the question of whether (or not) structural inheritance of pre-existing structures facilitated the activation of faults later during the rifting may be addressed.

The Midyan (Ifal) Basin at the northeastern end of the Red Sea is an Oligo-Miocene rift basin bounded to the east by the Ifal East Fault (IEF), which juxtaposes basement rocks against Oligocene-Recent strata (Figure 4.1). The IEF southern segment, here termed the Jabal az Zuhd Fault (JZF), is oriented along a pre-existing basement trend (NW-SE) oblique to the trend of the Red Sea (Tubbs

et al., 2014). To the southeast, a fault zone, here termed the South-Eastern Fault (SEF), strikes along the JZF trend and juxtaposes basement on basement. To the southwest, Miocene extension was accommodated by a NW/WNW-trending and SW-dipping fault, here termed Sharma Fault (ShF)), that juxtaposes basement against Miocene carbonates (Hughes and Johnson, 2005; Figure 4.1).

Unlike the high topographic relief and high elevation of JZF footwall block (JZ Mountain), the SEF is characterised by low relief and elevation (Figure 4.2). The gradual decrease of the elevation from the JZF footwall block towards the southeast (Figure 4.2b-c) could indicate either 1) a diminishing displacement near the JZF tip or 2) an enhanced erosion of the SEF footwall block. In the first scenario, strain localisation at the SEF is expect to be confined only at small faults (compared to the JZF) with slip directions that are compatible with pre-Oligocene regional stress regimes. Conversely, in the second scenario the deformation is expected to be localised at a major fault and distributed away from it with kinematic indicators suggesting similar stress regime to that causing the Oligo-Miocene deformation at the JZF.

The aim of this chapter is to decipher the structural context of this area to evaluate the extent of the Red Sea rifting by assessing how deformation varies away from a known Oligo-Miocene normal fault (i.e. JZF; Figure 4.1). To achieve this aim, the following objectives are pursued:

1) Examining the nature of the SEF to identify its role during the Red Sea rifting by comparing its structural style of deformation with that of the JZF, which is known to have been active during the Red Sea Cenozoic rifting.

2) Deducing stress orientations from fracture sets and kinematic indicators from the SEF, JZF and the ShF (and nearby grabens) and putting them into a tectonic regional perspective.

As the area surrounding the SEF is underlain by basement rocks with no dateable stratigraphy or volcanic rocks, using the structural measurements to invert for a sequence of stages of different paleo-stresses is out of the scope of this study. However, the overall time-integrated stress orientations may be inferred and compared with existing regional studies from the literature.

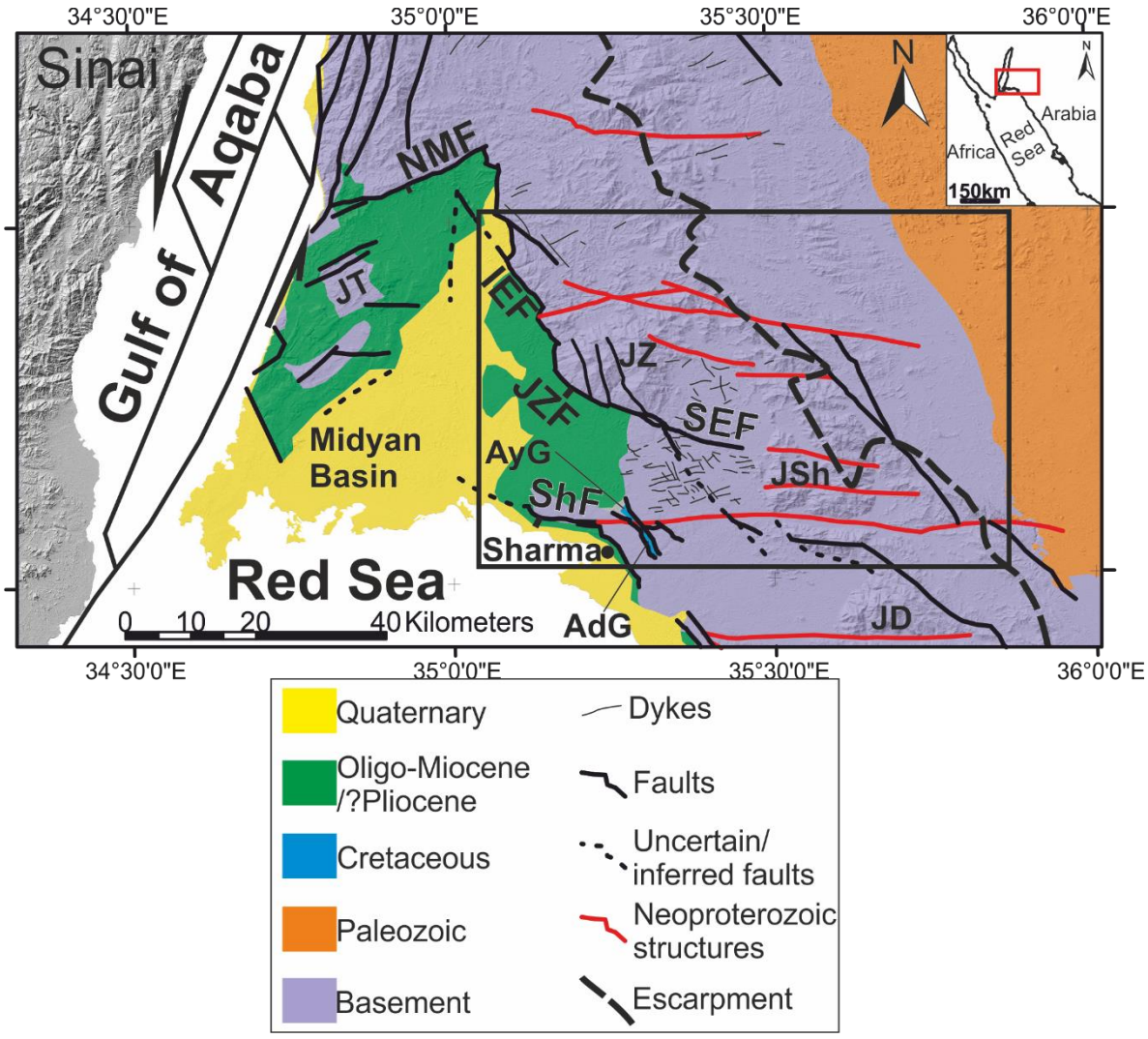

Figure 4.1: A simplified geological map of the Midyan Peninsula (note location with respect to the Red Sea in the inset map) overlaid on a hillshaded DEM (Modified from Clark (1987)). Note that the mappable Cretaceous unit occurs only in the AyG and AdG. The black box outlines Figure 4.4. NMF: Northern Midyan Fault; IEF: Ifal East Fault; JZF: Jabal az Zuhd Fault; JZ: Jabal az Zuhd Mountain; SEF: South-Eastern Fault; JSh: Jabal ash Shati mountain; JD: Jabal Dabbagh Mountain; ShF: Sharma Fault; AdG: Adaffa Graben; AyG: Aynunah Graben.

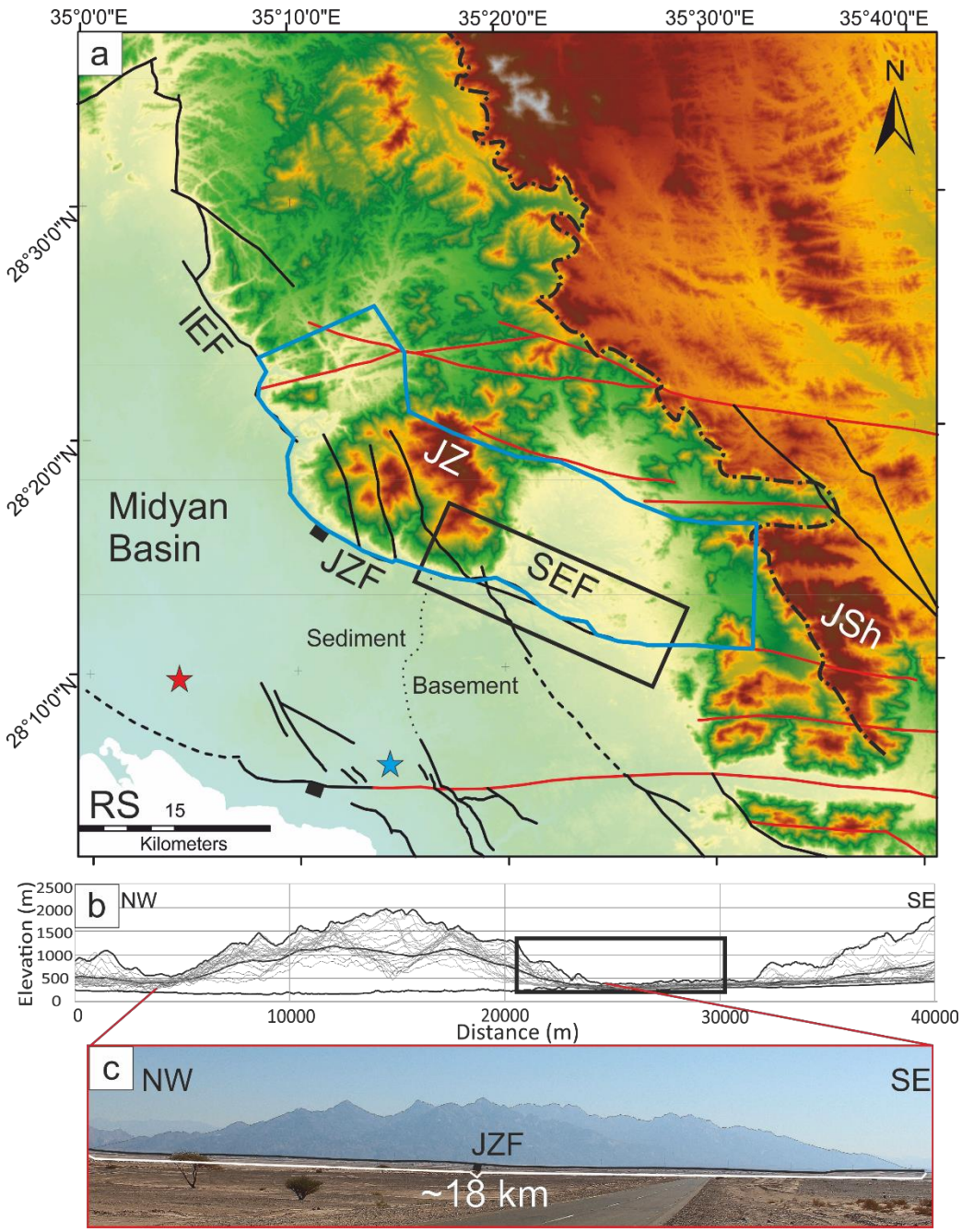

Figure 4.2: (a) A DEM map of the eastern side of the Midyan Peninsula. Note the sediment-basement contact (thin dotted line) and the escarpment (dash-dotted line). (b) A composite topographic profile along JZF and SEF as observed from the southwest (from the blue star) composed of 20 profiles covering the blue polygon in (a) and are parallel to its NE and SW boundaries. Profiles close to the observer have dark shading, and vice-versa. (c) A photograph showing the topographic profile of the JZF. Black boxes on (a) and (b): the mapping area; Red star on (a): location where photograph (c) was taken. RS: Red Sea; JZ: Jabal az Zuhd; JZF: Jabal az Zuhd Fault; SEF: South-Eastern Fault; IEF: Ifal East Fault; JSh: Jabal ash Shati.

4.2 Stress history and structures around the northern Red Sea

In this section, the different orientations of structures that formed around the northern Red Sea prior to and during the Cenozoic rifting are summarised from the literature. This summary provides a basis for interpreting the stress orientations deduced from this study and putting them in a regional context. Figure 4.3 shows a summary of how stress orientation changed in the area around the northern Red Sea since the Late Cretaceous and includes the latest stage of deformation during the Neoproterozoic basement building stage.

In the Midyan Peninsula, the pre-existing Precambrian basement structures trend NW-SE and form the northernmost part of the sinistral strike-slip Najd Fault System (Meyer et al., 2014; Tubbs et al., 2014; Figure 4.3). Further south, similar structures are aligned with the Wadi Azlam Basin bounding fault, the northern bounding fault of the Al Wajh Basin, as well as the Gebel Duwi on the Egyptian margin (Bosworth et al., 2005). Analysis of structural data from this large fault system and from Neoproterozoic dykes suggests an overall NNW/SSE-oriented maximum horizontal extension at the Midyan area during the Neoproterozoic (Johnson et al., 2011).

Mesozoic deformation has been described in the northern Red Sea. At the faults bounding the Gebel Duwi and the surrounding basement to the west of Quseir on the Egyptian Red Sea margin, Bojar et al. (2002) argued for sinistral strike-slip deformation with an ENE/WSW-oriented $\sigma 1$ and a NNW/SSE-oriented $\sigma 3$ that reactivated pre-existing basement structures and formed pull-apart basins during the Late Cretaceous (Figure 4.3). Upper Cretaceous sedimentary units are present southeast of the Midyan Basin at the NW-oriented Adaffa Graben (AdG) and the Aynunah Graben (AyG), both approximately 1 km-wide and separated by an E-W Proterozoic fault (Hughes et al., 1999; Figure 4.1). If these grabens formed in response to the same stress regime, it is reasonable to assume that the ENE/WSW-oriented $\sigma 1$ and a NNW/SSE-oriented $\sigma 3$ also affected the Midyan area.

During the Cenozoic, the northern Red Sea tectonics were driven by the Oligo-Miocene NE-SW extension (Bosworth et al., 2005; Figure 4.3). In the Midyan Peninsula, the Oligo-Miocene Ifal East Fault (IEF) is made up of a number of fault segments with orientations changing from NNW-SSE to NW-SE but the overall trend is semi-perpendicular to the extension direction (Tubbs et al., 2014; Figure 4.1).

Lastly, the main faults that formed in response to the Gulf of Aqaba sinistral strike-slip tectonics starting from the Middle Miocene are oriented NNE-SSW (Bosworth et al., 2005; Tubbs et al., 2014). These faults were associated with pull-apart basins within the gulf and in the Midyan Basin that indicate trans-tension in this part of the margin (Tubbs et al., 2014). These observations are supportive of the suggested NNE/SSW-oriented maximum horizontal extension at the northern Red Sea (Bosworth and Strecker, 1997; Figure 4.3). Since then, the northern Red Sea was characterised by trans-tension rather than extension, which is also suggested by the present-day stress vectors and GPS-measured plate motions (ArRajehi et al., 2010; Figure 4.3).

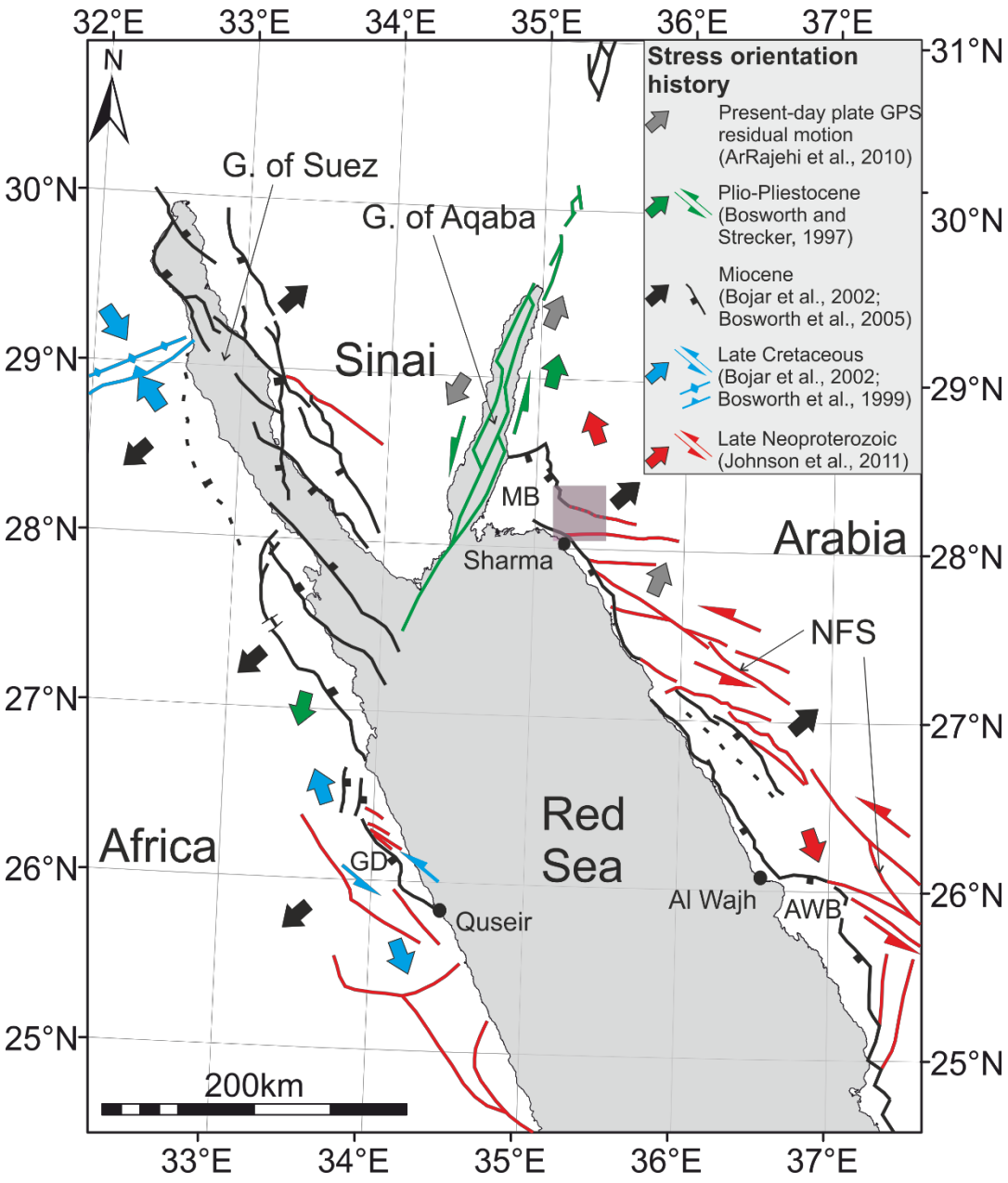

Figure 4.3: Summary map of the different stress orientations that have affected the area surrounding the northern Red Sea since the Late Cretaceous as well as the late evolution during the Neoproterozoic (see legend for references). The coloured arrows represent the extension direction (and the compression direction at Wadi Araba (WA)). The coloured structural symbols represent the dominant structural response to the stress orientation. The translucent purple square indicates this chapter study area. MB: Midyan Basin; AWB: Al Wajh Basin; GD: Gebel Duwi; WA: Wadi Araba; NFS: Najd Fault System.

4.3 Methodology

4.3.1 Field mapping approach

The structural mapping aims to characterise the extent, style and intensity of the brittle deformation southeast of the Midyan Basin. The field study area was divided into two smaller areas: the JZF-SEF area and the ShF-AyG-AdG area. The primary focus area is the JZF-SEF with the objective of the structural mapping of the SEF and comparing its structures to those along the JZF (Figure 4.4). Other structural measurements were collected from localities that are not within either the JZF-SEF or the ShF-AyG-AdG areas (e.g. southwest of the Jabal ash Shati, northeast of the SEF and along the IEF to the north-northwest of the JZF).

The mapping involved the identification of faults, and measurement of fractures and slip surface orientations as well as slip direction indications (e.g. slickensides and slickenlines). Due to the lack of stratigraphic markers in the basement domain of the SEF, faults were identified based on the occurrence of fault rocks within the same lithology in basement rock and between different Proterozoic units. Moreover, the orientation of ductile deformational features (primarily foliations) were recorded where present.

In order to characterise the complexity of the fault zones, mapping and systematic measurements were undertaken at specific localities selected for their good exposure and structural position. Two mapping approaches were implemented for this purpose. Firstly, to assess fracture density and compare it to fracture orientation (to see whether dense fracturing is aligned with the Red Sea trend), several locations along the SEF and JZF were selected to collect detailed and systematic structural measurements of the fractures (Figures 4.5a and 4.6). These measurements were recorded along metre-scale transects perpendicular to the local structures, whereby all features that intersect the transect line are noted and their orientation and distance along the line recorded. The orientations recorded from these metre-scale lines are incorporated into the stereonet plots, which include also other structural measurements not recorded at these transects.

Secondly, to show the variety and complexity of deformation across the SEF, selected outcrops along the Wadi Aynunah valley (which crosses the fault) that provide some of the best exposure across the fault zone were used to produce photographic panels (Figure 4.5b). These panels were utilised in the mapping and interpretation of the faults as well as the structures within the basement blocks in-between these faults. On these photographic panels, annotation of fractures and other features was done so that it reflects the relative density of these features when the corresponding localities are compared and contrasted.

4.3.2 Stereographic analyses

The analysis of the measurements was performed after stereographic projection of planes of fractures and slip directions had been undertaken using Stereonet 10.0 (Allmendinger et al., 2011; Cardozo and Allmendinger, 2013) and FaultKin 8.0 (Marrett and Allmendinger, 1990; Allmendinger et al., 2011). The stereonets were plotted in an equal-area projection and projected on a lower hemisphere.

The orientations of joints and shear fractures were plotted and contoured as poles to the planes using Stereonet 10.0. With respect to the shear fractures, FaultKin 8.0 was used to plot the fracture orientations as lines (i.e. projections of the fracture planes) and the slip directions (i.e. trends and plunges) and sense of displacement as points (with arrows indicating the direction). The resultant plots from FaultKin 8.0 and Stereonet 10.0 were integrated and plotted on the structural map.

The fracture orientations were grouped to construct six stereonets along the strikes of both the JZF and the SEF (see stereonet figures in Section 4.4). To assess the kinematics of the structures that are located closer to the Red, structural readings were grouped to construct stereonets to the east of the ShF, AyG and AdG.

4.3.2.1 Estimating principal paleo-stress orientations

The stereographically projected data can be used to determine the overall paleo-stress orientations at each major structural element, whereby kinematic indicators were used to delineate $\sigma 1$, $\sigma 2$ and $\sigma 3$. The stress orientations were deduced mainly from the directions of the slip indicators (i.e. slickenlines) found on the shear

fractures. However, as will be shown in the results section (Section 4.4), the slip indicator data points are scarce in some areas along the SEF and the JZF. In these instances, particularly clear in the JZF (see Section 4.4), well-defined joint sets were used to estimate the principal stress orientations such that $\sigma 3$ is perpendicular to the structure defined by these sets. It is important to point out that the measurements were obtained in basement rocks, which introduces an uncertainty with respect to the timing of events that formed the features. As will be seen later in the discussion of these measurements, the calculated stress orientations can be linked to orientations recognised in the literature over the regional scale, which reduces the uncertainty implied by the lack of dateable strata/volcanics.

The principal stress orientations were calculated using Structural Geology to Post Script (SG2PS) software and plotted on lower hemisphere equal-area projected stereonets (Sasvári and Baharev, 2014). To invert for the paleo-stress orientations, the inversion methodology by Angelier (1990) was used and specified in SG2PS. The inverted stress orientations, however, cannot be directly linked to a particular time in the past and are instead time-integrated spanning the time since the Neoproterozoic. The input data into the software are only the shear fracture orientations and their slip directions. In the case of the JZF, where only joints orientations were measured, the extension is assumed to be perpendicular to the strike of the joints.

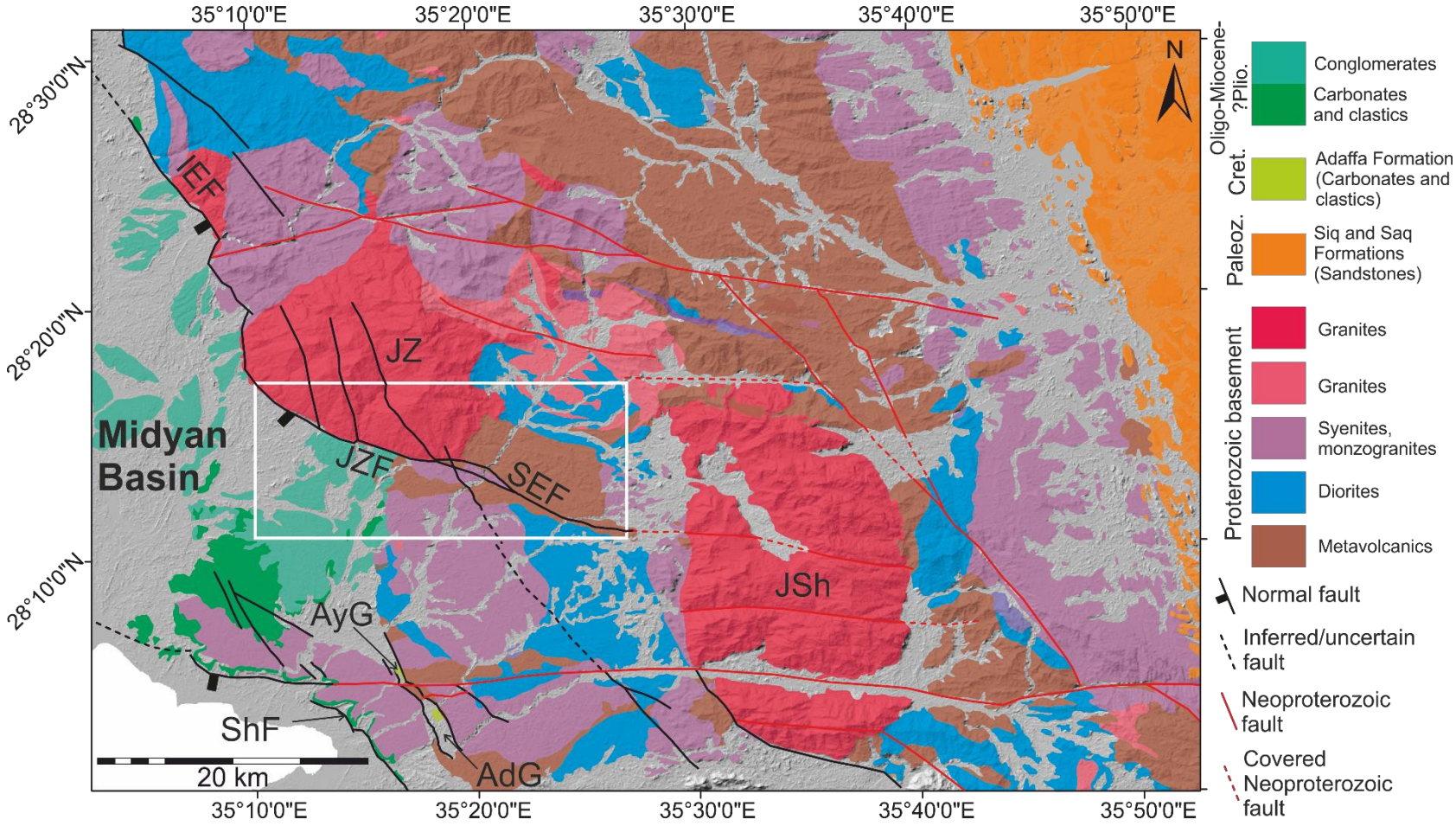

Figure 4.4: A geological map of the southeastern part of the Midyan Peninsula (Modified from Clark (1987)). Location of map is shown in Figure 4.1 and the white box outlines the location of Figure 4.5a. JZ: Jabal az Zuhd; JZF: Jabal az Zuhd Fault; SEF: South-Eastern Fault; IEF: Ifal East Fault; JSh: Jabal ash Shati; ShF: Sharma Fault; AdG: Adaffa Graben; AyG: Aynunah Graben.

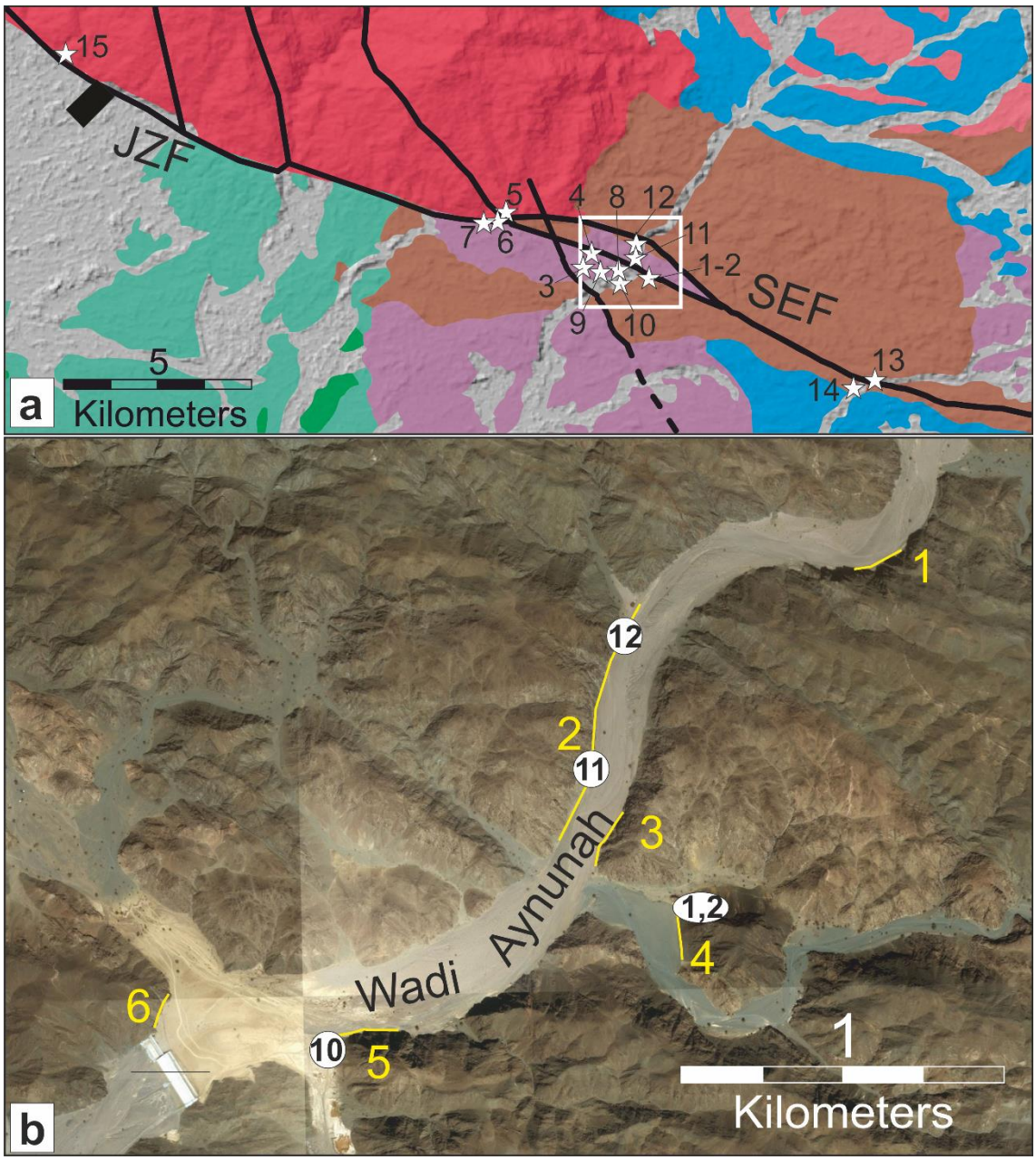

Figure 4.5: (a) A close-up on the SEF (South-Eastern Fault) and JZF (Jabal az Zuhd Fault) showing the locations of systematic transect measurements of structural features (white stars). The white box outlines the location of Figure 4.5b. (b) Locations of the panels (outcrops along the Wadi Aynunah Valley) that were used to map part of the structural features of the SEF. Note locations of systematic transect measurements (white circles) that are close to the panels.

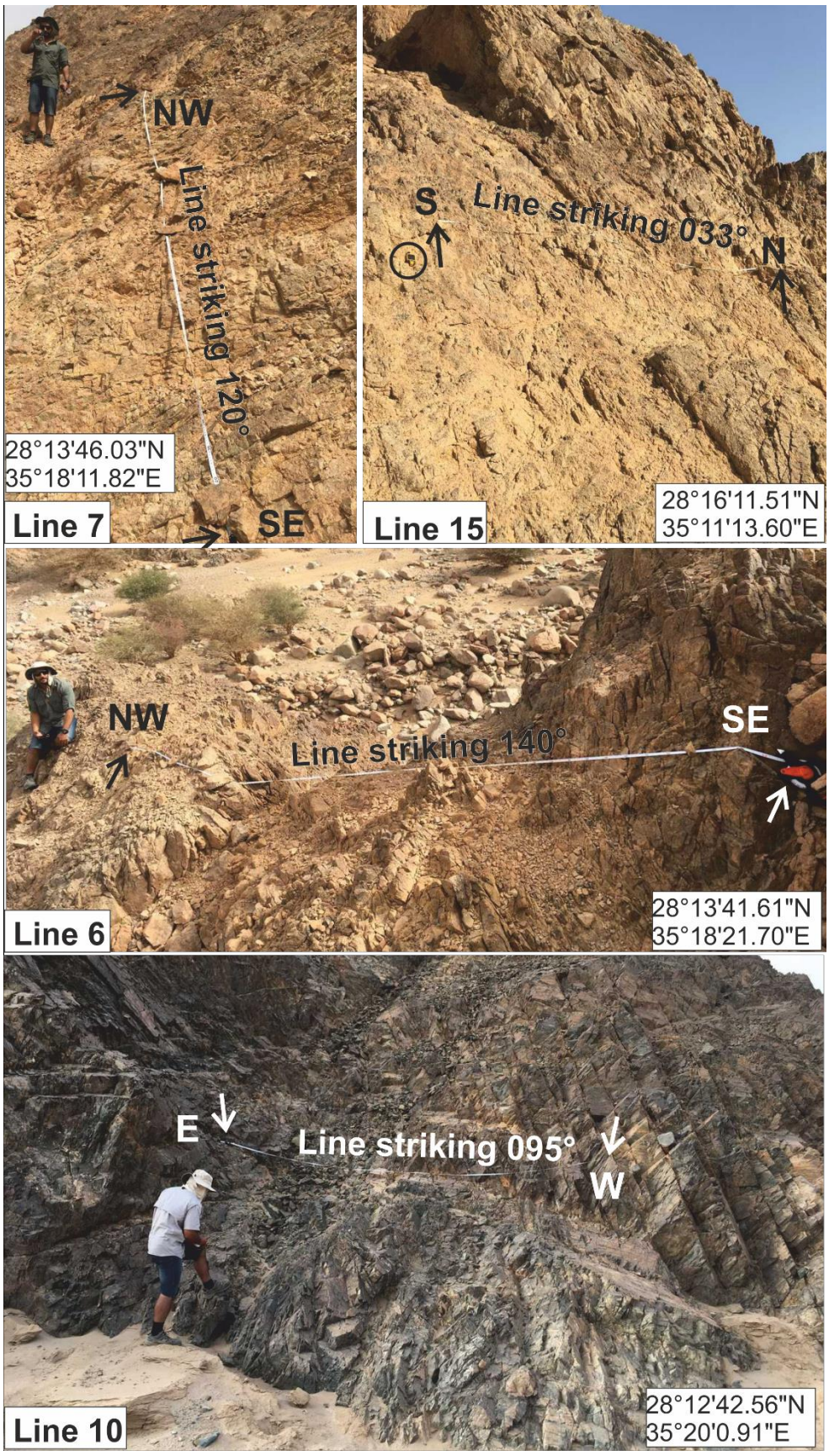

Figure 4.6: Examples of the metre-scale transect lines along which all fracture orientations were measured. The black and white arrows define the start and end of each line. The circle in Line 15 photo encloses a GPS device for scale. Locations of these lines (6, 7, 10 and 15) are also shown in Figure 4.5a.

4.4 Results

4.4.1 Structural mapping results

In the field study area the dominant regime indicated by the measured features is that of brittle deformation. A structural map of the study area and stereographic projections of the orientation measurements are shown in Figure 4.7a-b. Moreover, detailed measurements of fracture spacing along metre-scale transects at the southeastern and northwestern parts of the JZF and at the northwestern part of the SEF are shown in Figure 4.8. The measurements collected along these metre-scale lines are also incorporated into the stereonet plot for the corresponding location in Figure 4.7b.

The observed brittle features include joints (no observable displacement at the outcrop and hand specimen scale), shear fractures (indicating mm to cm displacements) and faults. Kinematic indicators including slickenlines and steps on shear fracture of fault surfaces were also observed and recorded. Ductile deformation occurs in the study area but is much less frequent than the brittle deformation, and included foliation and mylonitic zones observed at some locations.

The following sections describe in detail the structural observations from the JZF, SEF as well as the southern part of the study area (ShF, AdG and AyG).

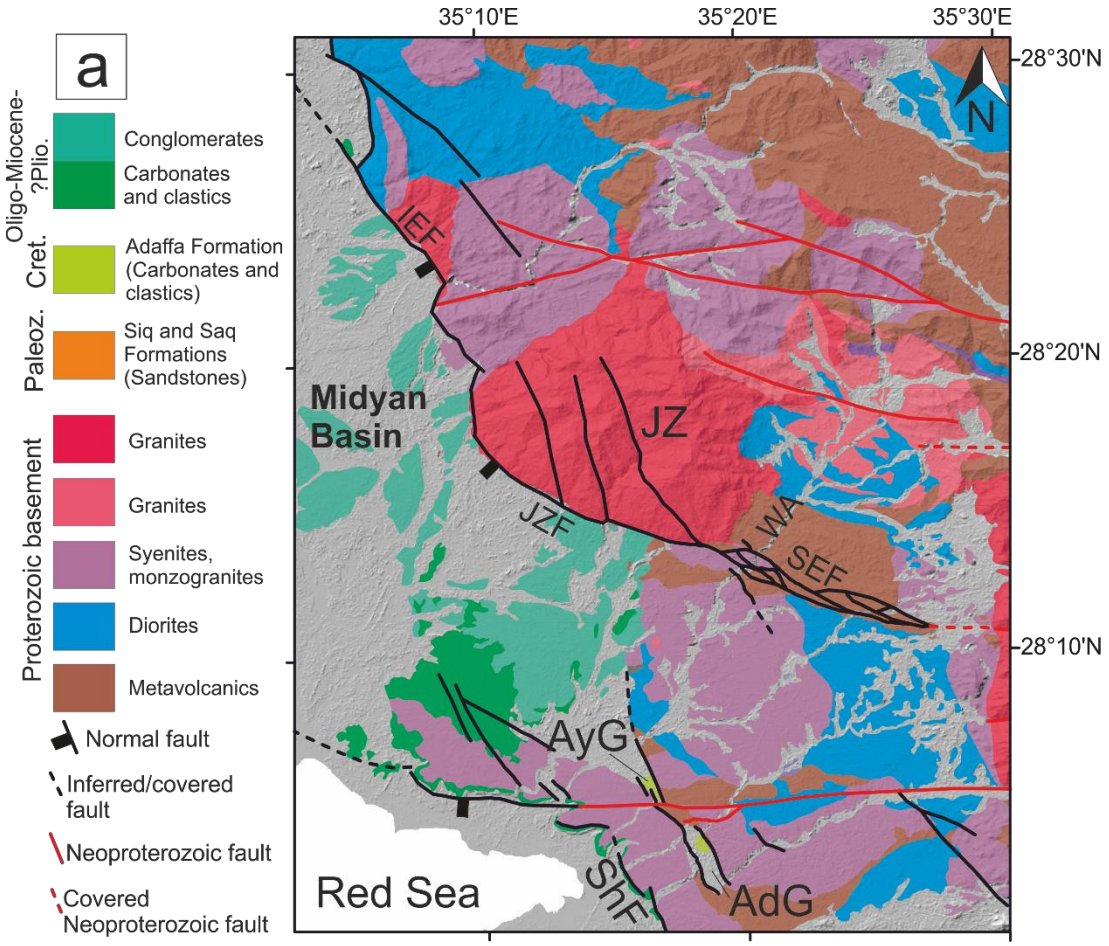

Figure 4.7: (a) A structural geology map of the study area with detailed mapping of SEF structures (Lithology modified from Clark (1987)). JZ: Jabal az Zuhd mountain; JZF: Jabal az Zuhd Fault; IEF: Ifal East Fault; WA: Wadi Aynunah Valley; SEF: South-Eastern Fault; AyG: Aynunah Graben; AdG: Adaffa Graben; ShF: Sharma Fault. (b) The same map in (a) showing lower hemisphere equal-area projected stereonets of joints and shear fractures generated using Stereonet 10.0 (Allmendinger et al., 2011; Cardozo and Allmendinger, 2013). The slip directions were plotted using FaultKin 8.0 (Marrett and Allmendinger, 1990; Allmendinger et al., 2011) then added to the stereonets. The number next to each stereonet plot is the number of data points (i.e. joint/shear fracture plane orientation). The rainbow contours are plotted for the density of the poles to planes. The slip direction arrows in the stereonet plot marked by the asterisks (*) were coloured in red only for clarity given the dark background. The double-headed coloured arrows to the bottom-left corner of the map represent the regional horizontal extension direction from the literature: red: Late Neoproterozoic (Johnson et al., 2012); blue: Late Cretaceous (Bojar et al., 2002; Bosworth et al., 2005); black: Miocene (Bojar et al., 2002; Bosworth et al., 2005); green: Plio-Pleistocene (Bosworth and Strecker, 1997); grey: Present-day (ArRajehi et al., 2010). The stratigraphy and structure key is as shown in (a).

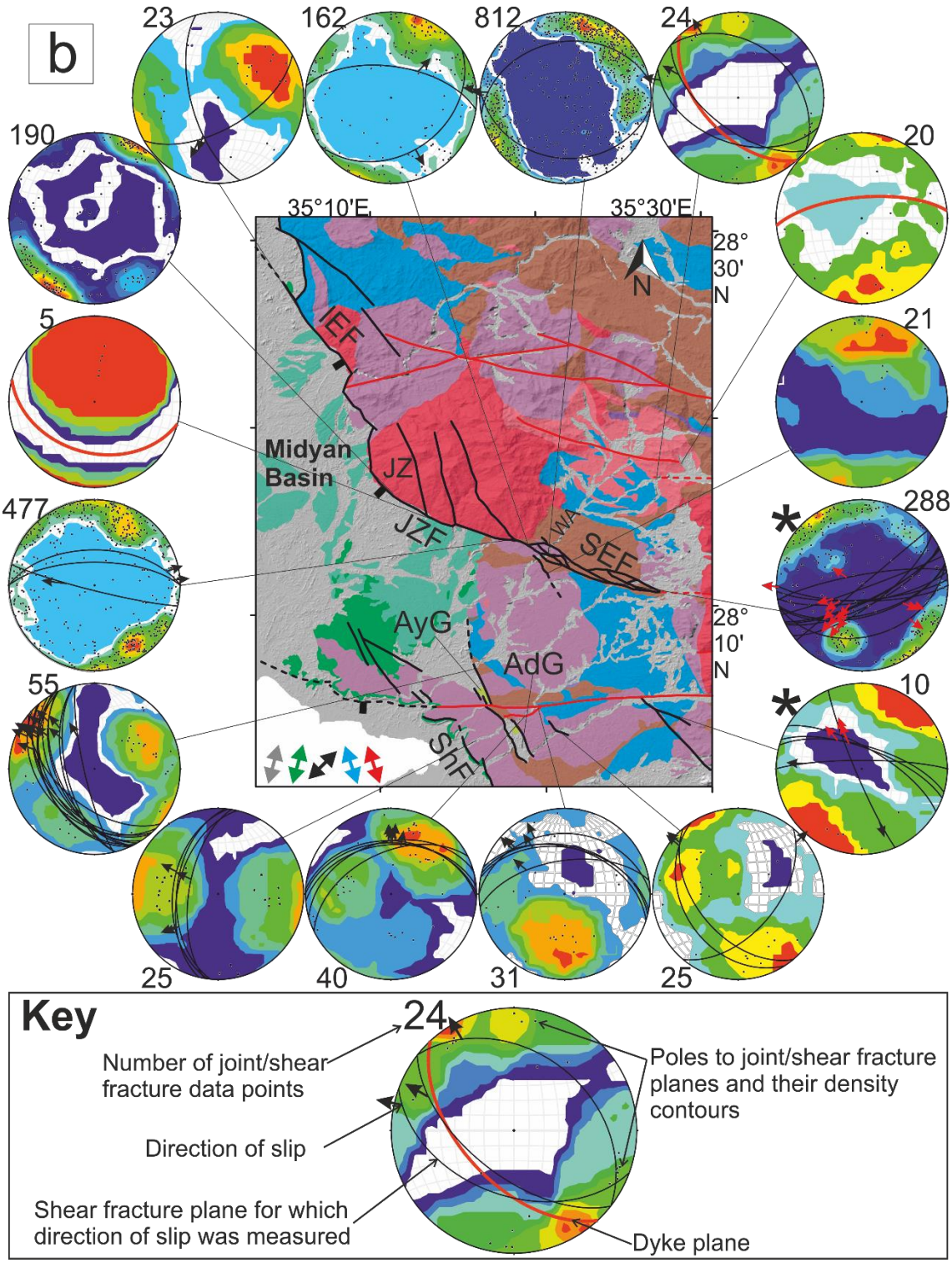

Figure 4.7 (continued).

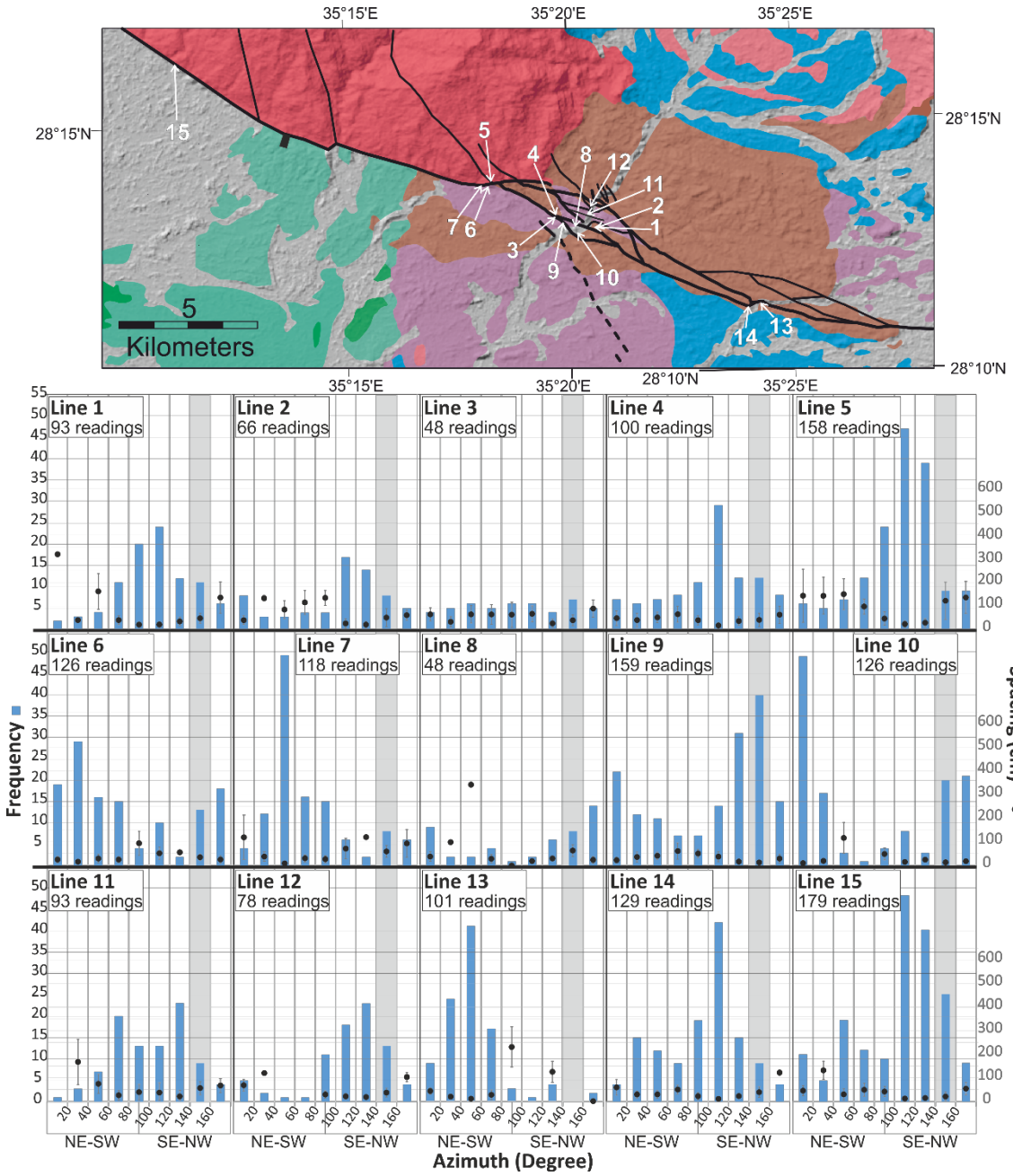

Figure 4.8: Spacing and frequency of fractures with respect to their orientation (bottom frequency graphs), measured at a selected line transects that are perpendicular to local structural orientation along the SEF and JZF (top map). The lithology code is as per Figure 4.7. The black dots in the graphs represent the spacing between the fractures, whereas the blue columns represent the number of fractures corresponding to each zone of strike angles (horizontal axis). The grey angle band represents the general Red Sea trend.

4.4.1.1 JZF-SEF structures

4.4.1.1.1 JZF

The JZF is the southern segment of the Ifal East Fault, which forms the eastern boundary of Midyan Basin (Figure 4.7). The JZF has an average strike of ~120° and an average dip value of ~65° towards the southwest. It juxtaposes granitic basement rock to the east against Neogene sedimentary units to the west. At the surface, conglomerates are juxtaposed against this fault at its southeastern part (Figure 4.9).

The JZF is characterised by a localised, 10-20-m-wide, zone of intense brittle deformation with fracturing intensity increasing from the NE to the SW towards the fault core, which is not wholly exposed (Figure 4.9). Furthermore, approximately 60 m up-dip of the basement-sediment contact, a 30-metre-thick zone of fault gouge is noted with similar orientation to the JZF (Figure 4.9d-e).

Different sets of joints were observed along and near the JZF, and their orientations change along strike. Close to the northwestern tip of the JZF, two dominant sets of fractures dip steeply (>70°) both towards the NE and SW with a strike trend of ~ 303°/84°N that is parallel to the JZF (Figure 4.7). The systematic measurements show that the dominant joints, associated with high intensity (spacing reaching 1 cm), are oriented ESE-SE (~110-130°; line 15 in Figure 4.8). A much smaller set striking SW (050°) is oriented near-perpendicular to the general trend of the JZF (Figures 4.7-4.8). This latter set is characterised by smaller intensity compared to the former two sets with spacing of ~10 cm (line 15 in Figure 4.8).

Midway along the strike of the JZF, a 15-20-m-wide fault zone is characterised by the highest deformation. This zone is oriented along a WNW-ESE trend and dips towards the SW at 56° (Figure 4.7a). The measured fracture orientations near this fault zone are mostly aligned with it and are dipping towards the SSW.

Close to the southeastern end of the JZF, the fracture sets become less defined. Broadly, two sets may be defined with a wide dip-angle range (30° to 85°); NW-SE-oriented fractures dipping towards the SW, and SW-NE-oriented fractures dipping towards the NW (Figure 4.7). This latter set is oriented near-perpendicular to the JZF and is similar in orientation to the less pronounced set described earlier from the northwestern part of the JZF. Fracture orientation

measurements taken systematically along the metre-scale transects show that these two sets dominate the southeastern corner of the JZ Mountain in terms of fracture intensity and spacing; NE (030°-050°) and SE (120°) with some scatter in the data (lines 5-7 in Figure 4.8). The two trends are associated with high fracture intensity with spacing down to 1 cm. A less defined set includes fractures striking NW to NE, dipping mostly towards the east and with a similarly wide range of dip magnitudes (Figure 4.7).

At this part of the fault, notable at some of the shear fracture surfaces is the existence of striations and slickenlines indicating left-lateral strike-slip and strongly oblique-normal sense of slip (Figure 4.10). The shear fracture surfaces where these kinematic indicators are found are oriented semi-perpendicular to the JZF general trend.

Oblique to the JZF, large-scale NNW fracture corridors are observed cutting across the Jabal az Zuhd footwall block with an orientation that is semi-parallel to the Red Sea trend (Figure 4.7). No detailed measurements were taken from these features, but where they intersect the JZF, the measurements do not show significant influence by them (lines 5-7 in Figure 4.8).

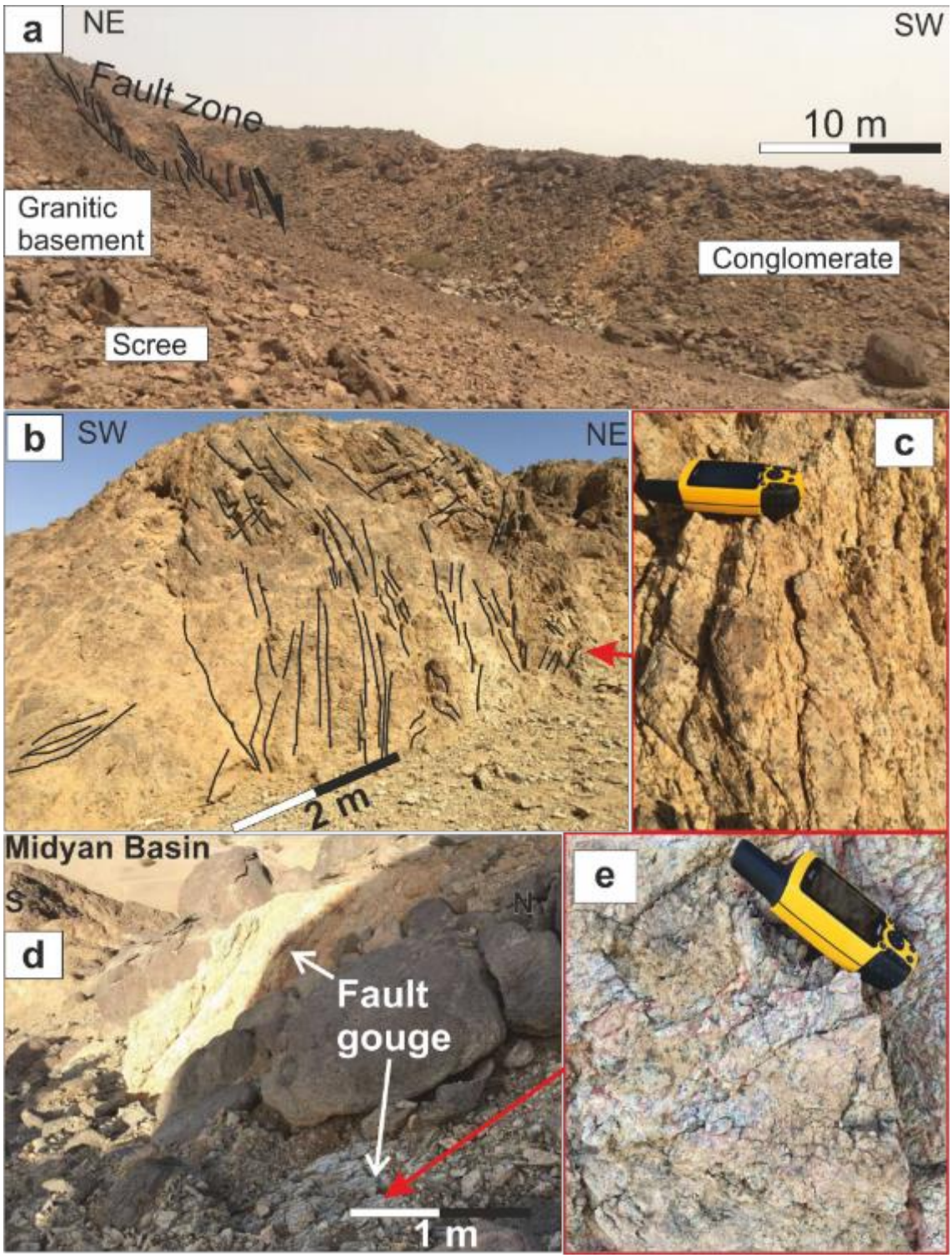

Figure 4.9: (a) An overview photograph of the JZF showing basement rock to the left (NE) and conglomerate to the right (SW) (28°14'13.99"N, 35°16'20.62"E). The fault zone is about 10 m in this view. (b) Fracturing at a basement granitic outcrop associated with the JZF (28°16'11.44"N, 35°11'13.71"E). (c) A close-up of the fractured basement shown in (b). (d-e) An example of fault gouge with orientation semi-parallel to the JZF (28°16'15.61"N, 35°11'16.69"E).

Figure 4.10: An example of striations indicating local left-lateral strike-slip deformation at the southeastern end of JZF (28°13'55.73"N, 35°17'22.50"E). Displacement direction (i.e. movement of the removed rock) is indicated by the white arrow and number.

4.4.1.1.2 SEF zone

As opposed to the JZF, brittle deformation at the SEF is spread across a NW-trending zone that is approximately 2.5 km-wide at the Wadi Aynunah Valley (Figure 4.7). Within this zone, brittle deformation is complex with localisation of strain detected at multiple faults with variable orientations instead of a thoroughgoing major fault. The complexity of the deformation at the SEF is clearly noted on the panels interpreted from the sides of the Wadi Aynunah Valley, which crosses this fault zone (Figures 4.11-4.16).

The multiple faults that comprise the SEF partition the deformation zone forming lens-shaped, less deformed, basement host rock (Figure 4.7). These faults have a maximum thickness of approximately 2-3 metres (e.g. Figure 4.16), comparatively smaller than the JZF. The lens-shaped blocks vary in scale from metre-scale blocks (bounded by small scale faults) to kilometre-scale block that can be observed on satellite imagery (Figures 4.11, 4.12 and 4.15).

The major faults dip mostly to the southwest with dip values ranging from 60° to 84° (e.g. Figure 4.16). However, the dip directions of smaller faults separating the lens-shaped blocks vary from dominantly west-ward to dominantly east-ward (Figures 4.11-4.16). Moreover, the dip values of the individual faults

change across strike and, more clearly, along strike to accommodate the lens-shapes of these blocks.

At the Wadi Aynunah Valley section of the SEF, the fracture sets are characterised by variable orientations (Figure 4.7b). Three steeply dipping sets may be defined based on their pole orientations trending at the NW-SE, NNW-SSE and the N-S. Across the strike of the SEF, the NW/NNW sets characterise most of the interpreted panels along the Wadi Aynunah valley (e.g. Panels 2, 4 and 6; Figures 4.12, 4.14 and 4.16). The N-S trending fractures, on the other hand, are mostly confined to the southwestern part of the SEF zone (Panel 5; Figure 4.15).

The systematic measurements of the fractures orientations along the metre-scale transects indicate that the dominant fracture sets are associated with high fracture frequency and small spacing (Figure 4.8). Shear fractures with kinematic indicators, however, are scarce and oriented E-W indicating local strike-slip movement with both sinistral and dextral senses of displacement (Figure 4.7b).

At the southeastern part of the SEF, fractures form two well defined sets (Figure 4.7b). These sets are high angle fractures dipping to the NNW and SSE and oriented along a range of trends between WSW-ENE to ESE-WNW. Fracture intensity and spacing are highest and lowest, respectively, where the fractures strike NE (~050°) and NW (~110°; lines 13-14 in Figure 4.8). Slip indicators in the form of slickenlines, however, cluster on E-W to NE-SW oriented fractures that dip mostly to the SSE (Figure 4.7b). These indicators suggest dominantly normal sense of slip towards the south with strike-slip components (Figure 4.17).

Overall, the SEF may be divided into two smaller SW-dipping zones of faulting at the Wadi Aynunah valley section, separated by ~1 km-wide granitic lens-shaped block (Figure 4.18). These two zones have antithetic and synthetic faults that splay out and into them. In between the faults, the brittle deformation is lower in intensity (e.g. Figure 4.13), whereas near local structures the fracture intensity increases as suggested by fracture spacing frequency plots (Figures 4.8, 4.12, 4.14 and 4.15).

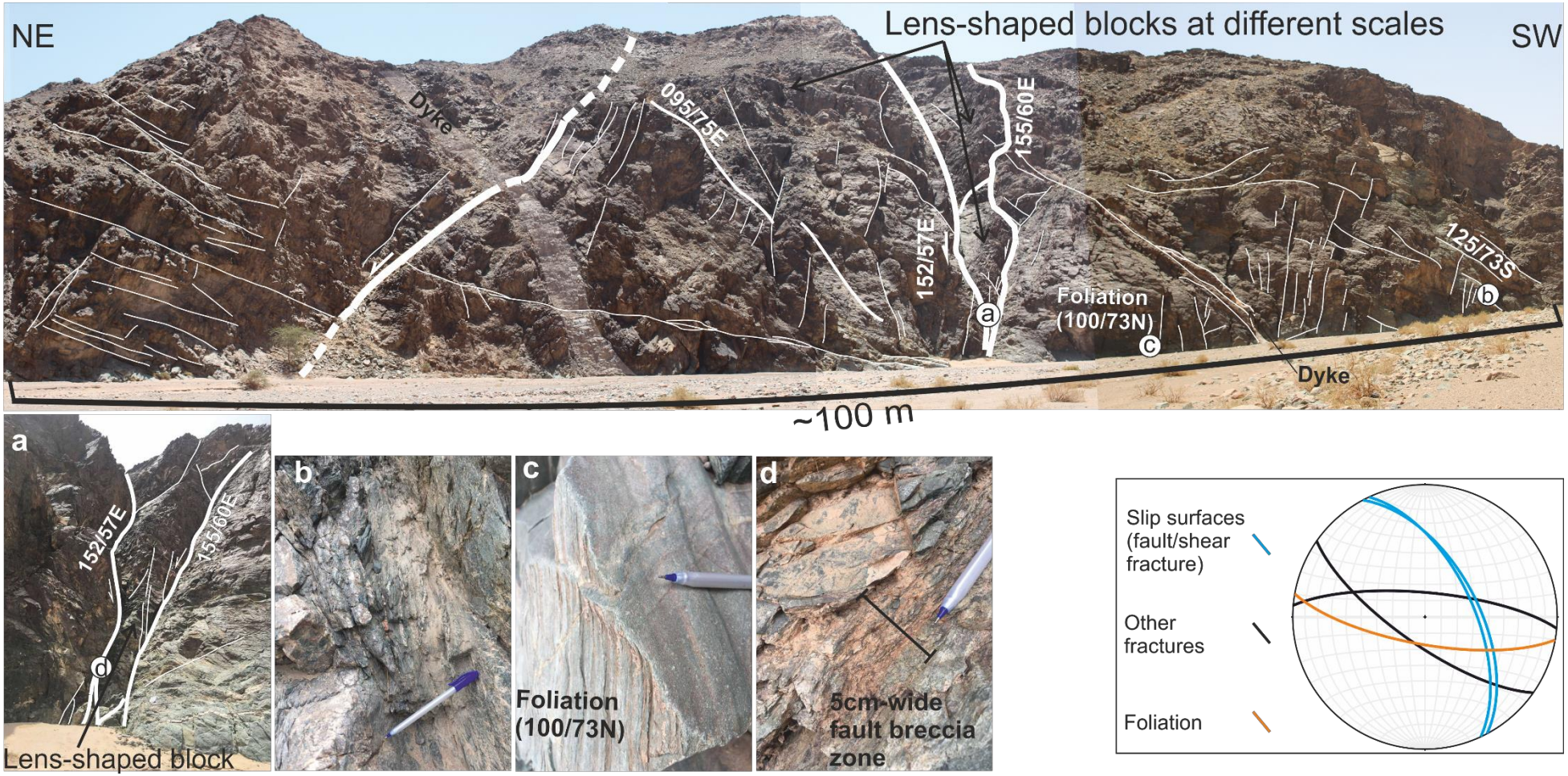

Figure 4.11: Panel 1 interpretation. Note the lens-shaped blocks over different scales. The deformation is concentrated at a number of faults bounding blocks that are less deformed. The orientations of the structural features are plotted on the stereonet at the bottom right.

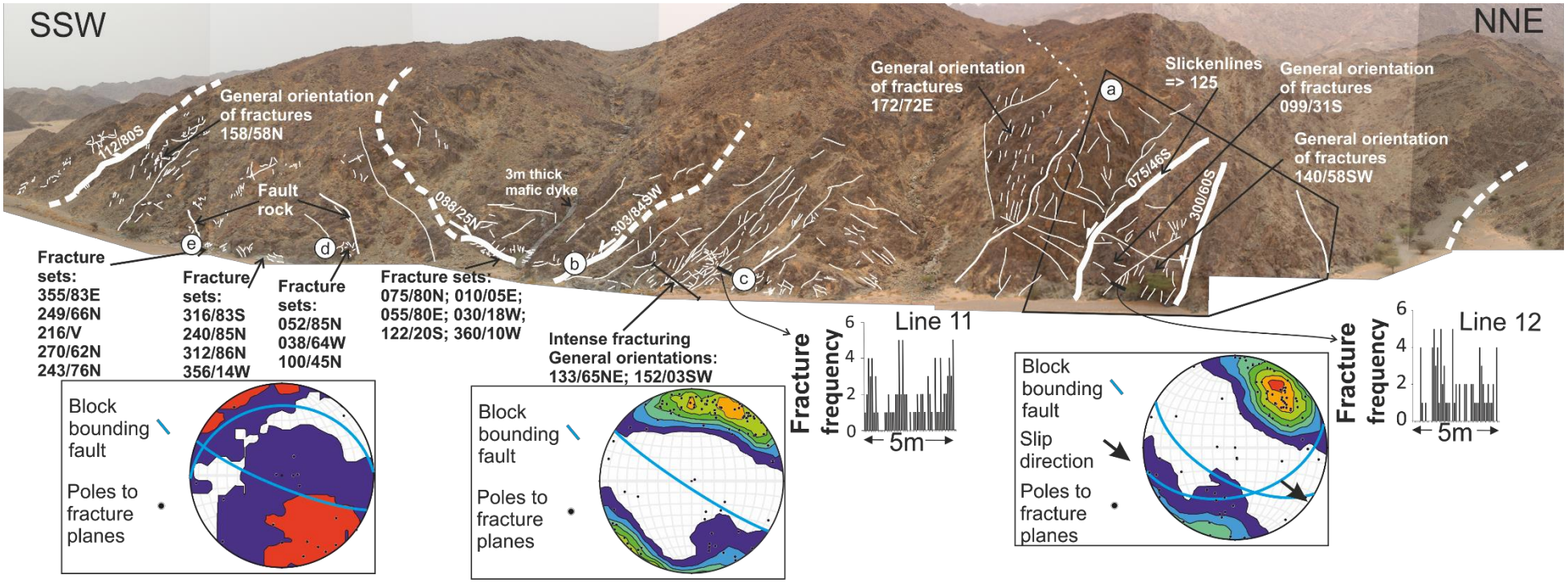

Figure 4.12: Panel 2 interpretation showing complex brittle deformation. The foreground of the view is ~850 m-wide. Note the fracture distribution with respect to distance along lines 11 and 12 (a bin size of 10 cm was used to produce the histograms). The fracture density varies along the metre-transect lines within the basement blocks. For fracture spacing and frequency distribution with respect to fracture strike see Figure 4.8. Complex brittle and some ductile deformations over a number of scales are shown in a-e (next page). The orientations of the structural features along the panel are plotted on the stereonets at the bottom.

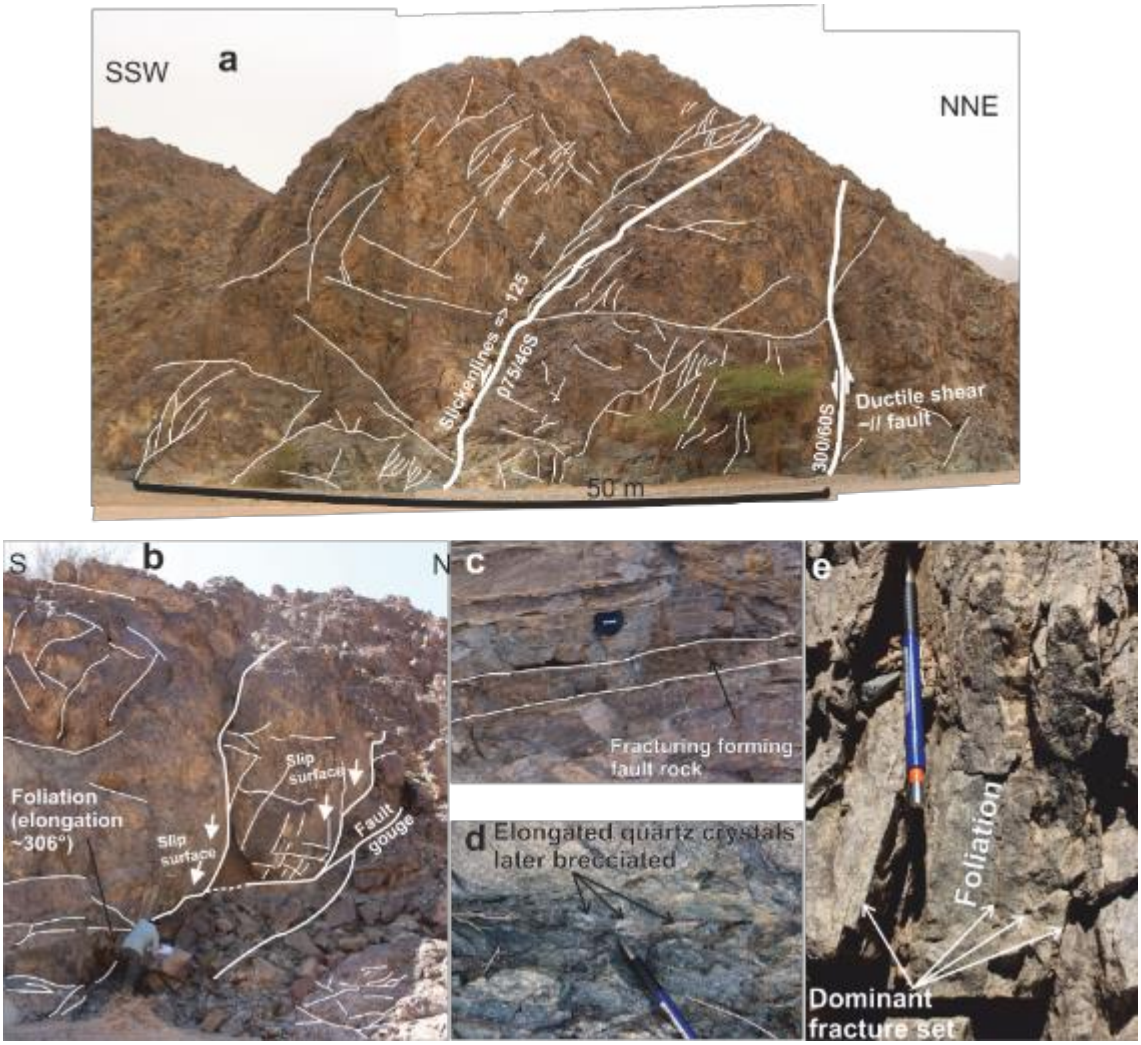

Figure 4.12 (continued).

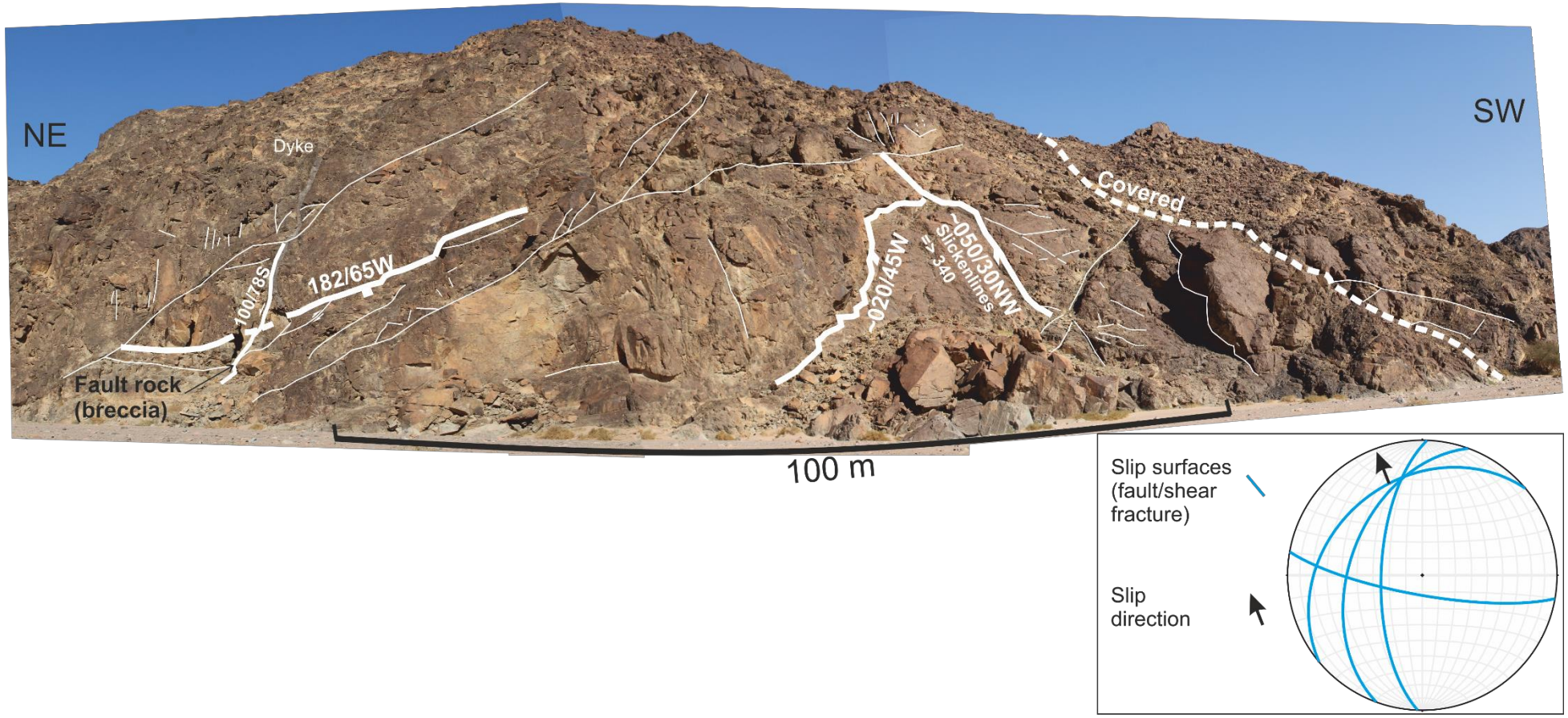

Figure 4.13: Panel 3 interpretation showing faults of various orientations separating zones of less deformation. This outcrop features less fracturing compared to other panels, which is related to its position within a less deformed, low strain, host basement rock (see Figure 4.18). The orientations of the slip surfaces and faults are plotted on the stereonet at the bottom right.

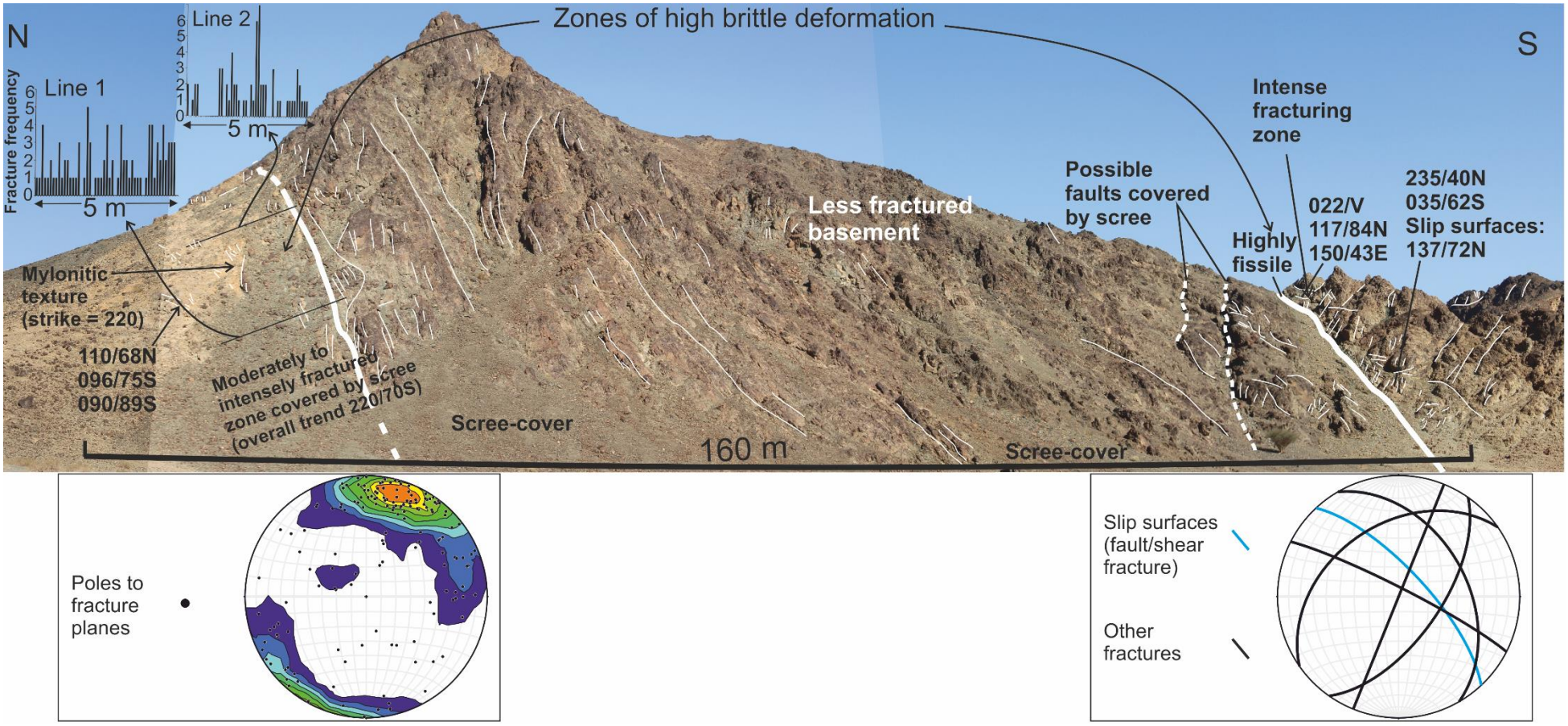

Figure 4.14: Panel 4 interpretation showing two zones of relatively high brittle deformation bounding a lower strain basement block. Note the fracture distribution with respect to distance along lines 1 and 2 (top left; a bin size of 10 cm was used to produce the histograms). Notice the general increase in fracture number at the southern sides of the metre-transect lines towards the fault. For fracture spacing and frequency distribution with respect to fracture strike see Figure 4.8. The two stereonets at the bottom show the structural orientations.

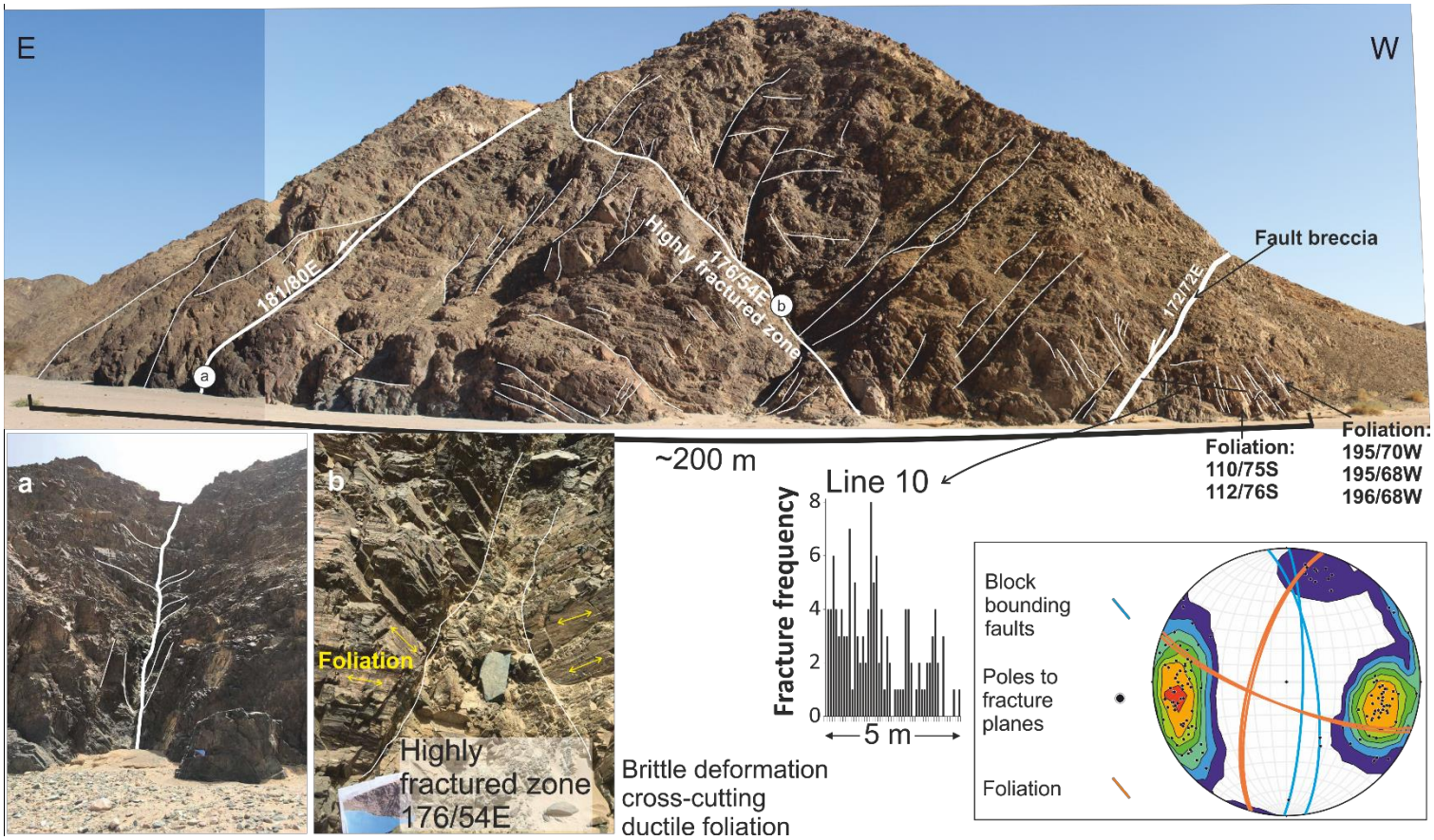

Figure 4.15: Panel 5 interpretation showing lenses of fractured basement between zones of higher brittle strain/faulting. Note the relationship between foliation and brittle deformation. Note the fracture distribution with respect to distance along line 10 (bottom right; a bin size of 10 cm was used to produce the histogram), where the fracture density increases towards the fault. For fracture spacing and frequency distribution with respect to fracture strike see Figure 4.8. The stereonet at the bottom right shows the structural orientations.

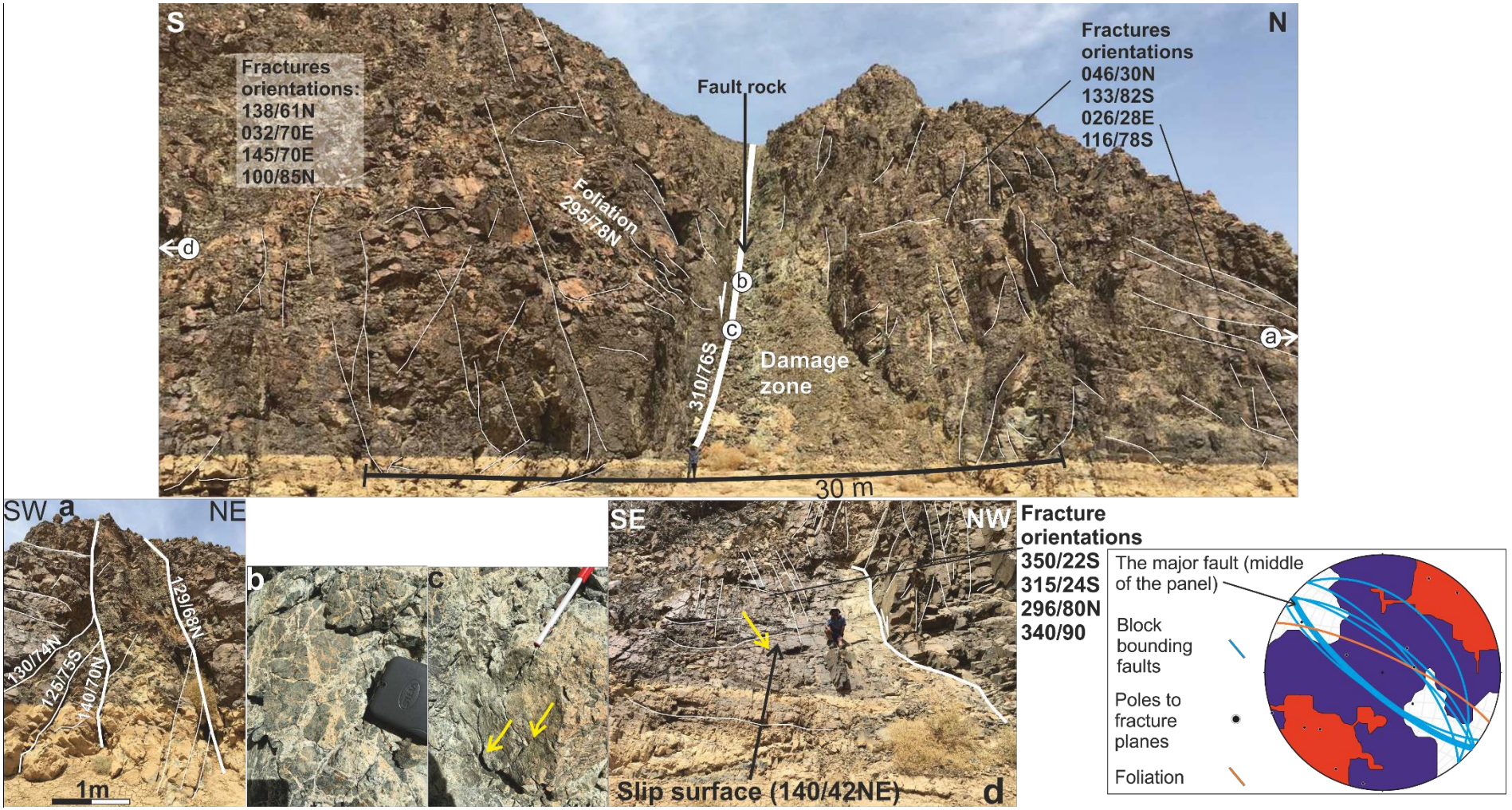

Figure 4.16: Panel 6 interpretation showing a 3-4 metre thick south-dipping fault. Note the existence of metre-scale lens-shaped blocks (a), fault rock (b) and slip surfaces (yellow arrows in c-d). The stereonet at the bottom right shows the structural orientations.

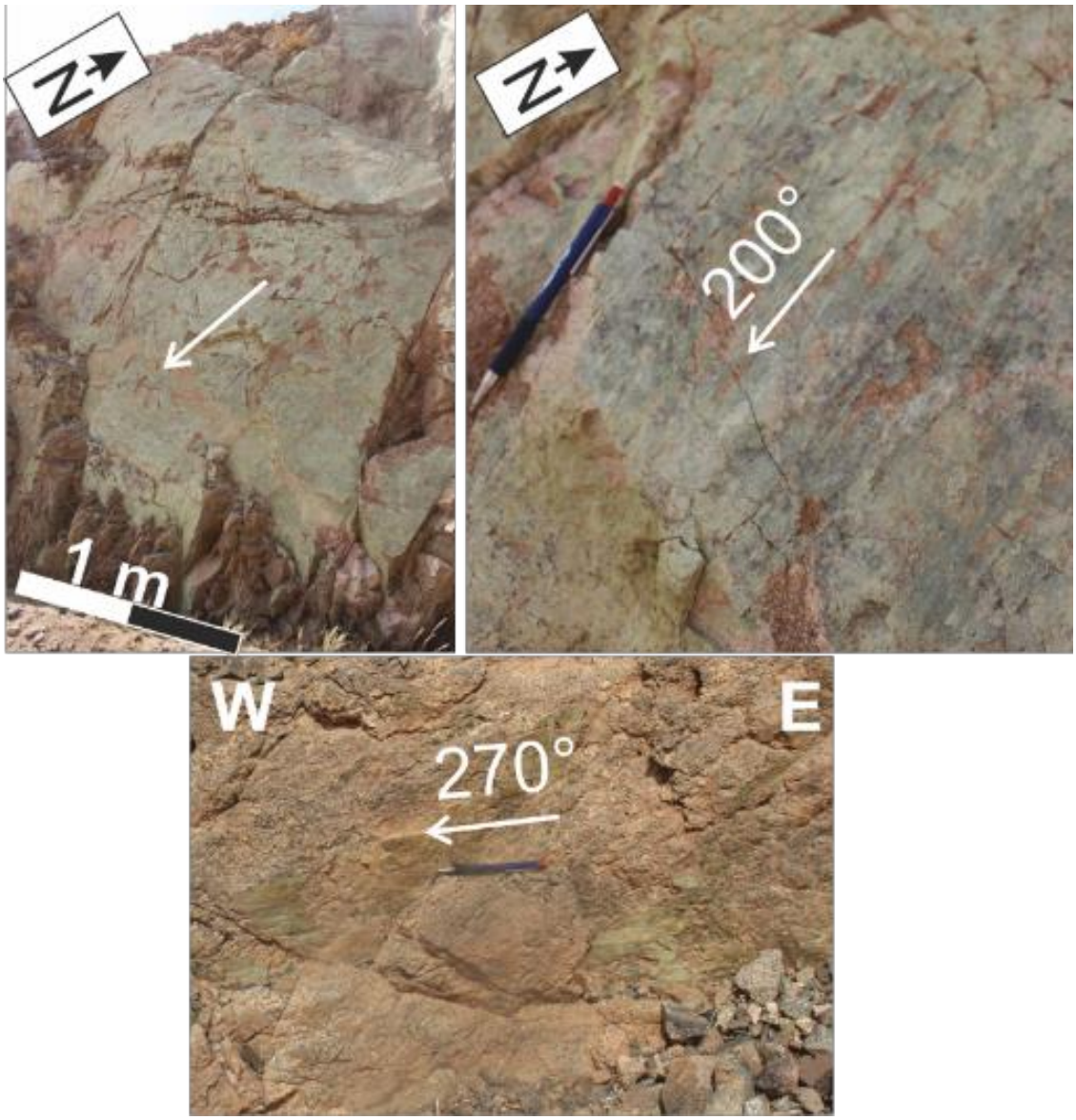

Figure 4.17: Examples of slip surfaces from the southeastern part of the SEF (28°11'24.12"N, 35°25'49.90"E). The white arrows and bearings represent the direction of slip of the removed rock.

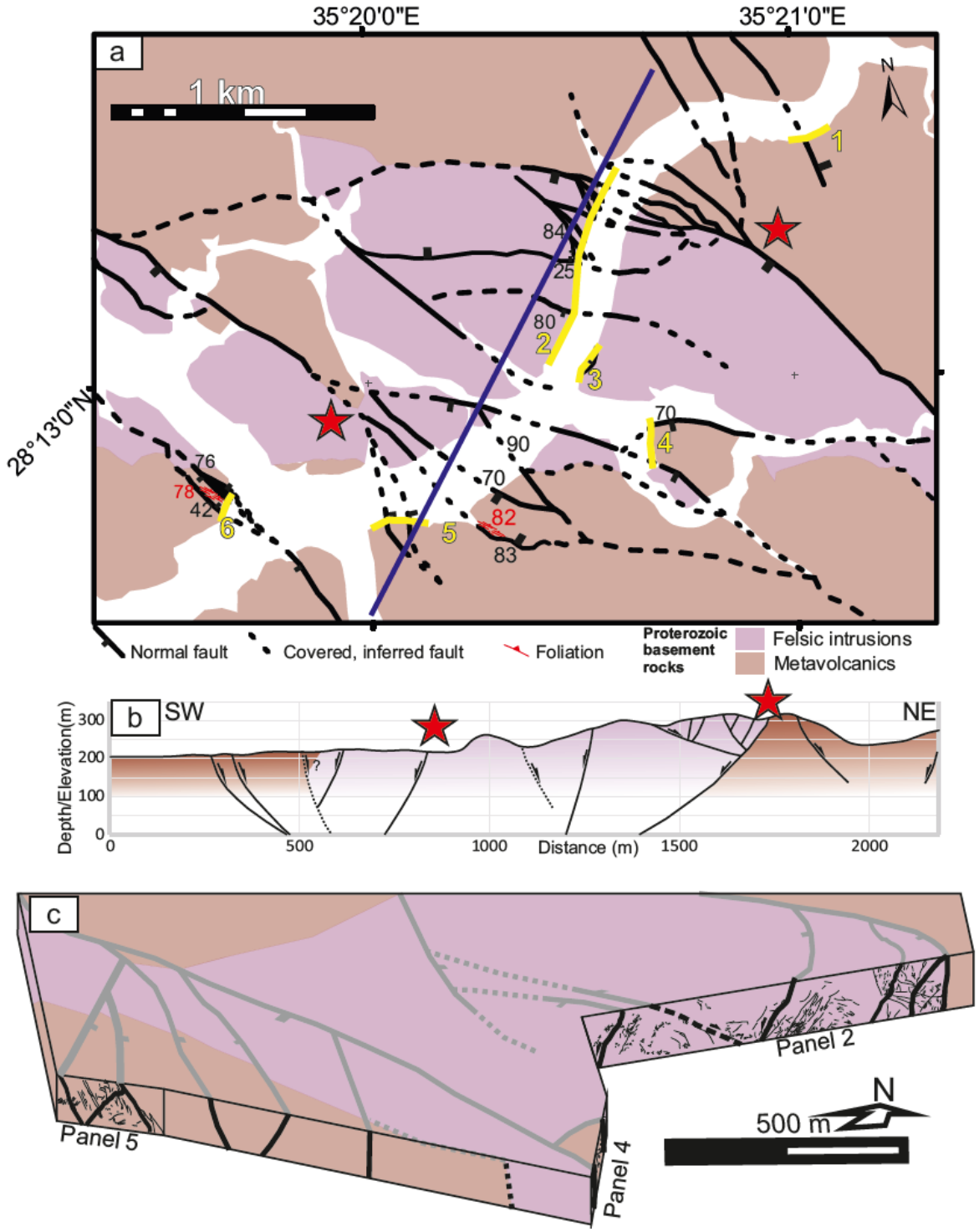

Figure 4.18: (a) A detailed structural map of the SEF at Wadi Aynunah, showing the complexity of this zone (solid lines are mapped faults and dashed lines are inferred and uncertain faults). (b) A simplified cross-section along the purple line in (a). (c) A 3D view of the fault zone constructed to show its complexity. The red stars denote the two zones of brittle deformation bounding the granitic block. Note the interpretations of panels 2 (Figure 4.11), 4 (Figure 4.14) and 5 (Figure 4.15).

4.4.1.2 ShF-AyG-AdG structures

Fractures close to, and in the footwall block of, the ShF near the town of Sharma have orientations ranging between N-S and NNE-SSW, dipping both towards the east and west (Figure 4.7). The shear fractures, albeit few in number (4 measurements), however, indicate displacement towards the NW and SW. The kinematic indicators on the fracture surfaces are in agreement with normal sense of displacement (Figures 4.7 and 4.19).

Approximately 2 km NE of the Adaffa Graben (AdG) and along the pre-existing Proterozoic basement structure that strikes E-W, the shear fractures are aligned with this major fault (i.e. E-W) and dip mostly towards the north (Figures 4.7b and 4.20). The kinematic indicators suggest normal to slightly oblique (dextral) sense of displacement. The oblique sense of motion is deduced from kinematic indicators from E-W to NW-SE oriented shear fractures located just south of this large structure (Figures 4.7b).

At the eastern boundary of the Aynunah Graben (AyG), fractures sets with orientations varying from NW-NNW to NE-NNE were measured (Figures 4.7b and 4.21). However, the shearing is rather focussed on the NW/NNW-oriented fractures as indicated by slickenlines on their surfaces (Figure 4.21). These kinematic indicators suggest normal-to-oblique (~NW) sense of displacement given the orientation of the fractures (Figure 4.7b).

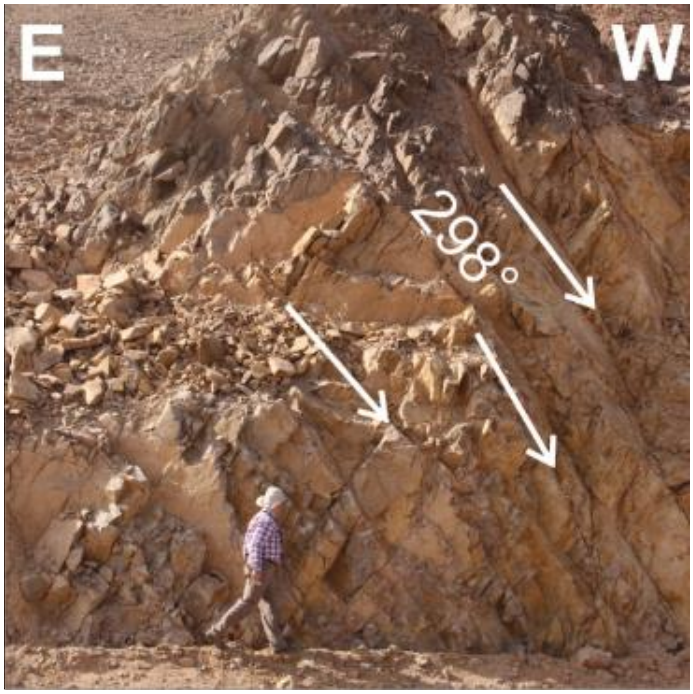

Figure 4.19: Overview outcrop photograph of the slip surfaces at the footwall of Sharma Fault (ShF; 28° 3'0.40"N, 35°15'50.22"E). The white arrows and bearings represent the direction of slip of the downthrown rock.

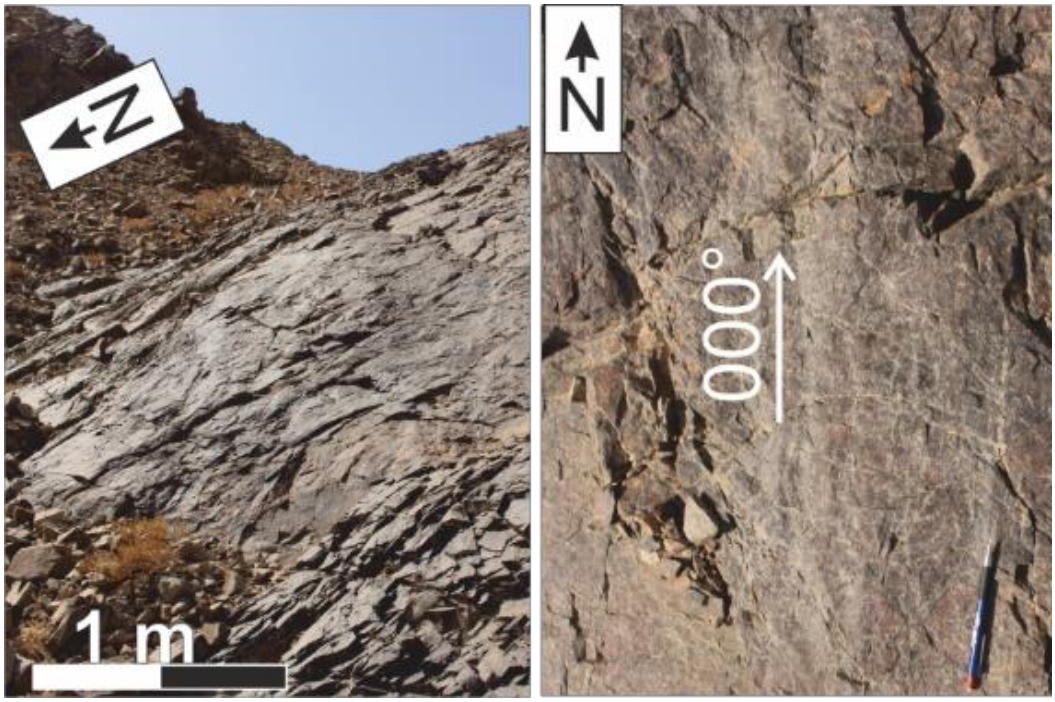

Figure 4.20: Examples of a fault surface approximately ~1 km northeast of Adaffa Graben (AdG; 28° 4'19.30"N, 35°18'51.05"E). (Left) A fault surface dipping to the north. (Right) Striations along the surface indicate normal sense of slip of footwall rock towards the north. General slip direction is indicated by the white arrow.

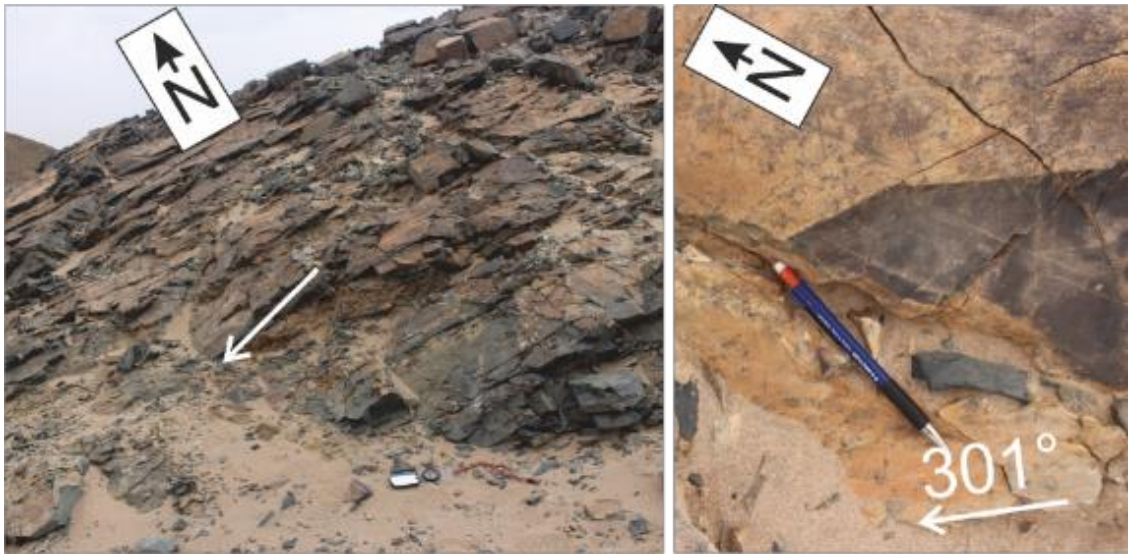

Figure 4.21: Examples of faulting along the eastern boundary of Aynunah Graben (AyG; 28° 6'34.40"N, 35°16'5.02"E). General slip directions are indicated by the white arrows. (Left) Fractures and slip surfaces dipping mostly to the west. (Right) Striations that indicate highly oblique to normal sense of displacement.

4.4.2 Principal paleo-stress orientations

Since the study area is mostly within basement rock domain where no dateable stratigraphy or volcanics exist, using the structural measurements to invert for paleo-stress evolution is not possible. However, the overall time-integrated paleo-stress orientations at the different locations of the study area may be inferred by analysing the orientations and directions fractures and slip indicators. For the purpose of comparing and contrasting the paleo-stress estimates at the main structures in the study area with each other and with the regional paleo-stress directions (as per the relevant literature), the study area is divided into two main areas: JZF-SEF and the ShF-AyG-AdG.

4.4.2.1 JZF-SEF

Along the JZF-SEF strike, the fracture orientations vary significantly (Figure 4.7b). Close to the northwestern end of the JZF, the joints have a mean orientation of ~ 303°/84°N and the mean strike here is parallel to the trend of the fault (Figure 4.22). As no shear fractures were measured in this part of the fault, it is assumed that the fractures have accommodated displacement normal to the strike

of their planes. Provided that this assumption holds, the join orientations indicate a semi-vertical σ1 direction, a SE/NW-oriented semi-horizontal σ2 and a SW/NE-oriented semi-horizontal σ3 (Figure 4.22).

Close to the southeastern end of the JZF and the northwestern end of the SEF, however, the shear fractures have a mean vector orientation of ~275°/71°N in stark contrast to the joint orientations at the northwestern part of the JZF (Figure 4.22). Furthermore, the slip directions indicate highly oblique to dextral sense of displacement towards the east and west. However, combining the shear fracture orientations and the slip senses and directions, the directions of σ1, σ2 and σ3 are similar to those at the northwestern part of the JZF (i.e. semi-vertical, semi-horizontal SE/NW-oriented and SW/NE-oriented, respectively; Figure 4.22).

At the Wadi Aynunah section of the SEF, more scatter characterises the fracture orientations (Figure 4.7b). Few shear slip measurements were available with strike-slip displacement along ~E-W fracture planes, but they are not enough to predict the causal stress orientation. At the southeastern part of the SEF, however, more slip measurements were collected along shear fractures that have a mean orientation of ~071°/73°S (Figure 4.22). The dominant slip along these shear fractures is directed towards the SW suggesting highly oblique to normal sense of movement. These observations are indicative a semi-vertical σ1 direction, an E/W-oriented semi-horizontal σ2 and a S/N-oriented semi-horizontal σ3 (Figure 4.22).

To sum up, the deduced principal stress orientations along the strike of the JZF-SEF are all similar in that σ1 is always semi-vertical, which suggests extensional to trans-tensional tectonics (Figure 4.22). The orientations of the semi-horizontal σ2 and σ3 change along the strike of the JZF-SEF. Their change imply that the maximum horizontal extension change from approximately N-S at the southeastern end of the SEF, to NNE/SSW at the intersection of the SEF and JZF and finally to a NE-SW at the northeastern end of the JZF (Figure 4.22).

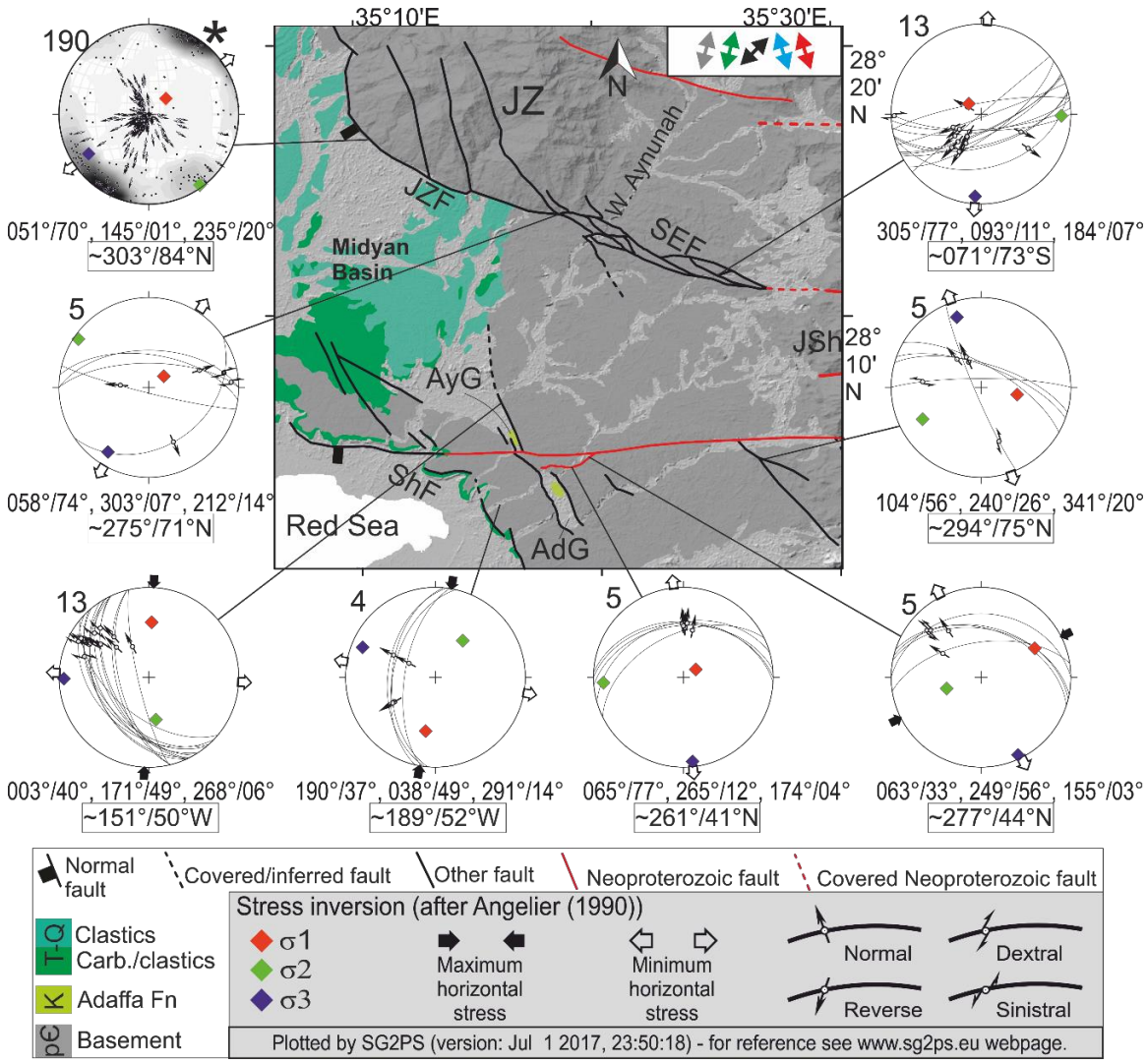

Figure 4.22: Paleo-stress analysis of shear fractures using SG2PS (Sasvári and Baharev, 2014). σ1, σ2 and σ3 orientations are indicated below each stereonet, respectively. The mean vectors of the shear fractures are shown in the rectangles below each stereonet. The number of data points is indicated at the top left of each stereonet. The asterisks * indicates where the joints were used for the stress inversion assuming perfectly normal slip as no slip indicators were measured (joint poles plotted and contoured using Stereonet 10.0 (Allmendinger et al., 2011; Cardozo and Allmendinger, 2013)). The double-headed coloured arrows (top right of map) indicate the regional horizontal extension: red: Late Neoproterozoic (Johnson et al., 2012); blue: Late Cretaceous (Bojar et al., 2002; Bosworth et al., 2005); black: Miocene (Bojar et al., 2002; Bosworth et al., 2005); green: Plio-Pleistocene (Bosworth and Strecker, 1997); grey: Present-day (ArRajehi et al., 2010). JZ: Jabal az Zuhd mountain; JZF: Jabal az Zuhd Fault; SEF: South-Eastern Fault; JSh: Jabal ash Shati; AyG: Aynunah Graben; AdG: Adaffa Graben; ShF: Sharma Fault.

4.4.2.2 ShF-AyG-AdG

At the southern part of the study area (ShF, AyG and AdG), the orientations of the shear fractures differ from one location to the other (Figure 4.22). Approximately 1 km to the NE of the ShF, the shear fractures have a mean vector orientation of ~189°/52°W, which is slightly oblique to the NNW/SSE orientation of the ShF. The slip directions along the shear fractures are towards the NW and SW and the kinematic indicators suggest plunging NNE/SSW-oriented σ1 and NE-SW-oriented σ2, and a semi-horizontal σ3 that is oriented WNW/ESE (Figure 4.22).

The fault to the east of the AyG, where the shear fracture orientations were measured, is parallel to the ShF (Figure 4.22). The shear fractures here are semi-parallel to the boundary of the graben with a mean vector orientation of ~151°/50°W. The slip vectors, however, are highly oblique-to-normal with respect to the fracture planes with slip directed towards the NW. Therefore, oblique principal stress orientations are deduced with plunging N/S-oriented σ1 and σ2, and an E/W-oriented semi-horizontal σ3 (Figure 4.22).

Approximately 1 km to the NE of the AdG, the shear fractures have ~E-W orientations (mean vector: ~261°/41°N) that are starkly different to those of the ShF and AyG fractures (Figure 4.22). Such different orientations are likely related to the E-W pre-existing basement structure to which the fractures are semi-parallel. The slip senses and directions indicate normal displacement with a semi-vertical σ1, an E/W-oriented near-horizontal σ2 and a N/S-oriented horizontal σ3 (Figure 4.22). Further to the east (ca. 1 km from this location), the shear fractures are also oriented in an overall E-W trend (mean vector: ~277°/44°N). However, the slip directions are more oblique and indicate a highly oblique ENE/WSW-oriented σ1, a near-vertical σ2 and a SSE/NNW-oriented horizontal σ3 (Figure 4.22).

In addition to the aforementioned locations, slip measurements were also taken from the area to the SW of the Jabal ash Shati (JSh; Figure 4.22). At this location, variable shear fracture orientations are noted with a mean vector of ~294°/75°N. The slip directions are highly oblique-to-normal with respect to the fracture planes. These suggest an oblique ESE/WNW-oriented σ1, a less oblique WSW/ENE-oriented σ2 and a near-horizontal NNW/SSW-oriented σ3 (Figure 4.22).

The above stress analysis indicates that both the footwall block of the ShF and the eastern boundary of the AyG have experienced E-W to WSW-ENE maximum horizontal extension but the relationship between the principal stress orientations and the fracture planes suggest trans-tension tectonics (Figure 4.22).On the other hand, the fracture and principal stress orientations from the area to the east and NE of the AdG indicate N-S to NNW-SSE extension and trans-tension.

4.5 Discussion and conclusions

As opposed to the Midyan Basin bounding fault (i.e. the JZF), brittle deformation to the southeast at the SEF is spread across a zone that is approximately 2.5 km-wide at the Wadi Aynunah Valley with strain localisation occurring at several small faults (Figures 4.7 and 4.23). The contrast in deformation styles is also indicated by the variation in stress orientations. That is, the JZF developed in response to NE-SW extension whereas the SEF (as deduced from the shear fractures at its southeastern part) experienced ~N-S extension oblique to the mostly ENE/WSW-oriented fractures (Figure 4.22). With respect to the JZF fault, the principal stress orientations are aligned with the stress regime that characterised the Oligo-Miocene Red Sea rifting (black double-headed arrow in Figure 4.22; Bojar et al., 2002; Bosworth et al., 2005 *and references therein*; Tubbs et al., 2014).

Compared to the regional orientations of the paleo-stress, the SEF N-S maximum horizontal extension is only semi-parallel to the Middle Miocene to Present extension directions (green and grey double-headed arrows in Figure 4.22; Bosworth and Strecker, 1997; ArRajehi et al., 2010). However, a causal link between the slip indicators and these stress regimes is unlikely given that most of the deformation that was associated with the Gulf of Aqaba tectonics is focussed near the gulf (e.g. Bosworth et al., 2017) and that the SEF is approximately ~70 km-away from the gulf.

The Neoproterozoic and Late Cretaceous regional paleo-stress orientations (red and blue double-headed arrows in Figure 4.22; Bojar et al., 2002; Bosworth et al., 2005; Johnson et al., 2012) are only slightly aligned with the stress directions estimate from the southeastern SEF. The fracture orientations, however, are perpendicular to both the Neoproterozoic and Late Cretaceous maximum

horizontal extension directions. Furthermore, it can be seen that maximum horizontal extension rotate along the strike of the JZF-SEF until $\sigma 3$ becomes perpendicular to the JZF. If this along-strike variation resulted from the influence of the Oligo-Miocene extensional tectonics (i.e. becoming more dominant towards the JZF) then it is likely that the southeastern part of the SEF formed as a result of a NNW/SSE-oriented maximum horizontal stress during the Neoproterozoic or Late Cretaceous (resulting in the ENE/WSW-striking fractures) and was later affected by the Oligo-Miocene NE-SW extension. In this case, the paleo-stress orientation represents a time-integrated estimate that encompasses the small effect of the Oligo-Miocene NE-SW extension and the more dominant effect of the older NNW-SSE extension (or trans-tension) in a way that no large-scale faulting at the SEF occurred during the Red Sea rifting. During the Oligo-Miocene, it is more likely that this zone of brittle deformation was positioned at an accommodation zone (relay ramp), which makes it possible that it accommodated a small part of the strain (Fossen and Rotevatn, 2016) between the JZF and the ShF, both of which were active during this period (Hughes et al., 1999; Tubbs et al., 2014).

Considering that the JZF was active during the Oligo-Miocene, and that the SEF is oriented parallel to the JZF, the SEF orientation is deemed optimal to accommodate extensional strain during the Red Sea rifting. Therefore, to further test the interpretation that the SEF was not significantly activated (i.e. did not accommodate km-scale displacement), the temporal relationship of the fault zone needs to be assessed. This will be addressed in Chapter 5 where the temporal framework for the structural geometries of the SEF and JZF is investigated using low-temperature thermochronology.

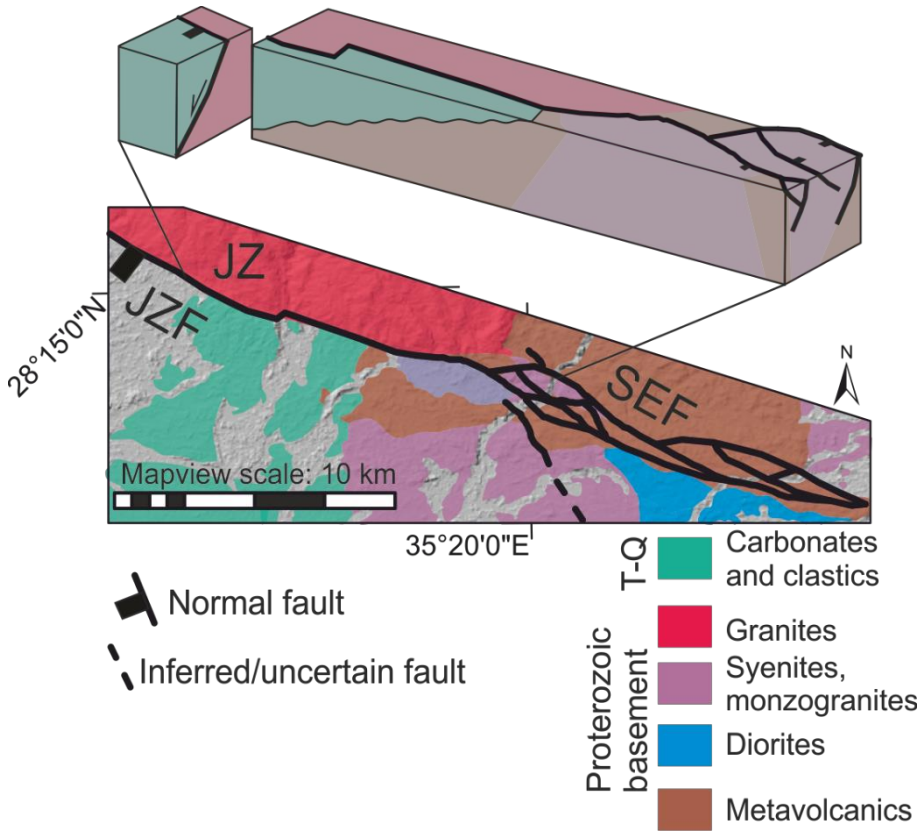

Figure 4.23: A simplified 3D view of the SEF and JZF highlighting the along-strike variation in structural styles from localised Oligo-Miocene normal faulting at the JZF to more distributed deformation (localisation at smaller faults) at the SEF.

The principal stress orientations deduced from the footwall block of the ShF and the eastern boundary of the AyG indicate mostly E-W extension, which is not aligned with any of the regional stress regimes since the Neoproterozoic (e.g. Bosworth and Strecker, 1997; Bojar et al., 2002; ArRajehi et al., 2010; Johnson et al., 2012; Figure 4.22). Conversely, the orientation of the ShF and the eastern boundary of the AyG (NNW-SSE) is semi-perpendicular to the regional maximum horizontal extension that resulted in the Red Sea rifting during the Oligo-Miocene (Bosworth et al., 2005). However, the ShF is shown to have been active as indicated by the faulted Miocene carbonates (Hughes et al., 1999). Therefore, the deduced stress orientations from the footwall of the ShF is unlikely to be representative of a regional stress during that time, which might be caused by the low number of data points used in the stress inversion (i.e. 4; Figure 4.22).

At the eastern bounding fault of the AyG, the NW-directed slip indicators, the ESE/WNW-oriented maximum horizontal extension and the highly oblique N/S-

oriented σ1 suggest that this location experienced trans-tension (Figure 4.22). The maximum horizontal extension direction, however, is not aligned with the Oligo-Miocene extension (e.g. Bosworth et al., 2005). It is concluded here that the deduced ESE-WNW extension was local to this location and that the stress orientations are rather indicative of transfer tectonics between the ShF and the JZF, which is compatible with these fractures being formed during the Oligo-Miocene. Upon more strain localisation, the eastern boundary of the AyG might have formed a transfer fault that links the ShF with the JZF similar, for instance, to the N-S Nezzazat Fault along the eastern Gulf of Suez, which links the Hammam Faraun Fault with the faults of the Gebel Abu Durba and Gebel Araba blocks (Sharp et al., 2000) or the hard linkage along the East Ifal Fault (Koeshidayatullah et al., 2016).

The Upper Cretaceous pre-rift Adaffa formation has been identified at AdG and AyG (Hughes et al., 1999). In the basement domain west and south of Quseir at the Egyptian side, which when restored to pre-rift state would be located within ~100 km southwest of AdG and AyG, Bojar et al. (2002) argued for Cretaceous strike-slip deformation with an ENE-WSW oriented σ1 and a NNW-SSE oriented σ3 (blue double-headed arrow in Figure 4.22). The kinematic indicators to the east of AdG (and even further to the east at the southwestern side of JSh) show similar stress orientations to those in the Egyptian side, which suggests that this graben was tectonically active during the Late Cretaceous.

Chapter 5 Tectono-geomorphic evolution of the northeastern Red Sea margin during and after rifting: insights from low-temperature thermochronology

This chapter assesses the exhumation history across the area to the southeast of the Midyan Basin. Interpretations made here are assessed against and incorporated with fault-scale interpretations of the same study area (Chapter 4) and larger-scale uplift estimates of the whole northeastern Red Sea margin (Chapter 3).

5.1 Introduction

The spatial extent and distribution of syn-rift-related uplift and erosion are important aspects of extensional tectonics, the understanding of which can give insights on the tectonic and sedimentary aspects of the basins (e.g. Tinker et al., 2008). Furthermore, sub-aerial post-rift uplift and erosion are critical in the evolution of passive margins even if the majority of the tectonic strain has migrated towards the oceanic basin.

Low-temperature thermochronology has been widely used to evaluate the thermal evolution across normal faults (e.g. Wells et al., 2000; Stockli, 2005; Hendriks et al., 2010) and passive margins (e.g. Gallagher and Brown, 1999). Apatite fission track analysis (AFTA) and apatite (U-Th)/He analysis (AHe) are two of the most used low-temperature thermochronometers to study the thermal evolution of the upper crustal regime as they are sensitive to temperatures between ~125 to 40°C (Lisker et al., 2009) that correspond to depths of ~5 to 1.6 km when using a geothermal gradient of 25°C/km.

The southeastern part of the Midyan Peninsula is mainly composed of Proterozoic basement rocks, with a covering of Paleozoic clastics further to the northeast;

whereas Mesozoic-Cenozoic clastics, carbonates and evaporites crop out in the western and southeastern sides (Clark, 1987; Hughes et al., 1999). Southeast of the Midyan Basin the South-Eastern Fault (SEF), the Jabal az Zuhd Fault (JZF) and the Sharma Fault (ShF; introduced in Chapter 4) form a fault-bounded terrace within the basement domain. Geomorphologically, this area is characterised by low relief, and the elevation increases gradually from the coastline towards the east and northeast. Approximately 30-40 km towards the northeast, the low-elevation coastal area gives way to a west-facing escarpment and a plateau. The escarpment has a topographic relief of ~1,000 m and the plateau surface slopes gently to the east (Figure 5.1).

Low-temperature thermochronology (apatite (U-Th)/He) shows that the Jabal az Zuhd footwall block experienced a cooling signal during the Early Miocene (~23 Ma) indicative of exhumation (Stockli and Bosworth, 2019; Figure 5.1a). Similarly, zircon and apatite (U-Th)/He data from Jabal Dabbagh Mountain (approximately 65 km SSE of Jabal az Zuhd block) indicate a pronounced exhumation driven by more than 6 km of throw at the coastal fault during the same period (Stockli and Bosworth, 2019). Moreover, at the hangingwall block of ShF, syn-rift carbonate rocks attest to the activity of this fault during the Early Miocene (Hughes et al., 1999; Tubbs et al., 2014).

The southeastern part of the Midyan Peninsula is an ideal location to assess rift-related and post-rift geomorphic evolution and evaluate its tectonic history given the aforementioned neighbouring constrained areas (Figure 5.1a). The effect of rifting on the geomorphology and the post-rift evolution can be compared to the different models of margin evolution (Gallagher et al., 1998). However, the lack of dateable sedimentary cover or extrusive volcanics, particularly across the SEF, inhibits determining the Cenozoic tectonics extent and the post-rift geomorphic evolution. In Chapter 4, deformation at the SEF was shown to be localised at several small structures compared to the JZF and the structural measurements do not suggest a large-scale reactivation during the Miocene but a temporal framework for this spatial interpretation is needed.

In this chapter, the question of how the geomorphic and structural state of the northeastern Red Sea margin evolved is addressed. Two models that could

potentially explain the geomorphic state of the margin are put forward here to be tested: a) faulting at the SEF occurred during the Red Sea rifting, and erosion and the formation of the escarpment occurred by scarp retreat or a stripping down of stratigraphy with a pinned drainage divide; b) a protracted period of tectonic quiescence with no sedimentation and the formation of the escarpment as depicted in a downwarp model. Low-temperature thermochronometry, building on the structural synthesis in Chapter 4, is used here to address the aforementioned question and test the proposed models, focussing on two aspects of the margin:

1) The activity of the SEF and the distribution of exhumation of both the hangingwall and footwall blocks are assessed in light of the structural interpretation presented in Chapter 4 by applying AFTA and AHe techniques to assess the thermal history of the basement rocks across the fault zone. These techniques can resolve exhumation-driven cooling greater than 1.6 km (assuming 25 °C/km geothermal gradient), and therefore provide valuable insight into whether a measurable displacement was accommodated by the SEF during the Red Sea rifting. Lesser exhumation-driven cooling (e.g. small fault displacement) would not be recorded but may, nonetheless, have occurred.

2) The geomorphic evolution of the margin is considered through the presentation of a transect trending perpendicular to the margin that traverses the coastal area, escarpment and plateau in order to assess the exhumation distribution across the whole margin, and to relate that to models of escarpment evolution.

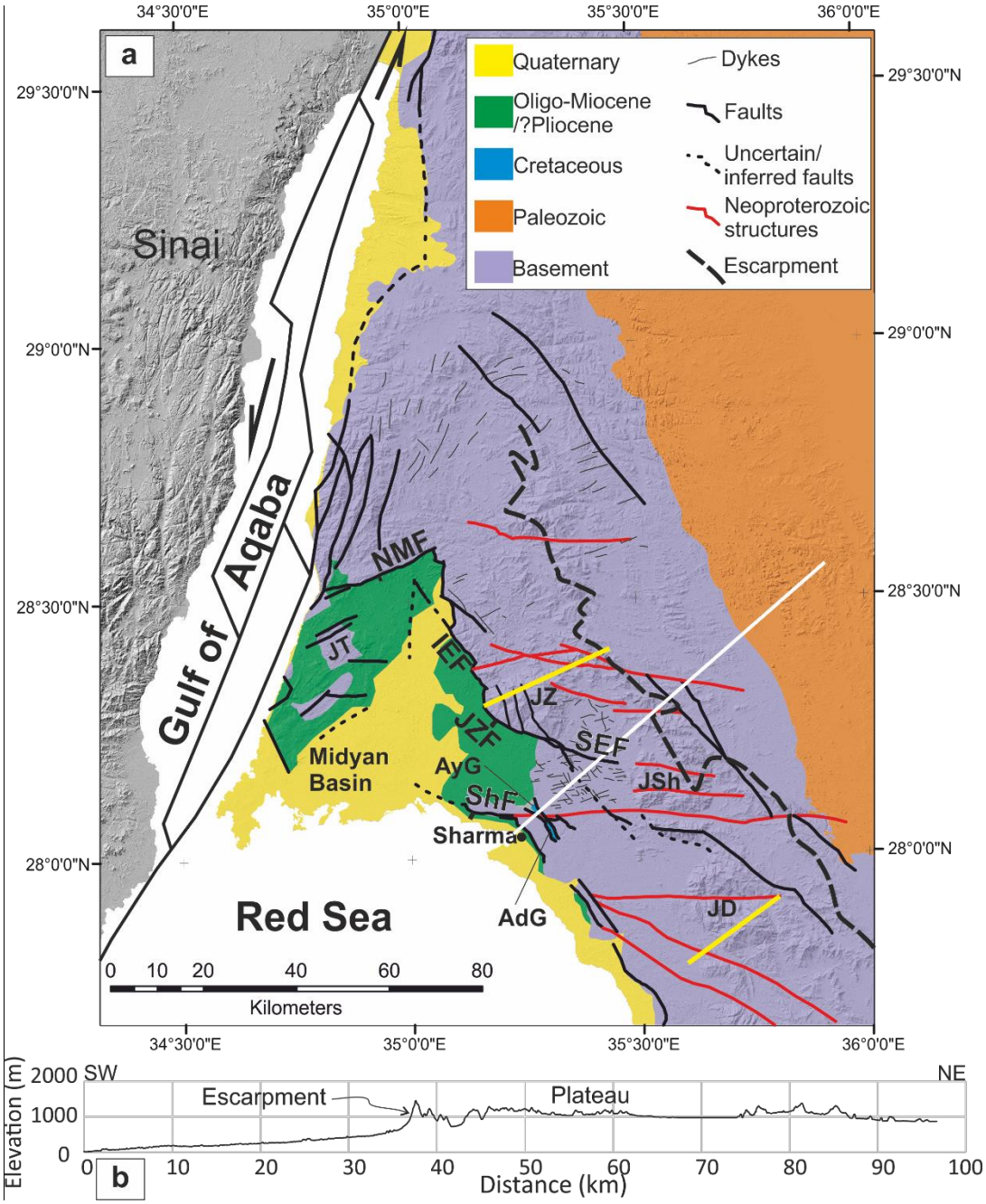

Figure 5.1: (a) A simplified geological map of the Midyan Peninsula overlaid on a hill shaded DEM (Modified from Clark (1987)). The white line is the position of (b). The two yellow lines are approximate positions of the apatite and zircon (U-Th)/He transects presented in Stockli and Bosworth (2019). NMF: Northern Midyan Fault; IEF: Ifal East Fault; JZF: Jabal az Zuhd Fault; JZ: Jabal az Zuhd mountain; SEF: South-Eastern Fault; JSh: Jabal ash Shati mountain; JD: Jabal Dabbagh mountain; ShF: Sharma Fault; AdG: Adaffa Graben; AyG: Aynunah Graben. (b) A topographic cross-section showing the main geomorphic elements of southeastern Midyan (see line of section on (a).

5.2 Low-temperature thermochronology

Thermochronology refers the use of radioactive parent and radiogenic daughter isotopes and crystallographic damage tracks (caused by the fission decay process in, e.g., apatite and zircon grains), which are time and temperature dependent, to predict the geological thermal history experienced by the rocks (Lisker et al., 2009). Different thermochronometric systems related to different mineral types are suitable for deciphering the thermal history over particular temperature ranges, spanning temperatures from 40 to 800°C (Figure 5.2). In this section, the theory behind the application of low-temperature thermochronology is reviewed.

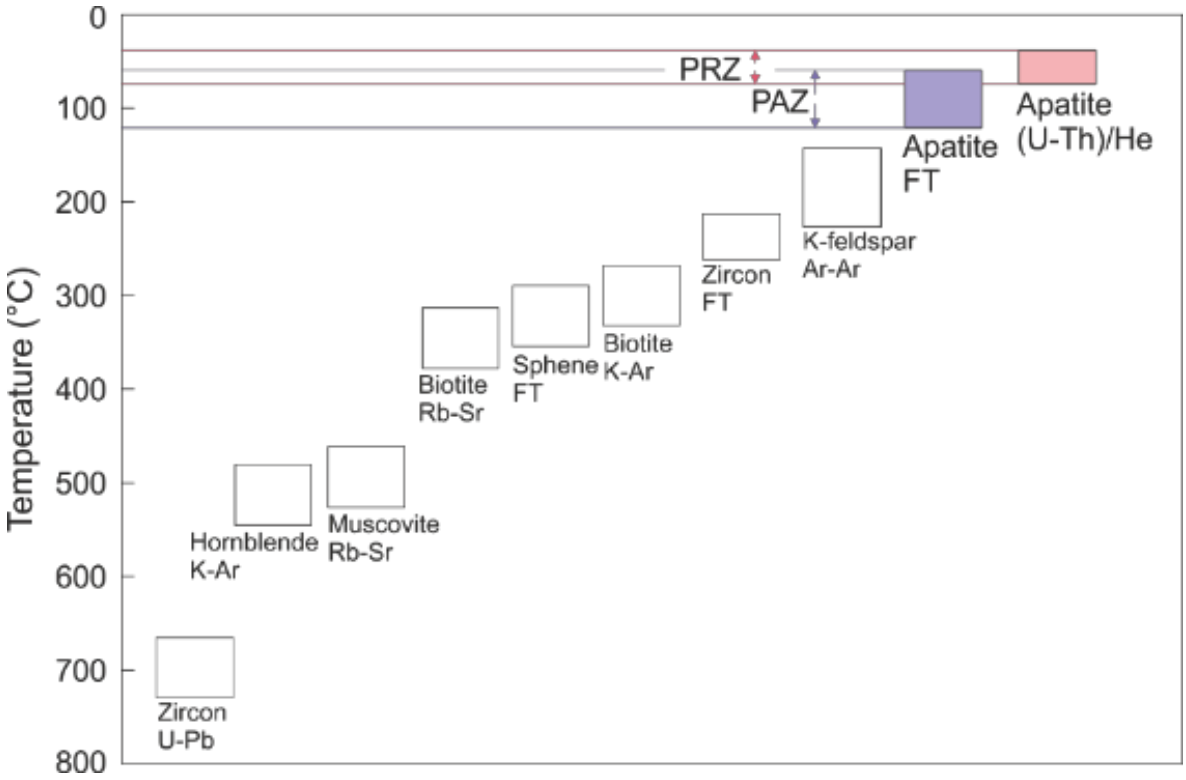

Figure 5.2: Nominal temperature ranges for different thermochronometric systems (Modified from Gallagher and Brown (1999) and Peyton and Carrapa (2013)). The apatite FT and (U-Th)/He (purple and pink boxes, respectively) represent the most suitable of these systems for quantifying thermal evolution of the uppermost continental crust. PAZ: apatite FT partial annealing zone; PRZ: apatite (U-Th)/He partial retention zone (see text for explanation).

The focus in this section is on the thermochronometric systems that are sensitive to temperatures of the uppermost continental crust. Apatite fission tracks (AFT)

and apatite uranium-thorium/helium ((U-Th)/He) or AHe) analyses are chief among the systems used to assess the evolution of rocks in the upper crustal ranges due to their sensitivity to relatively low temperatures between ~40-125°C (Lisker et al., 2009; Figure 5.2).

Radioactive decay of ^{238}U occurs due to the instability of its heavy nucleus irrespective of the host mineral in the rock. The decay process occurs most frequently by releasing α-particles (i.e. He nuclei) and one ^{206}Pb atom (Friedlander et al., 1981; Donelick et al., 2005; Vermeesch, 2019 *and references therein*). The amount of radiogenic He and radioactive U are the components that are input into calculating (U-Th)/He ages. Comparatively, a significantly smaller number of the ^{238}U nuclei decays by nuclear fission in which the nuclei split to more stable components leaving tracks where the process occurs (Friedlander et al., 1981). In this case, the radiogenic products are the fission tracks, and their density within the host grain, along with the U content, is used to calculate FT ages (Vermeesch, 2019).

Unlike other geochronological techniques that measure the absolute age of rocks, low-temperature thermochronology utilises the concept of closure temperature (T_c) higher than which the thermochronological age is zero because the radiogenic daughter is lost at such high temperatures. At temperatures lower than T_c, however, the rock, theoretically, retains radiogenic daughters in the form of gas isotopes (helium) or traces of crystallographic damage (fission tracks), and the calculated ages are related to when the rock cooled through this temperature. Since each thermochronometer is sensitive to a range of temperatures, different T_c values are associated with the AFT and apatite (U-Th)/He systems (Figure 5.2).

The use of low-temperature thermochronology has been shown to be a valid technique to date movements across faults in extensional tectonic settings (e.g. Ghebreab et al., 2002; Stockli, 2005; Mortimer et al., 2016). If a normal fault is associated with significant displacement and footwall uplift/erosion, the cooling ages of AFT and/or AHe can be used to estimate the age (or at least the minimum time) at which faulting started (e.g. Stockli and Bosworth, 2019). This is done by determining at what point in time the slope of the relationship between age and

elevation changes and, by inference, cooling becomes rapid (Fitzgerald and Malusà, 2019).

Moreover, the evolution of passive margins that are characterised by an escarpment separating a low coastal area and a high plateau can be assessed by analysing how the thermochronometric data vary across the margin on the basis that cooling can be driven by erosion (e.g. Gallagher and Brown, 1999). The three end-member models of passive margin (and escarpment) evolution, explained in the introduction to this chapter, have characteristic signatures on the age-vs-distance across the margin (Gallagher et al., 1998; Figure 5.3). These different signatures are a reflection of the variation of the amount of erosion and exhumation, which are assumed to have the main control on the thermochronometric age, across the margin.

In the downwarp model, no initial fault scarp is implied and the maximum erosion occurs closer to the escarpment than to the coast (Figure 5.3a). In this model, the FT ages are expected to all be older than the age of rifting. Old ages are expected near the coast, becoming progressively younger towards the escarpment before becoming rapidly older across the escarpment and at the plateau.

In the scarp retreat model, an initial fault scarp forms during rifting and the maximum erosion occurs at the immediate footwall block of a controlling fault rather than near the escarpment (Figure 5.3b). With more erosion, the drainage divide migrates inland along with the escarpment that initiated as a fault scarp. The ages near the margin bounding fault are youngest and represent the age of rifting (or younger), and become older towards the escarpment and the plateau.

In the pinned divide model, an initial fault scarp forms during rifting and the maximum erosion occurs also at the fault footwall but the erosion occurs through strata stripping on either side of the escarpment (Figure 5.3c). In this model, the drainage divide does not shift spatially with time, but is rather fixed to a pre-rift position that is characterised by minimal erosion. The age behaviour is similar to that of the scarp retreat model except that the ages at the escarpment are the oldest and they become gradually younger at the plateau towards the interior.

It is important to note, however, that the mechanisms of preserving the radiogenic daughters of the two systems are different, and, therefore, it is crucial to be cautious when integrating their ages. For example, several studies have shown that AHe ages can be older than AFT ages for the same rocks even though the latter is sensitive to a higher range of temperatures, which falls short of explaining the thermal history if factors other than temperature are not taken into consideration in interpreting the data (e.g. Green and Duddy, 2018 *and references therein*).

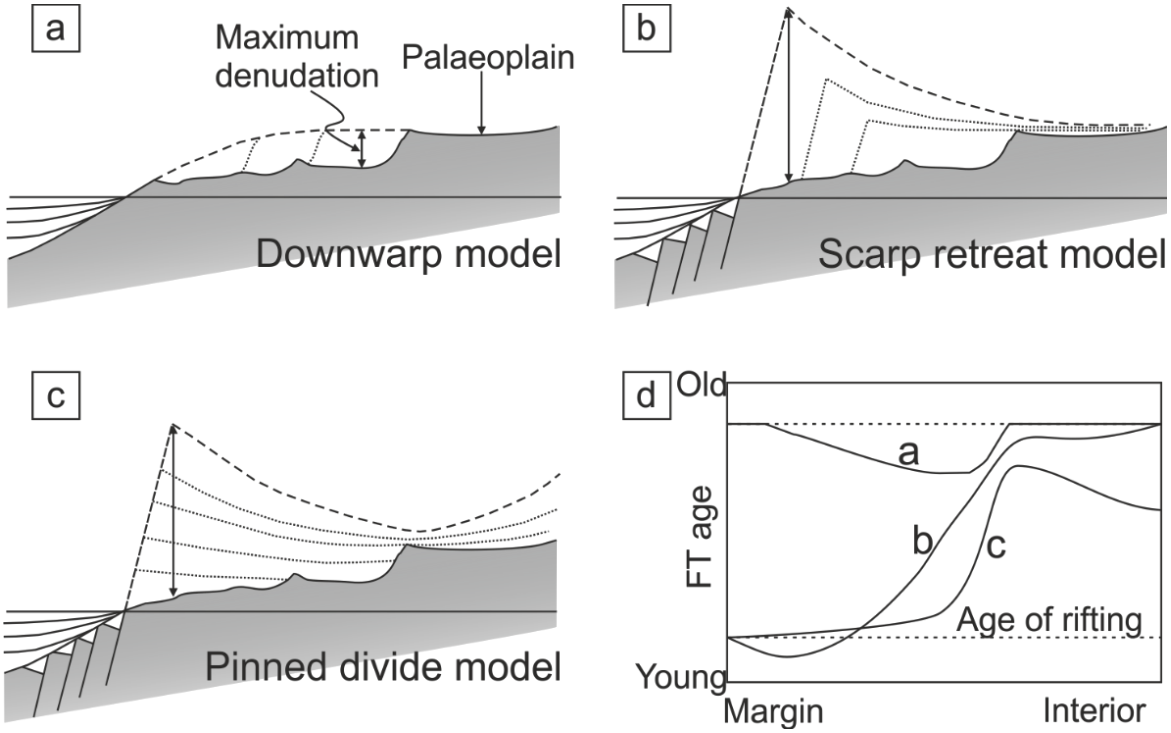

Figure 5.3: (a-c) Cartoon cross-sectional view of the end-member models of passive margin escarpment evolution (Modified from Gallagher et al. (1998)). (d) The low-temperature thermochronological age-vs-distance plots corresponding to the end-member models. Note that even for the same topography, the expected behaviour of the FT ages across the margin for each model is different.

5.2.1 Apatite fission track analysis (AFTA)

Natural radioactivity of ^{238}U causes fission of the nuclei resulting in a discontinuity (track) with a certain length at a rate that depends on the uranium concentration (Donelick et al., 2005). As temperature increases, the tracks become partially annealed (i.e. partially closed) reducing their length until a maximum temperature

is reached when the existing track lengths stop changing (Braun et al., 2006). After the maximum paleo-temperature is reached, further fission creates tracks longer than the existing ones, and the distribution of the lengths along with the AFT age (computed using the density of the tracks and the uranium content) can be used to evaluate the thermal history (Braun et al., 2006).

The annealing of the fission tracks is mainly a time and temperature-dependent process. The annealing process results in the younging of cooling ages until, when annealing rate is higher than fission rate, which occurs at temperatures higher than a critical value, all tracks disappear and the thermochronological age becomes zero (Donelick et al., 2005; Reiners et al., 2005). In the case of apatite, below ~110-120^{o}C, the rate of annealing decreases in a non-linear fashion until, at ~60^{o}C and below, annealing becomes negligible to non-existent allowing fission tracks to be preserved. The range of temperatures from ~120 to 60^{o}C for apatite crystals is referred to as the Partial Annealing Zone (PAZ), and the ~120^{o}C temperature point is the closure temperature (T_c) for the AFT system (Peyton and Carrapa, 2013). Within the PAZ fission tracks can form and anneal at the same time, below it the tracks are totally annealed, and above it they are preserved even though very slow annealing rates may affect them (Gleadow and Brown, 2000).

Other factors governing the annealing process are the chemistry and the orientation of the tracks with respect to the crystal structure (Green et al., 1986; Donelick et al., 2005 *and references therein*). Chemical varieties of apatite can span a spectrum depending on the fluorine:chlorine ratio. In simple terms, higher chlorine content leads to an increased resistance to annealing and is, therefore, associated with higher closure and total annealing temperatures (Ketcham, 2005 *and references therein*). D_{par}, which is the mean long diameter of a chemically etched track parallel to the crystallographic c-axis (aka the track pit on the surface of the grain), serves as an approximate, relative, indicator of the Cl-content (Donelick et al., 2005; Peyton and Carrapa, 2013).

The use of the fission track analysis in the reconstruction of the thermal history of a sample is powered by measuring the lengths of the tracks and determining their distribution (Ketcham, 2005). This property of the technique stems from the observation that, due to annealing, young tracks are longer than old tracks. With

respect to the track length, it has been long observed that tracks that are at high angle to the apatite c-axis are shorter and anneal faster than those that are at low angle to the axis (Ketcham, 2005). Therefore, measuring the angle between the track and the c-axis provides a means into projecting the track lengths as if they were parallel to the c-axis, a particularly useful procedure when inverting to solve for the likely thermal history (Ketcham, 2005).

5.2.2 Apatite (U-Th)/He analysis (AHe)

Conceptually, Uranium (^{235}U and ^{238}U) and Thorium (^{232}Th) decay to Lead (Pb) by *α*-emission (Helium ^{4}He), the accumulation and diffusion of which are mainly temperature-dependent (Farley, 2002). The (U-Th)/He thermochronology technique utilises the retention of the radiogenic ^{4}He in the mineral crystals as a basis for studying the thermal history of the sample. Utilisation of this technique in dating the cooling of the crustal zone of relatively low temperature was first recognised by Zeitler et al. (1987).

Diffusion of ^{4}He out of the host grain increases with temperature, and total leakage occurs after exceeding the maximum temperature of a partial retention zone (PRZ; Braun et al., 2006). For apatite, the PRZ is approximately ~55-80°C but the lower temperature boundary can be as low as 40°C (Reiners et al., 2005). The PRZ encompasses the closure temperature, which depends on the mineralogy/chemistry, crystal size and rate of thermal change (Reiners et al., 2005; Braun et al., 2006; Peyton and Carrapa, 2013).

It is necessary to mention, however, that diffusion is not the only mechanism by which the amount of helium in a grain is reduced. The decay process itself results in the ejection of the *α*-particles (^{4}He), and it takes some distance for these particles to come to rest (stoppage distance; Farley et al., 1996; Ketcham, 2005). In apatite, the stoppage distance is approximately 20 microns, but varies in the range ~10-30 μm for the ejection from the different decay series (^{235}U, ^{238}U and ^{232}Th; Farley et al., 1996).

Experimental evidence has demonstrated the temperature-dependent diffusive nature of He from the standard Durango apatite crystals (Zeitler et al., 1987). However, the time aspect of slow cooling during the uplift and erosion of

continental crust introduces complexity in the understanding of the kinematics of the diffusion and retention processes (Farley, 2002). Therefore, integration with other constraints is paramount in order to reduce the uncertainty of the interpretation. In this study, the AHe ages are integrated with the AFT data (ages and track lengths) to provide a more rigorous study of the thermal evolution.

5.3 Cenozoic exhumation history of the northern Red Sea margins

Prior to the development of the Red Sea, a near flat topography, mostly submerged below sea-level, characterised western Arabian and northeastern Africa between the Late Cretaceous and the Early Oligocene (Bohannon et al., 1989). The timing and magnitude of exhumation associated with tectonic uplift of rift-related normal footwall blocks and the erosional escarpment retreat that has occurred around the Red Sea has been investigated using several low-temperature thermochronometers (e.g. Kohn and Eyal, 1981; Bohannon et al., 1989; Omar et al., 1989; Steckler and Omar, 1994; Omar and Steckler, 1995; Feinstein et al., 2013; Szymanski et al., 2016; Stockli and Bosworth, 2019). These authors reported ages that cover the range from Paleozoic to Cenozoic from a multiple thermochronometers (Figure 5.4).

Paleozoic and Mesozoic thermochronometric ages have been described from different parts around the northern Red Sea, the Gulf of Suez and the Gulf of Aqaba. Feinstein et al. (2013) showed that heating-cooling events, recorded in their thermal modelling of AFT data from southwestern Jordan, occurred at the Late Devonian-Permian and Early Cretaceous. Furthermore, through modelling of apatite and zircon (U-Th)/He data, Szymanski et al. (2016) described an exhumation even at 350 Ma (Early Carboniferous) at the Central Arabian Rift Flank (CARF).

Younger exhumation events have been linked to the Late Oligocene-Early Miocene onset of the Red Sea-Gulf of Suez rift. AFT analysis of samples from the western side of the Gulf of Suez suggests that flank uplift started within the period 23-21 Ma, which when anchored to subsidence of the gulf basin supports a slightly earlier

commencement of the rift compared to the uplift, but shows that the uplift commenced prior to or at the onset of a rapid extension phase (Omar et al., 1989). Following the initial uplift, the escarpment retreated at an average rate of 3-5 mm/a, which was associated with uplift-driven exhumation (Omar et al., 1989). Also, on the Egyptian margin, an unconformity described at the top of Cretaceous/base of Cenozoic stratigraphic levels from south and central Egypt (Issawi, 1972) has been suggested by Omar et al. (1987) to be caused by the Early Miocene regional uplift and erosion.

Similarly, AFT ages from samples within a 100-km distance from the northwestern Red Sea coast have values of ~23-22 Ma suggesting exhumation associated with the early rifting (Omar and Steckler, 1995). From the Quseir area along the Egyptian Red Sea margin, an AFT age of one sample of 23±2 Ma along with structural data and sedimentary ages have been used to conclude coeval uplift, rifting and erosion (Bojar et al., 2002).

Closer to the area investigated in this study, Stockli and Bosworth (2019) showed that AHe ages from a vertical transect of the Jabal az Zuhd cluster around 23 Ma irrespective of elevation (Figure 5.1). They concluded that exhumation resulted from the Early Miocene rift faulting coeval with the age of the earliest syn-rift sedimentary unit (Al Wajh Formation; Hughes et al., 1999; Tubbs et al., 2014; Stockli and Bosworth, 2019). Furthermore, exhumation was interpreted to have taken place at a location ca. 50 km SSE of this study area (at Jabal Dabbagh) as zircon (U-Th)/He (ZHe) ages have values of ~23 Ma, suggesting km-scale displacement on the border fault (Stockli and Bosworth, 2019; Figure 5.1).

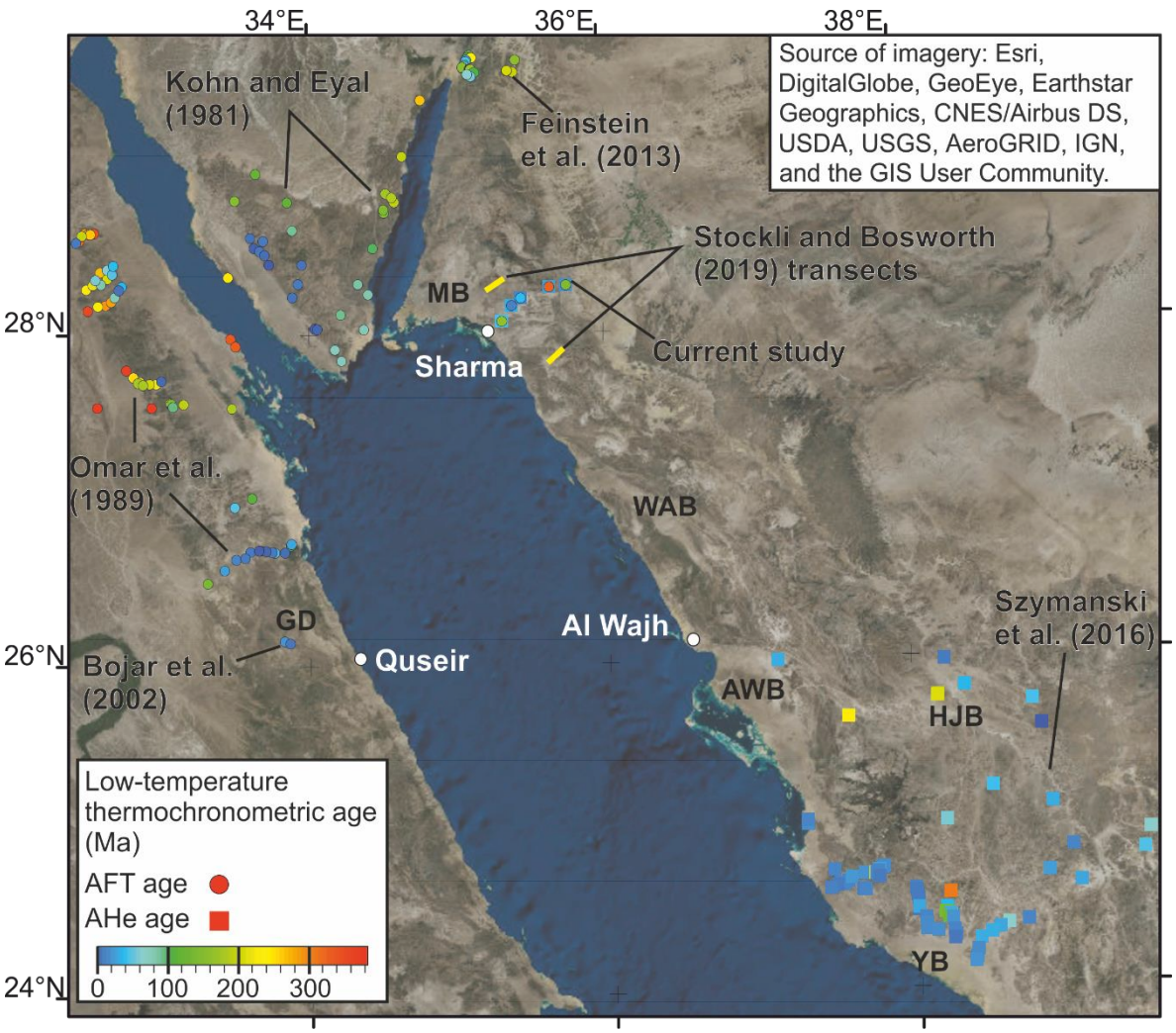

Figure 5.4: A compilation of northern Red Sea and nearby margins AFT and AHe data from existing studies (citations in figure) and the current study. Yellow lines: approximate locations transects presented in Stockli and Bosworth (2019) and discussed in text. MB: Midyan Basin; WAB: Wadi Azlam Basin; AWB: Al Wajh Basin; HJB: Hamd-Jizl Basin; YB: Yanbu Basin; JZ: Jabal az Zuhd; JD: Jabal Dabbagh; GD: Gebel Duwi.

Feinstein et al. (2013) showed, through thermal modelling of samples collected from the southeastern margin of the Dead Sea Rift (DSR), that there is no obvious thermal signal related to the timing of DSR sinistral strike-slip tectonics (i.e. Middle Miocene) but that there is an earlier period of cooling that commenced at the Oligocene. Given its timing, this cooling event was most likely to be related to the regional tectonic reorganisation of this part the Arabian Plate as the Red Sea tectonics were starting to take place (Feinstein et al., 2013).

Moreover, older (Eocene-Oligocene) cooling ages have been reported from AFT and zircon FT (ZFT) analyses. AFT Late Eocene-Early Oligocene ages (~34 Ma by Omar and Steckler (1995) and 36±6 Ma (one sample) by Bojar et al. (2002)) have been reported from the western Gulf of Suez and Egyptian Red Sea margins, respectively. Omar and Steckler (1995) interpreted this cooling event to be an earlier phase of uplift and erosion of the Red Sea that was followed by the Early Miocene phase. Late Eocene to early Oligocene (35-33 Ma) AFT ages from the southeastern Egyptian basement were interpreted to record regional uplift and erosion that has also been interpreted from an unconformity separating Eocene and Miocene strata (Omar et al., 1987).

Estimating paleo-geothermal gradient is important for constraining exhumation via low-temperature thermochronology. However, existing paleo-geothermal gradient estimates from around the study area are variable. Feinstein et al. (2013) used a value of 17.5 °C/km based on inverse modelling of AFT age and length distributions from vertical profile samples from southwestern Jordan, ~200 km away from the reconstructed position of the early Red Sea rift. Such a low value might be expected given the great distance between their study area and the main rift.

On the CARF, Szymanski et al. (2016) showed that the model fits of AHe and ZHe data of sample arrays have high clustering when using significantly higher paleo-geothermal gradients of 30-40 °C/km. They suggested that even higher values might have characterised areas surrounding Tertiary dykes. Similarly, from the African side in southeastern Egypt, Omar et al. (1987) estimated a geothermal gradient of ~40-53 °C/km during the Oligocene. This was based on the assumption that estimates of maximum Cretaceous to Middle Eocene sedimentary thicknesses (assumed based on relevant studies from west of the Nile and east of the Arabian basement) could not have been more than 1.5 km. Therefore, the sedimentary burial alone would not have been the only driver for resetting their AFT ages (Omar et al., 1987).

5.4 Methodology

AFT and AHe dating techniques were employed in this study as they are most useful in the analysis of the thermal history of basement rocks within the uppermost crust. Several steps were involved in the analyses starting from the selection of the sample locations until the estimation of the most likely thermal history.

As will be illustrated thoroughly in the sub-sections below, the work involved the efforts of several people from different institutions. The sampling of basement rocks, and the thermal modelling and interpretation of the results were conducted by myself in the field and at the University of Leeds, respectively. The selection of the best samples for the laboratory processing was conducted at the Scottish Universities Environmental Research Centre (SUERC) in East Kilbride at meetings between myself and Professor Finlay Stuart (SUERC and University of Glasgow). The laboratory analyses and the determination of the ages were conducted by the laboratory staff at SUERC.

5.4.1 Sample transect: The Sharma-Tabuk Road Transect

One transect was selected to perform low-temperature thermochronological analysis (Figure 5.5 and Table 5.1). This transect, named here the “Sharma-Tabuk Road transect (Samples 16-T1-#)”, trends NE-SW extending from ~4 km east of the Red Sea coastline near the town of Sharma approximately ~60 km towards the ENE. This transect spans a low relief area close to the shore, the escarpment, and the plateau and so encompasses a profile across the entire sub-aerial margin.

The aim of the analysis of this transect is to establish the exhumation history perpendicular to the margin, and to test whether the SEF has been significantly active during the Red Sea rifting as to have caused a discernible contrast in cooling history between its footwall and hangingwall. Additionally, analysing the thermochronometers along this transect could provide a means to assess the escarpment evolution.

Structural and geomorphic considerations determined the transect location and orientation. The choice of the specific locations of the samples, however, was

subject to an additional lithological consideration. Using the existing lithology map (Clark, 1987), a variety of intrusive rocks of granitic-affinity along the transect line were targeted for sampling as they are more likely than other basement rocks (e.g. meta-volcanics) to contain apatite grains. The samples were taken from rocks that were least affected by weathering processes and for this reason, where possible, road cuts were targeted for sampling.

Two issues were encountered during the sample location selection in the field. The first is that road cuts were not abundant due to the low relief of the area, which limits the locations to be targeted. The other is that the outcrops were affected by fracturing that could facilitate weathering.

A total of 10 locations along the ~63-km-long transect line were targeted for sampling, with one to three samples collected from each location during a fieldwork excursion in 2016 (Figure 5.5 and Table 5.1). The samples were collected from basement granitic units away from dykes that may be of Cenozoic age. The exception is sample 16-T1-5a, which, due to the lack of good quality exposures of basement rock and the extensive dyking, was collected from a road cut ~35 m away from two basaltic dykes. The range of elevation of the sample locations extends from 86 m (16-T1-2a) to 1,144 m (16-T1-10a).

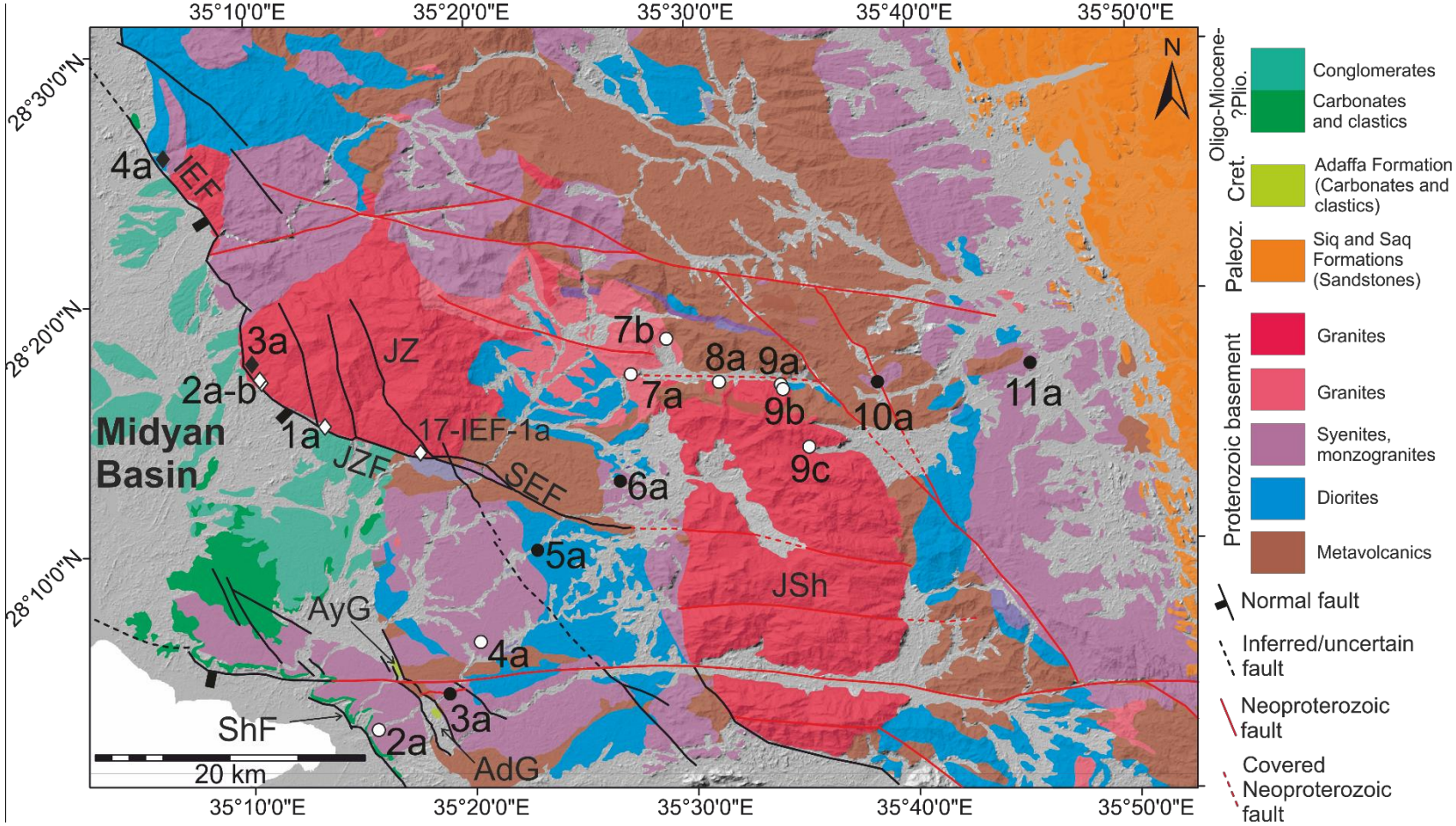

Figure 5.5: A geological map of the southeastern part of the Midyan Peninsula (Modified from Clark (1987)) showing the locations of samples collected for thermochronological analysis along the Sharma-Tabuk Road Transect (black circles: apatite grains extracted; white circles: no apatite grains extracted).

Table 5.1: Samples collected along the Sharma-Tabuk Road Transect, southeastern Midyan Peninsula. The light blue shading highlights the samples for which the analyses were performed. The asterisk * samples were dismissed at the visual inspection stage as unsuitable for analysis before preparation; the double asterisk ** samples did not yield apatites after laboratory separation was conducted. AFT = AFT dating; AHe = AHe dating; AFTL = AFT length measurements. Note the correlation between different granitic rocks and the apatite yield.

Sample name	Elevation (m)	Latitude, Longitude	Lithology	Apatite yield	Analysis performed
16-T1-2a	86	28° 3.000'N, 35° 15.843'E	Granite	No apatite**	-
16-T1-3a	134	28° 4.322'N, 35° 18.851'E	?Syenite	Acceptable	AFT; AHe
16-T1-4a	189	28° 6.558'N, 35° 20.246'E	Granite	No apatite**	-
16-T1-5a	269	28° 10.017'N, 35° 22.944'E	Monzogranite (biotite granite)	Good	AFT; AFTL; AHe
16-T1-6a	433	28° 12.681'N, 35° 26.724'E	Monzogranite (biotite granite)	Good	AFT; AFTL; AHe
16-T1-7a	438	28° 16.909'N, 35° 27.388'E	Monzogranite (biotite granite)	No apatite*	-
16-T1-7e	357	28° 18.336'N, 35° 29.028'E	Monzogranite (biotite granite)	No apatite**	-
16-T1-8a	664	28° 16.638'N, 35° 31.184'E	Granite	No apatite*	-
16-T1-9a	773	28° 16.503'N, 35° 34.015'E	Granite	No apatite*	
16-T1-9b	827	28° 16.402'N, 35° 34.050'E	Granite	No apatite*	
16-T1-9c	1291	28° 13.956'N, 35° 35.260'E	Granite	No apatite**	-
16-T1-10a	1135	28° 16.471'N, 35° 38.456'E	Syenite to alkali felds. granite	Very good	AFT; AFTL; AHe
16-T1-11a	1031	28° 17.102'N, 35° 45.385'E	Syenite to alkali felds. granite	Good	AFT; AFTL; AHe

5.4.2 Sample selection

The collected samples were visually inspected at the Scottish Universities Environmental Research Centre (SUERC) to determine which samples are likely to yield apatite grains upon the sample processing in the laboratory (next section). Sample selection was discussed with Professor Finlay Stuart (SUERC and University of Glasgow) upon performing the visual inspection, taking into account the aims of the transect and the quality of the samples (i.e. their likelihood to contain apatite grains). Four samples from the Sharma-Tabuk Road Transect were dismissed at this stage; namely, 16-T1-7a, 8a, 9a and 9b.

5.4.3 Laboratory procedure

The apatite grains were extracted and analysed at SUERC, and the processes of preparing the samples and extracting the grains were performed by the SUERC laboratory staff.

5.4.3.1 Apatite grains extraction

The visual inspection of the rock samples was followed by several physical steps to separate the apatite grains out of the rest of the rock components. After selecting the candidate rock samples, they were crushed and the product was sieved and washed to remove components small components, before the remaining portion was heated-dry at 50°C.

Afterwards, separation based on density was conducted using liquids of known densities and considering the 3.19g/cm^3 density of apatite. Magnetic minerals were then removed from the remaining portion by applying a magnetic field, leaving apatite grains as the final product.

Having performed these steps, only five samples from the Sharma-Tabuk Road Transect yielded apatite grains (16-T1-3a, 5a, 6a, 10a and 11a; Figure 5.5 and Table 5.1). The apatite yield differs between these samples with one having a very good (16-T1-10a), three good (16-T1-5a, 6a and 11a) and one acceptable (16-T1-3a; Table 5.1). Therefore, only these five samples were used in further analysis, interpretation and modelling. Afterwards, manual picking of grains that did not show inclusions or damage was performed by laboratory personnel at SUERC. These grains were then inspected under the optical microscope to choose the best candidates.

After these preparatory steps, the procedures for AFT and AHe analyses took different routes.

5.4.3.2 AFT

To calculate the AFT age for each grain, the amounts of radiogenic parent and daughter need to be determined. The parent (^{238}U) concentration was calculated using the Laser Ablation-Inductively Coupled Plasma-Mass Spectrometry method (LA-ICP-MS). Laser-ablation of each grain was conducted for 20 seconds and the resultant quantities of ^{238}U, along with ^{232}Th, ^{43}Ca and ^{35}Cl were determined using mass spectrometry.

To measure the radiogenic daughter (tracks) concentration, the density of tracks needs to be measured for each grain. First, the selected apatite grains were polished. For the tracks to be detectable under the microscope, the grains had to be chemically etched, using 5.5 M HNO_3 for 20 seconds at 21°C, to enlarge the tracks. After etching, the fission tracks were counted using a Zeiss Axioplan Microscope and a Trevor Dumitru stage system. With a magnification of x1250, the tracks were counted using the FT Stage 4.04 software.

Understanding the annealing process is complicated by the chemistry of the apatite, which causes deviation from the theoretical temperature-dependency relationship, resulting in different ranges of the PAZ. For each counted grain, a minimum of three D_{par} measurements was performed. Additionally, the ratio of U:Ca was determined for each grain as it is used in the age determination (below). The age determined for each apatite grain was calculated using the following equation (Donelick et al., 2005):

$$t = \frac{1}{\lambda_d} ln\left(\lambda_d \zeta g \frac{\rho_s}{P} + 1\right) \qquad \text{(Equation 5.1)}$$

Where λ_d = 1.55125x10^{-10} a^{-1} (^{238}U total decay constant), g = 0.5 (related to the geometry of the polished surface), ρ_s is the number of spontaneous fission tracks per unit area, P = $^{238}U/^{43}Ca$, and ζ = 19.66±0.62 (a calibration factor for using the LA-ICP-MS method calculated using 86 apatite standard grains (Durango apatite)). Upon the calculations of the single grain ages, ages that are associated with possible incorrect P values (i.e. ^{238}U concentration) were not included in the statistical determination of the sample age.

Having determined the FT age for each apatite grain, representative ages are calculated for each rock sample. Two ages are reported; a central age and a pooled age. The central ages for the samples were calculated using the Galbraith radial plots (Galbraith, 1988; Galbraith, 1990), which are effective in plotting the individual grain ages with the corresponding standard error for each age, and then determining an age for the population of grains. That is, these plots provide a more visual way of presenting several single-grain age estimates (and their uncertainties) for the purpose of determining age populations more easily and comparing the uncertainties of the single-grain ages with the mean value of the sample age (Vermeesch, 2009). Here, the single grain ages, their standard errors and D_{par} values were input into RadialPlotter, developed by Vermeesch (2009), which outputs radial plots and calculates the central age, age dispersion (%), and the χ^2 value.

The pooled age (t_p) is calculated by:

$$t_p = \frac{1}{\lambda_d} ln\left(\lambda_d \zeta g \frac{\sum N_s}{\sum PA} + 1\right) \qquad \text{(Equation 5.2)}$$

Where N_s is the number of spontaneous tracks counted over an area (*A*) for each grain (Donelick et al., 2005).

5.4.3.2.1 FT length measurement

Out of the samples analysed in this study, apatite grains from sample 16-T1-11a contained the most abundant number of tracks for which the lengths were measured (n = 153). The other samples yielded much smaller number of measureable tracks (19 tracks for 10a, 25 tracks for 6a and 51 tracks for 5a). Along with the track length, mean D_{par} and the angle between the track and the c-axis were reported. The frequency of the track lengths was calculated and the distribution plotted. As will be seen in Section 5.4.4, using the thermal modelling software (HeFTy) the track length distribution can also be plotted after accounting for the shortening that is related to the angle the track makes with the c-axis.

5.4.3.3 AHe

Unlike the AFT analysis, the decay parent and daughter nuclei in the AHe technique are both measured using mass spectrometry. The accumulation of

the radiogenic ^{4}He (α) particles in the mineral is governed by the following equation:

$$^{4}He = 8 * {}^{238}U(e^{\lambda_{238}t} - 1) + 7 * {}^{235}U(e^{\lambda_{235}t} - 1) + 6 * {}^{232}Th(e^{\lambda_{232}t} - 1)$$

(Equation 5.3)

In this equation, ^{238}U, ^{235}U and ^{232}Th are the concentrations of each isotope, *t* is the age of the accumulated He and *λ* is the decay constant for each isotope. The uranium and thorium are the parent isotopes, whereas the helium is the daughter isotope.

The extraction process of He from the grains was conducted by SUERC staff using laser ablation. The laser heats the grain in a step-wise fashion and the majority of the radiogenic He (≥99%) is expected to be released at this stage. Any relatively significant (>1% of that of the originally released volume in the first step) volume of He would indicate another source of He (mainly from inclusions). Grains showing this behaviour were dismissed from further analysis.

Following the release of He by heating, heavy gas components released with He are separated out and removed by a process of cooling. Finally, He is channelled through to a mass-spectrometer for quantification. To measure the parent isotopes, the grains were dissolved and the contents of the solution are measured using ICP-MS.

5.4.4 Inverse thermal modelling

Inverse thermal modelling utilises the thermochronometric data (i.e. AFT and AHe single grain ages and AFT length distribution) to statistically resolve the likely thermal histories that the grains have experienced before reaching the surface (Peyton and Carrapa, 2013). The modelling in this study was performed by myself at the University of Leeds using the HeFTy software (Ketcham, 2005). Using this software, specified annealing and helium diffusion behaviours are used to calculate time-temperature (t-T) paths that reproduce the measured thermochronometric data given certain time and temperature constraints. In a nutshell, forward models are generated and the measured thermochronometric data are compared to the forward modelling predictions, which are then assigned a goodness-of-fit (GOF) value (Ketcham, 2005).

The annealing behaviour model for the AFT modelling, i.e. the model based on which the track length shortening (age reduction) with time and temperature is calculated, is that of Ketcham et al. (2007) (Figure 5.6). This model takes into account possible multiple kinetic populations that may characterise the AFT data. For the helium diffusivity, the Radiation Damage Accumulation and Annealing Model (RDAAM) by Flowers et al. (2009) was used as a calibrating model. Additionally, the model of Ketcham et al. (2011) was selected to correct for the α-ejection stopping distance.

In practice, the AFT and AHe measured data were input into HeFTy sequentially. For each apatite grain, the AFT data included the number of fission tracks (Ns), the area of the grain examined by the microscope (cm^2), the U/Ca ratio and its 1st standard error, and the average D_{par} value (Figure 5.6). Only data for the highest-quality grains were used in the modelling. Furthermore, fission track lengths were input into the HeFTy model along with the angles with the c-axis and the D_{par} for each track (except for sample 3a). The addition of the length data is important to narrow down the likely t-T paths of the sample. Using these data, HeFTy calculates the age of the sample applying LA-ICP-MS ratio and using a zeta value (ζ) of 19.66±0.62. Finally, single grain AHe ages were added separately to the HeFTy model (Figure 5.6). For the purpose of modelling, a standard deviation of 20% of each input single AHe grain age was used and a 60 μm radius was assumed.

To constrain the paths on the t-T space, constraining boxes were inserted on the t-T space before running the simulation. To test all of the possible scenarios, the boxes were constructed to cover the temperature range from the apatite total annealing zone (a value of 200°C was used in this case) to the surface temperature of 20°C. With respect to the time covered by the constraints, the boxes were constructed so as to extend from the present-day to a time that is older than double the central AFT age. This was done in order to make sure that the models start when the tracks were within the total annealing zone.

An additional constraint from nearby areas was also input into the modelling. AHe ages of samples from Jabal az Zuhd footwall block as well as AHe and ZHe ages from samples ~50 km to the SSE (Jabal Dabbagh) show clustering at ~23-25 Ma (Stockli and Bosworth, 2019; see also Section 5.3 and Figure 5.1a).

Therefore, a constraint was added to the modelling of sample 16-T1-3a at the Late Oligocene-Early Miocene, which is located only ~7 km east of Early Miocene Sharma Fault (ShF; Figure 5.5).

The inverse modelling was then performed using a Monte-Carlo approach to generate random paths in the time-temperature (t-T) space that were simultaneously compared to the measured input data. The modelling was performed with 100,000 simulations for each sample. The modelling started by using the AFT ages alone as inputs, then sequentially adding the AFT lengths and the single grain AHe ages.

The results of the modelling were plots on the t-T space that describe the likely scenarios that led to the final measured outcomes (i.e. the cooling paths that would result in the measured ages and track length distributions). By comparing the modelled ages and length distributions that the t-T paths satisfy to the measured ages and length distributions for each sample, HeFTy assigned a goodness-of-fit (GOF) value to the model outcomes (good fit: GOF >0.5; acceptable fit: GOF >0.05; Ketcham (2005)). The calculation of the GOF uses different methods for the ages and the track lengths, summarised in Ketcham (2005).

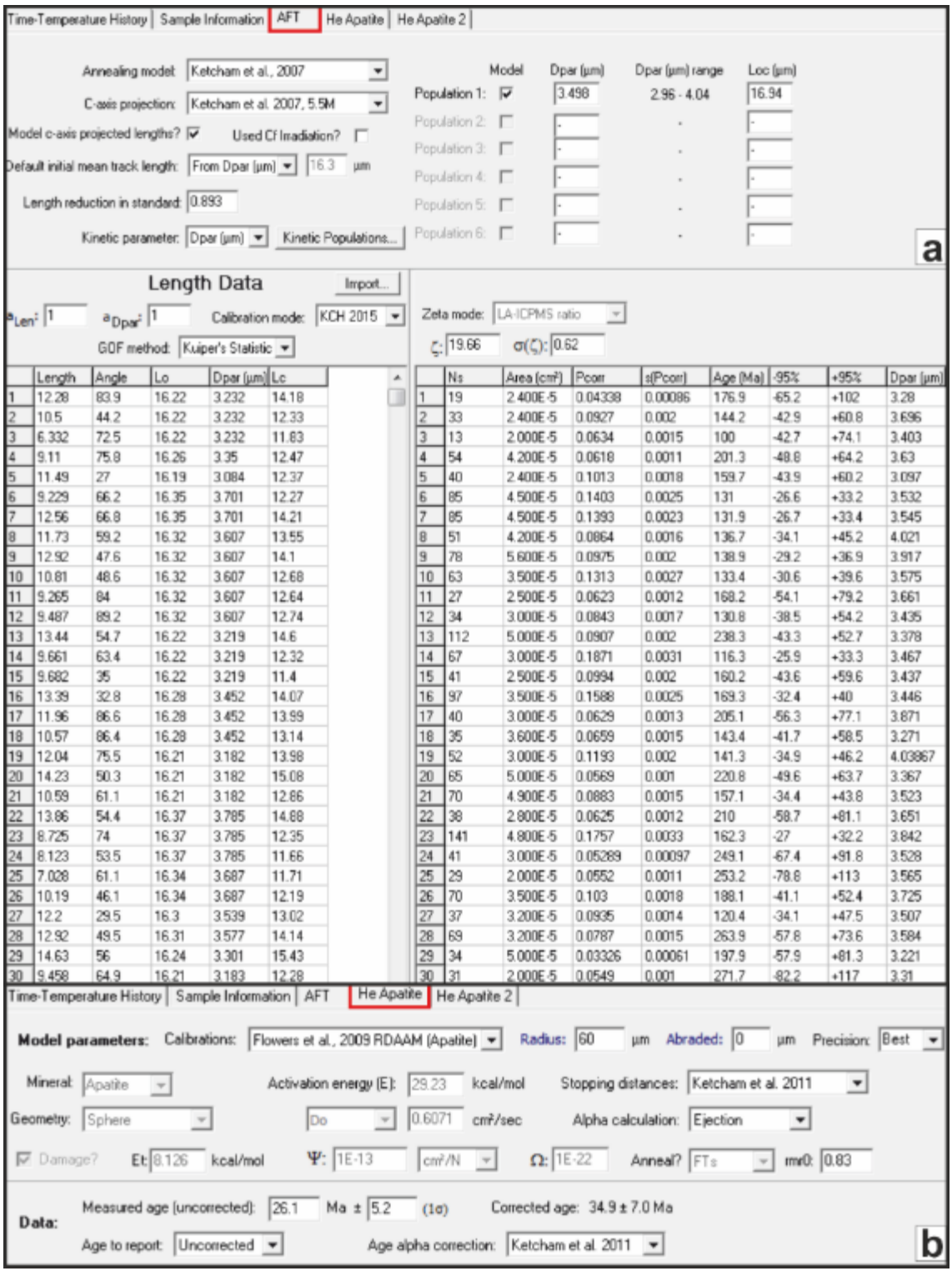

Figure 5.6: An example of the HeFTy data input interface and parameters (sample 16-T1-11a). (a) Input of AFT data. Note: only 30 (out of 153) length measurements are shown in this figure. (b) Input and parameters of a single grain AHe age.

5.5 Results

5.5.1 AFT analysis

The AFT data for samples 16-T1-3a, 5a, 6a, 10a and 11a are presented in Table 5.2 and their positions with respect to the structures are shown on the cross-section in Figure 5.7. The pooled and central ages are all younger than the Proterozoic formation ages of the host basement rocks (Clark, 1987).

The individual grains have variable qualities, with grains from sample 16-T1-11a having the highest quality as reported by the SUERC staff. Quality deterioration arises from surface damage and possible uranium zonation were noted by the laboratory personnel in samples 16-T1-3a, 5a, 6a and 10a. Another issue that was noted, particularly in samples 16-T1-3a and 5a was the existence of large D_{par} values for some of the grains (Figures 5.8-5.9). The large D_{par} values are suggestive of compositional variation that could increase the closure temperature for the system.

The AFT pooled ages range from 27.71±1.62 Ma to 291.23±17.21 Ma, whereas the central ages are between 29.20±3.00 Ma and 346.00±30.00 Ma. As some of the apatite grains were of low quality, another set of ages were determined after the dismissal of these low-quality grains. Therefore, except for sample 16-T1-11a, calculation of pooled and central ages from samples 16-T1-5a, 6a and 10a was performed on a selected number of grains that were considered to have the highest quality. These best grains have a pooled age range from 27.94±1.72 Ma to 332.84±25.84 Ma and a central age range from 27.90±2.40 Ma to 345.00±25.00 Ma.

The $P(X^2)$ values are low due to the dispersion that characterises the single grain ages (Table 5.2). Therefore, the pooled ages are likely to be more descriptive of the cooling age. However, the analysis of single-grain age distributions using radial plots (RadialPlotter; Vermeesch (2009)) shows that the central ages are in some samples composed of more than one population. Individual grain ages in 16-T1-5a and 6a form two age populations for each sample (Figures 5.9b and 5.10b). Therefore, it is interpreted that the whole-sample central and pooled ages for these samples are misrepresentative of the cooling ages, and instead represent mixed ages.

The mean track length measurements were conducted on samples 16-T1-5a (51 tracks measured), 6a (25), 10a (19) and 11a (153). The distribution of the track lengths measured for four samples (16-T1-5a, 6a, 10a and 11a) are shown in Figures 5.9-5.12. These tracks were not projected with respect to the grain c-axis and have mean track lengths range from 9.19±2.66 μm to 12.78±2.53 μm. The projected track length distributions will be presented in Section 5.5.3.

Samples 16-T1-5a and 6a have track length distributions that are characterised by a pronounced negative skewness (Figures 5.9c and 5.10c). The long track lengths dominate the length distribution histograms, whereas the short tracks form a tail (16-T1-5a) and a small peak (16-T1-6a). This distribution corroborates the interpretation introduced earlier based on the individual grain age distributions that the central and pooled ages are mixed ages. The track length median values from these two samples are 13.55μm and 12.28μm, respectively.

The track length distribution for sample 16-T1-10a also shows a negative skewness, albeit less defined than those of 16-T1-5a and 6a, with a long tail towards the short tracks (Figure 5.11c). The FT distribution has a mean value of 9.19±2.66μm and a median value of 9.16μm. However, the smaller number of measured tracks (19) means that such distribution could be misleading, increasing the uncertainty of further interpretation of this sample's thermochronometric results.

The track length distribution histogram for sample 16-T1-11a is characterised by a moderate negative skewness whereby the mean track length is 10.84±2.48μm whereas the median is 11.24μm (Figure 5.12b). The distribution histogram shows a longer tail towards the short track lengths and a shorter tail towards the long tracks. Such a distribution indicates that the calculated AFT age is most likely representative of a mixed age.

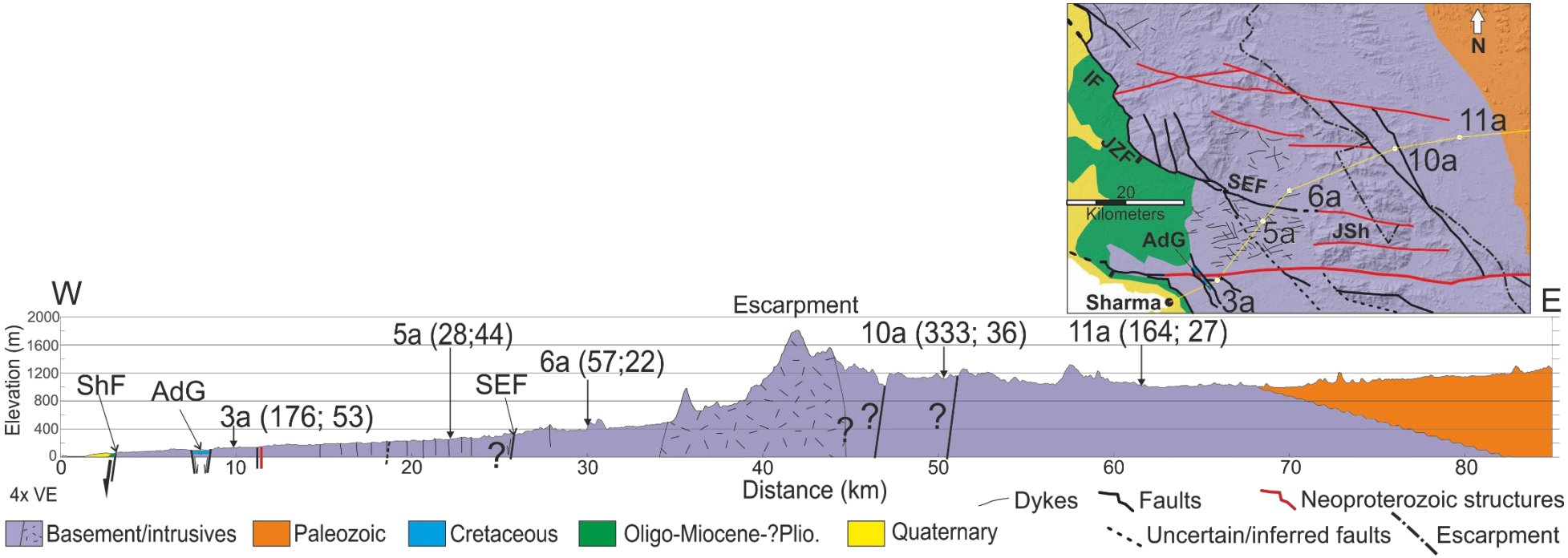

Figure 5.7: A cross-section along the Sharma-Tabuk Road transect, showing samples 16-T1-3a, 5a, 6a, 10a and 11a. Between the brackets, the pooled AFT age and AHe age are shown in Ma (rounded to the nearest Ma), respectively. The SEF is plotted as one fault rather than a zone of faults for simplicity. The simplified geological map (top right) shows the position of the transect line (yellow line) and the locations of the samples with respect to the main structures.

Table 5.2: AFT ages and mean track lengths of the Sharma-Tabuk Road transect samples. ρs is the ratio of the number of tracks per area.

	Age calculation									**Track length calculation**	
Sample (16-T1-#)	Total # of grains (best grains)	Pooled age ±1σ (Ma) (best grains)	Pooled age ±1σ (Ma) from all grains	Central age ±1σ (Ma) (best grains)	Central age ±1σ (Ma) from all grains	U/Ca	Central age $P(X^2)$ all grains (best grains)	Average D_{par}±1σ	Average ρs±1σ	# of tracks	Mean track length ±1σ (μm)
3a	17		175.69±23.05		199.00±26.00	0.0072±0.0030	0.49	3.30±0.70	0.12±0.06		
5a	22 (16)	27.94±1.72	27.71±1.62	27.90±2.40 (two peaks: 35.50±3.6 & 20.60±2.50)	29.20±3.00	0.1514±0.0656	0.00 (0.01)	3.30±0.70	0.45±0.19	51	12.78 ±2.53
6a	20 (17)	57.01±3.66	45.45±2.63	77.00±10.00 (two peaks: 127.00±20.00; 49.20±3.70)	67.20±9.20	0.1150±0.1154	0.00 (0.00)	2.61±0.24	0.56±0.42	25	11.49 ±3.25
10a	27 (20)	332.84±25.84	291.23±17.21	345.00±25.00	346.00±30.00	0.0169±0.0282	0.00 (0.78)	2.34±0.19	0.50±0.44	19	9.19 ±2.66
11a	30		163.71±6.61		168.70±7.80	0.0914±0.0391	0.00	3.55±0.23	1.55±0.55	153	10.84 ±2.48

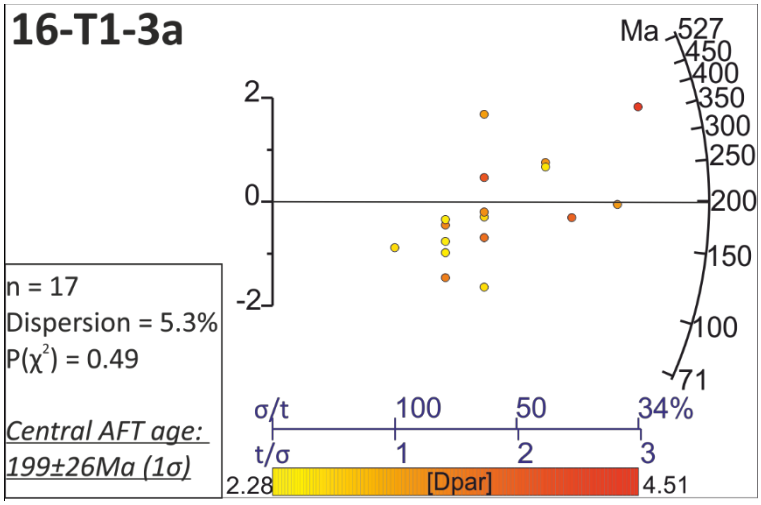

Figure 5.8: A radial plot showing single grain age dispersion and whole sample central age for sample 16-T1-3a. The axes are: age (Ma; right), single-grain precision increasing to the right (bottom) and single grain age deviation from the mean (i.e. deviation from a line connecting the origin (0,0) and the central mean to the right (left). The points are coloured according to the D_{par} value. n is the number of grains for which ages were calculated.

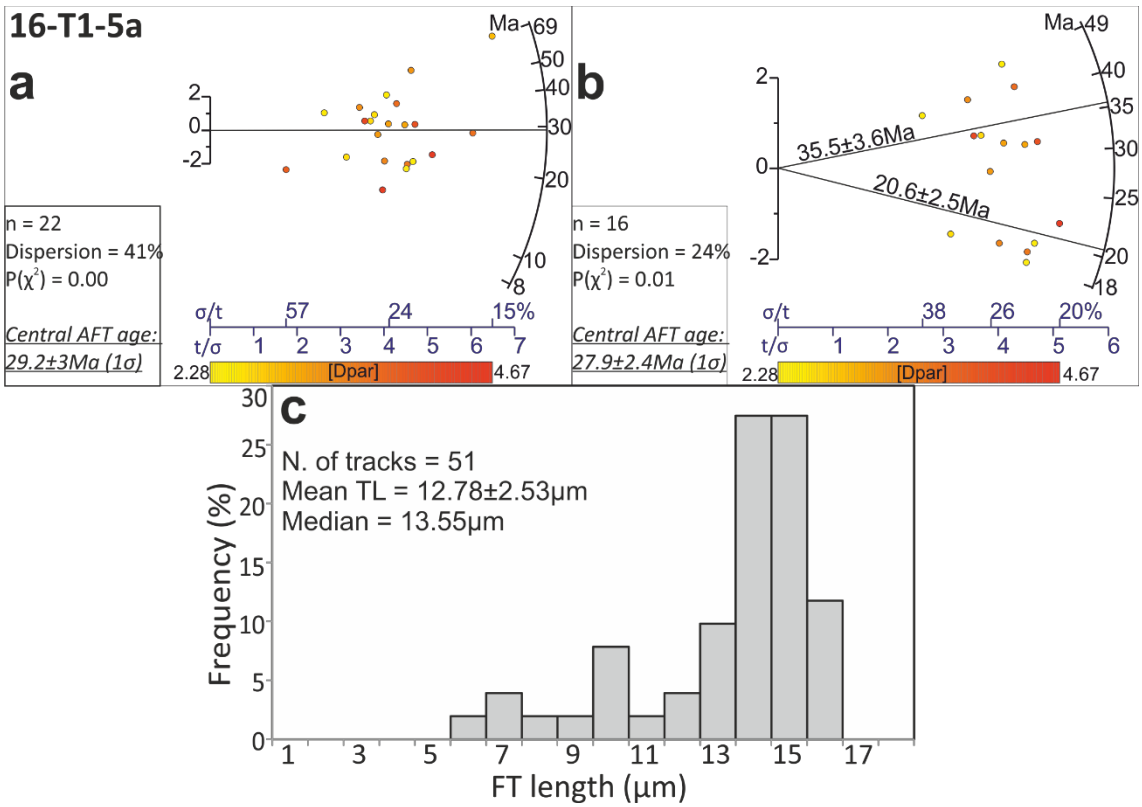

Figure 5.9: (a-b) Radial plots showing single grain age dispersion and whole sample central age for sample 16-T1-5a, using all of the analysed grains (a) and a selected number of the highest quality grains (b). Note that there are two age peaks that can be deciphered from the point distribution. The axes are: age (Ma; right), single-grain precision increasing to the right (bottom) and single grain age deviation from the mean (i.e. deviation from a line connecting the origin (0,0) and the central mean to the right (left). The points are coloured according to the D_{par} value. n is the number of grains for which ages were calculated. (c) Distribution of track lengths measured from sample 16-T1-5a. TL= track length.

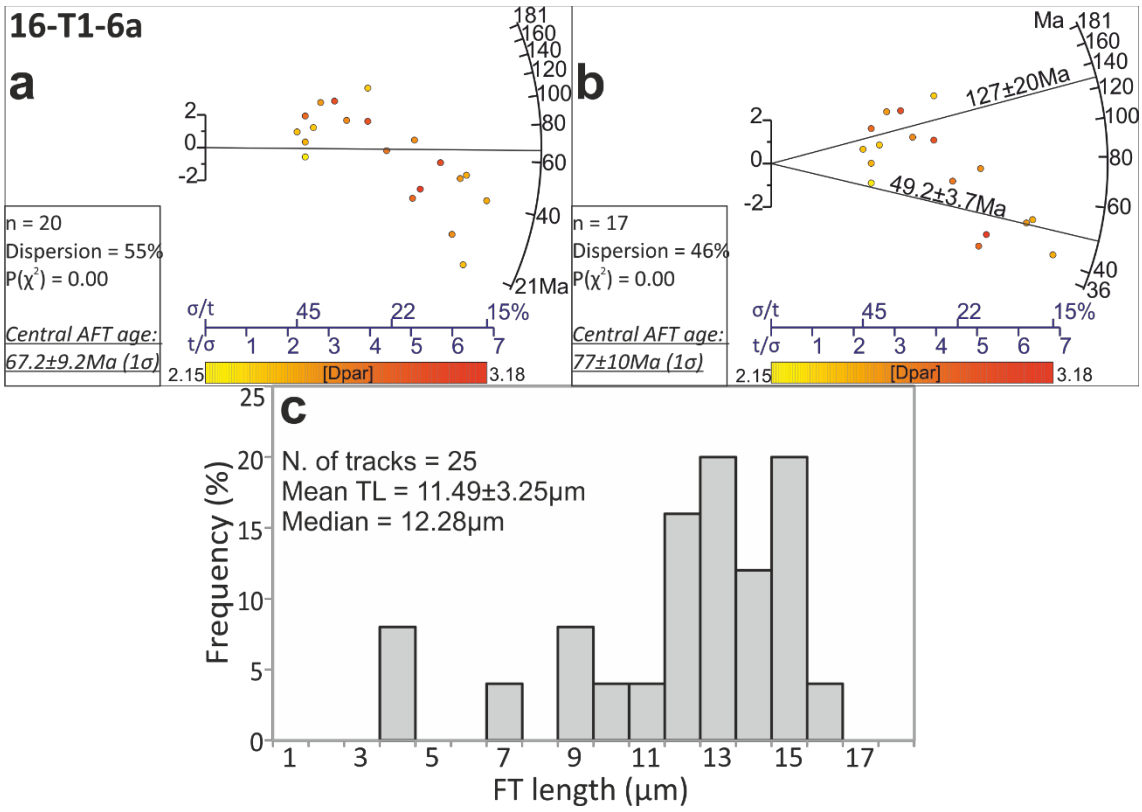

Figure 5.10: (a) and (b) Radial plots showing single grain age dispersion and whole sample central age for sample 16-T1-6a, using all of the analysed grains (a) and a selected number of the highest quality grains (b). Note that there are two age peaks that can be deciphered from the point distribution. The axes are: age (Ma; right), single-grain precision increasing to the right (bottom) and single grain age deviation from the mean (i.e. deviation from a line connecting the origin (0,0) and the central mean to the right (left). The points are coloured according to the D_{par} value. n is the number of grains for which ages were calculated. (c) Distribution of track lengths measured from sample 16-T1-6a. TL= track length.

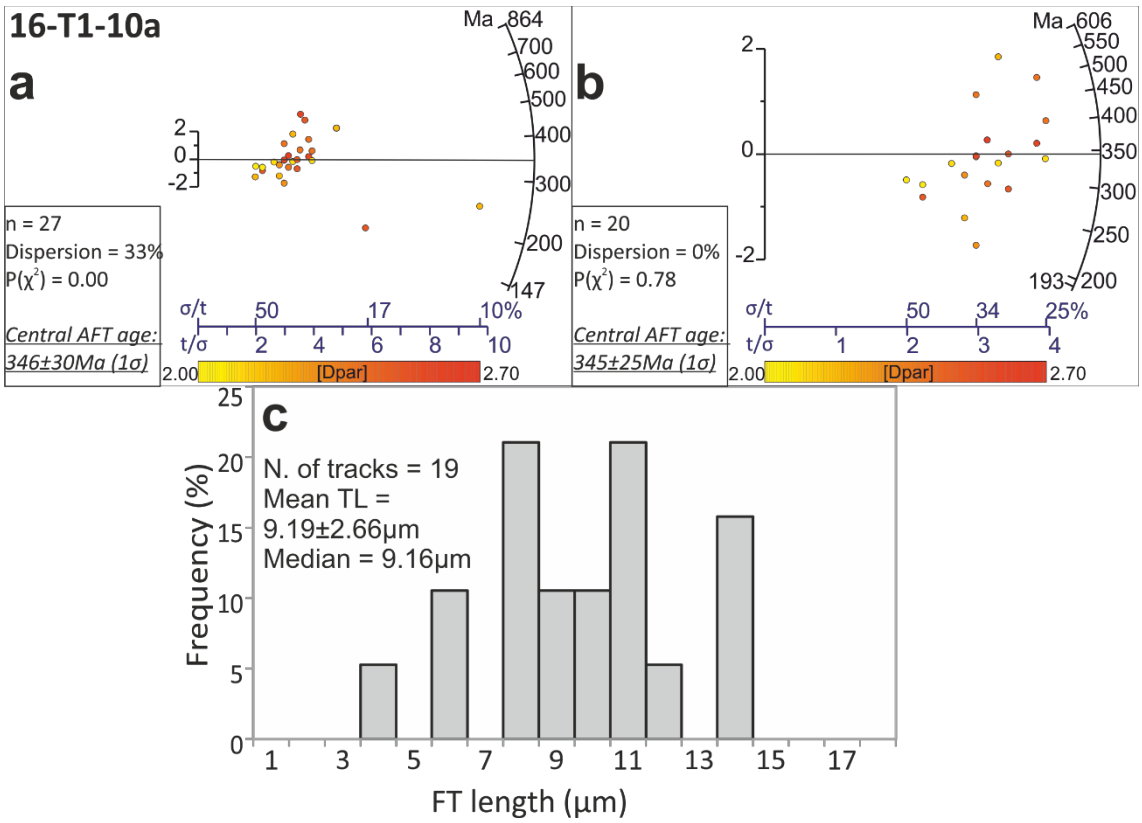

Figure 5.11: (a) and (b) Radial plots showing single grain age dispersion and whole sample central age for sample 16-T1-10a, using all of the analysed grains (a) and a selected number of the highest quality grains (b). The axes are: age (Ma; right), single-grain precision increasing to the right (bottom) and single grain age deviation from the mean (i.e. deviation from a line connecting the origin (0,0) and the central mean to the right (left). The points are coloured according to the D_{par} value. n is the number of grains for which ages were calculated. (c) Distribution of track lengths measured from sample 16-T1-10a. TL= track length.

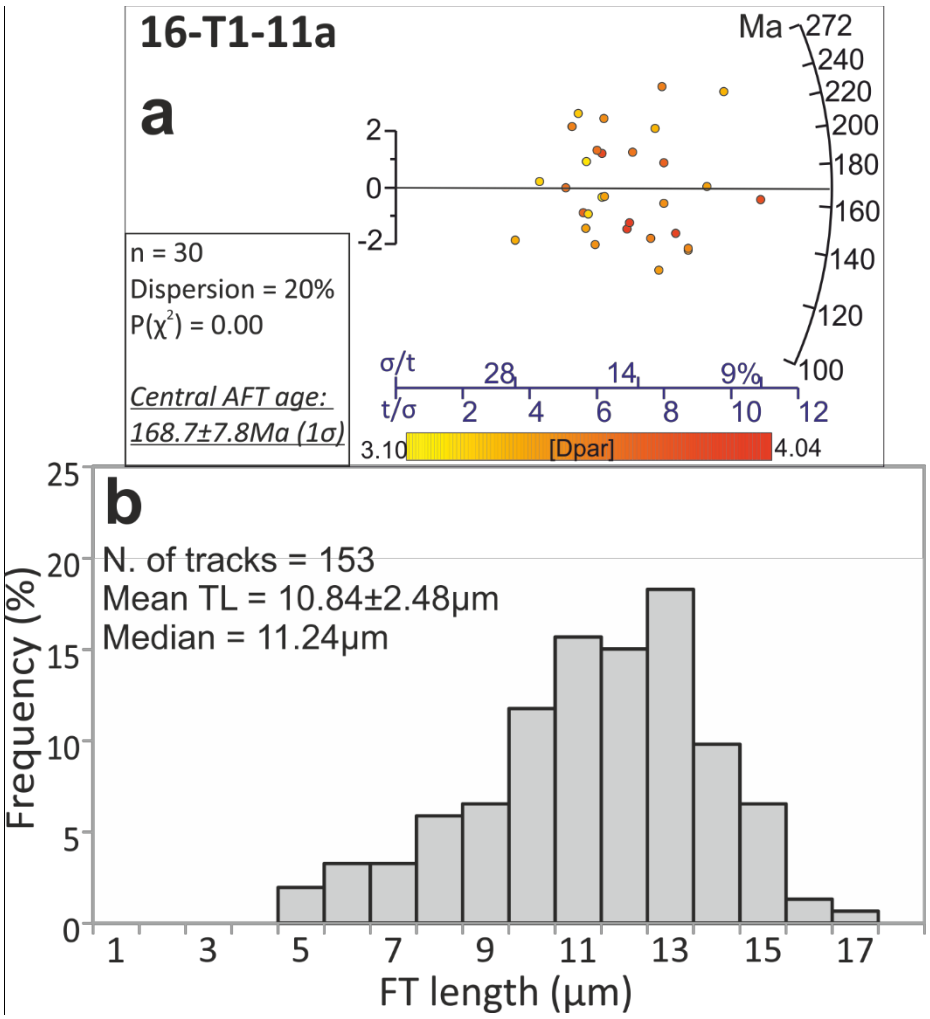

Figure 5.12: (a) A radial plot showing single grain age dispersion and whole sample central age for sample 16-T1-11a. The axes are: age (Ma; right), single-grain precision increasing to the right (bottom) and single grain age deviation from the mean (i.e. deviation from a line connecting the origin (0,0) and the central mean to the right (left). The points are coloured according to the D_{par} value. n is the number of grains for which ages were calculated. (b) Distribution of track lengths measured from sample 16-T1-11a. TL= track length.

5.5.2 AHe analysis

The individual AHe grain ages are marked with dispersion, particularly for samples 16-T1-3a, 10a and 11a (Figure 5.13). The individual grain ages range between 19.5 Ma and 184 Ma, significantly younger than the formation age of the host basement rocks (Clark, 1987).

Most of the single grain AHe ages are younger than the pooled and central AFT ages for the corresponding samples. The exceptions are all of the single grain AHe ages for sample 16-T1-5a and the oldest single grain AHe age for sample

16-T1-3a (Figure 5.13 and Table 5.2). The single grain ages from 16-T1-5a are 39.3, 41.4, 50.3, 77, 79 and 82 Ma, whereas its AFT ages are 27.71±1.62 Ma (pooled age) and 29.20±3.00 Ma (central age; Figure 5.9). The oldest single grain AHe age from 16-T1-3a is 184 Ma, and is only older than the pooled AFT age (175.7±23 Ma; Figure 5.8).

Table 5.3 presents the mean AHe ages for each of the transect samples taken by calculating the arithmetic mean of the ages of the individual contributing grains that form an age cluster. The method of averaging a selected number of single grain ages instead of the whole population of ages can be justified as the use of all of the single grain ages in the thermal modelling (next section) does not result in any time-temperature (t-T) paths. Therefore, the incorporation of all of the single AHe ages with the AFT data cannot result in any model that would explain the thermal evolution. This is particularly true where the single grain age is older than the AFT age of the sample (e.g. sample 16-T1-5a).

Samples 16-T1-3a, 10a and 11a have clusters of single grain AHe ages that are composed of two or three ages (Figure 5.13). The single grain ages that are not within these clusters are spread out, with an outlier at sample 16-T1-3a (184 Ma). Conversely, more than one cluster of single grain ages are observed for samples 16-T1-5a and 6a, and the younger of these clusters have been used in the calculation of the average ages (Figure 5.13). The use of the older cluster for 16-T1-6a in the thermal modelling did not yield good t-T paths (next section), which suggests that it cannot be integrated with the AFT data. It is worth noting that during the thermal modelling (next section), the single grain AHe ages are input individually into the model, which rules out any effect of the averaging.

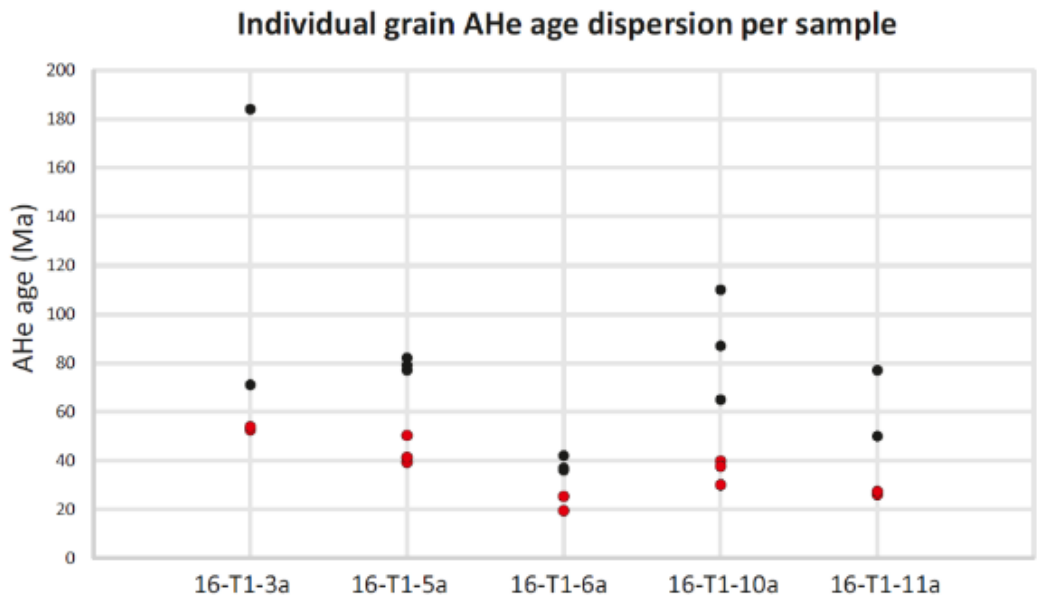

Figure 5.13: Dispersion of single grain AHe ages from the transect samples. Note the over-dispersion in samples 16-T1-3a, 10 and 11a and to some extent 5a. The red dots represent the single grain ages used in the calculation of the mean ages of the samples in Table 5.3.

Table 5.3: Mean AHe ages from the transect samples averaging selected single grain ages marked by red dots in Figure 5.13.

Sample	AHe age ±1σ (Ma)
3a	53.20±0.85
5a	43.67±5.84
6a	22.40±4.10
10a	35.87±5.10
11a	26.70±0.85

5.5.3 Thermal modelling results

Table 5.4 presents all of the models that were run with different input data. These models include runs that did not result in any resolved thermal history. The HeFTy models that yielded acceptable and good GOF paths on the t-T space are presented in Figure 5.14 and indicated in Table 5.4. The goodness-of-fit (GOF) for the AFT age solutions for all of the samples are very good (≥0.89). With respect to the modelled AFT length distributions, the GOF is more variable but is always greater than 0.5. The measured FT length distributions shown in Figure 5.14 have been projected on the crystallographic c-axis.

The use of both AFT and AHe data in the modelling of 16-T1-3a, 6a and 10a resulted in GOF values of ≥0.94 for the AFT ages, ≥0.77 for the AFT length distributions and ≥0.90 for the AHe ages (Figure 5.14). Conversely, using the AHe along with the AFT data resulted in no t-T solutions for 16-T1-5a and only a few t-T paths for 16-T1-11a (Table 5.4). Acquiring a good number of t-T paths with good fit for these latter samples was only possible after excluding the AHe ages.

Table 5.4: Summary of the models that were run and the data used as input. Where the modelling resulted in GOF values >50 the corresponding cell is marked with a tick (✓). * In this run only AFT ages and AHe ages were used as input data (i.e. no FT length measurements). ** In this run one single grain AHe age (19.5±3.9 Ma) yielded GOF value of 0.92 and the other (25.3±5.1 Ma) yielded a value of 0.23.The light blue cells indicate the best models that are considered in the discussion later.

	t-T paths resolved using the different thermochronometric data		
Sample	AFT ages	AFT ages & length measurements	AFT ages, length measurements & AHe ages
16-T1-3a	✓	No length measurements are available	✓*
16-T1-5a	✓	✓	No paths resolved
16-T1-6a	✓	✓	✓**
16-T1-10a	✓	✓	✓
16-T1-11a	✓	✓	Only 33 acceptable paths; no good paths resolved

For sample 16-T1-5a, the inability to produce a solution is expected because all of the single grain AHe ages are older than the AFT age. Such an inverted AFT-AHe age relationship (i.e. AHe age older than AFT age) has previously been discussed in the literature (e.g. Flowers and Kelley, 2011). These and other studies suggest that great uncertainties related to the use of AHe thermochronology (such as inverted relationships) are due to the over-dispersion of individual grain ages and/or unaccounted for high helium retention caused by radiation damage associated with the decay process (Green and Duddy, 2018). As the mechanisms that relate to helium retention and diffusion fall outside the scope of the current study, and due to the complexity inherent in the retention/diffusion of the helium, which needs further investigation (Green

and Duddy, 2018), the AHe age of sample 16-T1-5a was not used in the thermal modelling, nor in the interpretation of the thermal evolution of the margin and across the fault; however, as AFT ages are likely to be more robust in this instance they were still incorporated in the discussion.

For the AHe ages that were used in the modelling, good fits were produced for the two AHe ages of sample 16-T1-3a without a Late Oligocene-Early Miocene constraint added (GOF≥0.91). Similarly, the AHe ages calculated after adding the constraint were all well reproduced with GOF≥0.93 (Figure 5.14). Conversely, only one AHe age was closely reproduced during the modelling for sample 16-T1-6a (19.5±3.9 Ma; GOF=0.92) with a poor fit for the remaining input age (25.3±5.1 Ma; GOF=0.23; Figure 5.14). Similarly, only two AHe ages were reproduced with good fits for sample 16-T1-10a (37.7±7.5 Ma; GOF=0.90 and 39.8±8.0 Ma; GOF=0.89), whereas the youngest age (30.1±6.0 Ma) was excluded from the modelling as no t-T paths were produced when it was included (Figure 5.14).

The common observation from the modelling of all of the samples was that they have all experienced cooling since they entered the PAZ without any indication of reheating. Therefore, if reheating did occur then it would have resulted in the total annealing of the tracks and the resetting of the thermochronometric clock. Sample 16-T1-3a model displays a wide range of good fits on the t-T space, and the best fit path shows an approximately monotonic cooling (Figure 5.14). However, adding the constraint at the Late Oligocene-Early Miocene shows that it is more likely that the sample cooled from ~ 60±5 °C at the start of rifting (~23 Ma). This last cooling event is estimated to have been ~40±5 °C in magnitude (i.e. cooling from the 60±5 °C isotherm to the present-day surface temperature (assuming 20 °C)). This cooling magnitude indicates a cooling rate of ~1.96-1.52 °C/Myr since the onset of rifting. Furthermore, this constrained model also shows a possible earlier rapid cooling extending from ~200±20 Ma (above the PAZ temperature) to ~180±20 Ma (at 64±5 °C; Figure 5.14). This cooling event corresponds to a cooling rate of ~3.05-2.55 °C/Myr.

The cooling magnitudes of samples 16-T1-5a and 6a were better constrained without the need to impose a rift-related constraint on the t-T space (i.e. they have well defined t-T paths without significant scatter; Figure 5.14). The most rapid cooling experienced by any of the samples was revealed by the modelling

of the AFT data of 16-T1-5a, which shows a cooling of 100±5°C from above the PAZ temperature starting at ~27 Ma. This cooling event corresponds to a cooling rate of ~3.89-3.52 °C/Myr.

Comparatively, a less rapid cooling event is observed in the modelling output for sample 16-T1-6a, which cooled from above the PAZ temperature at the Late Cretaceous (~80±10 Ma; Figure 5.14). However, from that time until the present-day the cooling trend can be divided into three segments as indicated by the best fit model: an early rapid phase of cooling from ~80±10 Ma (~120 °C) until 37±5 Ma (~80 °C), a middle less rapid phase from 37±5 Ma until 27±5 Ma (~47 °C), and lastly a rapid phase from 27±5 Ma until the present-day (20 °C; Figure 5.14). These cooling magnitudes correspond to cooing rates of 1.43-0.69 °C/Myr, 3.3-1.65 °C/Myr and 1.23-0.84 °C/Myr for the three segments, respectively.

In contrast, east of the erosional escarpment, samples 16-T1-10a and 11a display an earlier period of slow cooling, starting in the late Neoproterozoic and early Mesozoic, respectively, and a later period of a more rapid Cenozoic cooling (Figure 5.14). This Cenozoic cooling was of smaller magnitude than that experienced by samples 16-T1-5a and 6a. The best fit model of sample 16-T1-10a shows that it cooled from ~70°C with a less constrained onset of cooling (~40±20 Ma) indicating that an amount of 50°C of cooling affected it. The cooling rate is not well constrained given the wide range of possible onset of cooling ages but ranges from 2.5-0.83 °C/Myr (Figure 5.14).

Similarly, the best fit model for sample 16-T1-11a indicates that it cooled from 75°C since ~23 Ma (i.e. 55°C cooling magnitude; Figure 5.14). The timing of onset of cooling is well constrained compared to sample 16-T1-10a but the low number of good fits indicates that this model is possibly associated with an increased uncertainty. The cooling rate calculated for this cooling event is ~2.39 °C/Myr.

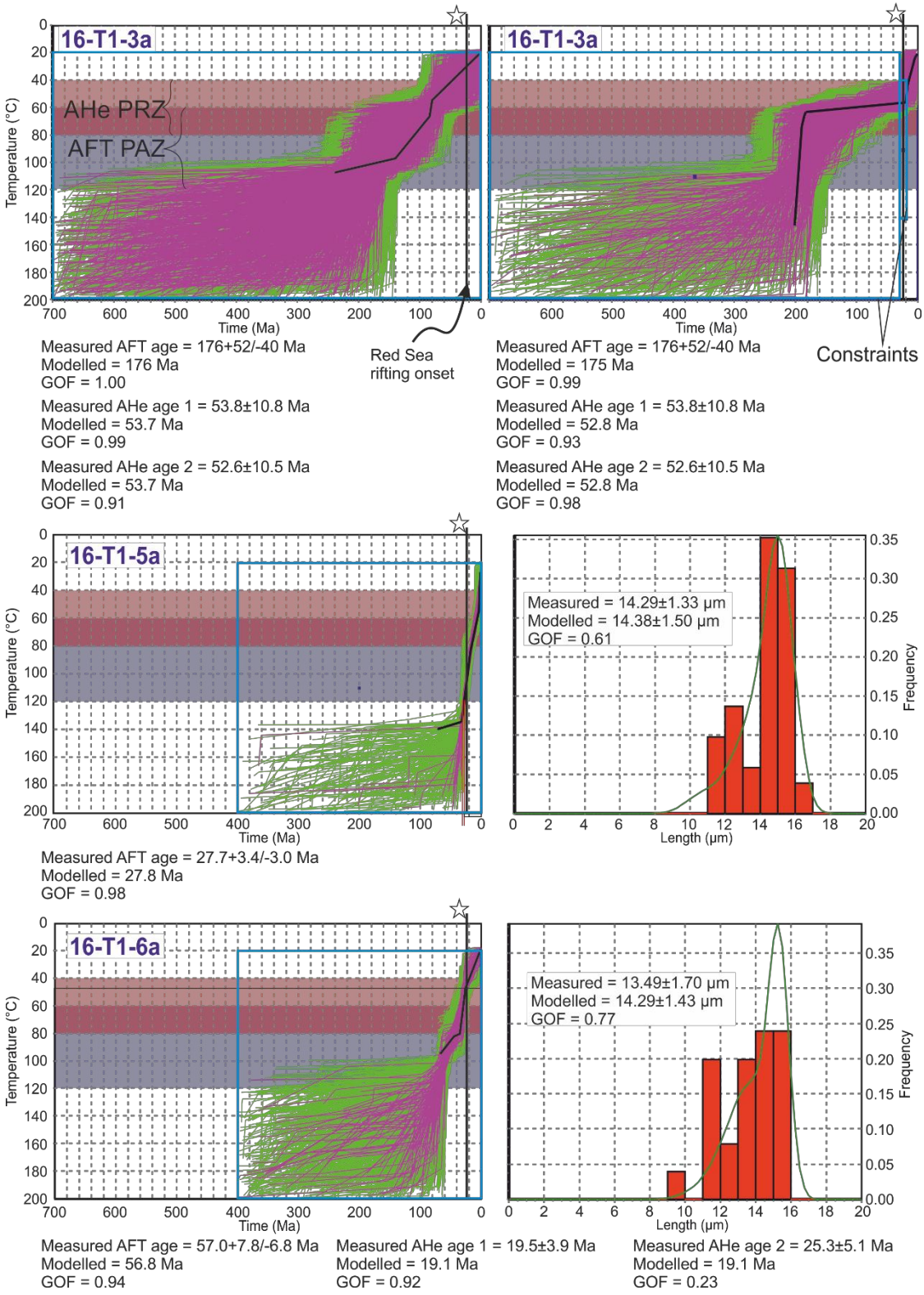

Figure 5.14: HeFTy models showing t-T paths, measured and modelled c-axis projected FT length distributions. Green lines: acceptable fit; pink: good; black: best. The model starting age is always older than double the AFT central age (see constraining boxes (blue rectangles)). 16-T1-3a was modelled with (right) and without (left) an imposed constraint at the onset of rifting (~23 Ma). Only AFT data were used in the modelling of 16-T1-5a and 11a. The vertical line with the star at the top represents the time of the onset of the Red Sea rifting.

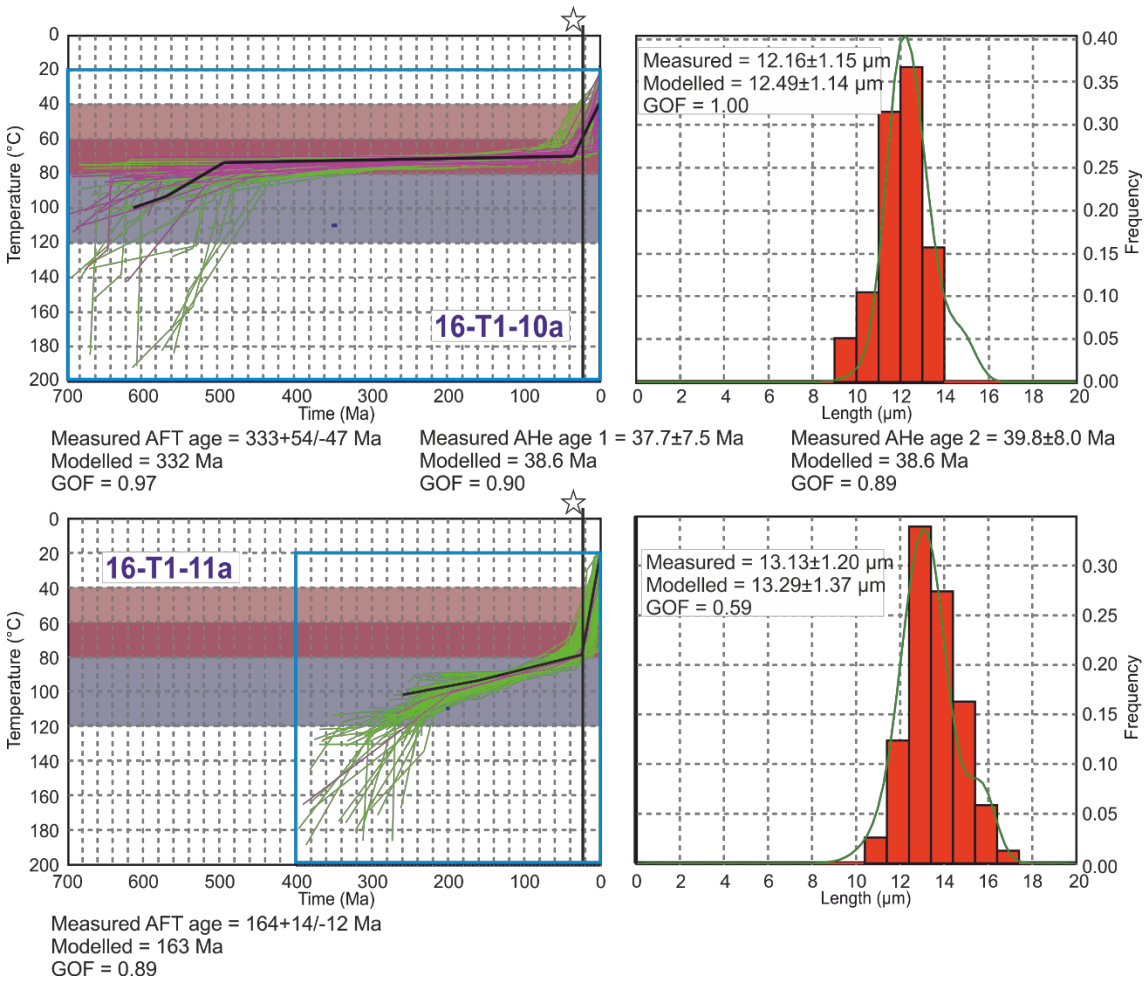

Figure 5.14 (continued).

5.6 Discussion

5.6.1 Tectono-geomorphic evolution at the fault block scale

5.6.1.1 Activity of the South-Eastern Fault (SEF) zone

Spatially, it was shown in Chapter 4 that the SEF zone features fractures and kinematic indicators that are not indicative of a particular period as suggested by the regional stress regimes (e.g. Bosworth and Strecker, 1997; Bojar et al., 2002; Johnson et al., 2011) but are rather representative of time-integrated stress orientations. Based on the stress orientations along the JZF-SEF, it was suggested in the conclusions to the previous chapter (Section 4.5) that the dominance of the Oligo-Miocene extension decreases from the JZF to the southeastern end of the SEF. To test whether the effect of this extension resulted in km-scale displacement across the SEF zone, AFT and AHe analysis is used to examine if faulting-induced vertical motion was sufficient to bring

rocks from the PAZ/PRZ or below to the surface. In this scenario, the expected paleo-tectono-thermal behaviour of sample 16-T1-6a (footwall block sample) is that of an exhumed rock with an Oligo-Miocene onset-of-cooling age. In contrast, sample 16-T1-5a (hangingwall block sample) is expected to show a lesser amount of cooling and exhumation, if any, over the same period.

As shown in Sections 5.4.4 and 5.5.2, 16-T1-5a AHe age cannot be used for the interpretation of the fault behaviour, and only the AFT data can be compared across the fault. Assuming no spatial variation in paleo-geothermal gradient, the AFT ages on either side of the SEF (older age for 16-T1-6a than 16-T1-5a) indicate more cooling in the hangingwall block compared to the footwall block over the time span from the Oligocene to the present-day. The same conclusion can be drawn from the thermal modelling and from the radial plots that show two age populations for each sample (Figures 5.9b, 5.10b and 5.14).

Another interpretation of the AFT ages based on the assumption of no variation in the paleo-geothermal gradient is that the fault zone as a whole dips to the northeast and that sample 16-T1-5a is on the footwall block rather than the hangingwall block. However, this interpretation is incompatible with the structural mapping results that indicate either normal dip-slip or oblique (trans-tensional) movements along the fault and shear fracture surfaces and show that the faults within the fault zone dip generally to the southwest (see Section 4.5).

So far, these data have been considered in terms of a constant geothermal gradient; however, this is likely to be an unrealistic approach and the interpretation of the ages and the HeFTy models needs to consider a variable spatial paleo-geothermal gradient. This is of particular importance to the interpretation of data from 16-T1-5a and 6a, whereby lateral variation in geothermal gradient would impact the inferences of relative uplift and exhumation across the SEF. To include all of the possible thermal evolution scenarios, a range of exhumation values (in km) necessary to result in the amount of cooling (in °C) modelled for each sample is calculated using a wide range of paleo-geothermal gradients (from 20 to 60°C/km; Figure 5.15). This range encompasses most of the paleo-geothermal gradient estimates around the Red Sea (e.g. Omar et al., 1987, Szymanski et al., 2016) and would account for abnormal heating that could have been caused by injection of dykes. Values

lower than 20°C/km (e.g. Feinstein et al., 2013) are not used here as the closeness to the rift would imply high paleo-geothermal gradient.

The block southwest of SEF, where 16-T1-5a (sampled close to dykes) is located, hosts a multitude of dykes in contrast to where 16-T1-6a was sampled (Clark, 1987). Onset of dyking events related to the Red Sea extension occurred at ~23-24 Ma (Bosworth et al., 2005). There is no evidence to suggest that all the dykes are of Oligo-Miocene age, but it is possible that those that are would have resulted in an increased local geothermal gradient. The use of a mixture model to interpret the single grain AFT ages for this sample shows that two age peaks are more representative of the data than a single age (Section 5.5.1). The youngest peaks, 20.6±2.5 Ma, is younger than the age of rifting and regional dyking event. It is, therefore, likely that the dyking had reset the AFT clock prior to the last cooling of the sample.

Paleo-geothermal gradients were probably greater than the present day during the onset of the Red Sea extension, particularly in localised areas near dykes (Szymanski et al., 2016). An extreme scenario, in which the paleo-geothermal gradient at 16-T1-5a is assumed to be much higher than that at 16-T1-6a, can be tested to address the possibility of any significant displacement. For this, the lower and higher boundaries of the paleo-geothermal gradient range (i.e. 20°C/km and 60°C/km) were used to calculate the exhumation at 16-T1-6a and 16-T1-5a, respectively. Assuming a flat pre-faulting topography and ~70° dipping normal fault, the maximum displacement that could have possibly been accommodated by the fault during the Red Sea rifting was less than ~600 m (Figure 5.15a-b). This extreme scenario implies that the amount of displacement across this fault zone during the Red Sea rifting, if any, was less than could possibly be recorded by low-temperature thermochronology.

This conclusion is in stark contrast to the exhumation estimate from the Jabal az Zuhd, which have been interpreted to be the result of rift-related uplift (Stockli and Bosworth, 2019). The magnitude and rate of cooling at sample 16-T1-6a (~27 °C and 1.23-0.84 °C/Myr, respectively), which sits along strike of the footwall block of the Jabal az Zuhd Fault, imply that a spatial variation of exhumation can be concluded to have characterised the JZF-SEF footwall blocks whereby the uplift driving the exhumation decreases from the NW towards the SE.

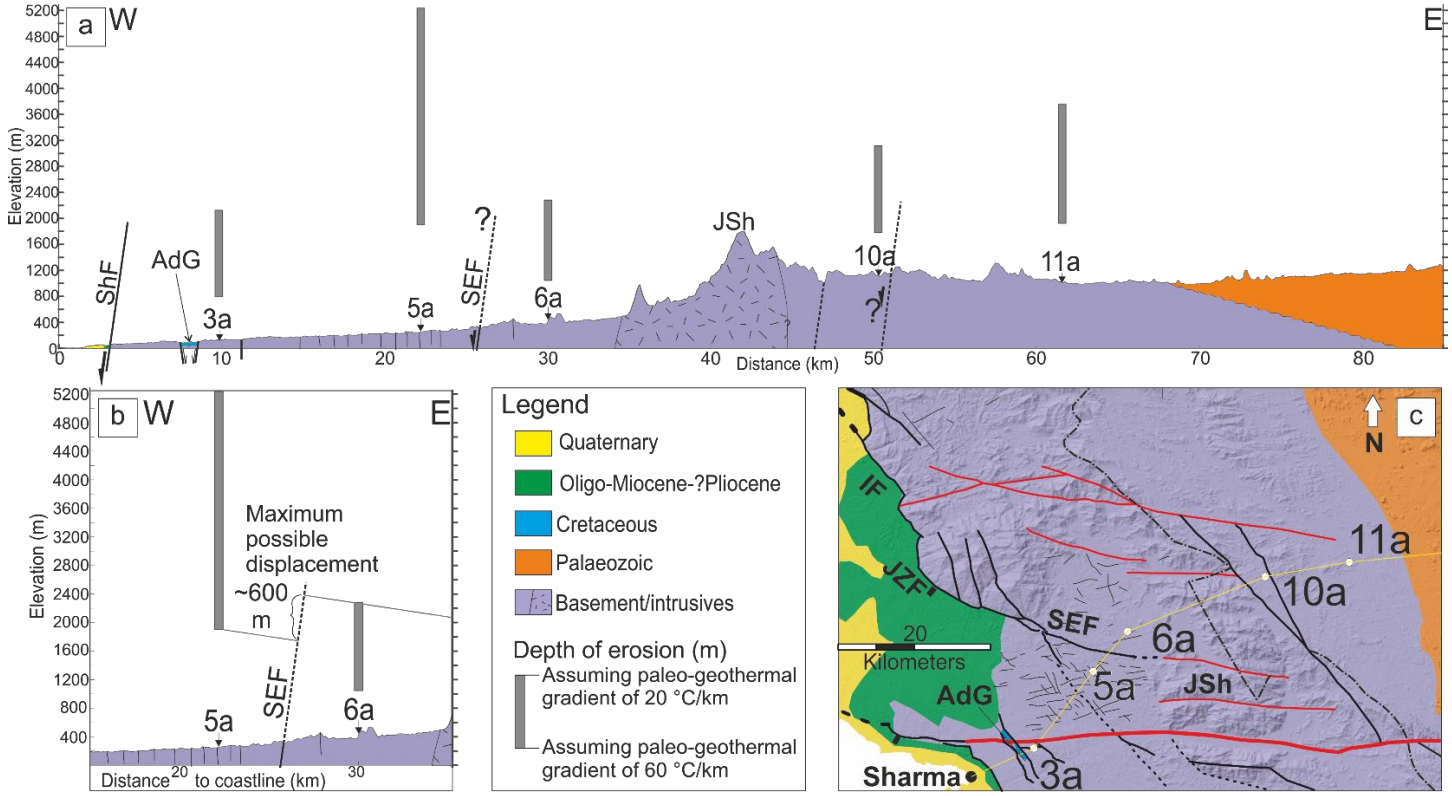

Figure 5.15: (a) A cross-section along transect 16-T1 showing the range of depths of erosion using a range of paleo-geothermal gradients (20-60 °C/km), where the maximum possible depth of erosion corresponds to the 20 °C/km gradient, and vice versa. Erosion depth estimation is based on the cooling magnitudes since the onset of rifting (~23 Ma) deduced from the HeFTy models. (b) Diagrammatic calculation of the maximum possible displacement across SEF, where end-member geothermal gradients are assigned to 16-T1-5a and 6a as shown. Note that, even with this extreme scenario, the maximum possible displacement across the SEF would not be detectable using the low-temperature thermochronology techniques employed here. (c) Simplified geological map showing the cross-section line.

5.6.1.2 Activity of the Sharma Fault (ShF)

Sample 16-T1-3a is located in the footwall block to the east of the AdG, which is located within the footwall block bounded by ShF where Miocene carbonate rocks are faulted near Sharma (Hughes et al., 1999; Figure 5.15a). The faulted contact suggests that footwall uplift occurred during or after the carbonate formation. However, sample 16-T1-3a has AFT and AHe ages that are older than the Late-Oligocene-Early-Miocene ages that characterise existing vertical transects from the northeastern Red Sea margin (Stockli and Bosworth, 2019). As discussed earlier, the ages here represent the time-integrated thermal history with a long residence in the PAZ causing significant annealing during cooling (see Omar et al. (1989) for similar examples from the western Gulf of Suez margin). Therefore, the ages do not represent a specific uplift (cooling) event, which implies that the exhumation and, by inference, the displacement across the ShF were not sufficient to yield ages similar to or younger than the rifting (i.e. tectonically driven exhumation has not brought rocks during Red Sea rifting from temperatures above the PAZ to the surface).

To corroborate this interpretation, the thermal modelling of sample 16-T1-3a suggests that a small fault scarp (~500-600 m) formed to its west, most likely at the ShF, and the ShF footwall block experienced small (<1 km) exhumation during the rifting of the Red Sea (Figure 5.15a). Similar to the JZF and the SEF, the interpretation here indicates a diminishing cooling (exhumation) from the footwall block where the Jabal Dabbagh is located (Stockli and Bosworth, 2019) towards the ShF. In other words, the fault displacement in this case would be decreasing from the SE towards the NW.

The rapid cooling signal at ~200±20 Ma modelled for sample 16-T1-3a is not detected in other samples in this study. However, this signal falls within a range of Permo-Triassic cooling ages from the CARF and southwest Jordan (Feinstein et al., 2013; Szymanski et al., 2016; Figure 5.14). Given this sample age, it is possible that Early Mesozoic rifts beneath the Arabian Platform (e.g. Faqira et al., 2009) and the eastern Mediterranean were associated with far-field stresses that were manifested in the form of uplift-driven exhumation and cooling in this study area.

5.6.1.3 On the spatial extent of extension inboard of the escarpment

A west-dipping normal fault is a possible explanation of the thermal modelling relationship of 16-T1-10a and 11a, whereby more cooling is noted in the 16-T1-11a model (Figures 5.14-5.16). Because this study did not focus on the possibility of rift-related faulting east of the escarpment, any faulting between 10a and 11a was not ground-truthed, although a previous map of the area (Clark, 1987) shows that a fault is present just to the east of the location of 16-T1-10a. Although this requires further work to affirm or dismiss, it is noted that it is located within a very wide zone of initial extension of the northern Red Sea (Stockli and Bosworth, 2019).

5.6.2 Tectono-geomorphic evolution at the margin scale

5.6.2.1 Evolution of the NE Red Sea escarpment

The thermal modelling shows that the evolution of the margin presented in this chapter does not conform to any one end-member model of escarpment evolution (Gallagher et al., 1998; Figure 5.16). It is proposed here that the escarpment evolution featured different characteristics of these models that influenced different parts of the margin. This complicated erosional evolution is likely controlled by the position of the study area at a relay zone between two Miocene rift faults (see below).

For instance, denudation is shown to have occurred on both sides of the escarpment advocating a pinned divide model. Conversely, no km-scale fault scarp developed near Sharma as inferred from the thermal modelling of sample 16-T1-3a suggesting, at least partly, a downwarp model; a proposition that is supported by the preservation of Upper Cretaceous units in AdG that would have been likely eroded if km-scale footwall uplift/erosion occurred. This interpretation is supported by AFT data of samples 16-T1-3a and 16-T1-6a where the age of 16-T1-3a (closest to the coastal fault) is older than that of 6a (closest to the escarpment; cf. Gallagher et al., 1998; Figure 5.16). It is possible that the small fault scarp of ShF retreated to form the present-day erosional escarpment without resulting in a Miocene age of the thermochronometric clocks at 16-T1-3a (escarpment retreat model). However, given the structural

context of this study area (relay zone; see below) and the likely NW-ward direction of the paleo-drainage that transported clastics to the Midyan Basin during the Early Miocene (Hughes et al., 1999) it is likely that such drainage dominated the erosion of the seaward part of the escarpment. This reduces the possibility that margin-perpendicular drainage was dominant during the early rifting, which would have driven the escarpment retreat.

Steckler et al. (1998) argued that on the western Gulf of Suez the development of the escarpment and the plateau was a consequence of the rifting. Here, this conclusion is not substantiated. The contrast in terms of uplift is interpreted here to be related to the structural context on both margins. That is, in this study area presented in this chapter the transect does not cross faults where significant uplift can be inferred and is rather positioned at low displacement parts of the faults.

The cooling of the samples east of the escarpment is interpreted to be regional in extent even if fault-driven uplift and erosion are not ruled out. Being on the plateau side of the escarpment would suggest that either a more regional uplift has caused this amount of exhumation during the Cenozoic, and/or significant erosion by fluvial processes resulted in the stripping of the pre-rift sedimentary cover. Miocene fluvial sediments in northeastern Sinai were interpreted to have been transported from the south (Zilberman and Calvo, 2013) and suggest that significant erosion by fluvial processes (supplying such sediments) could have occurred at and near the locations of 16-T1-11a and 10a.

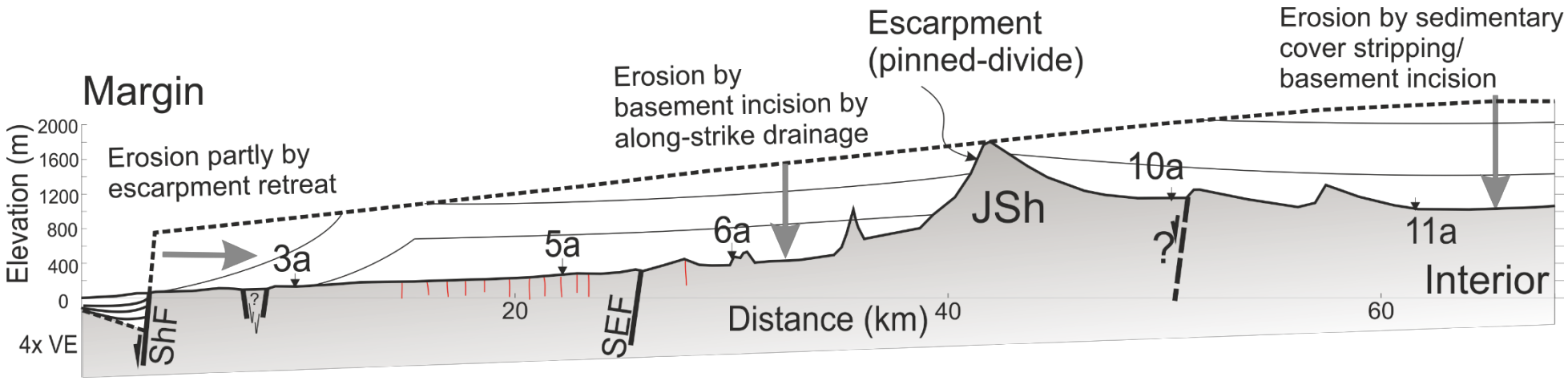

Figure 5.16: A proposed model for the tectono-geomorphic evolution of the NE Red Sea margin along the transect of the samples used for the thermochronological study (location of transect is the same as that of Figure 5.15). ShF: Sharma Fault; SEF: South-eastern Fault; JSh: Jabal ash Shati. The depth of erosion at each sample location is calculated using 50-55°C/km paleo-geothermal gradients. The dashed line does not exactly represent a paleo-surface, but is constructed based on depth of erosion from each sample. The thin black lines are schematic demonstrating how erosion evolved. Note that ShF could have initiated a fault scarp that retreat to form the present-day escarpment but the along-strike (NW-directed) drainage would have played a more major role. Note also that SEF did not have a measureable effect on the paleo-topography prior to the erosion and that the paleo-geothermal gradient at 16-T1-5a was possibly extremely high and local. The red lines represent dykes without reference to their age.

Given the tectono-geomorphic evolution deduced from the low-temperature thermochronometers (Figure 5.16), the aforementioned observations favour a model in which the SEF and ShF are located at or near the tip of faults whose activities exhumed the Jabal az Zuhd (JZF) and Jabal Dabbagh, respectively. In such a model, the study area represents a relay zone between the two active faults (Figure 5.17).

The structural mapping (Chapter 4) revealed that no through-going fault was established between the ShF and JZF or at the SEF. However, kinematic indicators on shear fractures measured just east of the Aynunah Graben are compatible with trans-tensional deformation that could have started to be accommodated between the ShF and JZF but did not progress to a transfer fault.

An example of a major transfer fault linking two normal faults that dip in the same direction is the N-S Nezzazat Fault along the eastern Gulf of Suez, which links the Hammam Faraun Fault with the faults of the Gebel Abu Durba and Gebel Araba blocks (Sharp et al., 2000). It is unclear at this stage why the ShF and JZF did not link in a similar manner given the significant displacements at the JZF and the coastal fault system of which ShF is part. Nonetheless, it is plausible that the change of the stress vectors that accompanied the onset of the Gulf of Aqaba tectonics during the Middle Miocene has had an influence in lessening the deformation near the rift flank and the migration of strain towards the rift axis.

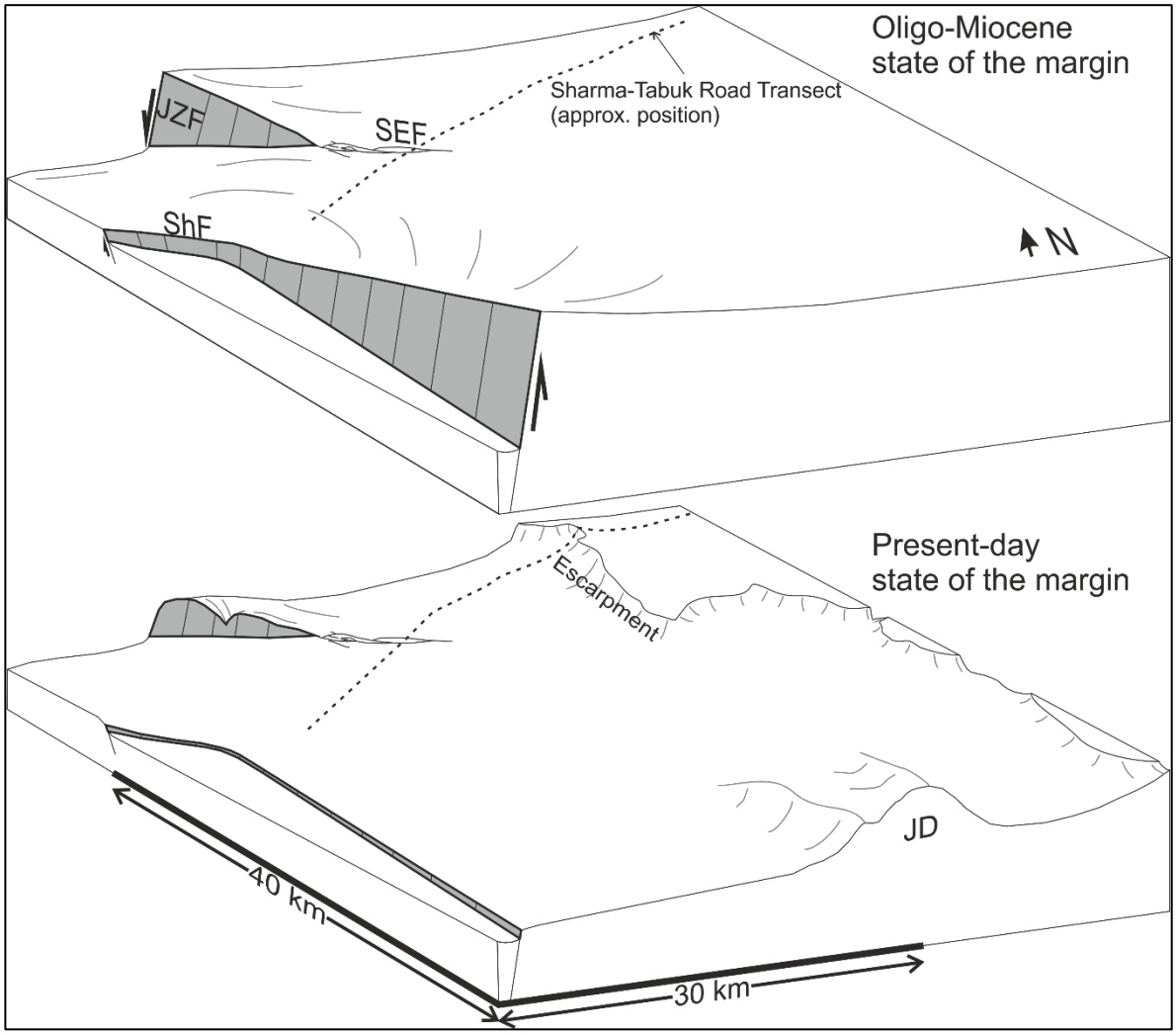

Figure 5.17: A schematic 3D model showing the interpretation deduced for the tectono-geomorphic history of the study area, proposing that the area represented a relay ramp between two SW/SWW-dipping normal faults. JZF: Jabal az Zuhd Fault; SEF: South-Eastern Fault; ShF: Sharma Fault; JD: Jabal Dabbagh. JD is shown to relate to the exhumation estimate by Stockli and Bosworth (2019).

5.7 Conclusions

Low-temperature thermochronological data across the South-Eastern Fault (SEF) of the Midyan Peninsula indicate that more cooling since the onset of rifting (earliest Miocene) has been experienced at the hangingwall block of the fault zone than the footwall block. Even with extremely different paleo-geothermal gradients (20°C/km at the footwall block and 60°C/km at the hangingwall block) and assuming a flat pre-faulting topography, the maximum estimate of possible

displacement accommodated by the fault during the Red Sea rifting is less than ~600 m, less than what could possibly be resolved by low-temperature thermochronology. The rapid and greater cooling of 16-T1-5a (located southwest of SEF) is here attributed to rapid Early Miocene cooling after heating had reset the clock (e.g. by magmatism as suggested by the spread of dykes).

The closeness of sample 16-T1-3a to the coastal fault (ShF) which was active during the Miocene rifting indicates that the AFT age (Jurassic) is more likely representative of a mixed age, and that the sample has experienced approximately 40°C of cooling since the onset of rifting. Therefore, the faulting-driven uplift of the ShF footwall block was enough to form a fault scarp that, later through erosion by escarpment retreat or along-strike fluvial drainage, resulted in the present-day erosional escarpment.

On the plateau, thermal modelling shows that more cooling has been experienced by 16-T1-11a than that by 16-T1-10a since the earliest Miocene. The cooling of these samples is interpreted to be regional in extent even if fault-driven uplift and erosion (caused by a possible fault between the two samples) are not ruled out. Being on the plateau side of the escarpment would suggest that either a more regional uplift has caused this amount of exhumation during the Cenozoic, and/or significant erosion by fluvial processes resulted in the stripping of the pre-rift sedimentary cover.

Subject to the uncertainty of the data, and taking into consideration the small number of data points, the most suitable tectono-geomorphic model to explain the low-temperature thermochronological data (here and from other authors around the study area) is that of a relay zone between two faults dipping towards the SW (i.e. JZF and ShF and its southern extension). Such a model shows the structural and geomorphic behaviour (in terms of fault displacement, uplift and erosion) that is expected at the scale of extensional half-grabens and relay zones.

Chapter 6 Drainage evolution across rifts and rifted margins: Implications on the sediment pathways into the northern Red Sea and nearby basins

This chapter extends the uplift estimates, the methodology of which were presented in Chapter 3, to cover Sinai and the African Gulf of Suez and Red Sea margins. The uplift estimates are then integrated with drainage network analysis to describe a model of the drainage evolution since the start of rifting. The conclusions reached on the activity of the rift faults and exhumation (Chapter 4 and Chapter 5) are taken into consideration as a more local case study to validate the drainage evolution model.

6.1 Introduction

Rift margin drainage in continental extensional domains has a great impact on the evolution of sediment routes, hence, sediment accumulation at the depocentres (Gawthorpe and Leeder, 2000). Understanding the uplift of the rift flank is important to predict the drainage evolution through time that influences the distribution of major clastic sedimentation in the rift basins and along the margin. Due to the interest in petroleum activities in rifts and passive margins being mostly focussed on offshore areas, the importance of the geomorphic evolution on exploration prospectivity can be overlooked.

The generation of accommodation space in response to continental rifting could result in the capture of drainage and the establishment of a base-level, resulting in a large-scale modification of the pre-rifting drainage that affects catchment sizes and drainage network (e.g. Allen, 2017). In addition to uplift at the footwall blocks, these factors interact and affect the rift-related drainage and should have an impact on the clastic sediments distribution along the margins.

This chapter aims to estimate the tectono-geomorphic evolution of the margins of the northern Red Sea, the Gulf of Suez and the Gulf of Aqaba focussing on the drainage evolution (Figure 6.1). In order to reconstruct the tectono-geomorphic history of the study area, the following objectives are considered:

1- Inverse modelling of stream profiles to estimate the uplift history is extended beyond the area covered in Chapter 3 (northeastern Red Sea and eastern Gulf of Aqaba margins) to include the African Red Sea/Gulf of Suez and the Sinai margins.

2- Flow direction of large-scale pre-rift paleo-drainage is estimated by integrating indications of relict landscape, drainage direction changes and the uplift history estimated from the drainage inversion.

Although constraining the mass balance of the sediments is not possible at this stage given inaccessibility to subsurface data for this project, the results of the study presented in this chapter should serve as a relative predictive tool for sediment dispersal along the northern Red Sea margin. This is of particular interest to petroleum exploration focussed on point-source clastic reservoirs in rifted margins.

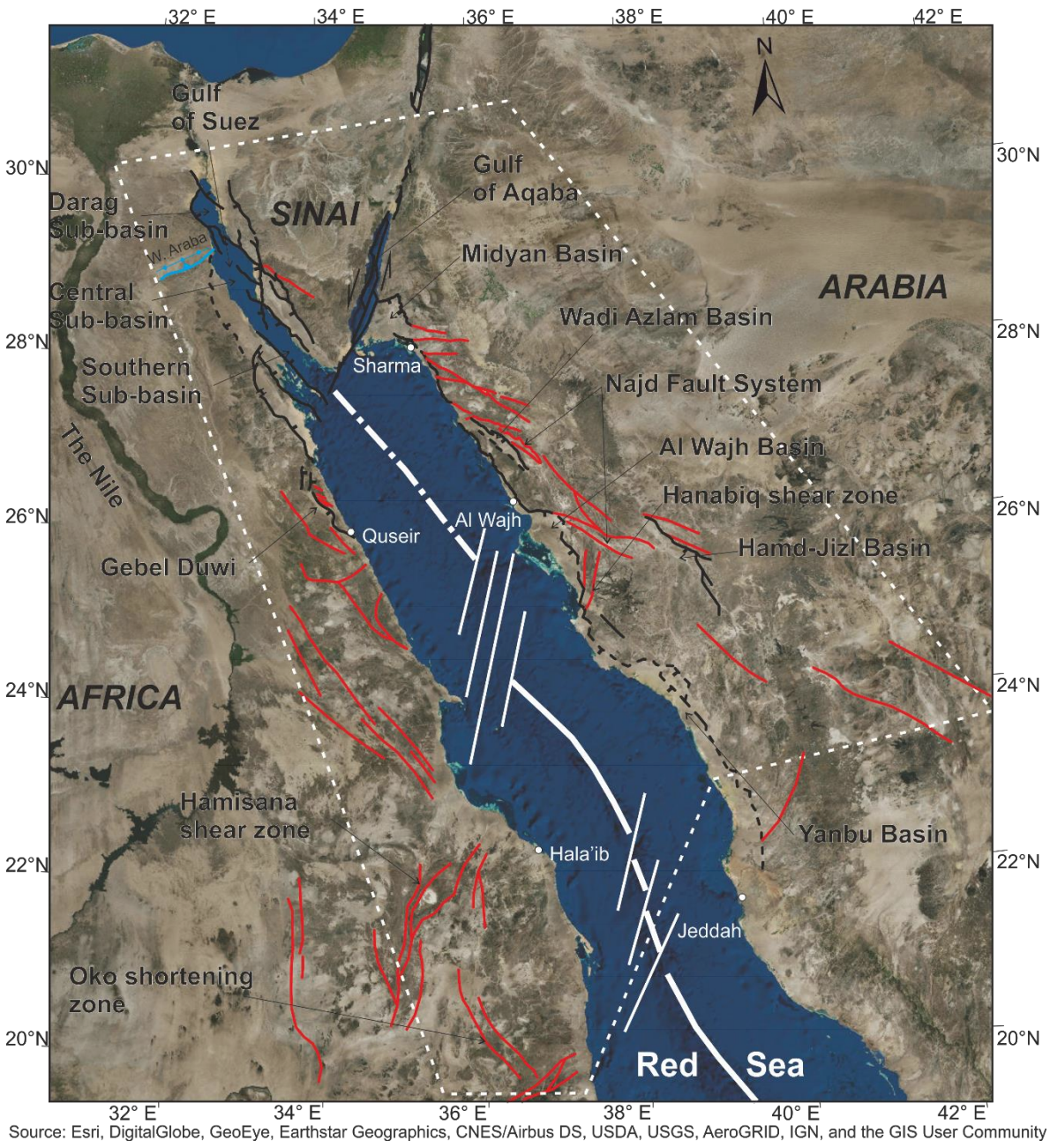

Figure 6.1: A satellite imagery map showing the study area (dashed white polygon). Also shown are the major rift basins and faults (black lines; Modified from Bosworth (1995), Tubbs et al. (2014), Bosworth (2015) and Szymanski et al. (2016)), the pre-rift Precambrian structures (Red lines: Modified from Bosworth et al. (2005) and Johnson et al. (2011)). Wadi Araba thrust and anticline (light blue) to the west of the Gulf of Suez are Late Cretaceous (Bosworth et al., 2005).

6.2 Paleo-drainage around the northern Red Sea: current understanding

Paleo-drainage since the Oligocene on the Arabia margin has been inferred to be generally directed to the north towards the Mediterranean Sea (Feinstein et al., 2013; Segev et al., 2017). Zilberman and Calvo (2013) suggested that the area covering eastern Sinai, the Dead Sea Rift and the western Jordanian Plateau was a site of Early Miocene fluvial sedimentation, partly sourced from the Precambrian Arabian-Nubian Shield basement. This sedimentological evidence further supports the northward drainage direction. Furthermore, the northward direction has been suggested for major drainage at the Hamd-Jizl Basin within the Central Arabian Rift Flank (CARF) prior to capture by a more west-directed drainage initiating near the Al Wajh Basin (Brown et al., 1989; confirmed in Chapter 3). Such a general direction of flow is expected given the plate-scale tilt that is caused by the Afar Plume during the Early Oligocene and the existence of the Neo-Tethys Ocean in the north (Avni et al., 2012).

On the African margin, the spatio-temporal evolution of the River Nile has been a matter of debate (e.g. Pik et al., 2003; Macgregor, 2012; Fielding et al., 2018). Macgregor (2012) concluded that significant drainage organisation affected the catchment, suggesting that most of the present-day course of the Egyptian River Nile was not established until the Late Miocene. In his model, Macgregor (2012) suggested that prior to the Late Miocene, the Red Sea Hills present-day tributaries of the Nile were generally directed further towards the west to join a northward flowing river approximately 700 km west of the present-day Nile course.

Conversely, using low-temperature (U-Th)/He thermochronology, Pik et al. (2003) argued for an Oligocene (25-29 Ma) initiation of the erosion by the Blue Nile (the Nile tributary that has headwaters on the Ethiopian Highlands). This older establishment of the Nile was concluded based on a provenance study of early Oligocene (~30-31 Ma) sedimentary units in the Nile delta that show geochemical signatures of the Ethiopian continental flood basalts (Fielding et al., 2018).

At the Red Sea offshore Halaib Triangle (Figure 6.1), Late Miocene to recent thick sedimentary units deposited over Middle Miocene salt were interpreted to have been sourced by the Halaib catchment, located in southeastern Egypt and northeastern Sudan (Macgregor, 2012). The main drainage trunk of the Halaib catchment, which is now a dry valley, is directed towards the north and northeast parallel to the Hamisana Shear Zone. This suggests that at least since the Late Miocene this valley hosted a north-directed river.

To sum up, the overall drainage of western Arabia and northeastern Africa prior to the Red Sea rifting was directed towards the north. Local variations, however, did occur where the drainage utilised pre-existing basement deformation resulting in directions that varied from northeast to northwest.

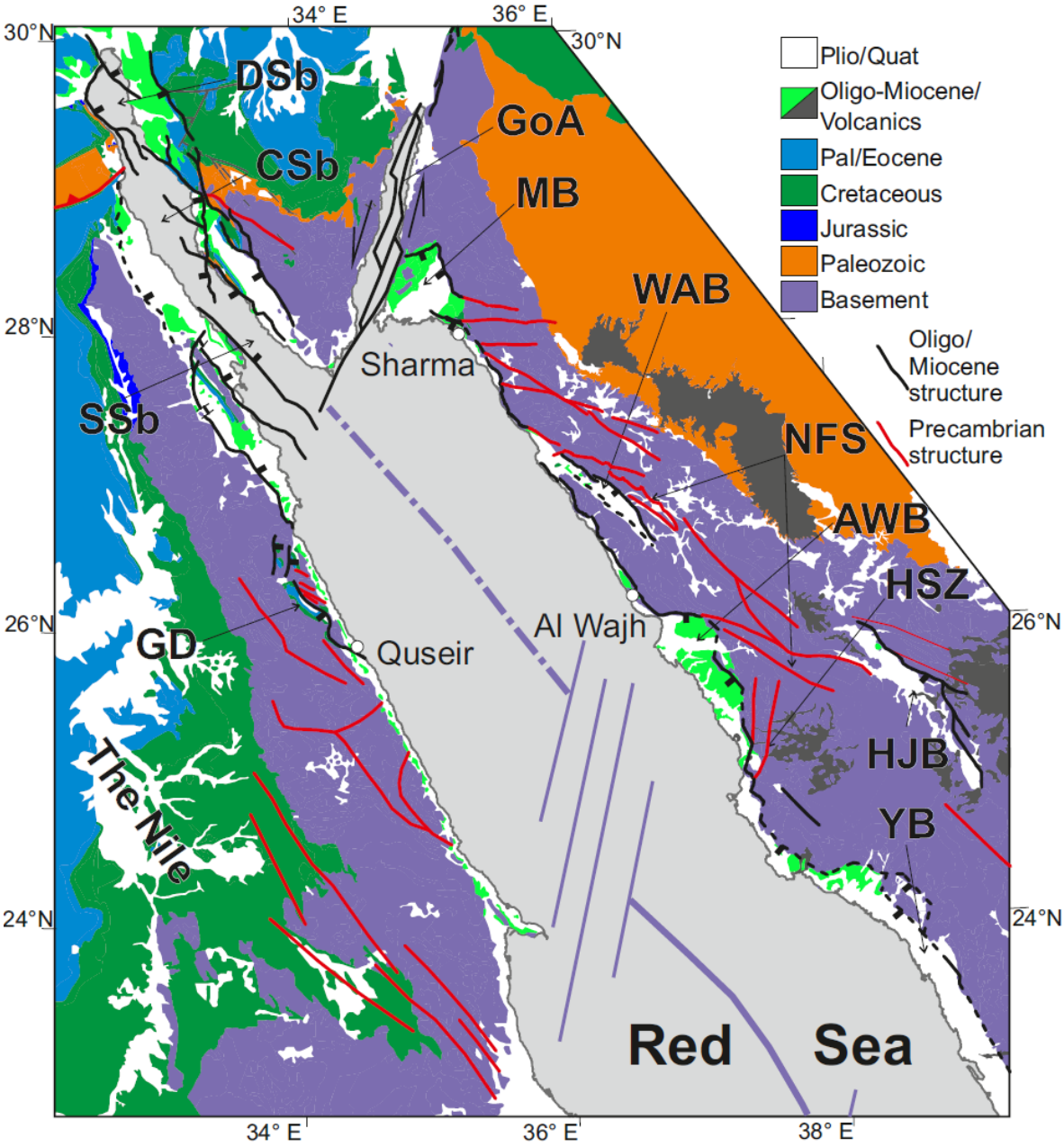

Figure 6.2: Simplified geological map of the study area, showing the pre-existing Proterozoic basement structures and rift faults. The Arabian geology is modified from Clark (1987), Brown et al. (1989) and Powell et al. (2014). The Egyptian and Sinai geology is modified from Egyptian Geological Survey and Mining Authority (1981). Midyan Basin (MB) faults are from Tubbs et al. (2014). Wadi Azlam Basin (WAB) and Gebel Duwi (GD) faults are from Bosworth (2015). Hamd-Jizl (HJB), Al Wajh (AWB) and Yanbu (YB) Basins faults are from Szymanski et al. (2016). Najd Fault System (NFS) and Hanabiq Shear Zone (HSZ) are from Johnson et al. (2011). DSb: Darag Sub-basin; CSb: Central Sub-basin; SSb: Southern Sub-basin. GoA: Gulf of Aqaba.

6.3 Methodology

6.3.1 Data

The dataset for this chapter is extracted from the Advanced Spaceborne Thermal Emission and Reflection Radiometer global digital elevation model (ASTER GDEM; ~30 x 30 m). The data were downloaded from https://gdex.cr.usgs.gov/gdex/ (ASTER GDEM is a product of NASA and METI). The data cover all margins of the northern Red Sea, Gulf of Aqaba and Gulf of Suez (Figure 6.1).

6.3.2 Methods

6.3.2.1 Catchment and drainage network extraction

The approach used in Chapter 3 and detailed in Section 3.2.2.1 for catchment and drainage network extraction was extended to cover the African Red Sea/Gulf of Suez and Sinai margins. The processes were done using ArcMap ArcToolbox. The approach starts by conditioning the DEM (filling data gaps) then calculating the drainage flow direction, which was used to extract the drainage catchments and calculate the drainage accumulation (i.e. number of raster cells pouring into a particular cell (Tarboton et al., 1991)). Raster cells with accumulation values greater than ~10 km^2 were extracted and converted into stream order vector format. Flow direction was then used to determine the boundaries of the catchments. Catchments with more than 200 km^2 of area were extracted along the Red Sea and Gulf of Suez margins and those larger than 20 km^2 were extracted along the Gulf of Aqaba.

The horizontal accuracy decreases where the profiles slopes become close to horizontal (e.g. elevated paleo-lakes). This is clear on the Egyptian side of the margin where the stream and catchment extraction process has resulted in streams that cross catchment boundaries. This issue, however, is not persistent and is limited to a few locations across the whole study area. Furthermore, no large catchments or streams were affected by this issue, which reduces the implications that any errors might have on the study.

6.3.2.2 Uplift from drainage inverse modelling

In addition to the northeastern Red Sea and eastern Gulf of Aqaba margins (Chapter 3), uplift estimation was extended to cover the Sinai Peninsula, the western Gulf of Suez and the African Red Sea margin. The approach used here to estimate uplift history is based on the inversion of drainage stream profiles, and the methodology was described in Chapter 3 (Section 3.2.2.2).

Beside the drainage stream profiles extracted and used in the uplift estimation in Chapter 3, extra profiles were extracted from the DEM data of the Egyptian catchments that pour into the Red Sea and the Gulf of Suez and from the Sinai catchments. For each drainage stream, its position (longitude and latitude), distance from the coastline, elevation, and drainage were been extracted at a spacing governed by the horizontal raster resolution of the input Digital Elevation Model (DEM; ~30 to 43 m). The same erosional parameters used in the Arabian margin were applied during the inversion of the drainage profiles from Sinai and African margins. The data were all extracted and sent to Dr. Gareth Roberts (Imperial College London) who performed the inverse modelling.

To stabilise the inversion model, data from other streams from outside the area of interest were added to the model. These include streams from the rest of the Arabian Peninsula and Nile tributaries. The latter profiles were provided by Dr. Roberts. The total number of profiles that were used as input data for the inverse modelling is 1079 (Appendix I).

Compared to the input data used in Chapter 3, the input data here are more spaced out (grid resolution ≈ 25 km). The reason for that is the addition of more data from outside the study area to stabilise the inversion, which inhibits producing high resolution models at the study area.

6.3.2.3 Plate restoration using GPlates

As the study area spans three tectonic plates (Africa, Arabia and Sinai), restoration was needed to better estimate the paleo-drainage across the eventual rifted margins and to put the uplift maps in a regional context. All of the input data that are used in the building of the drainage evolution maps were incorporated into a GPlates project and restored to time steps relevant to the rift history (e.g. Bosworth

et al., 2005). The restoration on GPlates uses the plate reconstruction rotation file by Seton et al. (2012). However, the motion was edited here according to Schettino et al. (2016) and Schettino et al. (2019) as their calculated motion vectors were more focussed on the Red Sea.

6.3.2.4 Determining paleo-drainage and subsequent evolution

The evolution of drainage in response to rifting and uplift modifies the paleo-drainage. However, vestiges of the pre-rift paleo-drainage can be deduced by examining the shapes and sizes of the catchments, the lateral arrangement of drainage network and the drainage stream profiles (i.e. elevation vs distance from the valley mouth). In essence, the incorporation of the pre-rift drainage into the rift drainage results in catchments and streams that deviate from the typical rift drainage (e.g. Gawthorpe et al., 1994).

Paleo-drainage can be interpreted within the drainage network by mapping drainage anomalies that signify the capture of pre-existing drainage by rift-related drainage. The capture of drainage is associated with an elbow of capture (an abrupt change of the direction of stream flow) that, on plan-view, is anomalous compared to the ambient drainage.

Determining the paleo-drainage streams was performed by locating low-gradient parts of long streams that form the main channels of the largest catchments in the study area. These low-gradient segments are located in the upstream parts of the catchments and are largely separated from the downstream segments by knickzones or knickpoints. The low gradient is characteristic of the pre-rift paleo-drainage in relict landscapes whereby the topography was mostly subdued. Using these low-gradient stream segments and integrating them with capture points and uplift loci, instances of drainage modification throughout the rifting were predicted.

6.4 Results

6.4.1 Uplift estimation

Overall, the modelled and observed are well fitted with a residual RMS misfit of 1.71 after performing the inversion using all of the 1079 profiles, which also include

profiles outside the northern Red Sea area as mentioned earlier. However, misfit occurs at some upstream sections of some profiles particularly at the Gulf of Aqaba region (Figure 6.3). Uplift estimates through the inverse modelling of the drainage profiles are controlled by the coverage of the input data. The coverage deteriorates with time and away from the streams used in the modelling (Figure 6.4). Moreover, the maps show that, in general, the Arabian margin has more data coverage. This has an impact on the confidence levels that can be attached to interpretation of the African and the Sinai margins.

Cumulative uplift and uplift rate maps were generated for the margins surrounding the northern Red Sea and restored using GPlates (Figures 6.5-6.8). The present-day coastline represents a limit to where uplift can be estimated as no input data (i.e. drainage profiles) were extracted below the present-day sea-level. Therefore, the white area in the uplift maps does not correspond to the extent of each tectonic plate but is rather produced because no data are available there.

In general, the spatial distribution of the uplift along the margins of the study area is asymmetric, which is reflected in the landward extent of the drainage catchments. That is, a narrow uplift zone is estimated where the short catchments are along the African Red Sea and a wider uplift zone is estimated along the Arabian Red Sea margin which hosts larger catchments.

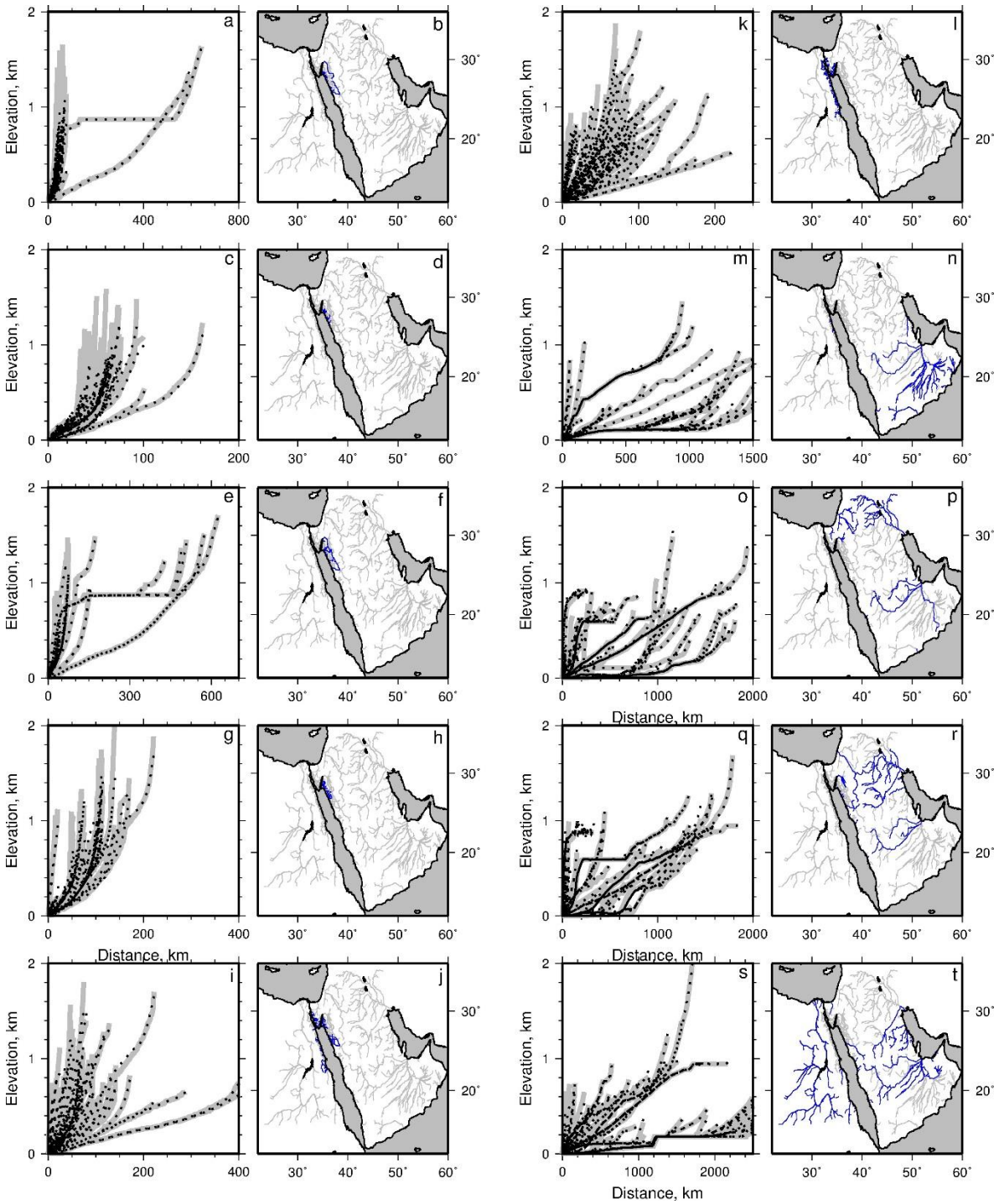

Figure 6.3: Cross-sectional and map views of the streams that were used to invert for uplift. On the cross-sections, the solid grey lines are the extracted stream profiles and the dotted black lines are the modelled profiles. Streams in (a), (c), (e), (g), (i) and (k) were extracted and conditioned by myself. The rest were provided by Dr. Gareth Roberts (Appendix I), who also performed the inverse modelling and generated the figure.

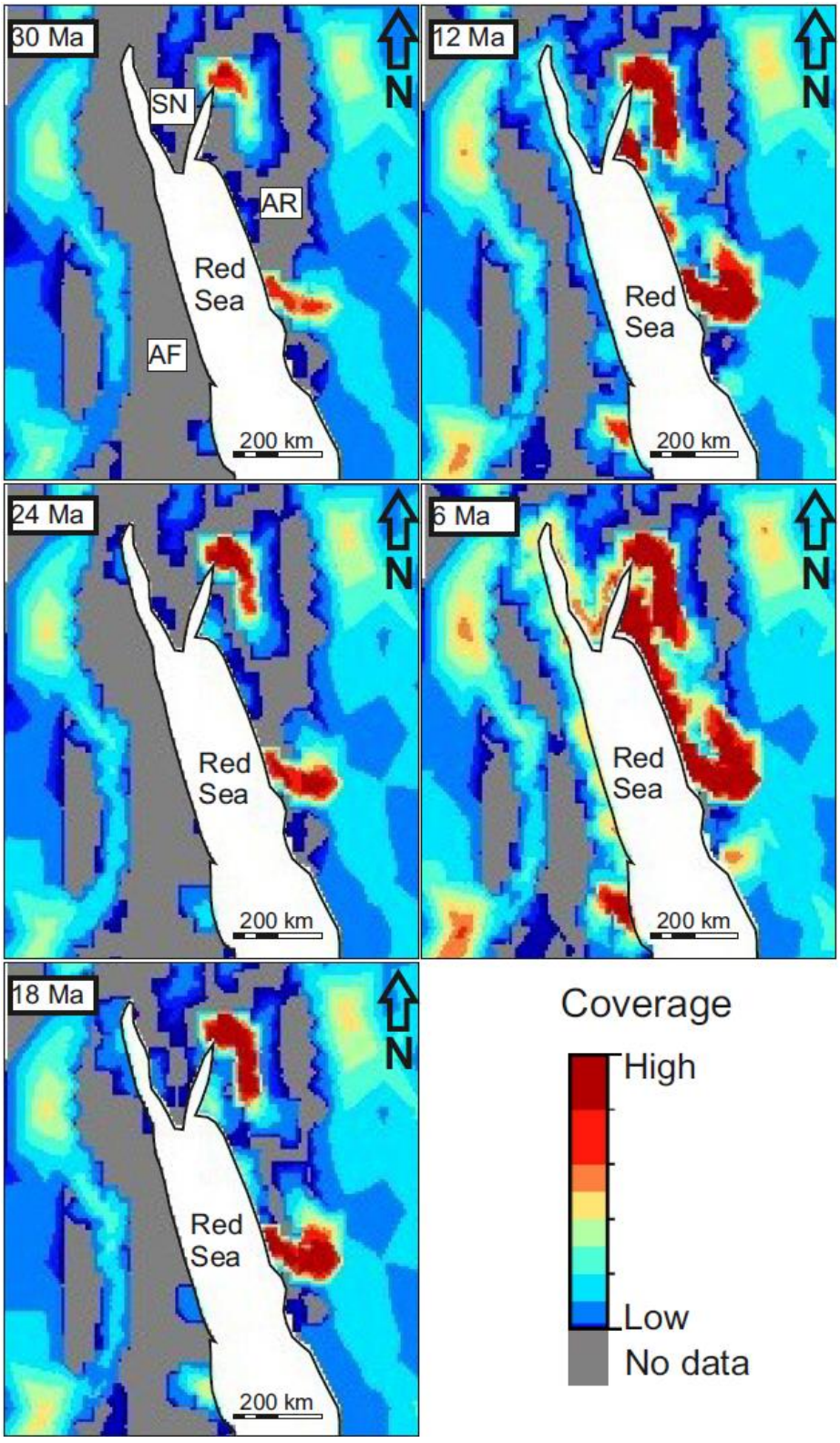

Figure 6.4: Maps of the study area showing the coverage (i.e. the unit-less number of data points used to extract the uplift rate value in a given cell) of the inverse modelling method through time. AR: Arabia, AF: Africa, and SN: Sinai. Maps in figure were generated by Dr. Gareth Roberts.

6.4.1.1 Arabian margin

Discrepancies are noted between the results of the uplift estimates in this chapter compared to the results in Chapter 3 (Section 3.3.2). These discrepancies are mostly in terms of the absolute values of the estimates with the spatial and temporal distribution of uplift in both cases being not too dissimilar. However, there are cases where relatively high uplift rate is estimated at one location in one study but not in the other.

The main differences are noted on the maps of the Early Miocene (22 and 20 Ma time maps) and the Pliocene (4 Ma time map; Figures 6.5 and 6.7). In this chapter, the estimate of the uplift rate during the Early Miocene at the southern part of the study area on the Arabian side (~0.05-0.10 mm/a) is lower compared to the results in Chapter 3 (~0.16-0.17 mm/a). On the other hand, the Pliocene map shows that the uplift at the northern part of the study area extends further towards the southeast compared its extent in Chapter 3.

Such differences are expected given the wider range of stream density (i.e. number of streams used in the modelling per unit area) in this chapter, which requires the upscaling of the results and the smoothing of the uplift estimates. Moreover, the use of drainage profiles from outside the zone of interest (Arabia drainage and Nile tributaries) would have an effect in smoothing the results.

Aside from these differences, the pattern of uplift, in general is similar. A similar trend of uplift shifting from the south of the study area to the north on the Arabian side is noted. Therefore, the interpretation of the uplift maps is done with caution. The uplift maps are best interpreted in terms of the relative timing of uplift events rather than their absolute magnitudes and absolute times.

6.4.1.2 African margin

On the African side, early Miocene uplift (22 and 20 Ma time maps) was focussed at two zones: a northern zone at the northwestern Gulf of Suez margin, and a southern zone at the central Egyptian Red Sea margins (Figure 6.5). These two zones of uplift extended ~100 km inland, perpendicular to the present-day coastline. The northern uplift zone was located at the footwall block of the east-dipping normal fault that bounds the Darag Sub-basin. The southern uplift zone,

however, does not correlate with a mapped fault. The uplift rates at these two zones were comparable to the uplift rates on the Arabian margin (~0.05-0.07 mm/a). Along the rest of the African side of the study area, the uplift rates were close to zero during the early Miocene.

During the Middle Miocene (14 Ma time map), uplift rates increased in the northern uplift zone (~0.1 mm/a), which increased in extent to cover a distance of ~170 km inland and 300-400 km along the rift axis (Figure 6.5). The uplift locus does not seem to correlate with the footwall of a single normal fault during this stage. Comparatively, the uplift rates in the southern uplift zone remained similar to the rates during the early rifting (~0.05-0.07 mm/a). Additionally, another uplift zone started to emerge during the Middle Miocene further to the south at the Halaib Triangle (14 and 12 Ma time maps in Figure 6.5).

From 10 Ma to 4 Ma uplift increased along the Egyptian margin (~0.13-0.15 mm/a) and became more distributed (Figure 6.7). The extent of the uplift across the margin became approximately 170 km inland. There are parts along the margin where more focused uplift is noted and can be associated with normal faults. An example is the uplift at the footwall of the faults that bound the southern Gulf of Suez (Figures 6.5 and 6.7).

At the present-day, high rates are more focussed at particular loci of uplift along the western margin of the Gulf of Suez and the central margin of the Egyptian Red Sea (Figure 6.7). The extent of these loci of uplift is approximately 100 km, perpendicular to the coastline. The smaller extent compared to the extent observed in older times, however, is likely related to the increased coverage towards the present-day. Therefore, the extents of the uplift in older times are likely to be overestimated and the ~100 km estimate from the present-day time map is more accurate.

6.4.1.3 Sinai

In Sinai, during the Early Miocene (22 and 20 Ma time maps) no clear uplift signal was recorded by the inverse model (Figure 6.5). During the Middle Miocene (14 Ma time map) two uplift zones were detected: a western zone along the central Gulf of Suez margin, and an eastern zone along the central Gulf of Aqaba margin.

The western uplift zone was located at the footwall block of the west-dipping fault that bounds the central Gulf of Suez sub-basin (Figure 6.5). This zone extended approximately 70-100 km towards the northeast and recorded uplift rates of approximately 0.1 mm/a. The eastern uplift zone was located next to the initiating Gulf of Aqaba faults and was smaller than the western zone both in extent (~50 km) and rate (~0.05-0.06 mm/a).

At 12 Ma, more uplift in terms of uplift rate (~0.1-0.12 mm/a) and extent (~70-100 km) affected the eastern zone along the Gulf of Aqaba southwestern margin extending towards the southern Sinai (Figure 6.5). On the other hand, the western uplift zone remained relatively similar in terms of extent and rate.

By the Late Miocene (8 and 6 Ma time maps) the south central Sinai became the locus of uplift, with rates reaching 0.14-0.15 mm/a and extent increasing along a north-south trend over ~150 km (Figure 6.7). Since the Pliocene (4 Ma time map) and continuing to the present-day, the uplift zone gradually increased both in extent to cover all of south Sinai and in rate reaching ~0.28 mm/a.

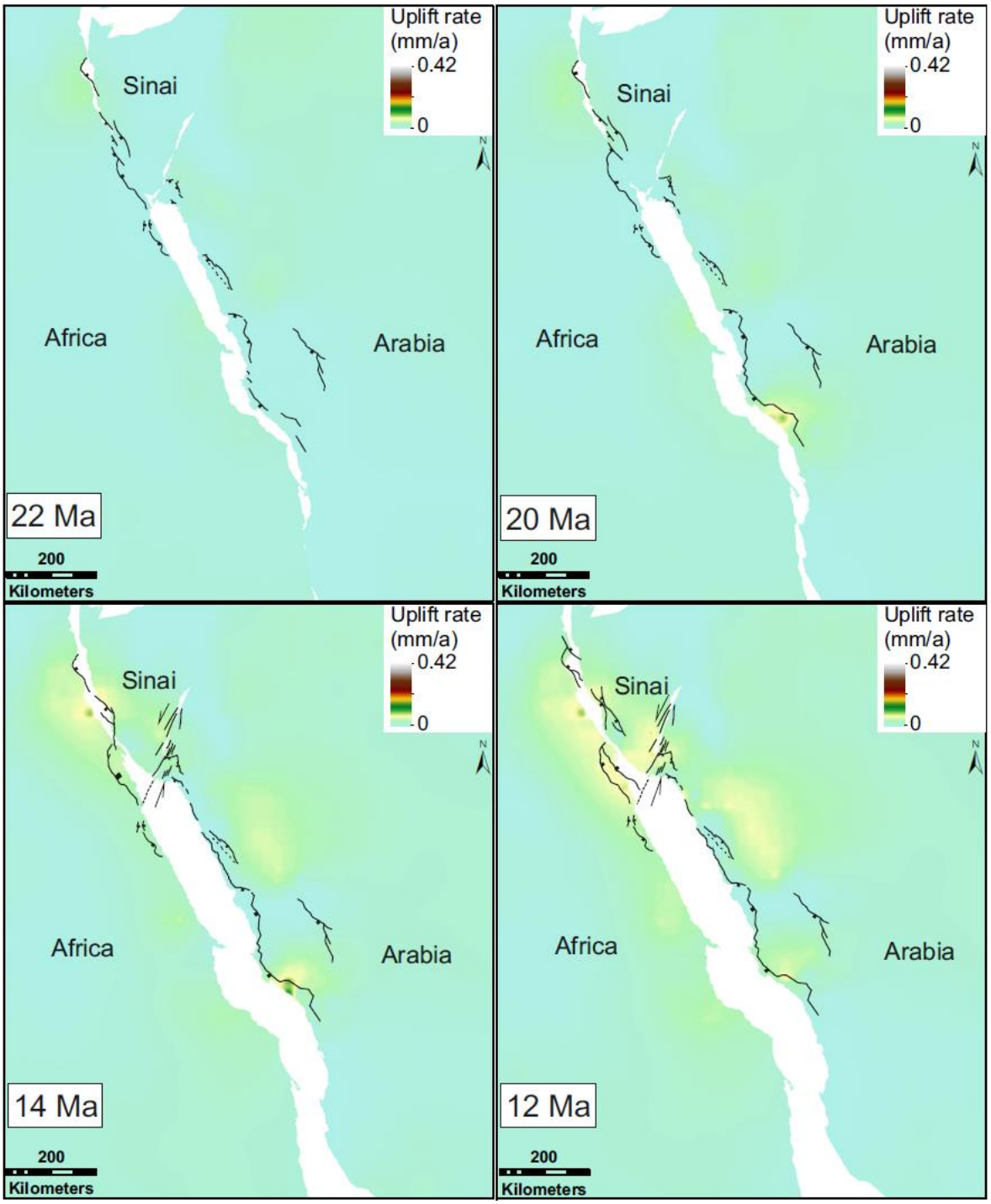

Figure 6.5: Uplift rate estimates of the study area during the early rift (22 Ma), the main rift (20 and 14 Ma) and the early strike-slip tectonics and oblique rifting (14 and 12 Ma). Rift and strike slip faults are shown as black lines.

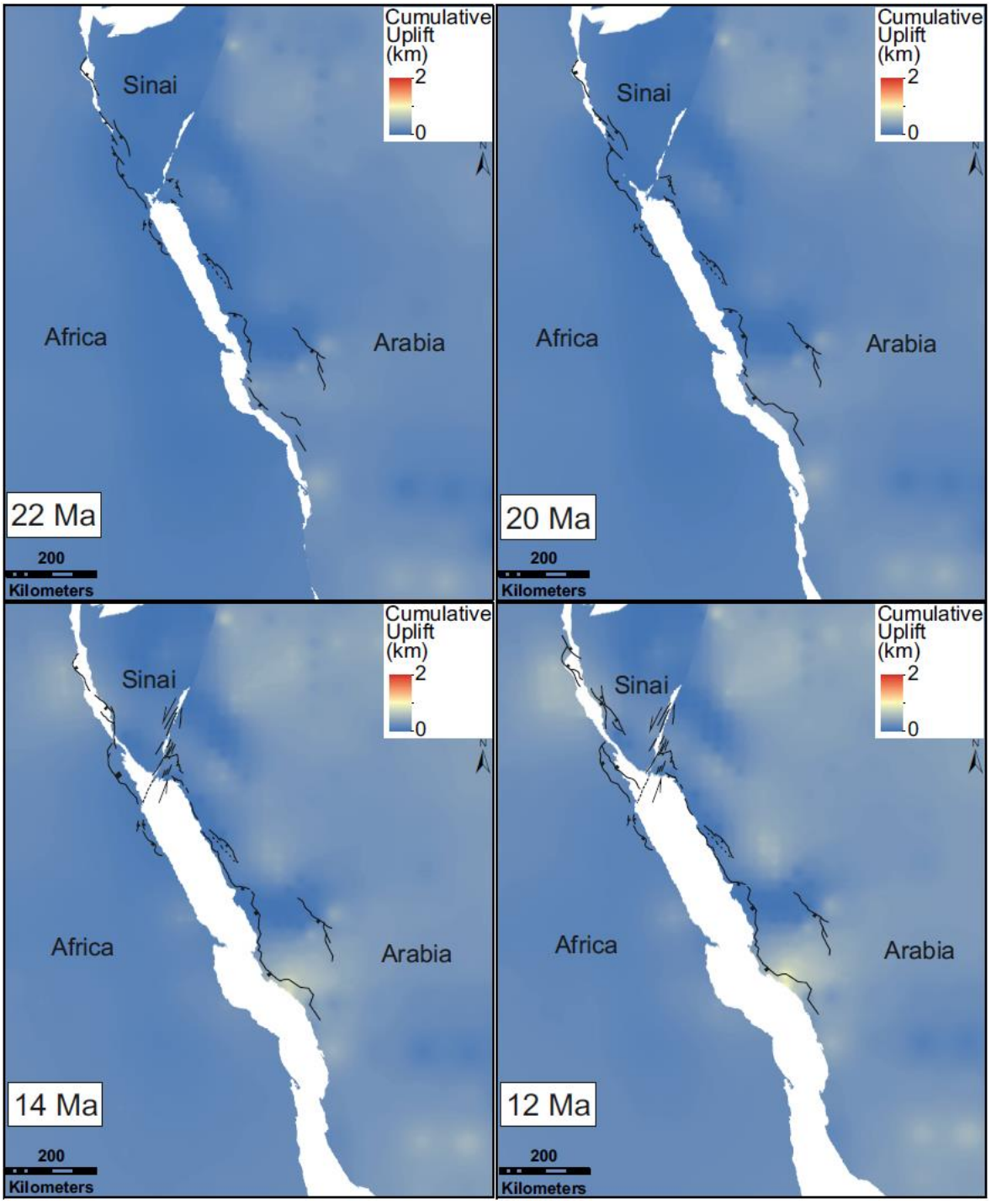

Figure 6.6: Cumulative uplift estimates of the study area during the early rift (22 Ma), the main rift (20 and 14 Ma) and the early strike-slip tectonics and oblique rifting (14 and 12 Ma). Rift and strike slip faults are shown as black lines.

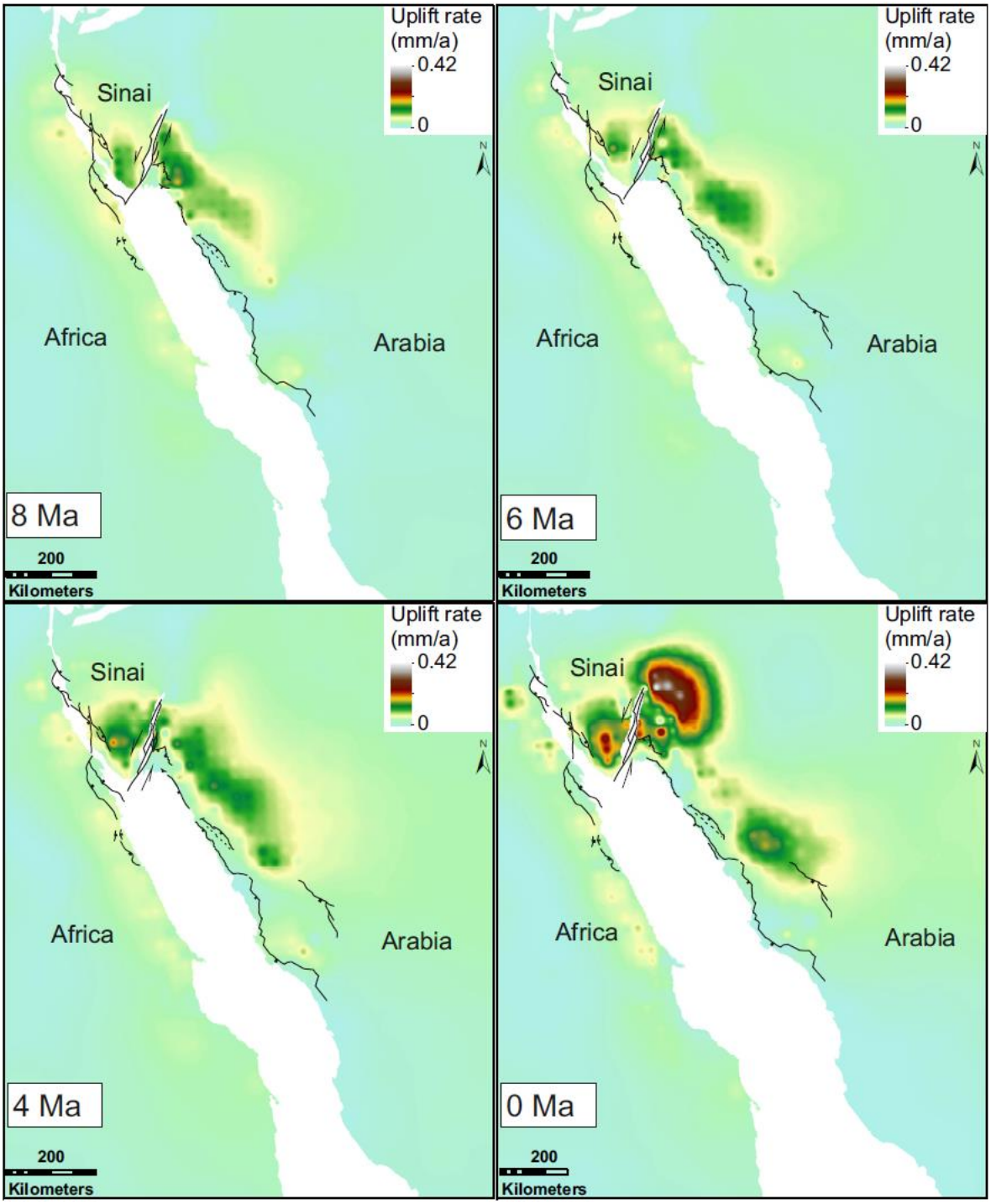

Figure 6.7: Uplift rate estimates of the study area during strike-slip tectonics and oblique rifting (8, 6 and 4 Ma) and the present day (0 Ma). Rift and strike slip faults are shown as black lines.

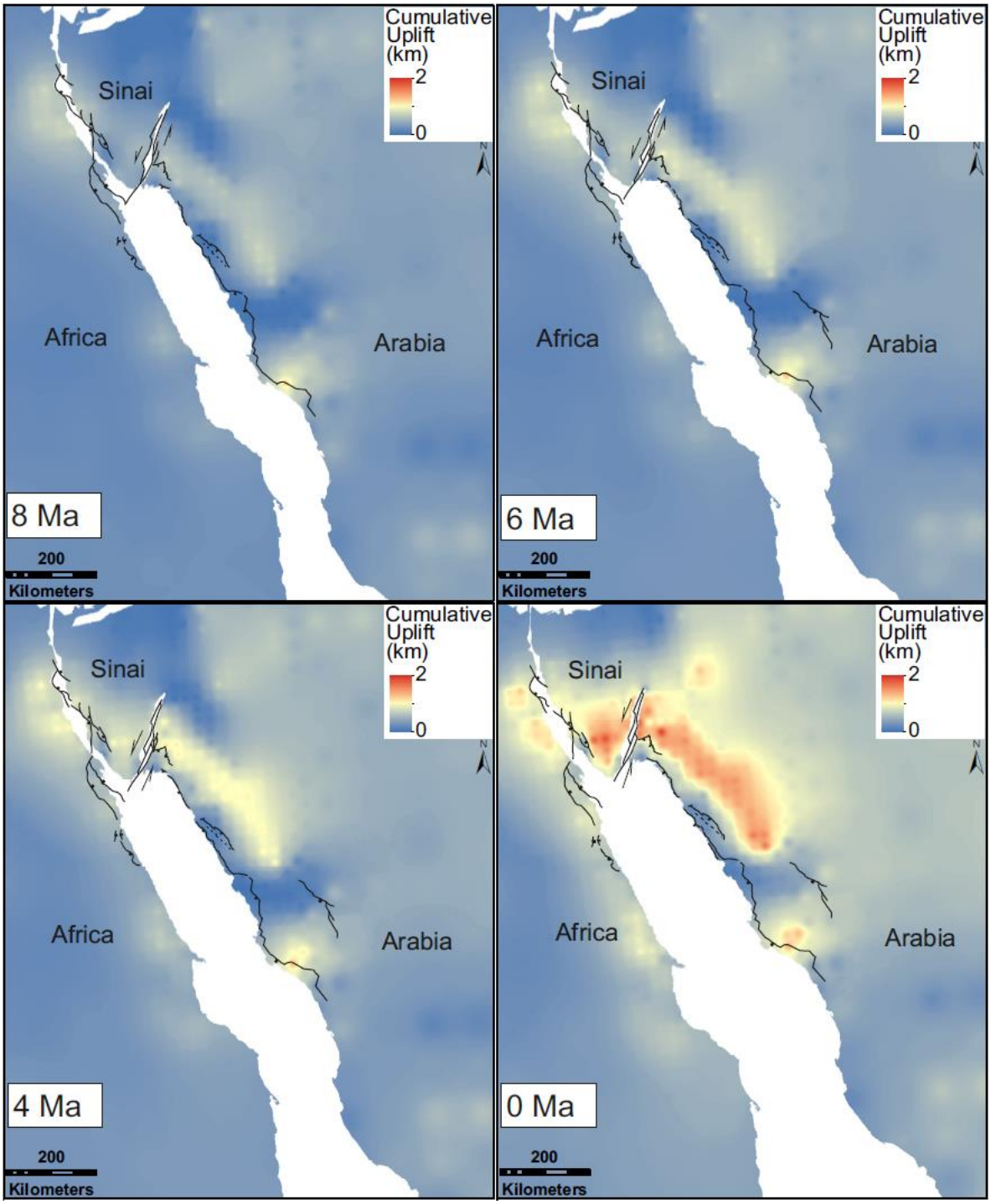

Figure 6.8: Cumulative uplift estimates of the study area during strike-slip tectonics and oblique rifting (8, 6 and 4 Ma) and the present day (0 Ma). Rift and strike slip faults are shown as black lines.

6.4.2 Drainage analysis

The drainage catchments in the surrounding landscape of the northern Red Sea, the Gulf of Aqaba and the Gulf of Suez are shown in Figures 6.9 and 6.10 and their areas are plotted on a frequency graph in Figure 6.11. The drainage network and catchments on the Arabian side have been briefly described in Chapter 3 (Section 3.3.1). Here, more characterisation of the drainage on the Arabian side is provided. Moreover, the African and Sinai catchments and the drainage patterns are described in details. Finally, the pre-rift paleo-drainage and structure-drainage interaction are interpreted, informed by the restoration of the plates to pre-rift settings to see how the catchments align with faults on either side of the Red Sea, the Gulf of Suez and the Gulf of Aqaba. The evolution of the drainage is predicted throughout the rifting stages in light of the structural evolution and the uplift estimation described in Section 6.4.1.

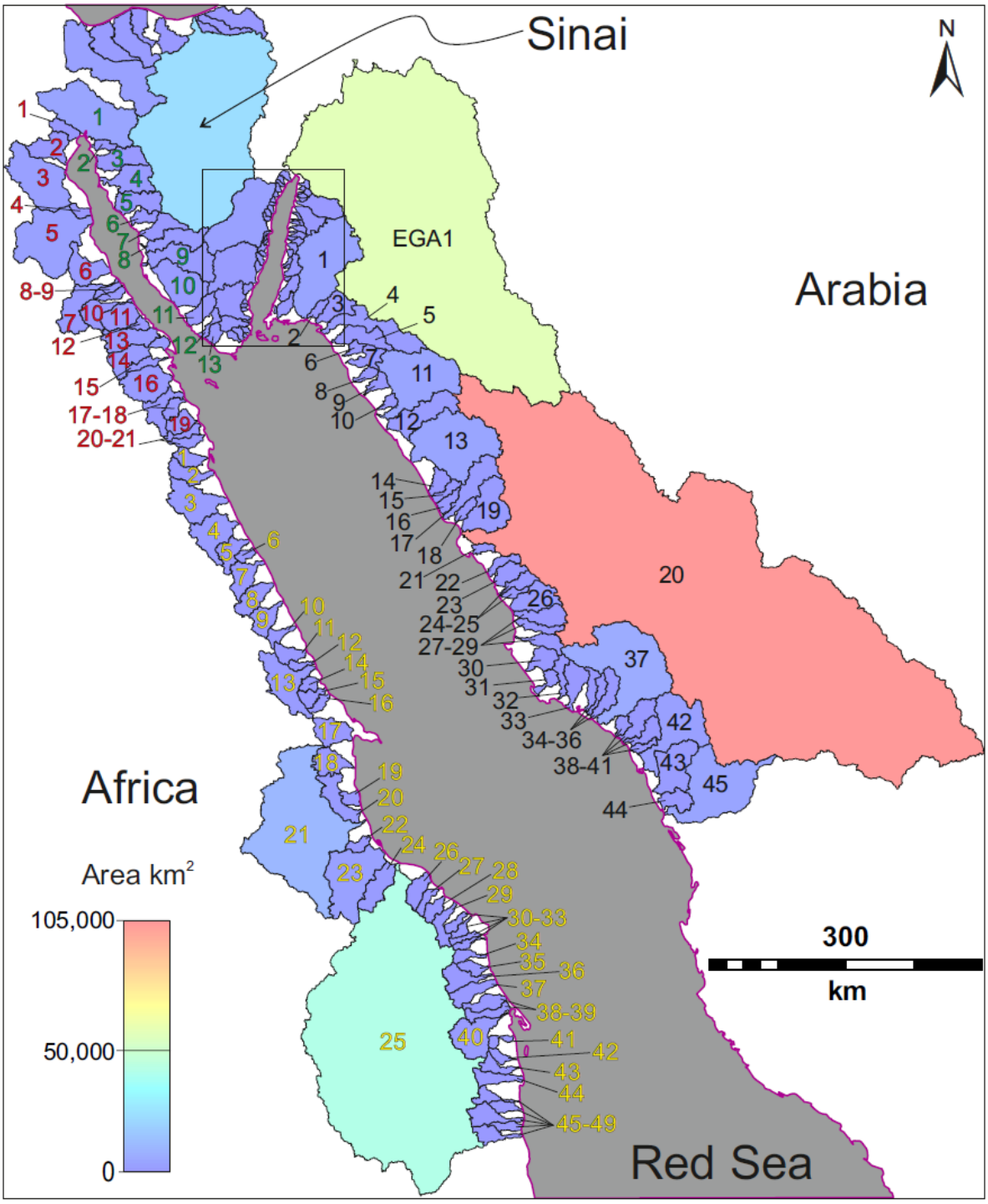

Figure 6.9: Catchments with outlets at the Red Sea, Gulf of Aqaba and Gulf of Suez showing their areas (WGS84, UTM zone 37°N). Numbers in black: NE Red Sea margin catchments (NERS); Yellow: SW Red Sea margin catchments (SWRS); Green: E Gulf of Suez catchments (EGS); Red: W Gulf of Suez catchments (WGS). Black box outlines Figure 6.10.

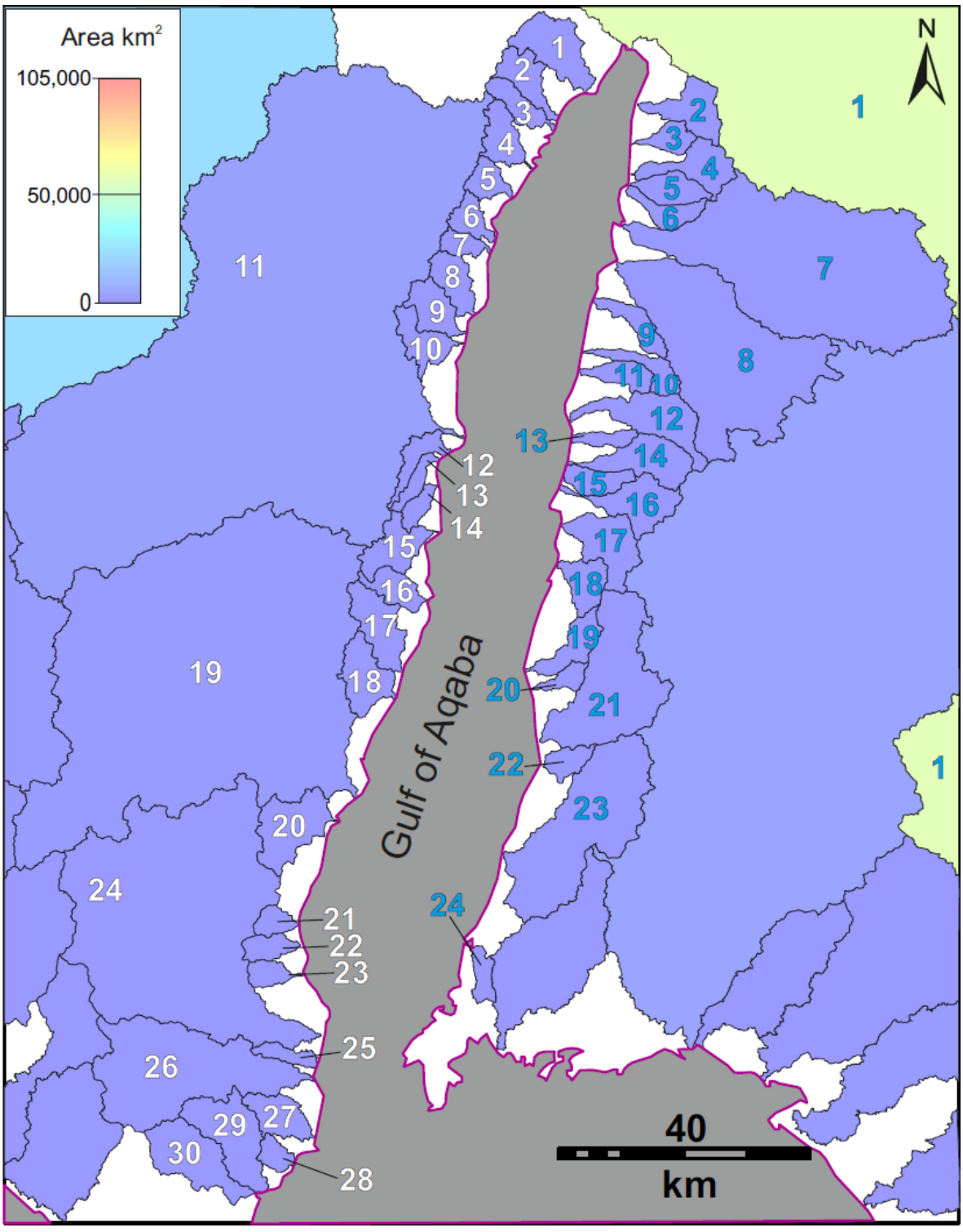

Figure 6.10: A close up of catchments with outlets at the Gulf of Aqaba coastline. Numbers in blue: E Gulf of Aqaba margin catchments (EGA); White: W Gulf of Aqaba margin catchments (WGA). Catchment 1 on the eastern Gulf of Aqaba margin (i.e. EGA1) extends beyond the figure view and is shown wholly in Figure 6.9.

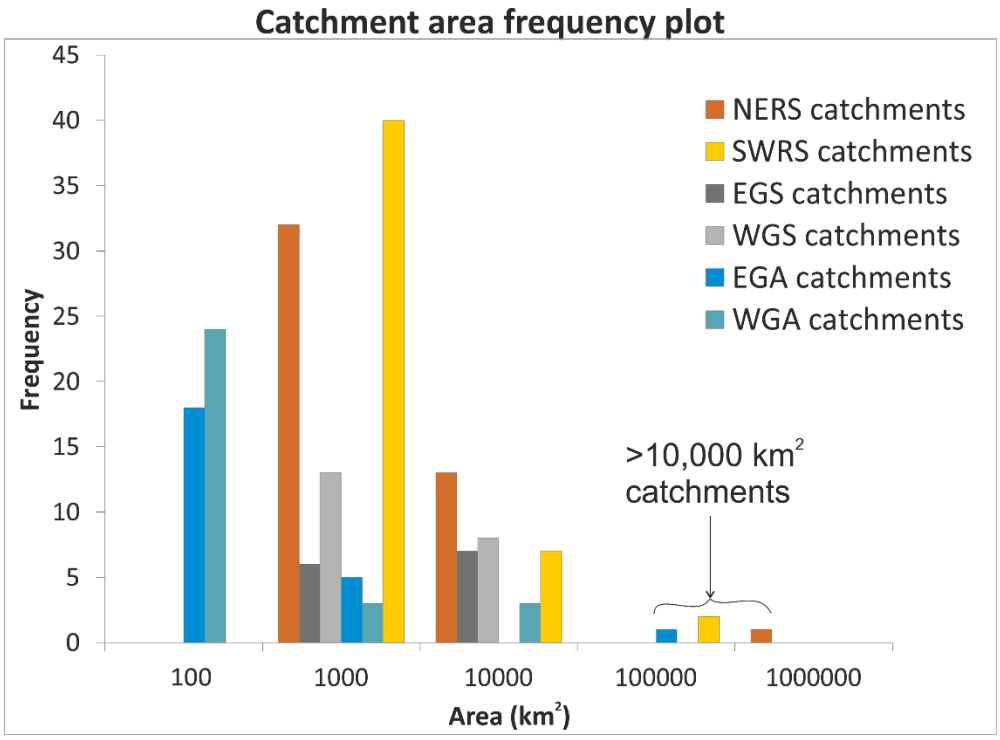

Figure 6.11: A frequency plot (logarithmic horizontal scale) of areas of all catchments extracted from the northern Red Sea, Gulf of Suez and Gulf of Aqaba margins (WGS84, UTM zone 37°N). Note that catchment larger than 10,000 km^2 exist on both Red Sea margins and the eastern Gulf of Aqaba margins.

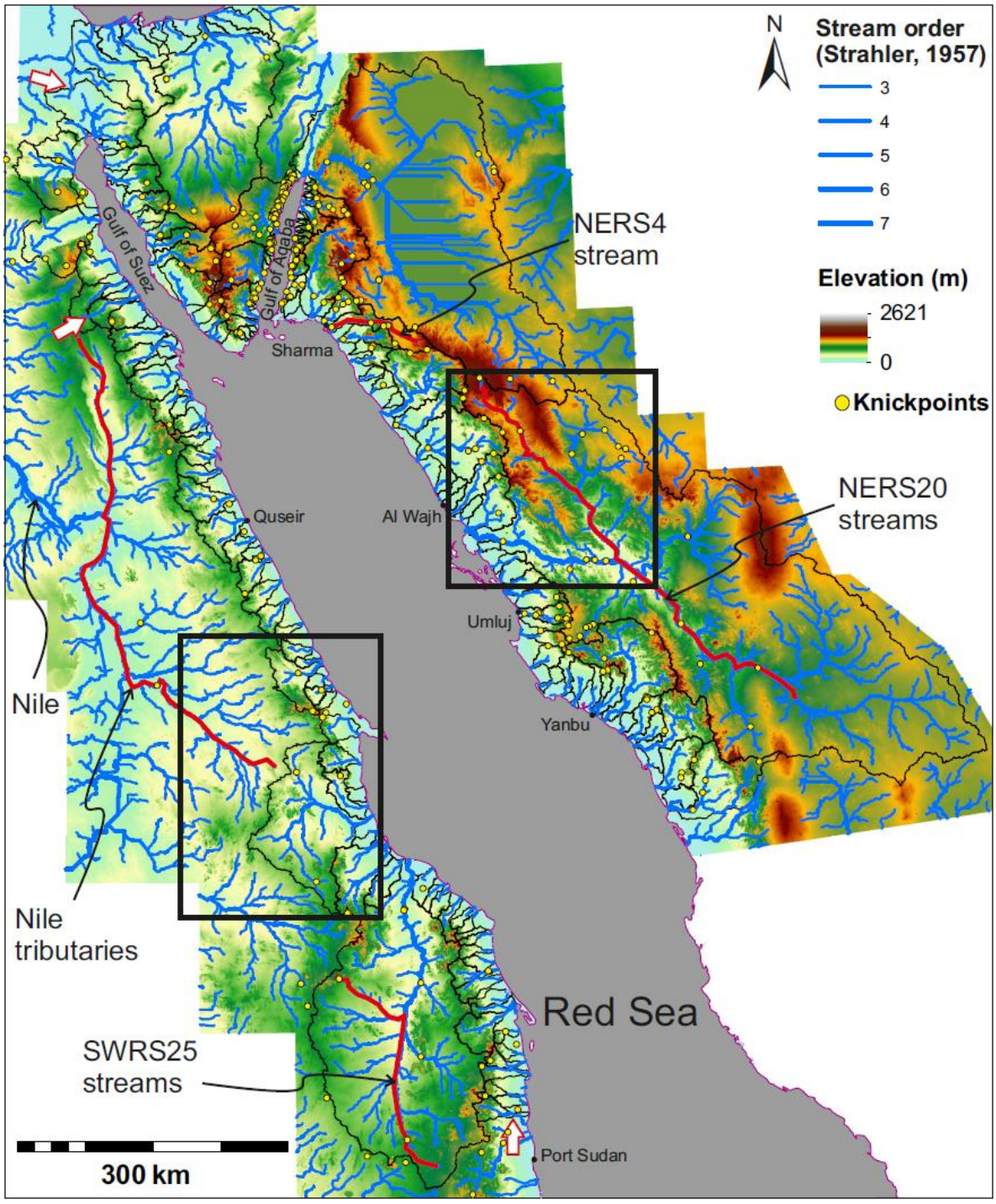

Figure 6.12: A DEM map showing the catchments, drainage and knickpoints along the northern Red Sea and the nearby gulfs. The map shows other streams outside the area of focus, including tributaries to the Nile. The white arrows show examples of data deterioration where extracted streams cross the catchments boundaries. The black boxes show the locations of Figure 6.13a (Arabian margin) and Figure 6.13b (African margin). The positions Figure 6.14 profiles are traced in red.

6.4.2.1 Arabian margin

On the Arabian side of the northern Red Sea, two zones of catchments are observed; a northern (catchments NERS 1-19) and a southern (catchments NERS 21-45; Figure 6.9). These two zones correspond spatially to two zones of relatively high escarpments that are separated by the outlet of the largest catchment on the Arabian side of the study area (NERS20).

Excluding catchments with areas less than 200 km^2, the northern zone has catchments with a mean area of ~1,400 km^2, whereas the southern zone contains smaller catchments with a mean value of ~1,100 km^2. The northern zone extends from ~50 to 100 km inland from the coastline, whereas the southern zone extends over a wider range from ~20 to 110 km (Figure 6.9).

In comparison, the catchment that separates these two zones (NERS20) covers a much more significant area of the northeastern Red Sea (105,000 km^2; Figure 6.9). This catchment extends to approximately 350 km inland from the coastline in its southern part and ~105 km in its northern part. Along with catchment EGA1, which drains towards the northern Gulf of Aqaba, the two catchments define the extent of the drainage divide in the northeastern Red Sea and eastern Gulf of Aqaba margins (Figures 6.9 and 6.12).

Overall, the small catchments within the two zones are characterised by elongated shapes and are, to a large extent, perpendicular to the coastline (Figure 6.12). However, the larger catchments (e.g. catchments NERS4, NERS11, NERS13 and NERS37) retain more irregular shapes that are narrow and perpendicular to the coastline close to their outlets and much wider away from the coastline. Also, catchments NERS4 and 5 have smaller areas with irregular shapes, displaying a remarkable change of direction, whereby the WSW-ENE orientation that is perpendicular to the Red Sea coastline changes to a NW-SE trend towards the east.

Catchment NERS1 has an elongated shape and occupies much of the Midyan Basin and the mountainous area to the northeast (Figures 6.9 and 6.12). The higher tributaries of the catchment originate east of the northern escarpment and flow initially towards the east and northeast before turning towards the north-

northwest. Eventually, the main channel joins a WSW-oriented channel that feeds into a SW-flowing valley towards the Red Sea.

The eastern Gulf of Aqaba catchments are much smaller than the Red Sea catchments, with only five catchments larger than 200 km^2 (Figure 6.10). One of these large catchments is EGA1, which is a regional catchment that extends approximately 220 km to the east and covers ~59,000 km^2. Excluding catchment EGA1 and catchments that are smaller than 20 km^2 in area, the average size of the eastern Gulf of Aqaba catchments is approximately 130 km^2 (Figure 6.10).

North of the Midyan Basin, the catchments are elongated in shape and perpendicular to the Gulf of Aqaba coastline (Figure 6.10). The distance from the coastline of these catchments increases from ~10 km in the central Gulf of Aqaba margin to ~55 km in the northern margin. On the other hand, along the western side of the Midyan Basin, the catchments are oblique to the Gulf of Aqaba coastline but are perpendicular to the trend of the Red Sea (Figure 6.10). These catchments extend approximately 15 to 20 km away from the coastline.

6.4.2.2 African margin

The most conspicuous difference between the geomorphology of the Arabian and African Red Sea margins is the distance between the coastline and the drainage divide (Figures 6.9 and 6.12). As opposed to the Arabian margin where the drainage divide is delineated by the extent of two regional catchments (NERS20 and EGA1; ~250-300 km from the coastline), the drainage divide along the African side is delineated mostly by the extent of much smaller catchments (~60-80 km from the coastline).

Except in the southern part where the large catchments SWRS21 and 25 extend approximately 140-230 km from the coastline, a much smaller distance between the coastline and the drainage divide (average = ~50 km) is noted along the African margin (Figures 6.9 and 6.12). In details, the extent of the catchments inland decreases from ~230 km in the south to ~30 km just north of SWRS21. Further north, the distance from the coastline to the drainage divide increases gradually until it reaches ~60 km at the northernmost part of the Egyptian Red Sea margin (Figure 6.9). The distance drops again to ~40 km at the southernmost part

of the western Gulf of Suez margin, before increasing gradually to ~70-95 km in the central and northern parts of the margin. It is worth noting that, unlike the eastern margins (NERS and EGA) and the Egyptian Red Sea (SWRS), the western Gulf of Suez margin (WGS) does not feature catchments that are larger than 10,000 km^2 (Figure 6.11).

Excluding catchments smaller than 200 km^2 in area, the catchments along the African Red Sea margin have an average area of ~1,700 km^2. Excluding the two largest catchments (SWRS21 [11,600 km^2] and 25 [42,400 km^2]), the average size drops to ~670 km^2. The catchments along the western Gulf of Suez, have a slightly larger size with a mean value of ~1,000 km^2 (Figure 6.9).

Along both the Egyptian Red Sea and the western Gulf of Suez margins, the catchments are mostly elongated with long axes that are near-perpendicular to the coastline (Figure 6.9). However, at the upstream sections of some of these catchments, the shape is elongated along a NNW-SSE trend semi-parallel to the coastline (e.g. WGS 3, 6, 7, 10, 14 and 17, and SWRS2, 3, 4, 5, 7, 13, 21 and 23). Moreover, the orientation of catchment SWRS25, the largest catchment on the African side of the study area, is N/NNE oblique to the overall Red Sea NNW trend, even though it has an elongated shape (Figures 6.9 and 6.12).

6.4.2.3 Sinai margins

The catchments draining the Sinai Peninsula can be divided into three zones: a western zone draining off to the Gulf of Suez, an eastern zone draining off to the Gulf of Aqaba and a northern zone draining off to the eastern Mediterranean (Figures 6.9 and 6.12).

Along the eastern Sinai margin, most of the catchments are characteristically small with a mean size of 44 km^2 (excluding catchments smaller than 20 km^2; Figure 6.10). However, four large catchments (WGA11, 19, 24 and 26) have outlets that separate the small catchments and a mean size of ~1,700 km^2. The small catchments along the eastern Sinai margin are elongated and near-perpendicular to the western coastline of the Gulf of Aqaba (Figure 6.10). The four large catchments, on the other hand, are characterised by shapes that deviate from the elongated shapes that have their long axes perpendicular to the coastline.

Instead, they are more irregular and their upstream parts are semi-parallel to the coastline. Furthermore, abutting catchment WGS11, the small catchments WGS12, 13 and 14 are elongated along a NNE-SSW trend, highly oblique to the coastline.

Along the western Sinai margin and excluding catchments smaller than 200 km^2 in area, the catchments have a mean size of approximately 1,100 km^2 (Figure 6.9). These catchments are comparable in size to the western Gulf of Suez catchments and the four large catchments on the eastern Sinai margin (WGA11, 19, 24 and 26 (Figures 6.9-6.10). Along the western Sinai margin, the catchments are characterised mostly by irregular shapes, unlike the elongated shapes observed along other margins in the study area (Figure 6.9). These irregular shapes are caused by upstream parts of the catchments being oblique to the coastline (e.g. EGS5, 7 and 9) or because of the existence of an axial drainage with respect to the rift faults that is semi-parallel to the coastline (e.g. EGS10; Figures 6.9 and 6.12).

The catchments that drain towards the north to the eastern Mediterranean are more variable in size (Figure 6.9). The largest catchment has an area of ~23,500 km^2. This catchment is elongated in a north-south trend and extends from central Sinai to the Mediterranean coast (230 km). The smaller catchments are confined to a distance from the coastline of ~45 km in the east to 120 km in the west (Figure 6.9). These catchments have areas that increase from ~265 km^2 in the east to ~4,100 km^2 in the west, with a mean value of ~1,100 km^2. These smaller catchments are mostly elongated along a NW-SE to WNW-ESE trend. However, the delineation of their boundaries might be affected by the very gentle topographic slope and the loose sediment cover, particularly within ~60-70 km of the coastline.

6.4.2.4 Indications of pre-rift drainage

In this section, geomorphic evidence is provided from catchment and drainage network analyses to show that the paleo-drainage flowed dominantly towards the north and northwest prior to rifting. The rifting-induced drainage, thereafter, modified the drainage network and catchments by capture and reversal.

A few catchments on the Arabian and African Red Sea margins are characterised by shapes that deviate from the perpendicular-to-coastline geometry, which characterises the fault-controlled catchments in the study area (Figure 6.9). The

main channels within these catchments are mostly oblique to the coastlines (Figure 6.12). These characteristics are interpreted to have resulted from capture and/or reversal of pre-rift paleo-drainage, which is also manifested in the observation that these catchments are mostly larger than the nearby fault-controlled catchments.

On the Arabian margin, the most conspicuous example is catchment NERS20, which has a main channel oriented along a NW-SE trend (Figure 6.12). This channel flows from both the northwest and the southeast and, at the Hamd-Jizl Basin, turns west-northwest towards the Al Wajh Basin and, eventually, to the Red Sea (Figures 6.9 and 6.12). Headward erosion by streams that developed initially in response to the faulting east of Al Wajh Basin resulted in the capture of this paleo-drainage. It is interpreted here that this capture was coeval with the reversal of an originally NW-directed northern part of the NERS20 main drainage (Figure 6.13a). The reversal occurred due to surface uplift near Harrat Uwayridh during the Middle Miocene and caused the flow to be redirected towards the southeast (Figure 6.5; see also Chapter 3 (Section 3.4.1)). The capture resulted in an elbow of capture within the hangingwall block of the Hamd-Jizl Basin, and the reversal is expected to have resulted in a wind gap at the northwestern corner of the NERS20 catchment (Figure 6.13a).

By examining the stream profile gradient of the catchment main channel, a low-gradient towards the northwest sloping segment is observed at the southern part of catchment above a knickzone that separates it from a steeper downstream segment (Figures 6.12 and 6.14). This observation supports the N to NW-ward gradient of the relict landscape, hence, the pre-rift paleo-drainage.

Other examples of elbow of capture suggesting northwest-directed paleo-drainage can be seen within catchment NERS20 at its western side (Figure 6.13a). To the east of catchments NERS17 and 19, anomalously northwest-directed valleys change their courses abruptly towards the south and the west-northwest forming elbows of captures. In fact, a clear drainage pattern can be seen, particularly in catchment NERS17, whereby upstream drainage is directed towards the northwest parallel to the interpreted paleo-drainage (Figure 6.13a).

In addition to catchment NERS20, smaller catchments with irregular shapes manifest the drainage evolution in the Arabian margin. For instance, catchments NERS4 and 5 have an upstream section that is oriented oblique to the Red Sea coast and a downstream section that is perpendicular to the coast. These two sections are separated by a knickpoint (Figure 6.14). This relationship demonstrates the incorporation of the paleo-drainage into the rift-related catchments through headward erosion.

Similarly, on the African Red Sea margin, spatial drainage network and stream profile gradients suggest a northwest-directed pre-rift drainage. Within catchment SWRS21, upstream drainage in the southern part of the catchment is oriented towards the northwest (Figure 6.13b). A capture event is interpreted where this drainage changes gradually to an east and southeast-directed drainage at downstream locations.

Furthermore, a low-gradient segment located at the southern parts (north-directed) of major drainage within catchment SWRS25 is observed, defined at their lowest elevations by a knickzone (Figures 6.12 and 6.14). When compared to the southern flowing stream within the same catchment (located at the northern part), the northward flowing stream is much shallower in gradient (Figure 6.14). Similar observation is noted when comparing southern and northern flowing tributaries of the Nile, west of the African Red Sea margin catchments, although no clear knickpoints are observed.

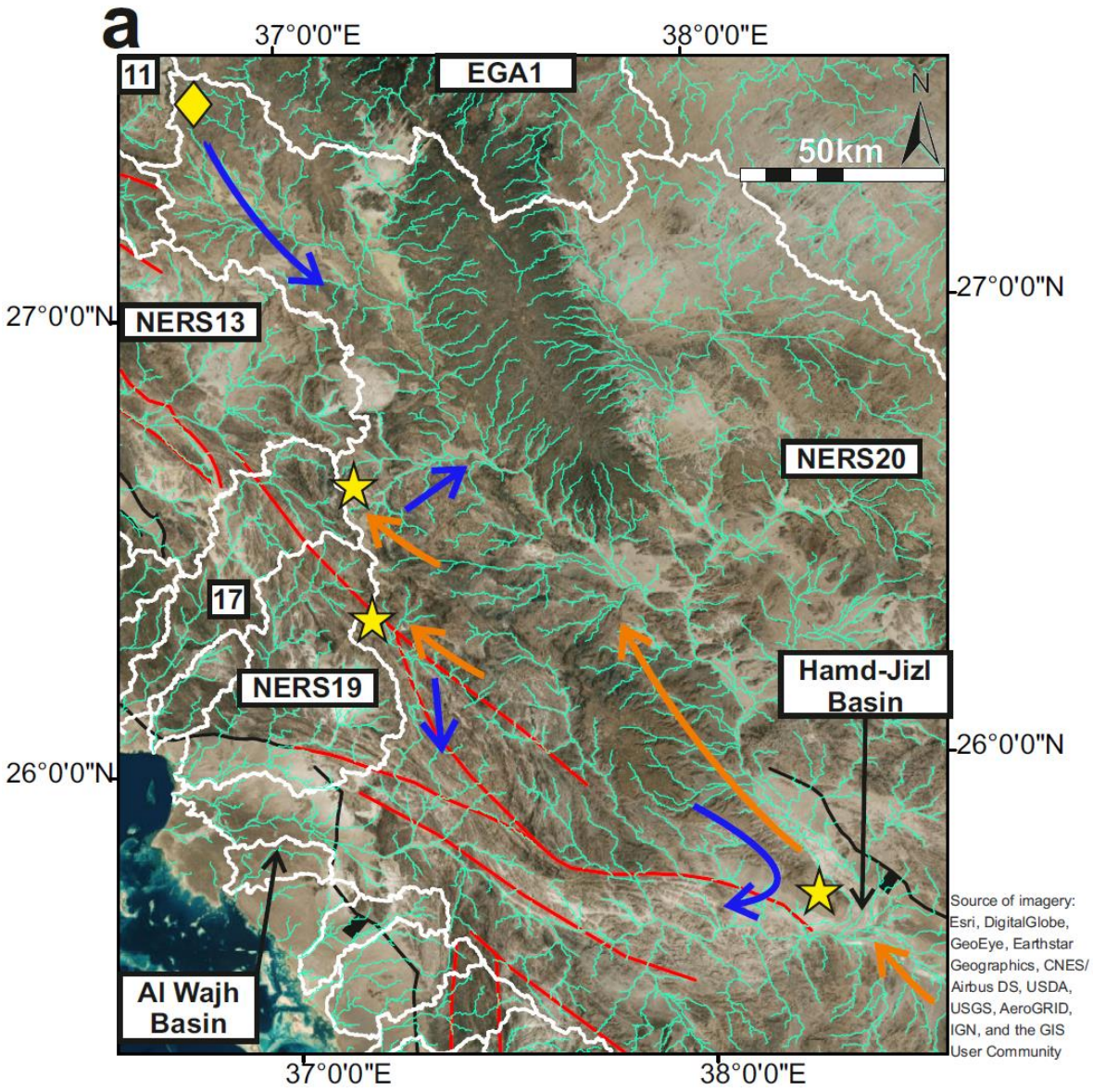

Figure 6.13: Satellite imagery showing examples of the interpretation of paleo-drainage directions that are incorporated into the present-day drainage from the Red Sea (a) Arabian and (b) African margins. Orange arrows represent the paleo-drainage direction interpreted here; yellow stars are locations of drainage capture; yellow diamond (top left of (a)) denotes approximate location of drainage reversal; blue arrows represent the direction of drainage after it has been modified. Red lines are Precambrian basement structures and black lines are Oligo-Miocene faults.

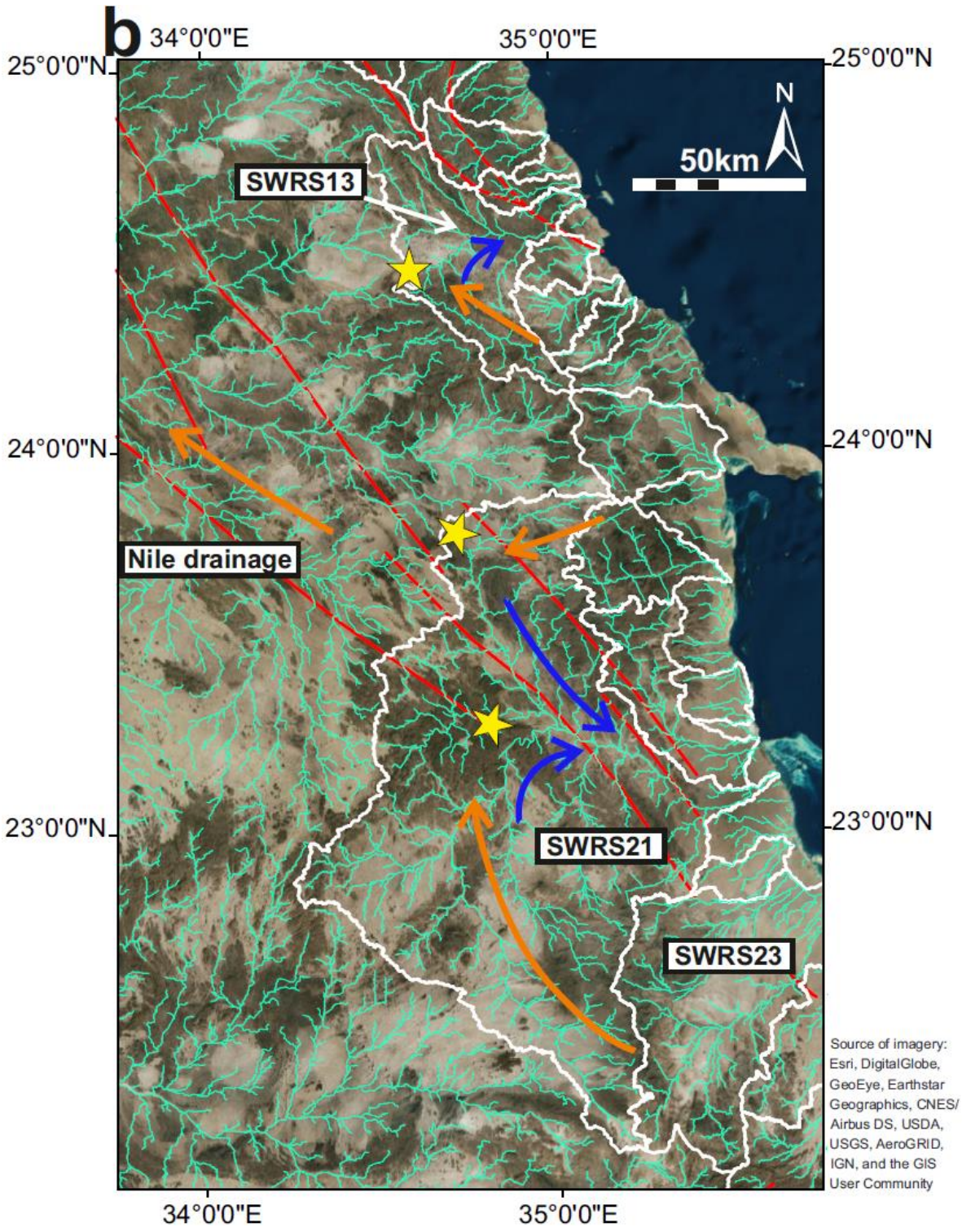

Figure 6.13 (continued).

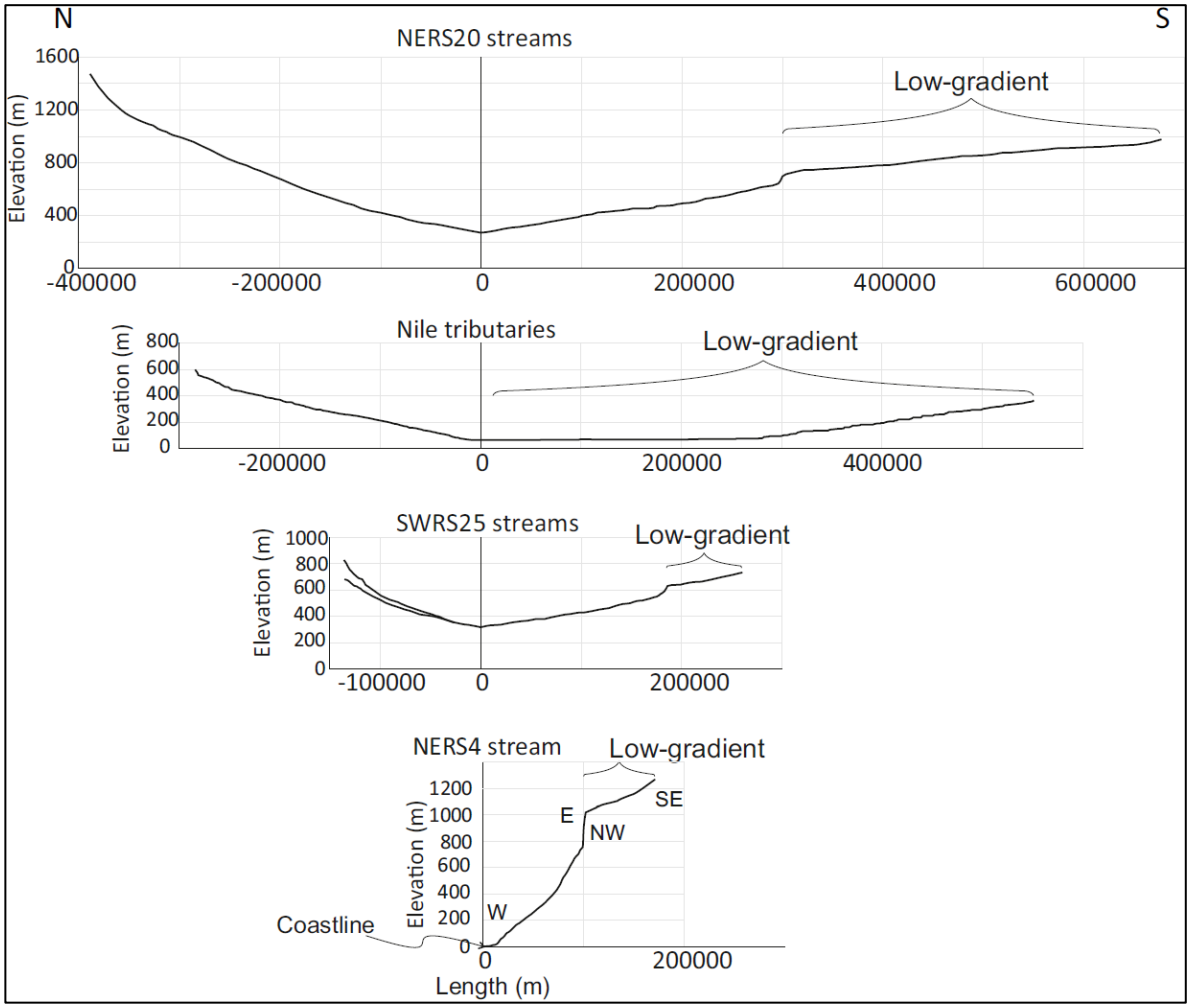

Figure 6.14: Selected stream profiles showing the overall shallower gradients of northward-flowing streams compared to southward-flowing streams within the large catchments in the study area as well as profiles of two Nile tributaries (Top three plots). The zero point along the Length axis is the point at which the streams join. Also shown is the incorporation of paleo-drainage into coastline-perpendicular rift-related drainage at NERS4 (Bottom). Locations are shown in Figure 6.12.

6.4.2.5 Drainage-uplift-structure interaction

The restoration of the plates to the pre-rift stage shows how catchments and rift structures on either side of the northern Red Sea are related to each other (Figure 6.15). The small catchments along the Arabian Red Sea margin are located on fault-controlled footwall blocks. Their long axes and areas decrease in magnitude from southeast to northwest. The overall trend, however, can be divided into segments each of which becoming shorter towards the northwest. These

segments are associated with the footwall blocks of relict rift basins along the margin; namely from southeast to northwest, the Yanbu Basin, the Al Wajh Basin, and the coastal footwall block of the Wadi Azlam Basin. As shown in Chapter 3 (Section 3.3.1.1.1), within catchment NERS20 watersheds at the footwall of the Hamd-Jizl Basin are reminiscent of the establishment of rift-related drainage inboard of the eventual rift axis of the Red Sea. Moreover, the small catchments on either side of the Gulf of Aqaba are examples of the drainage that was established upon the strike-slip tectonics that commenced during the Middle Miocene.

Larger catchments that are located seaward of the escarpments have outlets that are situated close to the tips of the rift basin-bounding faults. These catchments expand over an area that covers the structural accommodation zones between major rift segments. Examples of these catchments include NERS1, 11, 12, 17, 19 and 37. The exception is catchment NERS13, which does not exploit an accommodation zone but has an axial drainage within the Wadi Azlam Basin.

As explained earlier in Section 6.4.2.4, catchment NERS20 has likely evolved as a pre-rift paleo-drainage directed towards the northwest that during the rifting was captured by drainage that pours into the Al Wajh Basin. The capture of the drainage and the switching of the catchment outlet to the Al Wajh Basin is interpreted to have utilised pre-existing basement structures of the Najd Fault System along an early relay ramp.

Catchments on the African Gulf of Suez and Red Sea margins are mostly smaller than the Arabian counterparts, with the exception of SWRS21 and 25 (Figure 6.9). As indicated in Section 6.4.2.2, these catchments have either elongated shapes that are semi-perpendicular to the coastline or shapes where the upstream part of the catchments are elongated semi-parallel to the coastline.

The small sizes of these catchments maybe interpreted to represent footwall drainage (e.g. Gawthorpe et al., 1994). This interpretation is valid for the catchments at the southern and northern Gulf of Suez margins, where east-dipping normal faults have been interpreted (Figure 6.15). However, at the African Red Sea margin, no major rift related faults dipping towards the east have been mapped.

Relatively large catchments on the African side of the northern Red Sea (SWRS21 and SWRS25) are juxtaposed against SW-dipping faults of the Al Wajh Basin on the Arabian side. Catchment SWRS21 shows indications of paleo-drainage that was originally directed towards the west and northwest, away from the Red Sea (Figure 6.13b). It, therefore, may be interpreted to have evolved during the rifting by incorporating this pre-rift drainage and forming a hangingwall catchment with respect to the bounding fault of the depocentres at the Al Wajh Basin on the Arabian margin. This interpretation is supported by the catchment relatively large size and irregular shape compared to the small sizes and elongate shapes that characterise footwall catchments.

Catchment SWRS25 is the largest catchment with a main channel directed towards the N/NNE, oblique to the NNW Red Sea trend (Figures 6.9 and 6.12). The drainage pattern here is mostly dendritic, which suggests that it has generally assumed its pre-rift course even during rifting. The existence of a low-gradient drainage segment above knickzone along its main channel (Figure 6.14) suggests possibly that the upstream parts are part of pre-rift drainage. Upon plate restoration, it is shown that the outlet of this catchment is juxtaposed against an area ~60 km south of the Al Wajh Basin (Figure 6.15). The southern part of the Al Wajh Basin bounding fault is segmented by NNE-NE structures that were part of Proterozoic Hanabiq Shear Zone (a pre-rift continuation of the Hamisana Shortening Zone (Stern and Johnson, 2019)). On the African side, the major drainage of catchment SWRS25 is semi-parallel to pre-existing basement structures (Johnson et al., 2011), which were likely aligned parallel to an accommodation zone oriented NE-SW during the early rifting (Figure 6.15). The interpretation of an accommodation zone is compatible with the large size of this catchment as accommodation zones form preferable pathways for significant drainage to rift basins.

Other examples of accommodation zone drainage can be described from the Gulf of Suez. As the polarity of the normal faults bounding the three sub-basins change from east dipping in the south, to west dipping in the centre to east dipping in the north, the accommodation zones in between become favourable for drainage to exploit (Polis et al., 2005). Catchments WGS5 and 13 on the African margin and

catchments EGS 8 and 9 on the Sinai margin represent examples of accommodation zone drainage. The sizes of these catchments, particularly WGS13 and EGS 8 and 9, are smaller than other accommodation zone drainage on the Red Sea margins. The high uplift rates established during the Middle Miocene and continuing to the present-day around the Gulf of Suez are concluded here to have played a role in reducing the sizes of these catchments by keeping the drainage divide close to the coast.

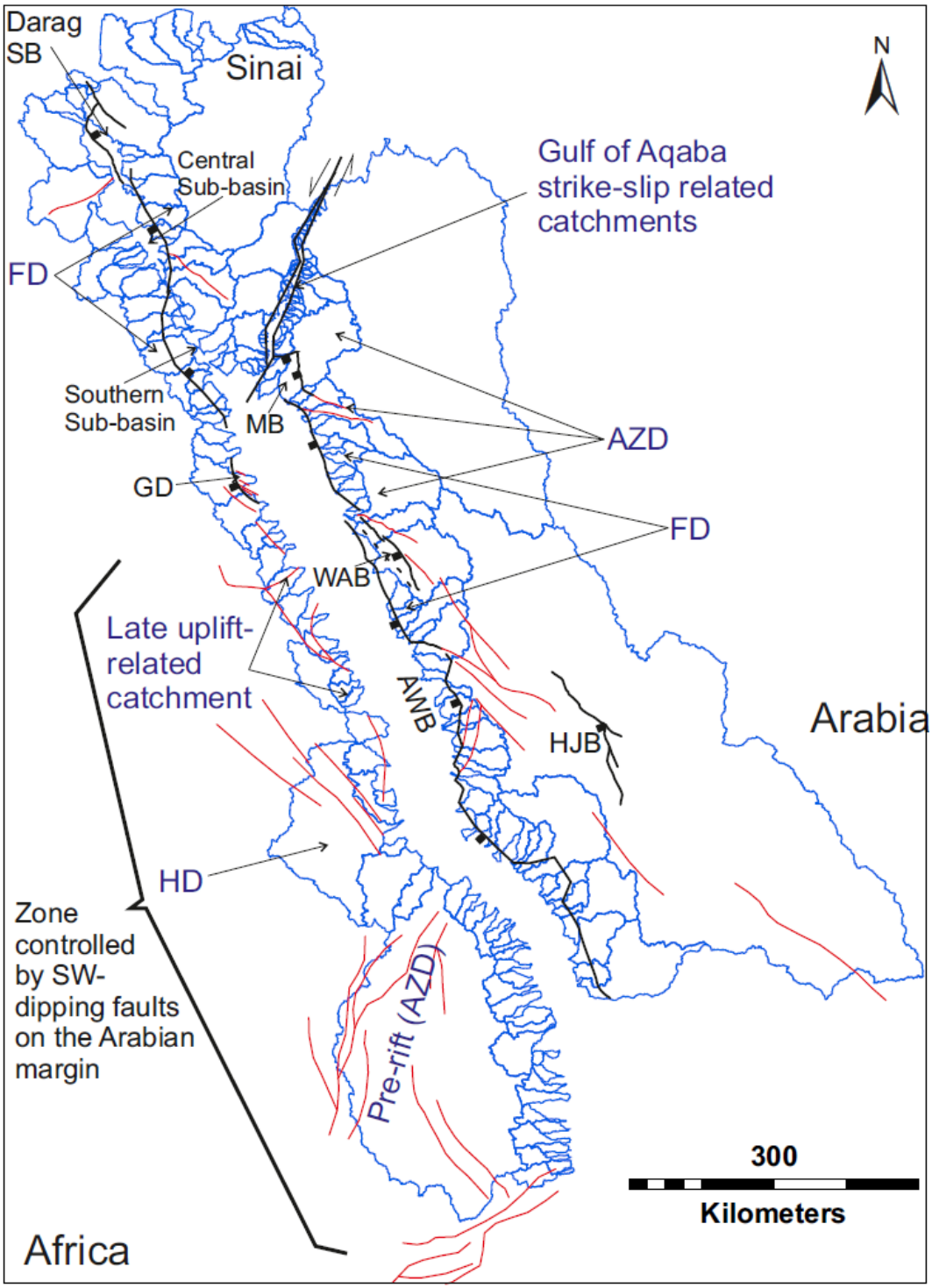

Figure 6.15: Present-day catchments along the northern Red Sea and nearby gulfs presented on restored plates to ~20 Ma. Note the relationship between the catchments and structures. Red lines: Precambrian structures; black lines: Cenozoic faults; blue polygons: catchments. FD: footwall drainage; HD: hangingwall drainage; AZD: accommodation zone drainage. Plate reconstruction was performed using Schettino et al. (2016) and Schettino et al. (2019) poles and angles or rotation.

6.4.3 Drainage evolution

Utilising the uplift distribution estimated through the inverse modelling of drainage profiles, the interpretation of the paleo-drainage, and the effect of structures on drainage, drainage evolution across the northern Red Sea is discussed here.

6.4.3.1 Pre-rift drainage

Pre-rift paleo-drainage was characterised by catchments that are elongated oblique to the trend of the Red Sea. The low relief and elevation that characterised the pre-rift northeastern Africa and northwestern Arabia (e.g. Feinstein et al., 2013) suggest that the paleo-drainage was composed of a small number of regional catchments. Fielding et al. (2018) demonstrated that the River Nile has assumed most of its present-day course since the Oligocene. This provides some constraints on the geomorphic evolution of the Egyptian Red Sea and western Gulf of Suez margins, making it reasonable to assume that a regional drainage divide has not moved significantly since the start of rifting. Moreover, the elbows of capture observed within some of the African Red Sea margin (e.g. SWRS4, 13 and 21) indicate that the pre-rift drainage was directed towards the proto-Nile catchment (Figure 6.13).

The effect of structures on the pre-rift drainage is suggested by the alignment of major drainage with pre-existing structures. For instance, the Najd Fault System to the east of the Al Wajh Basin is interpreted to have partly directed drainage during the pre-rift. Furthermore, the Hamisana Shear Zone and Oko shortening zone are located within at the boundaries of catchment SWRS25 and are largely parallel to its long axis. Assuming that no internal drainage occurred prior to rifting, the drainage influenced by these pre-rift structures is interpreted to have flowed across the proto-Red Sea.

6.4.3.2 Early-rift drainage

The paleo-drainage direction of flow is shown here to have been generally towards the north, compatible with previous interpretations (e.g. using fluvial sedimentary sequences, structures and morphology for Early Miocene paleogeography reconstruction; Zilberman and Calvo, 2013). The formation of grabens and half-

grabens as a consequence of early rift extension would result in perturbations of the local topographic slope. Therefore, the early rift basins now perched on the northeastern Red Sea margin would have captured the pre-rift drainage that flowed near them.

The sizes of the catchments that were formed during the early rifting varied depending on where major pre-rift drainage intersected the rift. As shown in Sections 6.4.2.4 and 6.4.2.5, pre-existing structures form lineaments that were exploited by pre-rift drainage. During the early rifting stage, some of these structures were partly reactivated and formed boundaries to accommodation zones between the rift basins (Bosworth et al., 2005). With respect to the drainage, regional catchments initially parallel to pre-existing weaknesses in the basement utilised the accommodation zones to access the rift.

Examples of the capture of large catchment areas are interpreted at the southern part of the Al Wajh Basin, where catchment SWRS25 was captured by the basin depocentre, and the Midyan Basin, where the catchment preceding NERS20 that flowed towards the north-northwest was captured by the basin depocentre. Another example where pre-rift drainage intersected the rift domain and likely was captured by a depocentre in the Gulf of Suez is a tributary of the Nile, presently flowing southward and located west of the southern Gulf of Suez (Figure 6.16).

The Al Wajh Formation (equivalent to the Abu Zenima and Nukhul Formations in the Gulf of Suez), which signifies the early rift stage has been interpreted to represent fluvial to lacustrine environments in the Midyan Basin and northern Red Sea (Hughes et al., 1999 *and references therein*). Early marine incursion has been described from other basins at ~ 21 Ma (e.g. Hughes and Johnson, 2005 *and references therein*), which was likely a result linking to the Mediterranean Sea through the Gulf of Suez). The marine incursion and the formation of lakes during the early rifting increased the base-level of the streams resulting in the disintegration of the initially large catchments into smaller catchments.

In the Hamd-Jizl Basin, ~130 km east of the Arabian Red Sea coastline, the early rift Qattar Formation was deposited in fluvial conditions (Szymanski, 2013). The lack of lacustrine sedimentary units is compatible with the interpretation that no

internal drainage resulted during the formation of the two half grabens and that the two depocentres were overfilled throughout. The axial drainage within the Hamd-Jizl Basin, therefore, was part of a large catchment that flowed to the northwest and that was initially a large pre-rift drainage catchment.

At accommodation zones where no large-scale pre-rift drainage intersects the rift, the catchments that formed were smaller (e.g. NERS11, 12, 19 and 37). The effect of the pre-rift structures and drainage can have influence on the shapes of these catchments and indicate stream capture of pre-rift drainage. However, as no large-scale catchment capture occurred, their sizes are much smaller than SWRS25 and NERS20 (Figure 6.9).

Catchment SWRS21 is comparable to the aforementioned catchments in scale. However, it is interpreted to have been evolved as a hangingwall catchment with respect to the early rift faults such as the Al Wajh Basin-bounding faults which dip dominantly towards the southwest (Figure 6.15). Pre-rift drainage within this catchment was interpreted to be directed towards the northwest. With the initiation of rifting, however, the pre-rift drainage was captured by drainage perpendicular to the rift as indicated by the elbow of capture, forming a large hangingwall catchment (Figure 6.13b).

The majority of the other catchments draining to the Red Sea and the Gulf of Suez are smaller in scale and mostly elongated perpendicular to the coastline and the basin bounding faults. Therefore, they represent footwall drainage that is mostly limited in scale (extending ~60 km away from the coastline). This control of the bounding faults on small-scale drainage catchments is even noticed within the inland Hamd-Jizl area where individual watersheds that are part of RS20 represent vestiges of the original rift drainage systems.

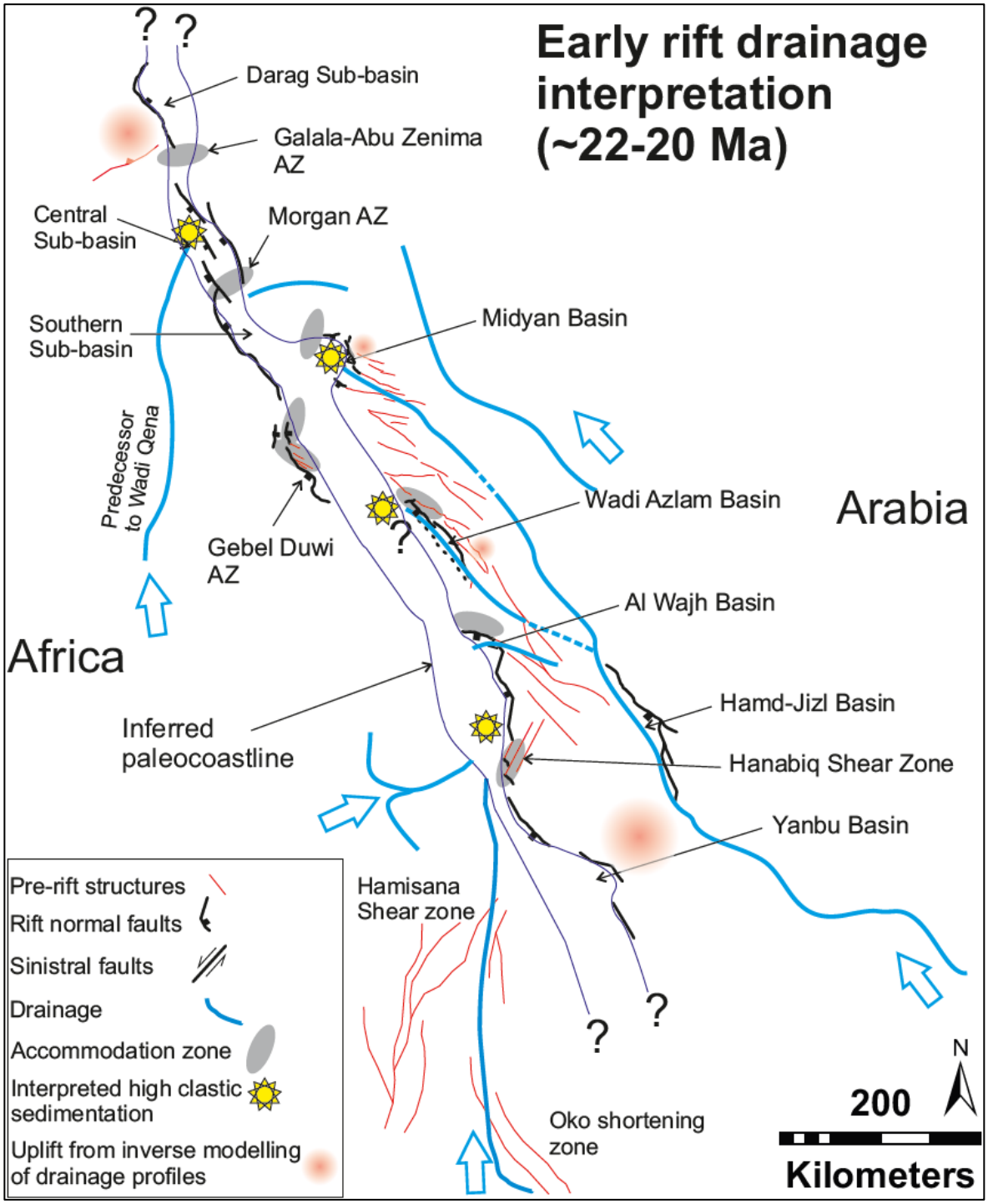

Figure 6.16: A proposed drainage evolution model around the northern Red Sea during the early rift stage (Early Miocene) devised by combining the uplift estimates, the structural evolution and the drainage interpretation. The blue lines are the inferred major rivers. AZ: Accommodation zone.

6.4.3.3 Oblique-rift and early strike slip drainage

Uplift to the east of the Wadi Azlam Basin (Figures 6.5-6.6) is interpreted to have caused the reversal of drainage at the northern part of catchment NERS20 (Figure 6.17). The effect of the uplift on the drainage would have been magnified by the extrusion of volcanics at the Harrat Uwayridh at ~12 Ma (Bosworth et al., 2005) that are characterised by hot mantle sourced basalts (Kaliwoda et al., 2007), which would have increased the surface elevation. Progressive capture of the NW-directed main channel of NERS20 by westward flowing streams has been suggested by Brown et al. (1989) and is supported by the interpretation here. Brown et al. (1989), however, mentioned that the drainage capture occurred during the Late Miocene. Although the drainage reversal itself is hard to date, the uplift signal emerging at the Middle Miocene and the age of the volcanics at Harrat Uwayridh suggest an earlier reversal of the drainage towards the SSE (Figure 6.17).

The lack of lacustrine sedimentary units in the Hamd-Jizl Basin is consistent with this drainage reversal being coeval with drainage capture of catchment NERS20 by headward erosion by streams utilising the accommodation zone north of the Al Wajh Basin (the Najd Fault System). Similarly, uplift to the east of the Midyan Basin was likely responsible for cutting off of the large drainage to the basin, resulting in the formation of catchment NERS1 (Figures 6.5 and 6.17).

On the African margin, uplift signals started to emerge around 16-14 Ma to the west of the Gulf of Suez (Figures 6.5-6.6). The effect on the drainage of this uplift would be the cutting off of any pre-rift drainage from the south and its reversal towards the south to be incorporated in the Nile catchment (Figures 6.5 and 6.17).

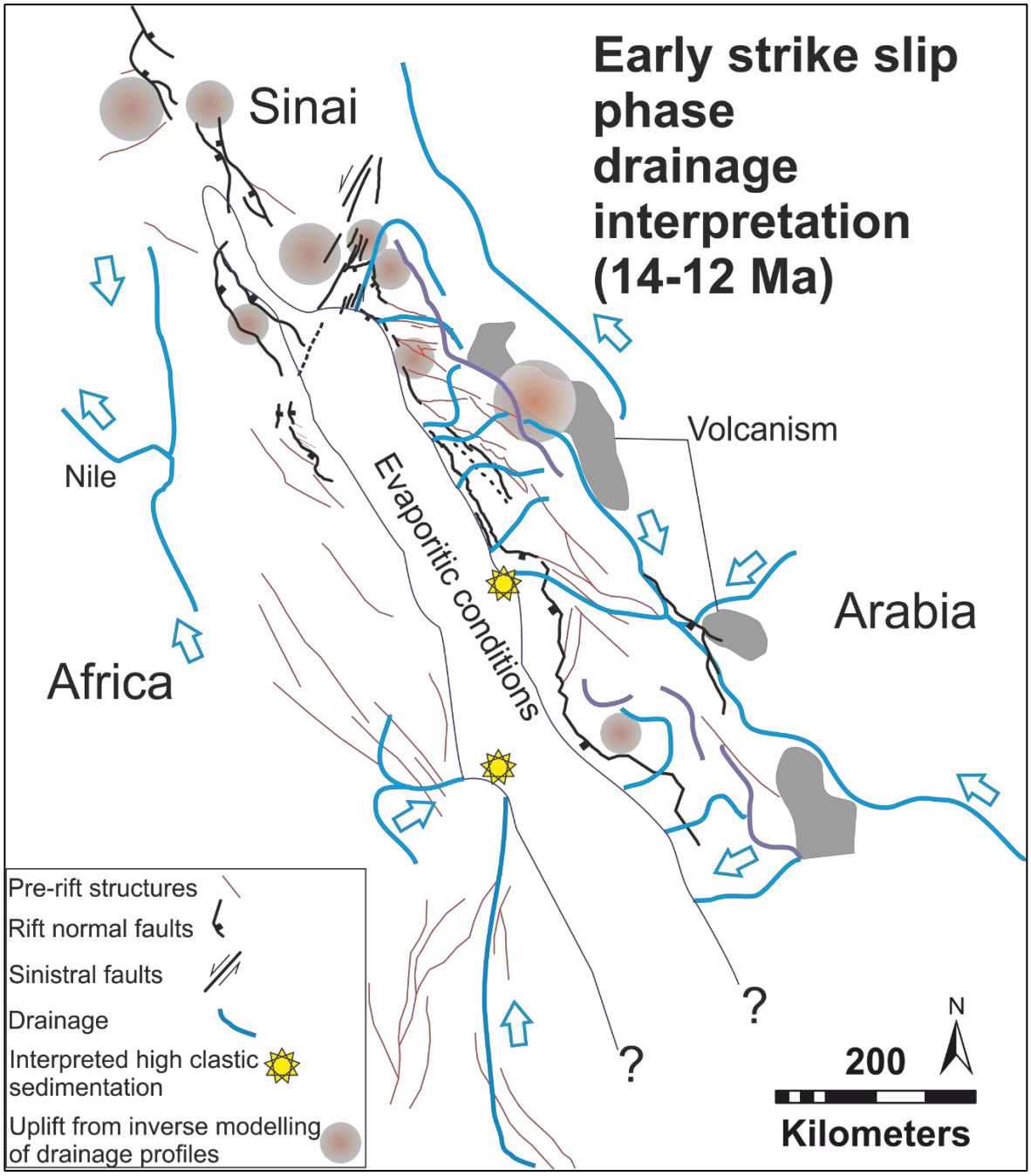

Figure 6.17: A proposed drainage evolution model around the northern Red Sea during the main rift stage and early strike-slip tectonics (Middle Miocene). Ages of volcanics are from Camp et al. (1991) and Bosworth (2005). The blue lines are the inferred major rivers.

6.4.3.4 Late-rift drainage

The latest stage of the rifting was characterised by the intensification of the deformation along the left-lateral Gulf of Aqaba transform starting at ~5 Ma

(Bosworth et al., 2005). The uplift rate estimation reflects the concentration of uplift to the southeastern side of the Sinai Peninsula and to the east of the Midyan Basin as well as the western Gulf of Suez margin (Figure 6.7).

This uplift pattern is also noted on the cumulative uplift maps where uplift is concentrated on either side of the Gulf of Aqaba (Figure 6.8). AFT analysis on samples collected from Sinai (Kohn and Eyal, 1981), on the other hand, indicates that more exhumation occurred along the western Sinai margin than the eastern margin. The AFT ages, however, are affected by the exhumation and the amount of removed overburden, whereas the drainage inverse model method estimates the uplift. This agrees with the fact that the Gulf of Aqaba tectonics are younger than the rifting at the Gulf of Suez. The implication is that uplift rate along the western Gulf of Aqaba margin is larger than the erosion rate.

This focus of uplift in the northeastern part of the study area indicates that the effect on the drainage during this stage is, therefore, interpreted to be local to the Gulf of Aqaba margins and Sinai. The generation of an accommodation space in the Gulf of Aqaba, resulted in the capture of nearby drainage. As for the Red Sea, the direction of the drainage prior to the generation of the accommodation space determines the sizes and shapes of the catchments.

The catchments that are aligned along most of the lengths of the Gulf of Aqaba coastlines have sizes much smaller than those flanking the Red Sea and the Gulf of Suez (Figure 6.10). The sizes of these catchments are controlled by the young uplift that accompanied the Gulf of Aqaba transform tectonics (Bosworth et al., 2017). That is, these catchments form in a topographic context similar to that of the normal fault footwall catchments, which are typically small.

A number of much larger catchments drain to the Gulf of Aqaba from both the Arabian and the Sinai margins. On the Arabian side, the second largest catchment on the northeastern Red Sea margin (EGA1) has its outlet at the northern tip of the gulf (Figure 6.9). Uplift to the east of the Midyan Basin and further north in Jordan had most likely imposed a control on the course of this catchment. Furthermore, catchments WGA11, 19 and 24 are larger than the nearby catchments along the Sinai southeastern margin and are characterised by upstream sections that are

elongated semi-parallel to the gulf trend. The sizes of these catchments could indicate pre-Gulf of Aqaba tectonics drainage that was later incorporated into the gulf drainage.

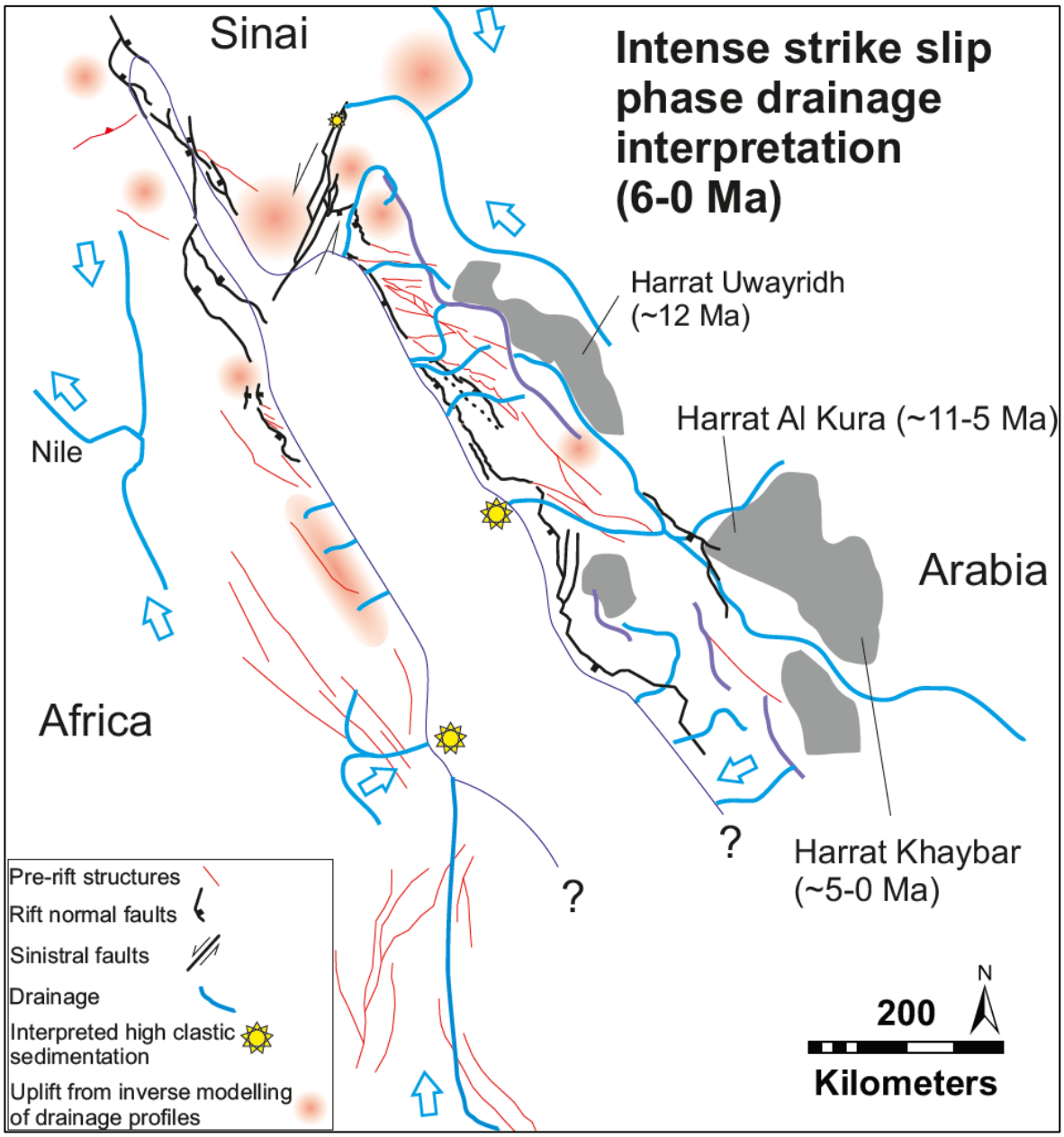

Figure 6.18: A proposed drainage evolution model around the northern Red Sea during the late rift stage and intense strike-slip tectonics (Pliocene). Ages of volcanic harrats are from Camp et al. (1991) and Bosworth et al. (2005). The blue lines are the inferred major rivers.

The width of cumulative uplift zone along the African margin is much narrower compared to that of the Arabian margin. This is a justifiable cause for the

comparatively limited retreat of the drainage divide and the escarpment inland (Cumulative uplift at present-day in Figure 6.8). In details, however, stream capture of drainage that flowed previously away from the rift is observed. For instance, catchments SWRS 4, 13 and 21 have drainage anomalies interpreted as elbows of capture of drainage that flowed westward as part of the proto-Nile catchment. Nonetheless, these adjustments of the drainage were in the scale of the streams rather than large drainage areas.

An uplift zone is interpreted to have affected a semi-linear area within ~100 km of the coastline to the south of Gebel Duwi during the Late Miocene-Pliocene (Figure 6.17). This uplift aligns well with the extent of the small catchments and, therefore, is suggested to have resulted in their formation. The lack of east dipping faults in this part of the margin and the young age of the modelled uplift (i.e. Late Miocene-Pliocene) argue against a footwall uplift origin for the small catchments along the Egyptian Red Sea margin.

6.5 Discussion

6.5.1 Assessment of uplift estimates

The resolution of uplift estimates using the inverse modelling approach drops from the present-day towards the early rifting stage as the data coverage of the model becomes smaller back in time (e.g. Rudge et al., 2015; Figure 6.4). This intrinsic issue of the method of the stream profile inversion has an impact on the resolution of the fault-driven uplift during the early rifting in the study area, particularly in terms of the strength of the uplift signal. An example of this effect is the lack of a strong signal on the uplift rate or cumulative uplift maps during the early rifting (23-22 Ma; Figures 6.5 and 6.6).

Taking into account this property of coverage deterioration, it is not likely that any pre-rift uplift can be deduced here. Furthermore, the low rates of uplift noted east of the Midyan Basin, northeast of the Al Wajh Basin and along the northwestern Gulf of Suez margin (Time 22 Ma in Figure 6.5) are interpreted to show where an uplift events occurred but do not represent a quantification of the absolute uplift rates. This interpretation is aligned with geological evidence that indicates that these

basins became active as rift basins around the Early Miocene (Bosworth et al., 2005; Tubbs et al., 2014). Evidence for the activity of the Midyan Basin border faults and the resultant uplift is given by the presence of granitic cobbles within the early rift Al Wajh Formation (Hughes and Johnson, 2005; Hughes et al., 1999) that suggests erosion of uplifted footwall blocks and the exhumation estimates at ~23 Ma (Stockli and Bosworth, 2019). In the southern part of the study area along the Arabian margin, exhumation assessment via AHe and ZHe analyses revealed that fault-driven uplift occurred during the Early to Middle Miocene (Szymanski et al., 2016).

Using AFT analysis on samples collected from the central and southern parts of the western Gulf of Suez margin and the northernmost part of the Egyptian Red Sea margin, Omar et al. (1989) proposed that uplift of the rift flank commenced after the onset of rifting during the earliest Miocene (21-23 Ma). Omar et al. (1989) concluded that the uplift continued even during an accelerated subsidence phase from 21-19 Ma. Other workers have shown that this accelerated subsidence occurred rather later during the period 19-16 Ma (Bosworth et al., 1998) or 20-15 Ma (Moretti and Colletta, 1987). In the inverse model presented here the uplift was focussed at the northern part of the western Gulf of Suez margin during the early rifting, and later in the Middle Miocene (14-12 Ma) it expanded over an area covering all of the western Gulf of Suez margin (Figures 6.5 and 6.17).

Also during Middle Miocene, uplift developed at that eastern Gulf of Suez, western Gulf of Aqaba and southern Sinai, coeval with the start of the Gulf of Aqaba tectonics at ~14-12 Ma (Bosworth et al., 2005). Two samples collected from the southwestern Sinai basement have AFT ages of 13.3±2.2 and 11.5±3.1 Ma (Kohn and Eyal, 1981).

The high uplift rates and cumulative uplift that started at 12 Ma (Figures 6.5-6.8) and continued to the present-day indicate an active uplift of the central and southern Gulf of Suez flanks. The high elevations that still characterise the southeastern Gulf of Suez margin (i.e. southern Sinai; reaching ~2600 m) and the coarse post-Miocene sediments in the Gulf of Suez support this argument (Steckler et al., 1998). Steckler et al. (1998) proposed that convection under the northernmost Red Sea contributed to the uplift in southern Sinai. It is proposed

here that even additional uplift in southern Sinai and southwestern Gulf of Suez was likely contributed tectonically by the Gulf of Aqaba strike-slip tectonics. When projecting the trend of the Gulf of Aqaba across the northern Red Sea towards the African margin, a marked difference between the uplift signals to the south and north can is noted particularly at the 12 Ma maps (Figures 6.5 and 6.7). In addition, along the eastern Gulf of Aqaba margin, the uplift in response to the transform tectonics initiation and intensification (Bosworth et al., 2017) is demonstrably shown on the uplift estimates at the Late Miocene to Pliocene (Figure 6.7).

6.5.2 Controls on drainage evolution in rifts and rifted margins

This study of the tectono-geomorphology of the northern Red Sea margins reflects the interplay between several factors in controlling the drainage evolution. As highlighted in the drainage evolution (Section 6.4.3), these factors may be divided broadly into three types with respect to their spatio-temporal effects on the drainage: pre-rift structures (that influence the orientation of pre-rift drainage), fault-driven uplift and late-rift uplift. These effects were shown to control the drainage evolution and possibly affect sediment entry points into the basins along the Arabian part of the study (see Section 3.4.3). As will be discussed in the subsequent sub-sections, the main effect of these factors is on the size of the resultant catchments, which should have an implication on the amount of sediments delivered to the rift.

6.5.2.1 Pre-rift structures

Pre-rift basement structures are usually aligned with regional drainage on both the Arabian and the African margins (e.g. SWRS25). Although the overall control on the pre-rift drainage would be the paleo-surface slope, the existence of such basement structures for a long time prior to the rifting provides preferential weakness zones that are suitable for pre-rift drainage to exploit resulting in large watersheds within a regional catchment.

During rifting, the pre-existing structures segment the rift and form relay zones in between rift units (Lambiase and Bosworth, 1995). In this case, the drainage is not

affected by any flexural uplift of the flank and resumes its course even during the rifting linking large-scale pre-rift catchments with the depo-centres at the rift.

6.5.2.2 Fault-driven uplift

Compared to the pre-rift drainage that evolves into regional catchments, fault-driven uplift results in the formation of smaller catchments that are limited in extent by the position of the fault scarps. Such catchments would likely results in km-deep erosion due to the significant fault-driven uplift (e.g. 3-6-km-uplift of the Jabal az Zuhd and the footwall block of the coastal fault near Duba; Stockli and Bosworth (2019)).

The effect of the fault-driven uplift, and possibly any unloading-related flexural response to the exhumation, is the deflection or reversal of pre-rift drainage away from the rift. For instance, the interpreted reversal of the originally north-directed pre-rift drainage in the Wadi Qena during the main rifting phase (Figure 6.17) was caused by the uplift of the footwall block of the bounding fault of the Gulf of Suez southern sub-basin and could be related to the initiation of the Gulf of Aqaba tectonics. This interpreted reversal is aligned with the model of Goudie (2005) as well as the conclusion that early rift clastics in the Gulf of Suez were sourced from the south, prior to the uplift and exhumation that lasted between approximately 19 and 15 Ma (Evans, 1990).

Furthermore, the distribution of the hangingwall drainage (African side) and the footwall drainage (Arabian side) reflects the polarity of the controlling faults being mostly on the Arabian margin and dipping towards the southwest (Figure 6.15). This interpretation is in agreement with the interpretation shown in Stockli and Bosworth (2019) of large scale polarity reversal along the northern Red Sea.

6.5.2.3 Late-rift uplift

Uplift that post-dated the onset of rifting, which was not a direct response to the rifting process, is proposed here to have affected the drainage in two ways. The two effects can be demonstrated with reference to the evolution of 1) catchment NERS20 along the Arabian margin, and 2) the small catchments along the Egyptian Red Sea margin (SWRS1-16; Figures 6.7-6.9).

With respect to the Arabian margin, the Middle Miocene uplift near the Harrat Uwayridh is interpreted to have caused reversal of the northwest-directed regional pre-rift drainage of the precursor to catchment NERS20 (Figure 6.17). The existence of this uplift near a volcanic field with extrusion that post-dates the onset of the rifting by ~11 Myrs (Bosworth et al., 2005) suggests that the uplift and volcanism are caused by the same process of dynamic mantle support (see also the discussion in Chapter 3 (Section 3.4.2)). Such a relationship highlights the potential impact of dynamic uplift events in modifying typical structure-drainage relationships by inducing drainage reversals. The effect in the case of the Arabian margin is the formation of the largest catchment and the shifting of its outlet towards the latitude of the Al Wajh Basin.

In the case of the Egyptian margin, the formation of the small catchments (SWRS1-16) is compatible with the modelling results that show a near-linear uplift zone along the coastline (Figure 6.18). However, if such uplift was driven by the displacement and flexure of the lithosphere along large-scale faults, then it would be plausible to detect such faults along the margin. However, this part of the margin mostly lacks such faults and is rather a part of a northeast-dipping domain that was controlled during the early rifting by southwest-dipping normal faults similar to the faults along the conjugate Arabian margin (e.g. Stockli and Bosworth, 2019). A comparison between the small catchments that were formed due to this uplift and catchment SWRS21, which falls outside the uplift zone, shows that the latter evolved more like a typical hangingwall catchment with comparatively much larger size. This conclusion does not substantiate suggestions that an early rift uplift drove the formation of these catchments and the establishment of a drainage divide between them and the Nile catchment (e.g. Goudie, 2005).

The aforementioned reflect the spatial and temporal correlations that can be made between the geomorphology and the estimated uplift. That is, geomorphologically, the extent of the drainage divide on the Arabian side (>200 km) is much greater than that on the Egyptian side (50-60 km). Similarly, the latest uplift events on both sides (since the Middle Miocene) were located ~100 km from the present-day coastline on the Arabian side (~12 Ma) and within ~60 km on the Egyptian side (~6 Ma).

6.5.3 Implications for sedimentation

During the early and the main rift stages, a small number of large catchments were formed as large tributaries of the pre-rift drainage were intersected by the Red Sea and the Gulf of Suez early rift basins at oblique angles (Figure 6.16). These include the proto-catchments of NERS20, SWRS25 and possibly the northeastern tributary of the Nile.

Szymanski et al. (2016) estimated that exhumation at the Central Arabian Rift Flank (CARF) was ~1.7±0.8 km starting at 23 Ma as rifting initiated. Their area of study is located mostly within NERS20. Given this km-scale exhumation and the fact that the catchment substrate currently is basement rocks, it is implied that most of the eroded material in response to uplift was delivered to the rift basins (currently relict rift basins). However, it is important to note that the present-day shape and size of NERS20 do not reflect those of the early and main rift predecessor catchment. Therefore, clastic input as a consequence to the uplift and erosion would have been into basins north of the Al Wajh Basin. This direction of the sediment pathways might be responsible for sourcing the pre-evaporite sediments in the Midyan Basin (Hughes et al., 1999) or even more northern basins (e.g. the Levant; Zilberman and Calvo, 2013).

The interpretation based on low-temperature thermochronology reached in Chapter 5 that the area to the southeast of the Midyan Basin continued to play a role as a relay ramp suggests that major drainage to the basin from the southeast continued until at least the Middle Miocene. This interpretation is in agreement with the conclusion reached in this chapter and in Chapter 3 that shows that 1) the predecessor to NERS20 flowed towards the north and had its outlet possibly at the Midyan Basin depocentre and 2) low uplift characterised the area to the southeast of the Midyan Peninsula allowing for this northward drainage to continue until reversal took place near Harrat Uwayridh.

Early sedimentation at the Al Wajh Basin, however, was most likely fed by the predecessor catchment of SWRS25, the largest Red Sea catchment on the African side. No significant drainage anomalies within this catchment exists that suggest capture of more drainage area during its evolution. The orientation of this

catchment reflects the influence of the pre-rift structures (Hamisana Shear Zone and Oko shortening zone). Upon plate restoration, The Hamisana shear zone on the African margin forms a continuation of the Hanabiq shear zone on the Arabian counterpart, which is aligned parallel to the southern segments of the Al Wajh Basin-bounding fault (Johnson et al., 2011).

Additionally, it is likely that catchment SWRS21 first formed as a hangingwall catchment controlled by the Al Wajh Basin eastern bounding fault. In rift settings, hangingwall catchments are usually smaller than catchments at the accommodation zones and relay ramps. However, they are larger than footwall draining catchments and would likely contribute a more significant amount of sediments to the basin (e.g. Gawthorpe et al., 1994).

6.6 Conclusions

Using an approach that integrates inverse modelling of drainage profiles, drainage network analysis and plate restoration, the evolution of uplift and the coeval drainage modification were assessed across the northern Red Sea during the Cenozoic rifting stages. Low rates of uplift (~0.01 mm/a) occurred east of the Midyan Basin, along the northwestern Gulf of Suez margin and at the southern Egyptian Red Sea margin during the early rifting phase. However, the low signal does not indicate a low magnitude of uplift but is caused by the deterioration of the coverage with time, an intrinsic issue in the method of the stream profile inversion.

Pre-rift paleo-drainage was characterised by a small number of regional catchments that are elongated oblique to the trend of the Red Sea, flowing generally towards the north (varying from the NW to the NE). This drainage was locally aligned with pre-existing structures (e.g. the Hamisana Shear Zone and Oko shortening zone), which likely formed zones of weaknesses for drainage to utilise.

The sizes of the catchments that formed during the early rifting were variable. Large catchments were the result of the incorporation of large pre-rift drainage into the rift system through accommodation (transfer) zones (e.g. NWRS25 and the predecessor to NERS20), as well as the formation of hangingwall dip-slope

drainage (e.g. SWRS21). Smaller catchments footwall drainage catchments (most of the Arabian Red Sea catchments). The catchment distribution indicates that early northern Red Sea rifting was accommodated by SW-dipping faults, with polarity changing further north into, and within, the Gulf of Suez.

On the Arabian side, as also shown in Chapter 3, Middle Miocene uplift to the east of the Wadi Azlam Basin is interpreted to have caused the reversal of drainage at the northern part of catchment NERS20, which was nearly coeval with its capture by headward eroding streams initiating at the Al Wajh Basin. Similarly, uplift to the east of the Midyan Basin caused the deflection of significant drainage away from the basin, resulting in the formation of catchment NERS1. On the African margin, uplift signals around 16-14 Ma to the west of the Gulf of Suez possibly caused the reversal of pre-rift drainage from the south to be incorporated in the Nile catchment.

The latest stage of the rifting was associated with the concentration of uplift to the southeastern side of the Sinai Peninsula and to the east of the Midyan Basin as well as the western Gulf of Suez margin. On the Arabian side, the second largest catchment on the northeastern Red Sea margin (EGA1) has its outlet at the northern tip of the gulf, and its drainage course was controlled by uplift to the east of the Midyan Basin and further north in Jordan. Late uplift at the northern part of the Egyptian Red Sea margin is interpreted to have reversed drainage towards the Nile catchment resulting in smaller catchments (compared, for example, to the hangingwall catchment SWRS21).

The observations of drainage modification in response to uplift variation throughout the Red Sea rifting indicate that the evolution of sediment routing to the basins along rifts and rifted margins in general is highly complicated by the pre-rift drainage direction (governed largely by pre-existing basement weaknesses) as well as uplift during and after rifting. In particular, the post-onset-of-rift processes are important as their effects on the drainage and sediment distribution would not be readily grasped from, for instance, observations from active rifts.

Part III: Summary and conclusions

Chapter 7 Summary and Concluding Remarks

7.1 Review of research focus

In this thesis, the tectono-geomorphic spatial and temporal evolution of the northern Red Sea and the nearby margins was investigated. The focus of this work was on the upstream areas of rifts and the rifted margins where early rift structures, uplift, exhumation and sediment sourcing occur. Processes occurring at the following three scales were investigated:

- Uplift history along the whole of the northeastern Red Sea margin and the eastern Gulf of Aqaba margin (length scales of 10s-100s km),
- Brittle deformation, rock uplift and exhumation across the southeastern Midyan Peninsula (northeastern Red Sea margin) with length scales of 20-30 km, and
- Drainage evolution across the northern Red Sea from pre-rift settings through the different rift stages, and its implications on sediment dispersal in the basins (length scales of 10s-100s km).

7.2 Synopsis of results

The following sections summarise and integrate the highlights from the detailed conclusions presented in chapters 3-6.

7.2.1 Uplift history

Along the northeastern Red Sea and eastern Gulf of Aqaba margins, the uplift estimated from the inverse modelling of drainage profiles evolved from an early (21-15 Ma) locus located in the southern part of the study area (near Yanbu) to a late (12-0 Ma) northern one east of the Gulf of Aqaba. The late phase of uplift is characterised by the concentration of uplift at the southeastern side of the Sinai Peninsula and the western Gulf of Suez margin. Along the northeastern Red Sea margin, spatial geomorphic variation (in terms of minimum volume of eroded material and topographic relief) is consistent with this south-to-north spatio-temporal variation in uplift rate and magnitude.

The distribution of uplift and existing studies on the exhumation of the margin (e.g. Szymanski et al., 2016) suggest that the early evolution of this margin represented early-rift uplift in the southern part of the study area that is a record of footwall uplift with a possible additional mantle dynamic support. The shift of the uplift towards the north represents footwall rebound and tilting due to fault coalescence and the isostatic response to transform tectonics that are still active at the Gulf of Aqaba. Although the Gulf of Aqaba faults are tectonically part of a transform system, a strong dip-slip component (Bosworth et al., 2017) explains the existence of this footwall uplift. The late uplift is also attributed to mantle processes in the northern part of the Arabian Red Sea margin (Harrat Uwayridh), where basalt geochemistry indicates hot shallow mantle-driven outpouring (Bosworth et al., 2005; Kaliwoda et al., 2007). However, the wavelength of uplift (~100-120 km) is smaller than the typical mantle plume doming (i.e. ~1000 km).

7.2.2 Exhumation history

An assessment of exhumation was conducted along a transect positioned across the northeastern Red Sea margin, to the southeast of the Midyan Basin. The South-Eastern Fault (SEF) zone of the Midyan Basin juxtaposes basement on basement, with a dominant dip direction of the major faults in the zone towards the WSW to SSW and strike orientations (~NW) that are oblique to the overall NNW Red Sea trend. Kinematic indicators in this zone suggest oblique-to-normal sense of movement, with oblique-to-strike-slip (both dextral and sinistral) displacements possibly related to local structure orientations guiding the stress field.

Low-temperature thermochronology (AFT and AHe) indicates that more cooling since the onset of rifting (earliest Miocene) has been experienced at the hangingwall block of the fault zone compared to the footwall block. This suggests that any displacement across the fault was less than could possibly be resolved by low-temperature thermochronology indicating that this fault zone was not significantly (i.e. with ~km-scale displacement) active during the Red Sea rifting.

Cooling estimates based on thermochronometric data and using HeFTy modelling (Sections 5.5.3) reveal that faulting-driven uplift of the ShF footwall block was enough to create a fault scarp (<1 km) that, later through erosion and escarpment

retreat, resulted in the present-day erosional escarpment. However, the fault scarp was not substantial as to have initiated erosion that would exhume rocks from deeper levels than the AFT partial annealing zone (PAZ). This and the aforementioned point argue that the SEF zone was a strain accommodation zone between the Midyan Basin to the north and the basin bounded by the Sharma Fault (ShF) to the south. The brittle deformation at the SEF, therefore, resulted from older deformation(s) that was only slightly affected by the Red Sea extension stress regime.

On the northeastern Red Sea margin plateau (i.e. east of the escarpment), exhumation is suggested to have been regional in extent. Such regional exhumation could have been driven by regional uplift and/or significant erosion by fluvial processes resulting in the stripping of the pre-rift sedimentary cover.

7.2.3 Drainage evolution

The catchments and streams across the northern Red Sea reflect the interplay of pre-rift drainage (mostly controlled by basement heterogeneities and a low-relief, low-elevation northward sloping pre-rift landscape) and tectono-geomorphic evolution during rifting that was associated with variable uplift. Pre-rift paleo-drainage was characterised by a small number of regional catchments that were elongated oblique to the trend of the Red Sea, flowing generally towards the north (e.g. the predecessor to catchment NERS20). This drainage was largely aligned with pre-existing structures (e.g. the Hamisana Shear Zone and Oko shortening zone), which would have formed preferential weak zones for fluvial processes. The overall northward slope was off the Afar dome that lay to the south of the study area.

Along the northeastern Red Sea margin, regional structural segmentation is highlighted by two zones of high escarpments, separated by low topography of a major relay zone. Upon rifting, early rift basins, now perched on the northeastern Red Sea margin, captured the pre-rift drainage that flowed near them. The sizes of the catchments that were formed during the early rifting varied depending on where major pre-rift drainage intersected the rift. Large catchments were captured by the Al Wajh Basin (SWRS25) and possibly the Midyan Basin (predecessor to

catchment NERS20). Another example of pre-rift drainage capture by rift basins is highlighted at the Egyptian margin where Wadi Qena, now flowing southward as a tributary to the Nile, is interpreted to have initially been flowing northward where it was incorporated into the rift-related drainage of the early Gulf of Suez.

The effect of structural evolution of the rift basins on the drainage is apparent where footwall and hangingwall catchments formed. Small catchments with relatively short and perpendicular-to-coastline streams are associated with footwall drainage, separating larger relay-zone catchments. This control of the bounding faults on small-scale drainage catchments is noticed even at great distances inland away from the coastline as in the Hamd-Jizl area where watersheds layout resembles that of footwall catchments.

On the Arabian side, uplift to the east of the Wadi Azlam Basin, and possibly the formation of a topographic high due to the extrusion of volcanics at the Harrat Uwayridh, during the Middle Miocene are interpreted to have caused a reversal of drainage at the northern part of catchment NERS20. This reversal was nearly coeval with the capture of the NERS20 catchment by headward eroding streams initiating near the Al Wajh Basin. Similarly, uplift to the east of the Midyan Basin caused the deflection of significant drainage away from the basin. Furthermore, the second largest catchment on the northeastern Red Sea margin (EGA1) has its outlet at the northern tip of the Gulf of Aqaba, and its drainage course was controlled by uplift to the east of the Midyan Basin and further north in Jordan.

On the African margin, uplift signals around 16-14 Ma to the west of the Gulf of Suez caused the reversal of pre-rift drainage from the south to be incorporated in the Nile catchment. Later during the rifting, the Late Miocene-Pliocene along the Egyptian Red Sea margin (south of Quseir) resulted in the formation of small catchments that resemble footwall catchments. These catchments were unlikely to be related to fault-driven uplift due to the uplift youth with respect to the rifting and the absence of east-dipping faults in the literature. Further south, catchment SWRS21 is interpreted to have formed as a hangingwall catchment. The lack of a young uplift phase at SWRS21 was possibly the cause for its present large size compared to the catchments further north.

On the Sinai side, large catchments (WGA11, 19 and 24) are indicative of pre-Gulf of Aqaba tectonics drainage that was later incorporated into the gulf drainage. The smaller catchments along the Gulf of Aqaba western margin are related to the later uplift during the strike-slip tectonics. Comparatively, larger catchments along the Gulf of Suez eastern margin are related to footwall and accommodation zone drainage.

7.3 Implications

7.3.1 Implications for the geodynamics

The work presented here highlights the topographic signature that geodynamic processes occurring throughout rifting can have. Three main geodynamic aspects are reflected on the distribution of uplift in time and space along the northern Red Sea margins; namely, large-scale normal faults, mantle support and the later strike-slip tectonics.

Along most of the study area, the coincidence of Early Miocene uplift and rifting (within a few million years, as opposed to their temporal separation at mature passive margins (see Japsen et al. (2012)) favours rift-related faulting as a driver of uplift. This is the case during early rifting along the Gulf of Suez margins and the northernmost part of the northeastern Red Sea margin (e.g. Streckler et al., 1988; Omar and Streckler, 1995), where relatively short-wavelength (~60 km) uplift is modelled. Corroborating this conclusion, no mantle-fed volcanism occurred at these parts of the study area. Furthermore, the uplift area modelled east of the Midyan Peninsula is spatially associated with by relatively high shear wave velocity (e.g. Yao et al., 2017), which indicates the absence of mantle dynamic support.

The large-wavelength (~200 km) uplift during the early rifting in the southern part of the Arabian study area (Chapter 3) was located just north of an uplift zone supported by mantle processes in southwestern Arabia (Wilson et al., 2014). This early uplift also coincides temporally and spatially with faulting-driven exhumation interpreted using low-temperature thermochronology (Szymanski et al., 2016). The deterioration back in time of the coverage of the drainage inverse modelling, however, might have caused the existence of the large-wavelength signal as the

uplift rates between sparse data points were smoothed. Therefore, it is concluded that the uplift was driven largely by fault rebound with a possible additional dynamic support, on a semi-regional scale, due to mantle upwelling.

A clearer influence of mantle support is indicated at the Harrat Uwayridh (1600-1700-m-high on the northeastern Red Sea margin), which was affected by an uplift episode at ~12 Ma (Chapter 3 and Chapter 6). The geochemistry of the basalt here indicates hot shallow mantle-driven outpouring (Bosworth et al., 2005; Kaliwoda et al., 2007), supporting the conclusion that this uplift was not an inherent feature of the rifting episode.

As revealed by the uplift estimation in Chapter 3 and Chapter 6, the strike-slip tectonics along the Gulf of Aqaba affected both margins of the gulf by inducing uplift. It is, however, clear that the eastern gulf margin (north of the Midyan Basin) was more uplifted than the western margin, which is compatible with the existence of a large dip-component to the transform tectonics (Bosworth et al., 2017). The uplift at the area between the western Gulf of Suez and Egyptian Red Sea margin was coeval with the strike-slip tectonics. It is likely that structures related to the stress field change that caused the strike-slip deformation extended beyond the Gulf of Aqaba and possibly into the African margin.

In this sense, the above supports the conclusion by Hosny and Nyblade (2014) who, upon estimating the distribution of the crustal thickness, suggested that uplift on the Arabian side of the Red Sea was driven by warm mantle flowing under western Arabia rather than the mechanism of rifting. However, the pure-shear mode of extension proposed by Hosny and Nyblade (2014) is not substantiated by the distribution of uplift during the early rifting (22-20 Ma) along both margins and the present-day arrangement of catchments with respect to the rift major faults located near the coasts. Instead, these geomorphic aspects of the Arabian and African margins support a simple-shear mode of extension (e.g. Voggenreiter et al., 1988; Wernicke, 1985). The geodynamics of the northern Red Sea, therefore, is better described by a hybrid model with passive asymmetric rifting during the Early Miocene through simple shear extension and mantle-driven uplift during the Middle Miocene on the Arabian side (Figure 7.1). This model differs to that proposed by Stockli and Bosworth (2019) in that the southwest-ward dipping

normal faults on the Arabian sides are also present in the northernmost part of the northeastern Red Sea (i.e. to the east of the Midyan Basin and along the coast near Duba). The model presented here is compatible with the geomorphic and volcanic asymmetry across the northern Red Sea (Almalki et al., 2015; Bosworth et al., 2005; Wilson et al., 2014) and with the basin bounding faults (e.g. Tubbs et al., 2014).

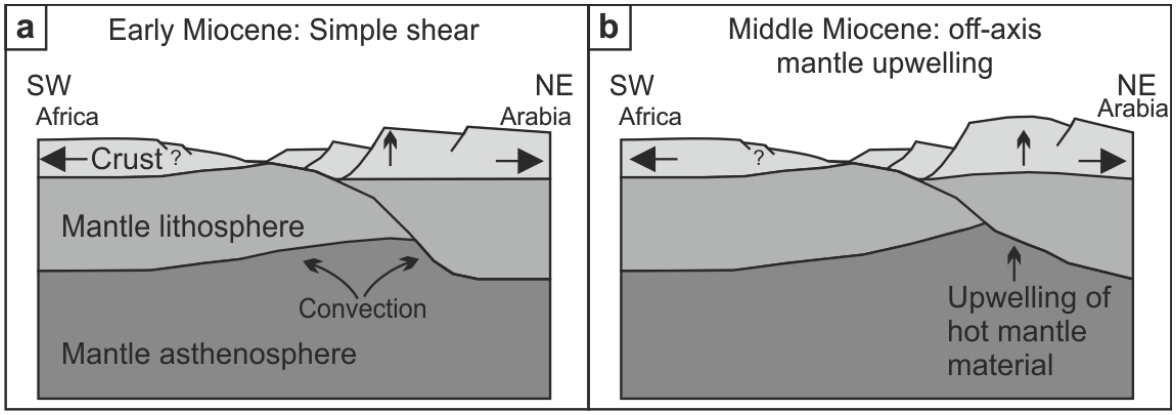

Figure 7.1: Proposed model for the geodynamic evolution of the northern Red Sea. Both stages feautured significant uplift on the Arabian margin (uplift denoted by vertical arrows).

The Late Miocene-Pliocene uplift along the Egyptian Red Sea margin was limited in width (~60 km) but was not associated with mapped normal faulting. This part of the margin was interpreted to have initiated within an east-dipping area controlled by west-dipping normal faults that became active during the Early Miocene on the Arabian margin (Stockli and Bosworth, 2019). The Late Miocene-Pliocene uplift, therefore, was driven by processes that were offset in time from the uplift that occurred during onset of rifting. Lithospheric density distribution estimates show that this zone is underlain by low density zone that extends approximately ~100 km west of the coastline (Kaban et al., 2018). This indicates reduced density due to heating, which might be related to the ascent of the asthenosphere prior to sea-floor spreading that has been suggested to be beginning to take place in the northern Red Sea (e.g. Cochran, 2005). However, the lack of other evidence (e.g. geochemical analysis of volcanic units) makes this conclusion uncertain.

7.3.2 Implications for hydrocarbon prospectivity in rifts and rifted margins

Several aspects of this thesis have implications for the potential for hydrocarbon exploration in rifts and rifted margins. These aspects stem from observations from the uplift and drainage interaction, the inferred paleo-geothermal gradient and structural mapping of the fault zone.

7.3.2.1 Uplift drainage interaction and sediment routing

During rifting, rivers reorganise their networks as uplift and erosion rates vary along the margins and in time. Along the northern Red Sea, catchment integration and disintegration interpreted in this study should have implications on the delivered sediments to the basins. Understanding this along-margin variation in syn-rift clastic deposition is of high importance for predicting reservoir rock distribution.

The interpretation that the catchment that preceded NERS20 had its outlet further north from where it is now (i.e. its paleo-outlet was at Wadi Azlam or the Midyan basins) has a major implication on the potential distribution of clastic sediments within the basins presently inboard of the coastline and along the northeastern Red Sea margin. The implication is that prior to the capture of the axial drainage at Hamd-Jizl Basin, early rift sedimentary thicknesses would have been greater at the Wadi Azlam Basin and further north compared to the Al Wajh Basin, which was fed by smaller hangingwall catchments sourced from the African margin. After the capture, the syn-rift clastic thicknesses would have increased at some point during the rifting stage at Al Wajh Basin with potentially much reduced thicknesses further north.

Another example of drainage reorganisation was described from the eastern part of the Midyan Peninsula. The late stage uplift at the end of the Miocene-start of the Pliocene east of the Midyan Basin has probably caused deflection of streams towards the east where they joined present-day catchment EGA1 streams, as indicated by misfit streams at catchment NERS1 boundaries. This implies that a larger paleo-catchment would have preceded the present-day catchment NERS1, which would have contributed to the larger clastic thicknesses in the Midyan Basin

during the Miocene. The reduction of the clastic input into the Midyan Basin during and after the Pliocene could be related to this drainage reorganisation in response to this and the previously noted uplift.

The conclusion that no major fault uplift developed at the Sharma Fault (ShF) or at the South-Eastern Fault (SEF) and that the SEF was likely a strain accommodation zone (i.e. relay ramp) indicates that this zone was a preferable location for early rift drainage. In addition to the interpreted large sediment input from the north of the Midyan Basin during the Miocene described earlier, the drainage that utilised this accommodation zone would have been influential in delivering sediments to the Midyan Basin from southeastern hinterland locations. This drainage was likely part of the catchment that preceded NERS20 prior to the drainage reversal discussed earlier.

7.3.2.2 Paleo-geothermal gradient

The results of the thermal modelling conducted during the low-temperature thermochronology study of the basement samples taken from the Sharma-Tabuk Road Transect show that there would have been spatial variation of the paleo-geothermal gradient across the margin (Sections 5.6.1 and 5.6.2). However, overall, a high paleo-geothermal gradient may be inferred based on the samples taken from the most inboard locations (i.e. samples 16-T1-10a and 11a), which is expected to have been even higher near the rift. In terms of hydrocarbon potential, this has great implications on the maturation of source rocks deposited in the rift basin (in this case the Midyan Basin).

7.3.2.3 Structural aspects

The structural mapping of the South-Eastern Fault (SEF) zone shows the complexity of such a wide zone of old brittle deformation, which during the Red Sea rifting coincided with a strain accommodation zone. The lens-shaped blocks that are bounded by the faults comprising this zone have scales that reach ~1 km in width.

Using this as an analogy, similar behaviour of fault zones are expected to exist in the subsurface where the basement is faulted, particularly away from localised

faulting (e.g. Jabal az Zuhd Fault). This deformation style is likely to affect overlying stratigraphic units with respect to their connectivity across the fault zone. From a hydrocarbon exploration standpoint, where reservoir rocks are cut by faults with similar behaviour, the effect would be in the form of compartmentalising reservoir units during brittle deformation.

7.4 Recommendations for future work

The results presented in this thesis may be used as a basis for future work. In particular, the following research routes may be pursued further:

- Drainage evolution interpreted from onshore areas can be integrated with subsurface data to better constrain paleo-drainage in the subsurface and predict paleo-spacing between sediment entry points along presently submerged basins with implications for sedimentary accumulation.
- Subsurface analysis using seismic and well data at basinal locations may be used to test the existence of along-margin variation in sediment thicknesses. The timing of any spatial shift in sediment accumulation may then be cross-checked against the predicted major drainage evolution events.
- In order to validate (or otherwise) the interpretation of paleo-drainage and sediment input locations into the early rift basins, measurement of paleo-current directions within the basins may be carried out. This interpretation could be done on oriented well cores, through the use of image logs or on outcrops. This is particularly relevant, for example, to the Al Wajh Basin, which is predicted to have received more sediments from the African margin during the early rifting stage and more sediments from the Arabian margin during the late rifting stage.

List of References

Abdelsalam, M.G. and Stern, R.J. 1996. Sutures and shear zones in the Arabian-Nubian Shield. *Journal of African Earth Sciences*. **23**(3), pp.289-310.

Allen, P.A. 2017. *Sediment routing systems: The fate of sediment from source to sink*. Cambridge: Cambridge University Press.

Allen, P.A. and Allen, J.R. 2005. *Basin analysis: Principles and applications*. 2nd ed. Oxford: Wiley-Blackwell.

Allmendinger, R.W., Cardozo, N. and Fisher, D.M. 2011. *Structural geology algorithms: Vectors and tensors*. Cambridge: Cambridge University Press.

Almalki, K.A., Betts, P.G. and Ailleres, L. 2015. The Red Sea–50 years of geological and geophysical research. *Earth-Science Reviews.* **147**, pp.109-140.

Angelier, J. 1990. Inversion of field data in fault tectonics to obtain the regional stress—III. A new rapid direct inversion method by analytical means. *Geophysical Journal International*. **103**(2), pp.363-376.

ArRajehi, A., McClusky, S., Reilinger, R., Daoud, M., Alchalbi, A., Ergintav, S., Gomez, F., Sholan, J., Bou-Rabee, F., Ogubazghi, G. and Haileab, B. 2010. Geodetic constraints on present-day motion of the Arabian Plate: Implications for Red Sea and Gulf of Aden rifting. *Tectonics*. **29**(3).

Avni, Y., Segev, A. and Ginat, H. 2012. Oligocene regional denudation of the northern Afar dome: Pre-and syn-breakup stages of the Afro-Arabian plate. *Geological Society of America Bulletin.* **124**(11-12), pp.1871-1897.

Beaumont, C., Kooi, H. and Willett, S. 2000. Coupled tectonic-surface process models with applications to rifted margins and collisional orogens. In: Summerfield, M.A. ed. *Geomorphology and global tectonics*. Chichester: Wiley, pp.29-55.

Bellin, N., Vanacker, V. and Kubik, P.W. 2014. Denudation rates and tectonic geomorphology of the Spanish Betic Cordillera. *Earth and Planetary Science Letters*. **390**, pp.19-30.

Bishop, P. 1995. Drainage rearrangement by river capture, beheading and diversion. *Progress in physical geography*. **19**(4), pp.449-473.

Bohannon, R.G., Naeser, C.W., Schmidt, D.L. and Zimmermann, R.A. 1989. The timing of uplift, volcanism, and rifting peripheral to the Red Sea: a case for passive rifting?. *Journal of Geophysical Research: Solid Earth*, **94**(B2), pp.1683-1701.

Bojar, A.V., Fritz, H., Kargl, S. and Unzog, W. 2002. Phanerozoic tectonothermal history of the Arabian–Nubian shield in the Eastern Desert of Egypt: evidence from fission track and paleostress data. *Journal of African Earth Sciences*. **34**(3-4), pp.191-202.

Bosence, D.W.J. 1998. Stratigraphic and sedimentological models of rift basins. In: Purser, B.H. and Bosence, D.W.J. eds. *Sedimentation and Tectonics in Rift Basins Red Sea:-Gulf of Aden*. Dordrecht: Springer, pp.9-25.

Bosworth, W. 1994. A model for the three-dimensional evolution of continental rift basins, north-east Africa. *Geologische Rundschau.* **83**(4), pp.671-688.

Bosworth, W. 1995. A high-strain rift model for the southern Gulf of Suez (Egypt). *Geological Society, London, Special Publications*. **80**(1), pp.75-102.

Bosworth, W. 2015. Geological evolution of the Red Sea: historical background, review, and synthesis. In Rasul, N.M.A. and Stewart I.C.F. eds. *The Red Sea: The Formation, Morphology, Oceanography and Environment of a Young Ocean Basin*. Berlin, Heidelberg: Springer, pp.45-78.

Bosworth, W. and Burke, K. 2005. Evolution of the Red Sea-Gulf of Aden rift system. In: Post, P.J., Rosen, N.C., Olson, D.L., Palmes, S.L., Lyons, K.T. and Newton, G.B. eds. *Petroleum systems of divergent continental margin basins. Gulf Coast Section SEPM Foundation 25th Bob F. Perkins Annual Research Conference, Houston, 4–7 Dec, 2005, CD-ROM*, pp342–372.

Bosworth, W. and McClay, K. 2001. Structural and stratigraphic evolution of the Gulf of Suez rift, Egypt: a synthesis. *Mémoires du Muséum national d'histoire naturelle.* **186**, pp.567-606.

Bosworth, W. and Strecker, M.R. 1997. Stress field changes in the Afro-Arabian rift system during the Miocene to Recent period. *Tectonophysics.* **278**(1-4), pp.47-62.

Bosworth, W., Crevello, P., Winn, R.D. and Steinmetz, J. 1998. Structure, sedimentation, and basin dynamics during rifting of the Gulf of Suez and north-western Red Sea. In Purser, B.H. and Bosence, D.W.J. eds. *Sedimentation and Tectonics in Rift Basins Red Sea:-Gulf of Aden*. Dordrecht: Springer. pp.77-96.

Bosworth, W., Darwish, M., Crevello, P., Taviani, M., and Marshak, S. 1996. Stratigraphic and structural evolution of Zabargad Island (Red Sea, Egypt) since the Early Cretaceous. In: Youssef, S.A. ed. *Proceedings of the Third International Conference on Geology of the Arab World, v.1*. Cairo: Cairo University, pp.161-190.

Bosworth, W., Guiraud, R. and Kessler, L.G. 1999. Late Cretaceous (ca. 84 Ma) compressive deformation of the stable platform of northeast Africa (Egypt): Far-field stress effects of the “Santonian event” and origin of the Syrian arc deformation belt. *Geology*. **27**(7), pp.633-636.

Bosworth, W., Huchon, P., and McClay, K. 2005. The Red Sea and Gulf of Aden basins. *Journal of African Earth Sciences*. **43**(1-3), pp.334-378.

Bosworth, W., Montagna, P., Pons-Branchu, E., Rasul, N. and Taviani, M. 2017. Seismic hazards implications of uplifted Pleistocene coral terraces in the Gulf of Aqaba. *Nature Scientific Reports*. **7**(1), pp.1-13.

Bosworth, W., Taviani, M. and Rasul, N.M. 2019. Neotectonics of the Red Sea, Gulf of Suez and Gulf of Aqaba. In: Rasul, N.M.A. and Stewart, I.C.F. eds. *Geological Setting, Palaeoenvironment and Archaeology of the Red Sea.* Cham: Springer, pp.11-35.

Bott, M.H.P. 2006. Mechanisms of rifting: geodynamic modeling of continental rift systems. In: Olsen, K.H. ed. *Continental Rifts: Evolution, Structure, Tectonics. Developments in Geotectonics, vol. 25*. Elsevier Science, pp.27-43.

Bradley, D.C. 2008. Passive margins through earth history. *Earth-Science Reviews*. **91**(1-4), pp.1-26.

Braun, J., Van Der Beek, P. and Batt, G. 2006. *Quantitative thermochronology: numerical methods for the interpretation of thermochronological data*. Cambridge: Cambridge University Press.

Brown, G.F., Schmidt, D.L., and Huffman Jr, A.C. 1989. Geology of the Arabian Peninsula; shield area of western Saudi Arabia (No. 560-A). US Geological Survey.

Buck, W.R., Martinez, F., Steckler, M.S. and Cochran, J.R. 1988. Thermal consequences of lithospheric extension: pure and simple. *Tectonics.* **7**(2), pp.213-234.

Burke, K. and Gunnell, Y., 2008. The African erosion surface: a continental-scale synthesis of geomorphology, tectonics, and environmental change over the past 180 million years. *Geological Society of America Memoir*. **201**, pp.1-66.

Camp, V.E., and Roobol, M.J. 1992. Upwelling asthenosphere beneath western Arabia and its regional implications. *Journal of Geophysical Research: Solid Earth*. **97**(B11), pp.15255-15271.

Camp, V.E., Roobol, M.J., and Hooper, P.R. 1991. The Arabian continental alkali basalt province: Part II. Evolution of Harrats Khaybar, Ithnayn, and Kura, Kingdom of Saudi Arabia. *Geological Society of America Bulletin*. **103**(3), pp.363-391.

Cardozo, N. and Allmendinger, R.W. 2013. Spherical projections with OSXStereonet. *Computers and Geosciences.* **51**, pp.193-205.

Castelltort, S., Whittaker, A. and Vergés, J. 2015. Tectonics, sedimentation and surface processes: from the erosional engine to basin deposition. *Earth Surface Processes and Landforms.* **40**(13), pp.1839-1846.

Chorowicz, J., 2005. The East African rift system. *Journal of African Earth Sciences*. **43**(1-3), pp.379-410.

Clark, M. D. 1987. Geologic map of the Al Bad quadrangle, sheet 28A, Kingdom of Saudi Arabia, scale 1: 250,000. Geological Map GM Saudi Arabia Dept. Ministry of Mineral Resources, GM-81C.

Clark, M.D. 1985. Late Proterozoic crustal evolution of the Midyan region, northwestern Saudi Arabia. *Geology*. **13**(9), pp.611-615.

Cochran, J.R. 2005. Northern Red Sea: Nucleation of an oceanic spreading center within a continental rift. *Geochemistry, Geophysics, Geosystems.* **6**(3), pp.1-34.

Coleman, R.G., Gregory, R.T. and Brown, G.F. 1983. Cenozoic volcanic rocks of Saudi Arabia (No. 83-788). US Geological Survey.

Cowie, P.A., Gupta, S. and Dawers, N.H. 2000. Implications of fault array evolution for synrift depocentre development: insights from a numerical fault growth model. *Basin Research*. **12**(3-4), pp.241-261.

Cyr, A.J., Granger, D.E., Olivetti, V. and Molin, P. 2010. Quantifying rock uplift rates using channel steepness and cosmogenic nuclide–determined erosion rates: Examples from northern and southern Italy. *Lithosphere*. **2**(3), pp.188-198.

Czarnota, K., Roberts, G.G., White, N.J. and Fishwick, S. 2014. Spatial and temporal patterns of Australian dynamic topography from River Profile Modeling. *Journal of Geophysical Research: Solid Earth*. **119**(2), pp.1384-1424.

Daradich, A., Mitrovica, J.X., Pysklywec, R.N., Willett, S.D., and Forte, A.M. 2003. Mantle flow, dynamic topography, and rift-flank uplift of Arabia. *Geology*. **31**(10), pp.901-904.

Davison, I.A.N., Al-Kadasi, M., Al-Khirbash, S., Al-Subbary, A.K., Baker, J., Blakey, S., Bosence, D., Dart, C., Heaton, R., McClay, K.E.N. and Menzies, M. 1994. Geological evolution of the southeastern Red Sea Rift margin, Republic of Yemen. *Geological Society of America Bulletin*. **106**(11), pp.1474-1493.

de Sordi, M.V., Salgado, A.A.R., Siame, L., Bourlès, D., Paisani, J.C., Leanni, L., Braucher, R., Do Couto, E.V. and ASTER Team. 2018. Implications of

drainage rearrangement for passive margin escarpment evolution in southern Brazil. *Geomorphology.* **306**, pp.155-169.

Dixon, T.H., Stern, R.J. and Hussein, I.M. 1987. Control of Red Sea rift geometry by Precambrian structures. *Tectonics*. **6**(5), pp.551-571.

Doglioni, C., Carminati, E. and Bonatti, E. 2003. Rift asymmetry and continental uplift. *Tectonics*. **22**(3), pp.1-13.

Donelick, R.A., O'Sullivan, P.B. and Ketcham, R.A. 2005. Apatite fission-track analysis. *Reviews in Mineralogy and Geochemistry*. **58**(1), pp.49-94.

Duffy, O.B., Brocklehurst, S.H., Gawthorpe, R.L., Leeder, M.R. and Finch, E. 2015. Controls on landscape and drainage evolution in regions of distributed normal faulting: Perachora Peninsula, Corinth Rift, Central Greece. *Basin Research*. **27**(4), pp.473-494.

Egyptian Geological Survey and Mining Authority (1981). *Geologic map of Egypt (1:2 000 000).* Cairo: Egyptian Geological Survey and Mining Authority.

Eliet, P.P. and Gawthorpe, R.L. 1995. Drainage development and sediment supply within rifts, examples from the Sperchios basin, central Greece. *Journal of the Geological Society*. **152**(5), pp.883-893.

Erratt, D., Thomas, G.M. and Wall, G.R.T. 1999. The evolution of the central North Sea Rift. *Geological society, London, petroleum geology conference series (Vol. 5, No. 1)*. London: Geological Society of London, pp.63-82.

Evans, A.L. 1990. Miocene sandstone provenance relations in the Gulf of Suez: insights into synrift unroofing and uplift history (1). *AAPG Bulletin*. **74**(9), pp.1386-1400.

Færseth, R.B., Gabrielsen, R.H. and Hurich, C.A. 1995. Influence of basement in structuring of the North Sea basin, offshore southwest Norway. *Norsk Geologisk Tidsskrift*. **75**(2-3), pp.105-119.

Fan, N., Chu, Z., Jiang, L., Hassan, M.A., Lamb, M.P. and Liu, X. 2018. Abrupt drainage basin reorganization following a Pleistocene river capture. *Nature communications*. **9**(1), pp.1-6.

Faqira, M., Rademakers, M. and Afifi, A.M. 2009. New insights into the Hercynian Orogeny, and their implications for the Paleozoic Hydrocarbon System in the Arabian Plate. *GeoArabia*. **14**(3), pp.199-228.

Farley, K.A. 2002. (U-Th)/He dating: Techniques, calibrations, and applications. *Reviews in Mineralogy and Geochemistry*. **47**(1), pp.819-844.

Farley, K.A., Wolf, R.A. and Silver, L.T. 1996. The effects of long alpha-stopping distances on (U-Th)/He ages. *Geochimica et cosmochimica acta*. **60**(21), pp.4223-4229.

Feinstein, S., Eyal, M., Kohn, B.P., Steckler, M.S., Ibrahim, K.M., Moh'd, B.K. and Tian, Y. 2013. Uplift and denudation history of the eastern Dead Sea rift flank, SW Jordan: Evidence from apatite fission track thermochronometry. *Tectonics*. **32**(5), pp.1513-1528.

Fielding, L., Najman, Y., Millar, I., Butterworth, P., Garzanti, E., Vezzoli, G., Barfod, D. and Kneller, B. 2018. The initiation and evolution of the River Nile. *Earth and Planetary Science Letters*. **489**, pp.166-178.

Fitzgerald, P.G. and Malusà, M.G. 2019. Concept of the exhumed partial annealing (retention) zone and age-elevation profiles in thermochronology. In: Malusà, M.G. and Fitzgerald, P.G. eds. *Fission-Track Thermochronology and its Application to Geology*. Cham: Springer, pp. 165-189..

Flowers, R.M. and Kelley, S.A. 2011. Interpreting data dispersion and “inverted” dates in apatite (U–Th)/He and fission-track datasets: an example from the US midcontinent. *Geochimica et Cosmochimica Acta,* **75**(18), pp.5169-5186.

Flowers, R.M., Ketcham, R.A., Shuster, D.L. and Farley, K.A. 2009. Apatite (U-Th)/He thermochronometry using a radiation damage accumulation and annealing model. *Geochimica et Cosmochimica Acta.* **73**(8), pp.2347-2365.

Fossen, H. 2010. *Structural geology*. Cambridge: Cambridge University Press.

Fossen, H. and Rotevatn, A. 2016. Fault linkage and relay structures in extensional settings-A review. *Earth-Science Reviews.* **154**, pp.14-28.

Friedlander, G., Kennedy, J.W., Macias, E.S. and Miller, J.M. 1981. *Nuclear and radiochemistry*. John Wiley & Sons.

Galbraith, R.F. 1988. Graphical display of estimates having differing standard errors. *Technometrics* **30**(3), pp.271-281.

Galbraith, R.F. 1990. The radial plot: graphical assessment of spread in ages. *International Journal of Radiation Applications and Instrumentation. Part D. Nuclear Tracks and Radiation Measurements.* **17**(3), pp.207-214.

Gallagher, K. 2012. Uplift, denudation, and their causes and constraints over geological timescales. In: Roberts, D.G. and Bally, A.W. eds. *Regional Geology and Tectonics: Principles of Geologic Analysis.* Amsterdam: Elsevier, pp.609-644.

Gallagher, K. and Brown, R. 1999. Denudation and uplift at passive margins: the record on the Atlantic Margin of southern Africa. *Philosophical Transactions of the Royal Society of London A: Mathematical, Physical and Engineering Sciences*. **357**(1753), pp.835-859.

Gallagher, K., Brown, R. and Johnson, C. 1998. Fission track analysis and its applications to geological problems. *Annual Review of Earth and Planetary Sciences*. **26**(1), pp.519-572.

Gawthorpe, R.L. and Leeder, M.R. 2000. Tectono-sedimentary evolution of active extensional basins. *Basin Research*. **12**(3-4), pp.195-218.

Gawthorpe, R.L., Fraser, A.J. and Collier, R.E.L. 1994. Sequence stratigraphy in active extensional basins: implications for the interpretation of ancient basin-fills. *Marine and petroleum geology*. **11**(6), pp.642-658.

Geurts, A.H., Cowie, P.A., Duclaux, G., Gawthorpe, R.L., Huismans, R.S., Pedersen, V.K. and Wedmore, L.N. 2018. Drainage integration and sediment dispersal in active continental rifts: A numerical modelling study of the central Italian Apennines. *Basin Research*. **30**(5), pp.965-989.

Ghebreab, W., Carter, A., Hurford, A.J. and Talbot, C.J. 2002. Constraints for timing of extensional tectonics in the western margin of the Red Sea in Eritrea. *Earth and Planetary Science Letters*. **200**(1-2), pp.107-119.

Giaconia, F., Booth-Rea, G., Martínez-Martínez, J.M., Azañón, J.M., Pérez-Peña, J.V., Pérez-Romero, J. and Villegas, I. 2012. Geomorphic evidence of active

tectonics in the Sierra Alhamilla (eastern Betics, SE Spain). *Geomorphology.* **145**, pp.90-106.

Gleadow, A.J. and Brown, R.W. 2000. Fission-track thermochronology and the long-term denudational response to tectonics. In: Summerfield, M.A. ed. *Geomorphology and global tectonics*. Chichester: Wiley, pp.57-75.

GLOBE Task Team and others (Hastings, David A., Paula K. Dunbar, Gerald M. Elphingstone, Mark Bootz, Hiroshi Murakami, Hiroshi Maruyama, Hiroshi Masaharu, Peter Holland, John Payne, Nevin A. Bryant, Thomas L. Logan, J.-P. Muller, Gunter Schreier, and John S. MacDonald), eds. 1999. The Global Land One-kilometer Base Elevation (GLOBE) Digital Elevation Model, Version 1.0. *National Oceanic and Atmospheric Administration, National Geophysical Data Center.* 325 Broadway, Boulder, Colorado 80305-3328, U.S.A. Digital data base on the World Wide Web (URL: http://www.ngdc.noaa.gov/mgg/topo/globe.html) and CD-ROMs.

Goudie, A.S., 2005. The drainage of Africa since the Cretaceous. *Geomorphology*. **67**(3-4), pp.437-456.

Green, P. and Duddy, I. 2018. Apatite (U-Th-Sm)/He thermochronology on the wrong side of the tracks. *Chemical Geology*. **488**, pp.21-33.

Green, P.F., Duddy, I.R., Gleadow, A.J.W., Tingate, P.R. and Laslett, G.M. 1986. Thermal annealing of fission tracks in apatite: 1. A qualitative description. *Chemical Geology: Isotope Geoscience section*. **59**, pp.237-253.

Gregersen, U., Knutz, P.C., Nøhr-Hansen, H., Sheldon, E. and Hopper, J.R. 2019. Tectonostratigraphy and evolution of the West Greenland continental margin. *Bulletin of the Geological Society of Denmark.* **67**, pp.1-21.

Griffin, D.L. 1999. The late Miocene climate of northeastern Africa: unravelling the signals in the sedimentary succession. *Journal of the Geological Society*. **156**(4), pp.817-826.

Gunnell, Y. and Harbor, D.J. 2010. Butte detachment: how pre-rift geological structure and drainage integration drive escarpment evolution at rifted

continental margins. *Earth Surface Processes and Landforms*. **35**(12), pp.1373-1385.

Gupta, S., Cowie, P.A., Dawers, N.H. and Underhill, J.R. 1998. A mechanism to explain rift-basin subsidence and stratigraphic patterns through fault-array evolution. *Geology*. **26**(7), pp.595-598.

Hansen, S.E., Gaherty, J.B., Schwartz, S.Y., Rodgers, A.J. and Al-Amri, A. 2008. Seismic velocity structure and depth-dependence of anisotropy in the Red Sea and Arabian shield from surface wave analysis. *Journal of Geophysical Research: Solid Earth.* **113**(B10), pp.1-16.

Hansen, S.E., Rodgers, A.J., Schwartz, S.Y. and Al-Amri, A.M. 2007. Imaging ruptured lithosphere beneath the Red Sea and Arabian Peninsula. *Earth and Planetary Science Letters*. **259**(3-4), pp.256-265.

Haworth, R.J. and Ollier, C.D. 1992. Continental rifting and drainage reversal: the Clarence River of eastern Australia. *Earth Surface Processes and Landforms*. **17**(4), pp.387-397.

Hendriks, B.W.H., Osmundsen, P.T. and Redfield, T.F. 2010. Normal faulting and block tilting in Lofoten and Vesterålen constrained by apatite fission track data. *Tectonophysics*. **485**(1-4), pp.154-163.

Hosny, A. and Nyblade, A. 2014. Crustal structure in southeastern Egypt: Symmetric thinning of the northern Red Sea rifted margins. *Geology.* **42**(3), pp.219-222.

Hughes G.W.G. and Johnson R.S. 2005. Lithostratigraphy of the Red Sea region. *GeoArabia*. **10**(3), pp.49-126.

Hughes, G.W., Perincek, D., Grainger, D.J., Abu-Bshait, A.J., and Jarad, A.R.M. 1999. Lithostratigraphy and depositional history of part of the Midyan region, northwestern Saudi Arabia. *GeoArabia*. **4**(4), pp.503-542.

Ilani, S., Harlavan, Y., Tarawneh, K., Rabba, I., Weinberger, R., Ibrahim, K., Peltz, S. and Steinitz, G. 2001. New K-Ar ages of basalts from the Harrat Ash Shaam volcanic field in Jordan: Implications for the span and duration of the

upper-mantle upwelling beneath the western Arabian plate. *Geology*. **29**(2), pp.171-174.

Issawi, B. 1972. Review of Upper Cretaceous-Lower Tertiary stratigraphy in central and southern Egypt. *AAPG Bulletin.* **56**(8), pp.1448-1463.

Jackson, J. and Leeder, M. 1994. Drainage systems and the development of normal faults: an example from Pleasant Valley, Nevada. *Journal of Structural Geology* **16**(8), pp.1041-1059.

Japsen, P., Chalmers, J.A., Green, P.F. and Bonow, J.M. 2012. Elevated, passive continental margins: Not rift shoulders, but expressions of episodic, post-rift burial and exhumation. *Global and Planetary Change*. **90**, pp.73-86.

Jarrige, J.J., Ott d'Estevou, P., Burollet, P.F., Montenat, C., Prat, P., Richert, J.P. and Thiriet, J.P. 1990. The multistage tectonic evolution of the Gulf of Suez and northern Red Sea continental rift from field observations. *Tectonics*. **9**(3), pp.441-465.

Johnson, P.R., Andresen, A., Collins, A.S., Fowler, A.R., Fritz, H., Ghebreab, W., Kusky, T. and Stern, R.J. 2011. Late Cryogenian–Ediacaran history of the Arabian–Nubian Shield: a review of depositional, plutonic, structural, and tectonic events in the closing stages of the northern East African Orogen. *Journal of African Earth Sciences*. **61**(3), pp.167-232.

Kaban, M.K., El Khrepy, S. and Al-Arifi, N. 2018. Density structure and isostasy of the lithosphere in Egypt and their relation to seismicity. *Solid Earth*. **9**(4), pp.833-846.

Kaliwoda, M., Altherr, R. and Meyer, H.P. 2007. Composition and thermal evolution of the lithospheric mantle beneath the Harrat Uwayrid, eastern flank of the Red Sea rift (Saudi Arabia). *Lithos* **99**(1-2), pp.105-120.

Kenea, N.H., Ebinger, C.J. and Rex, D.C. 2001. Late Oligocene volcanism and extension in the southern Red Sea Hills, Sudan. *Journal of the Geological Society*. **158**(2), pp.285-294.

Ketcham, R.A. 2005. Forward and inverse modeling of low-temperature thermochronometry data. *Reviews in mineralogy and geochemistry.* **58**(1), pp.275-314.

Ketcham, R.A., Carter, A.C., Donelick, R.A., Barbarand, J. and Hurford, A.J. 2007. Improved modeling of fission-track annealing in apatite. *American Mineralogist*. **92**, pp.799-810.

Ketcham, R.A., Gautheron, C. and Tassan-Got, L. 2011. Accounting for long alpha-particle stopping distances in (U-Th-Sm)/He geochronology: Refinement of the baseline case. *Geochimica et Cosmochimica Acta*. **75**, pp.7779-7791.

Khalil, S.M. and McClay, K.R. 2001. Tectonic evolution of the NW Red Sea-Gulf of Suez rift system. *Geological Society, London, Special Publications*. **187**(1), pp.453-473.

Koeshidayatullah, A., Al-Ramadan, K., Collier, R. and Hughes, G.W. 2016. Variations in architecture and cyclicity in fault-bounded carbonate platforms: Early Miocene Red Sea Rift, NW Saudi Arabia. *Marine and Petroleum Geology.* **70**, pp.77-92.

Kohn, B.P. and Eyal, M. 1981. History of uplift of the crystalline basement of Sinai and its relation to opening of the Red Sea as revealed by fission track dating of apatites. *Earth and Planetary Science Letters*. **52**, pp.129-141.

Lambiase, J.J. and Bosworth, W. 1995. Structural controls on sedimentation in continental rifts. *Geological Society, London, Special Publications*. **80**(1), pp.117-144.

Lazar, M., Ben-Avraham, Z. and Garfunkel, Z. 2012. The Red Sea–New insights from recent geophysical studies and the connection to the Dead Sea fault. *Journal of African Earth Sciences.* **68**, pp.96-110.

Leeder, M.R. and Jackson, J.A. 1993. The interaction between normal faulting and drainage in active extensional basins, with examples from the western United States and central Greece. *Basin research.* **5**(2), pp.79-102.

Levell, B., Argent, J., Doré, A.G. and Fraser, S. 2010, January. Passive margins: overview. In: Vining, B.A. and Pickering, S.C. eds. *Petroleum Geology: From*

Mature Basins to New Frontiers—Proceedings of the 7th Petroleum Geology Conference. London: Geological Society of London, pp.823-830.

Ligi, M., Bonatti, E., Bortoluzzi, G., Cipriani, A., Cocchi, L., Caratori Tontini, F., Carminati, E., Ottolini, L. and Schettino, A. 2012. Birth of an ocean in the Red Sea: initial pangs. *Geochemistry, Geophysics, Geosystems*. **13**(8), pp.1-29.

Lisker, F., Ventura, B. and Glasmacher, U.A. 2009. Apatite thermochronology in modern geology. *Geological Society, London, Special Publications*. **324**(1), pp.1-23.

Macgregor, D.S. 2012. The development of the Nile drainage system: integration of onshore and offshore evidence. *Petroleum Geoscience*. **18**(4), pp.417-431.

Manaa, A.A., Jones, B.G., McGregor, H.V., Zhao, J.X. and Price, D.M. 2016. Dating Quaternary raised coral terraces along the Saudi Arabian Red Sea coast. *Marine Geology*. **374**, pp.59-72.

Mann, P., Gahagan, L. and Gordon, M.B. 2003. Tectonic setting of the world's giant oil and gas fields. In: Halbouty, M.T. ed. *Giant oil and gas fields of the decade 1990-1999, AAPG Memoir* **78**. AAPG, pp.15-105.

Marrett, R.A. and Allmendinger, R.W. 1990. Kinematic analysis of fault-slip data. *Journal of Structural Geology.* **12**(8), pp.973-986.

McKenzie, D. 1978. Some remarks on the development of sedimentary basins. *Earth and Planetary science letters*. **40**(1), pp.25-32.

McNeill, L.C. and Collier, R.L. 2004. Uplift and slip rates of the eastern Eliki fault segment, Gulf of Corinth, Greece, inferred from Holocene and Pleistocene terraces. *Journal of the Geological Society*. **161**(1), pp.81-92.

Menzies, M.A., Baker, J., Bosence, D., Dart, C., Davison, I., Hurford, A., Al'Kadasi, M., McClay, K., Nichols, G., Al'Subbary, A. and Yelland, A. 1992. The timing of magmatism, uplift and crustal extension: preliminary observations from Yemen. *Geological Society, London, Special Publications.* **68**(1), pp.293-304.

Merle, O. 2011. A simple continental rift classification. *Tectonophysics*. **513**(1-4), pp.88-95.

Meyer, S.E., Passchier, C., Abu-Alam, T. and Stüwe, K. 2014. A strike-slip core complex from the Najd fault system, Arabian shield. *Terra Nova*. **26**(5), pp.387-394.

Miller, K.G., Kominz, M.A., Browning, J.V., Wright, J.D., Mountain, G.S., Katz, M.E., Sugarman, P.J., Cramer, B.S., Christie-Blick, N. and Pekar, S.F. 2005. The Phanerozoic record of global sea-level change. *Science*. **310**(5752), pp.1293-1298.

Molnar, P. and England, P. 1990. Late Cenozoic uplift of mountain ranges and global climate change: chicken or egg?. *Nature*. **346**(6279), pp.29-34.

Moore, A. and Blenkinsop, T. 2002. The role of mantle plumes in the development of continental-scale drainage patterns: the southern African example revisited. *South African Journal of Geology.* **105**(4), pp.353-360.

Moretti, I. and Colletta, B. 1987. Spatial and temporal evolution of the Suez rift subsidence. *Journal of Geodynamics.* **7**(1-2), pp.151-168.

Mortimer, E., Kirstein, L.A., Stuart, F.M. and Strecker, M.R. 2016. Spatio-temporal trends in normal-fault segmentation recorded by low-temperature thermochronology: Livingstone fault scarp, Malawi Rift, East African Rift System. *Earth and Planetary Science Letters*. **455**, pp.62-72.

Moustafa, A.R. and Khalil, M.H. 1995. Superposed deformation in the northern Suez Rift, Egypt: relevance to hydrocarbons exploration. *Journal of Petroleum Geology*. **18**(3), pp.245-266.

O'Callaghan, J.F. and Mark, D.M. 1984. The extraction of drainage networks from digital elevation data. *Computer vision, graphics, and image processing*. **28**(3), pp.323-344.

Olsen, K.H. and Morgan, P. 2006. Introduction: progress in understanding continental rifts. In: Olsen, K.H. ed. *Continental Rifts: Evolution, Structure, Tectonics. Developments in Geotectonics, vol. 25*. Elsevier Science, pp. 3-26.

Omar, G.I. and Steckler, M.S. 1995. Fission track evidence on the initial rifting of the Red Sea: two pulses, no propagation. *Science*. **270**(5240), pp.1341-1344.

Omar, G.I., Kohn, B.P., Lutz, T.M. and Faul, H. 1987. The cooling history of Silurian to Cretaceous alkaline ring complexes, south Eastern Desert, Egypt, as revealed by fission-track analysis. *Earth and Planetary Science Letters*. **83**(1-4), pp.94-108.

Omar, G.I., Steckler, M.S., Buck, W.R. and Kohn, B.P. 1989. Fission-track analysis of basement apatites at the western margin of the Gulf of Suez rift, Egypt: evidence for synchroneity of uplift and subsidence. *Earth and Planetary Science Letters.* **94**(3-4), pp.316-328.

Osmundsen, P.T. and Redfield, T.F. 2011. Crustal taper and topography at passive continental margins. *Terra Nova*. **23**(6), pp.349-361.

Pagli, C., Mazzarini, F., Keir, D., Rivalta, E. and Rooney, T.O. 2015. Introduction: Anatomy of rifting: Tectonics and magmatism in continental rifts, oceanic spreading centers, and transforms. *Geosphere*. **11**(5), pp.1256-1261.

Park, Y., Nyblade, A. A., Rodgers, A. J. and Al-Amri, A. 2008. S wave velocity structure of the Arabian Shield upper mantle from Rayleigh wave tomography. *Geochemistry, Geophysics, Geosystems*. **9**(7), pp.1-15.

Paul, J.D., Roberts, G.G. and White, N. 2014. The African landscape through space and time. *Tectonics*. **33**(6), pp.898-935.

Peyton, S.L. and Carrapa, B. 2013. An introduction to low-temperature thermochronologic techniques, methodology, and applications. In: Knight, C. and Cuzella, J. eds. *Application of structural methods to Rocky Mountain hydrocarbon exploration and development: AAPG Studies in Geology 65*. AAPG and RMAG, pp.15-36.

Pik, R., Marty, B., Carignan, J. and Lavé, J. 2003. Stability of the Upper Nile drainage network (Ethiopia) deduced from (U–Th)/He thermochronometry: implications for uplift and erosion of the Afar plume dome. *Earth and Planetary Science Letters*. **215**(1-2), pp.73-88.

Plaziat, J. C., Baltzer, F., Choukri, A., Conchon, O., Freytet, P., Orszag-Sperber, F., Raguideau, A. and Reyss, J.-L. 1998. Quaternary marine and continental sedimentation in the northern Red Sea and Gulf of Suez (Egyptian coast):

influences of rift tectonics, climatic changes and sea-level fluctuations. In: Purser, B.H. and Bosence, D.W.J. eds. *Sedimentation and Tectonics in Rift Basins Red Sea:-Gulf of Aden*. Dordrecht: Springer, pp.537-573.

Polis, S.R., Angelich, M.T, Beeman, C.R., Maze, W.B., Reynolds, D.J., Steinhauff, D.M., Tudoran, A. and Wood, M.V. 2005. Preferential deposition and preservation of structurally-controlled synrift reservoirs: Northeast Red Sea and Gulf of Suez. *GeoArabia*. **10**(1), pp.97-124.

Powell, J.H., Abed, A.M., and Nindre, L. 2014. Cambrian stratigraphy of Jordan. *GeoArabia-Middle East Petroleum Geosciences.* **19**(3), pp.81-134.

Prince, P.S., Spotila, J.A. and Henika, W.S. 2011. Stream capture as driver of transient landscape evolution in a tectonically quiescent setting. *Geology*. **39**(9), pp.823-826.

Pritchard, D., Roberts, G.G., White, N.J. and Richardson, C.N. 2009. Uplift histories from river profiles. *Geophysical Research Letters*. **36**(24), pp.1-5.

Ramsay, C.R., Drysdall, A.R. and Clark, M.D. 1986. Felsic plutonic rocks of the Midyan region, Kingdom of Saudi Arabia—I. Distribution, classification and resource potential. *Journal of African Earth Sciences (1983).* **4**, pp.63-77.

Reiners, P.W., Ehlers, T.A. and Zeitler, P.K. 2005. Past, present, and future of thermochronology. *Reviews in Mineralogy and Geochemistry*. **58**(1), pp.1-18.

Roberts, G.G. and White, N. 2010. Estimating uplift rate histories from river profiles using African examples. *Journal of Geophysical Research: Solid Earth.* **115**(B2), pp.1-24.

Roberts, G.G., Paul, J.D., White, N. and Winterbourne, J. 2012a. Temporal and spatial evolution of dynamic support from river profiles: A framework for Madagascar. *Geochemistry, Geophysics, Geosystems*. **13**, pp.1-23.

Roberts, G.G., White, N. and Lodhia, B.H. 2019. The generation and scaling of longitudinal river profiles. *Journal of Geophysical Research: Earth Surface*. **124**(1), pp.137-153.

Roberts, G.G., White, N.J., Martin-Brandis, G.L. and Crosby, A.G. 2012b. An uplift history of the Colorado Plateau and its surroundings from inverse modeling of longitudinal river profiles. *Tectonics*. **31**, pp.1-25

Rosenbloom, N.A. and Anderson, R.S. 1994. Hillslope and channel evolution in a marine landscape, Santa Cruz, California. *Journal of Geophysical Research*. **99**(B7), pp.14,013–14,029.

Rudge, J.F., Roberts, G.G., White, N.J. and Richardson, C.N. 2015. Uplift histories of Africa and Australia from linear inverse modeling of drainage inventories. *Journal of Geophysical Research: Earth Surface*. **120**, pp.894–914.

Salles, T., Flament, N. and Müller, D. 2017. Influence of mantle flow on the drainage of eastern Australia since the Jurassic Period. *Geochemistry, Geophysics, Geosystems*. **18**(1), pp.280-305.

Sasvári, Á. and Baharev, A. 2014. SG2PS (Structural Geology to Post Script Converter) – A graphical solution for brittle structural data evaluation and paleostress calculation. *Computers and Geosciences*. **66**, pp.81-93.

Schettino, A., Macchiavelli, C. and Rasul, N.M. 2019. Plate Motions around the Red Sea since the Early Oligocene. In: Rasul, N.M.A. and Stewart, I.C.F. eds. *Geological Setting, Palaeoenvironment and Archaeology of the Red Sea.* Cham: Springer, pp.203-220.

Schettino, A., Macchiavelli, C., Pierantoni, P.P., Zanoni, D. and Rasul, N. 2016. Recent kinematics of the tectonic plates surrounding the Red Sea and Gulf of Aden. *Geophysical Journal International*. **207**(1), pp.457-480.

Segev, A., Avni, Y., Shahar, J. and Wald, R. 2017. Late Oligocene and Miocene different seaways to the Red Sea–Gulf of Suez rift and the Gulf of Aqaba–Dead Sea basins. *Earth-science reviews*. **171**, pp.196-219.

Sengör, A.M. and Burke, K. 1978. Relative timing of rifting and volcanism on Earth and its tectonic implications. *Geophysical Research Letters*. **5**(6), pp.419-421.

Sepulchre, P., Ramstein, G., Fluteau, F., Schuster, M., Tiercelin, J.J. and Brunet, M. 2006. Tectonic uplift and Eastern Africa aridification. *Science*. **313**(5792), pp.1419-1423.

Seton, M., Müller, R.D., Zahirovic, S., Gaina, C., Torsvik, T., Shephard, G., Talsma, A., Gurnis, M., Turner, M., Maus, S. and Chandler, M. 2012. Global continental and ocean basin reconstructions since 200 Ma. *Earth-science reviews*. **113**(3-4), pp.212-270.

Sharp, I.R., Gawthorpe, R.L., Underhill, J.R. and Gupta, S. 2000. Fault-propagation folding in extensional settings: Examples of structural style and synrift sedimentary response from the Suez rift, Sinai, Egypt. *Geological Society of America Bulletin*. **112**(12), pp.1877-1899.

Shephard, G.E., Müller, R.D., Liu, L. and Gurnis, M. 2010. Miocene drainage reversal of the Amazon River driven by plate-mantle interaction. *Nature Geoscience*. **3**(12), pp.870-875.

Smith, W.H.F. and Sandwell D.T. 1997. Global seafloor topography from satellite altimetry and ship depth soundings. *Science*. **277**(5334), pp.1956-1962.

Smyth, H.R., Morton, A., Richardson, N. and Scott, R.A. 2014. Sediment provenance studies in hydrocarbon exploration and production: An introduction. *Geological Society, London, Special Publications*. **386**(1), pp.1-6.

Steckler, M.S. 1985. Uplift and extension at the Gulf of Suez: indications of induced mantle convection. *Nature*. **317**(6033), pp.135-139.

Steckler, M.S. and Omar, G.I. 1994. Controls on erosional retreat of the uplifted rift flanks at the Gulf of Suez and northern Red Sea. *Journal of Geophysical Research: Solid Earth*. **99**(B6), pp.12159-12173.

Steckler, M.S., Berthelot, F., Lyberis, N. and Le Pichon, X. 1988. Subsidence in the Gulf of Suez: implications for rifting and plate kinematics. *Tectonophysics*. **153**(1-4), pp.249-270.

Steckler, M.S., Feinstein, S., Kohn, B.P., Lavier, L.L. and Eyal, M. 1998. Pattern of mantle thinning from subsidence and heat flow measurements in the Gulf of Suez: Evidence for the rotation of Sinai and along-strike flow from the Red Sea. *Tectonics*. **17**(6), pp.903-920.

Stern, R.J. and Johnson, P. 2010. Continental lithosphere of the Arabian Plate: a geologic, petrologic, and geophysical synthesis. *Earth-Science Reviews*. **101**(1-2), pp.29-67.

Stern, R.J. and Johnson, P.R. 2019. Constraining the opening of the Red Sea: evidence from the Neoproterozoic margins and Cenozoic magmatism for a Volcanic Rifted Margin. In: Rasul, N.M.A. and Stewart, I.C.F. eds. *Geological Setting, Palaeoenvironment and Archaeology of the Red Sea.* Cham: Springer, pp.53-79.

Stewart, S.A. 2016. Structural geology of the Rub' Al-Khali Basin, Saudi Arabia. *Tectonics*. **35**(10), pp.2417-2438.

Stockli, D.F. 2005. Application of low-temperature thermochronometry to extensional tectonic settings. *Reviews in Mineralogy and Geochemistry*. **58**(1), pp.411-448.

Stockli, D.F. and Bosworth, W. 2019. Timing of Extensional Faulting Along the Magma-Poor Central and Northern Red Sea Rift Margin-Transition from Regional Extension to Necking Along a Hyperextended Rifted Margin. In: Rasul, N.M.A. and Stewart, I.C.F. eds. *Geological Setting, Palaeoenvironment and Archaeology of the Red Sea.* Cham: Springer, pp.81-111.

Strahler, A.N. 1957. Quantitative analysis of watershed geomorphology. *Eos, Transactions American Geophysical Union.* **38**(6), pp.913-920.

Summerfield, M.A. 1993. *Global geomorphology*. Essex: Longman Scientific & Technical.

Szymanski, E. 2013. Timing, kinematics, and spatial distribution of Miocene extension in the central Arabian margin of the Red Sea rift system (Doctoral dissertation, University of Kansas).

Szymanski, E., Stockli, D.F., Johnson, P.R. and Hager, C. 2016. Thermochronometric evidence for diffuse extension and two-phase rifting within the Central Arabian Margin of the Red Sea Rift. *Tectonics*. 35(12), pp.2863-2895.

Tarboton, D.G., Bras, R.L. and Rodriguez-Iturbe, I. 1991. On the extraction of channel networks from digital elevation data. *Hydrological processes*. **5**(1), pp.81-100.

Taviani, M., Montagna, P., Rasul, N.M., Angeletti, L. and Bosworth, W. 2019. Pleistocene coral reef terraces on the Saudi Arabian side of the Gulf of Aqaba, Red Sea. In: Rasul, N.M.A. and Stewart, I.C.F. eds. *Geological Setting, Palaeoenvironment and Archaeology of the Red Sea.* Cham: Springer, pp.341-365.

Tinker, J., de Wit, M. and Brown, R. 2008. Linking source and sink: Evaluating the balance between onshore erosion and offshore sediment accumulation since Gondwana break-up, South Africa. *Tectonophysics*, **455**(1-4), pp.94-103.

Tubbs, R.E., Fouda, H., Afifi, A., Raterman, N., Hughes, G. and Fadolalkarem, Y. 2014. Midyan Peninsula, northern Red Sea, Saudi Arabia: seismic imaging and regional interpretation. *GeoArabia*. **19**(3), pp.165-184.

Twidale, C.R. 2004. River patterns and their meaning. *Earth-Science Reviews*. **67**(3-4), pp.159-218.

van Balen, R.T., Van der Beek, P.A. and Cloetingh, S.A.P.L. 1995. The effect of rift shoulder erosion on stratal patterns at passive margins: Implications for sequence stratigraphy. *Earth and Planetary Science Letters*. **134**(3-4), pp.527-544.

Vermeesch, P. 2009. RadialPlotter: A Java application for fission track, luminescence and other radial plots. *Radiation Measurements.* **44**(4), pp.409-410.

Vermeesch, P. 2019. Statistics for Fission-Track Thermochronology. In: Malusà, M.G. and Fitzgerald, P.G. eds. *Fission-Track Thermochronology and its Application to Geology*. Cham: Springer, pp.109-122.

Voggenreiter, W., Hötzl, H. and Mechie, J. 1988. Low-angle detachment origin for the Red Sea Rift System?. *Tectonophysics*, **150**(1-2), pp.51-75.

Walford, H.L. and White, N.J. 2005. Constraining uplift and denudation of west African continental margin by inversion of stacking velocity data. *Journal of Geophysical Research: Solid Earth*. **110**(B4), pp.1-16.

Weissel, J.K. and Karner, G.D. 1989. Flexural uplift of rift flanks due to mechanical unloading of the lithosphere during extension. *Journal of Geophysical Research: Solid Earth*. **94**(B10), pp.13919-13950.

Wells, M.L., Snee, L.W. and Blythe, A.E. 2000. Dating of major normal fault systems using thermochronology: An example from the Raft River detachment, Basin and Range, western United States. *Journal of Geophysical Research: Solid Earth*. **105**(B7), pp.16303-16327.

Wernicke, B. 1985. Uniform-sense normal simple shear of the continental lithosphere. *Canadian Journal of Earth Sciences*. **22**(1), pp.108-125.

Whipple, K.X. and Tucker, G.E. 1999. Dynamics of the stream-power river incision model: Implications for height limits of mountain ranges, landscape response timescales, and research needs. *Journal of Geophysical Research: Solid Earth*. **104**(B8), pp.17661-17674.

White, R. and McKenzie, D. 1989. Magmatism at rift zones: the generation of volcanic continental margins and flood basalts. *Journal of Geophysical Research: Solid Earth*. **94**(B6), pp.7685-7729.

Whittaker, A.C. and Boulton, S.J. 2012. Tectonic and climatic controls on knickpoint retreat rates and landscape response times. *Journal of Geophysical Research: Earth Surface.* **117**(2), pp.1-19.

Willett, S.D., McCoy, S.W., Perron, J.T., Goren, L. and Chen, C.Y. 2014. Dynamic reorganization of river basins. *Science.* **343**(6175), pp.1-9.

Wilson, J.W.P., Roberts, G.G., Hoggard, M.J. and White, N.J. 2014. Cenozoic epeirogeny of the Arabian Peninsula from drainage modeling. *Geochemistry, Geophysics, Geosystems*. **15**(10), pp.3723-3761.

Wobus, C., Whipple, K.X., Kirby, E., Snyder, N., Johnson, J., Spyropolou, K., Crosby, B., Sheehan, D. and Willett, S.D. 2006. Tectonics from topography:

Procedures, promise, and pitfalls. *Geological society of America Special Paper.* **398**, p.55-74.

Yao, Z., Mooney, W.D., Zahran, H.M., and Youssef, S.E.H. 2017. Upper mantle velocity structure beneath the Arabian shield from Rayleigh surface wave tomography and its implications. *Journal of Geophysical Research: Solid Earth.* **122**(8), pp.6552-6568.

Yielding, G. 1990. Footwall uplift associated with Late Jurassic normal faulting in the northern North Sea. *Journal of the Geological Society*. **147**(2), pp.219-222.

Younes, A.I. and McClay, K. 2002. Development of accommodation zones in the Gulf of Suez-Red Sea rift, Egypt. *AAPG bulletin*. **86**(6), pp.1003-1026.

Zeitler, P.K., Herczeg, A.L., McDougall, I. and Honda, M. 1987. U-Th-He dating of apatite: A potential thermochronometer. *Geochimica et Cosmochimica Acta.* **51**(10), pp.2865-2868.

Zilberman, E. and Calvo, R. 2013. Remnants of Miocene fluvial sediments in the Negev Desert, Israel, and the Jordanian Plateau: Evidence for an extensive subsiding basin in the northwestern margins of the Arabian plate. *Journal of African Earth Sciences* **82**, pp.33-53.

Appendix I

Inverse modelling code and data

The code that was used to perform the modelling was developed by Rudge et al. (2015) and performed on the datasets presented in Chapters 3 and 6 by Dr. Gareth Roberts, Faculty of Engineering, Department of Earth Science and Engineering, Imperial College London.

The code is accessible via https://bitbucket.org/river-inversion/rivers2d/src/default/ where profile data from Madagascar are presented and used for the inversion for uplift histories by Rudge et al. (2015). An inventory of the stream profiles used as input data in Chapters 3 and 6 is presented below. Note that the data supplied by Dr. Roberts are in *italics.*

Catchment name	Stream no.	Head		Mouth		Max. elevation (m)	Length (km)	Catchment area (km^2)
		Long.	Lat.	Long.	Lat.			
NERS1	1	35.292	28.331	35.038	28.107	1657	60.80	4714.67
NERS1	2	35.279	28.343	35.038	28.106	1135	76.50	4714.78
NERS1	3	35.256	28.316	35.039	28.103	1044	57.38	4714.83
NERS1	4	35.236	28.320	35.039	28.103	1003	54.98	4714.83
NERS1	5	35.207	28.315	35.039	28.102	888	50.93	4714.83
NERS1	6	35.192	28.314	35.039	28.103	670	46.77	4714.83
NERS1	7	35.191	28.302	35.039	28.107	709	40.82	4714.77
NERS1	8	35.231	28.315	35.039	28.104	933	54.81	4714.82
NERS1	9	35.213	28.337	35.038	28.106	644	50.66	4714.78
NERS1	10	35.218	28.343	35.039	28.104	760	61.61	4714.82
NERS1	11	35.231	28.342	35.039	28.107	825	61.88	4714.77
NERS1	12	35.242	28.342	35.038	28.105	983	63.28	4714.79
NERS1	13	35.258	28.360	35.039	28.104	733	64.00	4714.83
NERS1	14	35.257	28.338	35.038	28.106	1046	66.16	4714.78
NERS1	15	35.276	28.369	35.039	28.104	634	65.41	4714.82
NERS1	16	35.298	28.358	35.039	28.104	658	73.48	4714.83
NERS1	17	35.319	28.353	35.038	28.107	751	75.86	4714.66
NERS1	18	35.317	28.378	35.039	28.104	636	72.89	4714.82
NERS1	19	35.268	28.289	35.036	28.111	820	51.90	4824.27
NERS1	20	35.307	28.341	35.039	28.102	1078	77.19	4714.83
NERS1	21	35.235	28.328	35.035	28.106	943	53.75	4824.41
NERS1	22	35.346	28.399	35.036	28.110	662	76.05	4824.31
NERS1	23	35.381	28.528	35.036	28.109	1478	93.69	4824.35
NERS1	24	35.207	28.639	35.039	28.104	842	98.16	4714.82
NERS1	25	35.329	28.553	35.039	28.103	1259	115.27	4714.83
NERS1	26	35.222	28.518	35.039	28.104	882	106.24	4714.82
NERS1	27	35.217	28.588	35.037	28.108	901	98.96	4714.66
NERS1	28	35.218	28.505	35.038	28.105	817	73.60	4714.79
NERS1	29	35.237	28.516	35.038	28.106	707	78.07	4714.78
NERS1	30	35.145	28.465	35.039	28.102	580	72.55	4714.83
NERS1	31	35.166	28.513	35.039	28.103	877	76.71	4714.83
NERS1	32	35.120	28.536	35.038	28.106	551	77.74	4714.78
NERS1	33	35.164	28.526	35.039	28.107	779	87.27	4714.77
NERS1	34	35.173	28.541	35.038	28.105	796	88.85	4714.79
NERS1	35	35.240	28.592	35.038	28.105	1026	102.59	4714.79
NERS1	36	35.320	28.645	35.038	28.107	1746	112.48	4714.67
NERS1	37	35.287	28.652	35.038	28.105	1585	111.51	4714.79
NERS1	38	35.270	28.652	35.039	28.104	1654	107.26	4714.82
NERS1	39	35.236	28.644	35.038	28.105	1177	102.79	4714.79
NERS1	40	35.126	28.630	35.039	28.104	536	91.88	4714.82
NERS1	41	35.246	28.658	35.039	28.103	1318	112.12	4714.83
NERS1	42	35.223	28.650	35.037	28.108	1254	103.60	4714.66
NERS1	43	35.194	28.639	35.038	28.105	676	99.19	4714.79
NERS1	44	35.292	28.669	35.039	28.104	1885	222.28	4714.82
NERS1	45	35.299	28.696	35.038	28.106	2215	141.12	4714.78
NERS1	46	35.281	28.701	35.038	28.105	1712	112.85	4714.79
NERS1	47	35.266	28.706	35.038	28.105	1303	111.37	4714.79
NERS1	48	35.281	28.679	35.038	28.106	1658	113.64	4714.78
NERS1	49	35.225	28.720	35.037	28.108	934	107.99	4714.66
NERS1	50	35.251	28.740	35.037	28.108	1395	113.93	4714.66
NERS1	51	35.262	28.731	35.039	28.104	1376	133.61	4714.82
NERS1	52	35.251	28.740	35.037	28.108	1395	113.93	4714.66
NERS1	53	35.231	28.762	35.039	28.104	957	113.86	4714.83
NERS1	54	35.218	28.720	35.039	28.107	904	110.03	4714.77
NERS1	55	35.209	28.776	35.039	28.103	851	112.05	4714.83
NERS1	56	35.180	28.771	35.039	28.103	781	114.24	4714.83
NERS1	57	35.150	28.758	35.039	28.104	687	104.79	4714.83
NERS1	58	35.213	28.727	35.038	28.107	831	108.92	4714.66
NERS1	59	35.385	28.565	35.040	28.111	1700	222.76	4866.52
NERS1	60	35.148	28.240	35.047	28.110	103	32.61	0.35
NERS2	61	35.286	28.316	35.054	28.112	1593	49.44	239.28
NERS2	62	35.240	28.303	35.054	28.112	1253	38.09	239.30
NERS2	63	35.240	28.300	35.054	28.113	1236	38.02	239.28
NERS2	64	35.261	28.303	35.056	28.114	1076	45.79	238.33
NERS2	65	35.262	28.296	35.055	28.114	1024	45.09	238.44

Catchment name	Stream no.	Head		Mouth		Max. elevation (m)	Length (km)	Catchment area (km^2)
		Long.	Lat.	Long.	Lat.			
NERS2	66	35.253	28.289	35.054	28.111	1137	44.24	239.33
NERS2	67	35.247	28.285	35.054	28.113	1070	42.83	239.28
NERS2	68	35.235	28.289	35.055	28.111	1084	43.54	239.34
NERS2	69	35.234	28.287	35.055	28.114	1079	42.70	238.44
NERS2	70	35.232	28.275	35.054	28.113	870	33.52	239.28
NERS2	71	35.219	28.283	35.055	28.111	1032	33.63	239.33
NERS2	72	35.208	28.300	35.055	28.114	777	34.37	238.44
NERS2	73	35.220	28.300	35.055	28.114	896	35.35	238.33
NERS2	74	35.210	28.286	35.056	28.115	744	34.38	238.29
NERS2	75	35.279	28.264	35.055	28.114	1142	43.63	238.33
NERS2	76	35.284	28.272	35.054	28.114	1104	44.33	238.45
NERS2	77	35.217	28.300	35.054	28.112	867	35.30	239.29
NERS2	78	35.293	28.301	35.054	28.114	1402	48.02	239.28
NERS3	79	35.474	28.348	35.153	28.069	1228	67.16	806.88
NERS3	80	35.503	28.333	35.153	28.069	1194	66.51	807.03
NERS3	81	35.515	28.312	35.153	28.069	1109	66.64	806.88
NERS3	82	35.468	28.313	35.148	28.068	573	61.53	807.39
NERS3	83	35.452	28.311	35.153	28.068	623	57.96	807.22
NERS3	84	35.525	28.306	35.153	28.068	1316	70.13	807.22
NERS3	85	35.506	28.304	35.148	28.069	932	63.69	807.38
NERS3	86	35.475	28.300	35.148	28.068	544	61.28	807.39
NERS3	87	35.518	28.272	35.149	28.069	698	63.51	807.37
NERS3	88	35.302	28.264	35.151	28.068	1167	39.12	807.24
NERS3	89	35.311	28.299	35.148	28.068	1512	51.76	807.39
NERS3	90	35.281	28.255	35.154	28.069	955	34.89	806.87
NERS3	91	35.445	28.174	35.149	28.069	342	44.91	799.84
NERS3	92	35.289	28.252	35.151	28.068	875	36.35	807.24
NERS3	93	35.530	28.257	35.150	28.069	1004	67.96	807.35
NERS3	94	35.325	28.301	35.152	28.068	1077	56.31	807.23
NERS3	95	35.309	28.281	35.153	28.068	1213	49.56	807.16
NERS3	96	35.321	28.256	35.150	28.069	800	42.48	807.35
NERS3	97	35.314	28.271	35.150	28.069	992	48.77	807.35
NERS3	98	35.317	28.312	35.150	28.069	1032	57.27	807.35
NERS3	99	35.310	28.315	35.149	28.069	1152	60.09	807.37
NERS3	100	35.298	28.327	35.152	28.068	1588	61.67	807.23
NERS3	101	35.305	28.334	35.152	28.068	1351	60.78	807.23
NERS3	102	35.335	28.354	35.152	28.068	833	63.84	807.23
NERS3	103	35.550	28.262	35.151	28.068	1232	68.07	807.24
NERS3	104	35.335	28.341	35.153	28.068	909	62.32	807.16
NERS3	105	35.346	28.335	35.148	28.068	738	61.58	807.39
NERS3	106	35.332	28.313	35.148	28.069	734	55.79	807.38
NERS3	107	35.353	28.360	35.153	28.069	653	64.55	806.88
NERS3	108	35.384	28.388	35.151	28.068	823	64.57	807.24
NERS3	109	35.518	28.262	35.153	28.068	918	63.46	807.22
NERS3	110	35.514	28.245	35.149	28.069	719	62.33	807.37
NERS3	111	35.569	28.251	35.148	28.068	1418	73.87	807.39
NERS3	112	35.585	28.251	35.153	28.068	1387	75.19	807.16
NERS3	113	35.616	28.258	35.153	28.069	1112	75.40	806.88
NERS3	114	35.401	28.404	35.153	28.069	1222	67.41	806.88
NERS3	115	35.355	28.373	35.151	28.069	606	64.62	807.32
NERS3	116	35.395	28.372	35.151	28.069	677	63.79	807.32
NERS3	117	35.395	28.344	35.152	28.068	638	60.18	807.23
NERS3	118	35.407	28.336	35.150	28.069	584	57.06	807.35
NERS3	119	35.413	28.348	35.148	28.068	682	60.79	807.39
NERS3	120	35.459	28.346	35.150	28.069	766	62.20	807.36
NERS3	121	35.560	28.225	35.151	28.068	1322	68.07	807.24
NERS3	122	35.589	28.196	35.153	28.069	1475	71.84	806.88
NERS3	123	35.593	28.175	35.152	28.068	1413	74.81	807.23
NERS3	124	35.597	28.159	35.152	28.068	1377	75.55	807.23
NERS3	125	35.569	28.157	35.148	28.068	870	73.34	807.39
NERS3	126	35.523	28.170	35.151	28.068	1064	73.89	807.24
NERS3	127	35.543	28.176	35.150	28.069	758	68.90	807.35
NERS3	128	35.522	28.196	35.150	28.069	766	64.41	807.35
NERS3	129	35.513	28.183	35.148	28.068	799	52.75	807.39
NERS3	130	35.483	28.355	35.153	28.068	1198	67.23	807.22

Catchment name	Stream no.	Head		Mouth		Max. elevation (m)	Length (km)	Catchment area (km^2)
		Long.	Lat.	Long.	Lat.			
NERS3	131	35.611	28.290	35.150	28.069	1135	75.29	807.35
NERS3	132	35.571	28.303	35.153	28.068	1158	76.18	807.16
NERS3	133	35.542	28.252	35.153	28.068	1303	70.39	807.22
NERS3	134	35.551	28.245	35.149	28.069	1332	70.31	807.37
NERS3	135	35.489	28.251	35.148	28.069	588	59.16	807.38
NERS3	136	35.445	28.174	35.140	27.814	1017	95.14	836.70
NERS3	137	35.498	28.207	35.152	28.068	503	52.15	807.01
NERS3	138	35.612	28.263	35.148	28.068	1066	74.26	807.13
NERS3	139	35.490	28.308	35.152	28.068	605	62.01	807.23
NERS3	140	35.421	28.387	35.154	28.069	872	64.90	806.87
NERS3	141	35.439	28.386	35.151	28.069	1204	65.77	807.24
NERS3	142	35.470	28.364	35.148	28.068	1148	67.23	807.39
NERS3	143	35.445	28.357	35.148	28.068	687	63.71	807.39
NERS4	144	35.663	28.240	35.200	28.029	1085	101.09	1907.54
NERS4	145	36.362	27.820	35.200	28.029	1488	173.08	1907.54
NERS4	146	35.530	28.159	35.202	28.027	1047	53.74	1892.32
NERS4	147	35.518	28.152	35.203	28.025	1036	51.47	1889.19
NERS4	148	35.504	28.141	35.200	28.029	1097	49.25	1892.37
NERS4	149	35.521	28.129	35.203	28.025	883	52.46	1889.19
NERS4	150	35.494	28.112	35.203	28.025	669	46.52	1889.19
NERS4	151	35.518	28.115	35.203	28.026	1059	51.28	1889.21
NERS4	152	35.917	28.063	35.201	28.027	830	96.51	926.65
NERS5	153	35.677	28.019	35.308	27.898	413	55.33	968.25
NERS5	154	35.479	28.016	35.291	27.912	230	33.31	158.34
NERS5	155	35.858	27.905	35.318	27.884	708	70.66	985.25
NERS5	156	36.016	27.803	35.319	27.888	1044	93.19	985.19
NERS6	157	35.718	27.857	35.444	27.753	1413	39.87	216.09
NERS6	158	35.609	27.908	35.443	27.753	295	35.42	216.09
NERS6	159	35.563	27.879	35.441	27.754	223	27.57	216.34
NERS6	160	35.555	27.870	35.441	27.754	203	26.12	216.33
NERS6	161	35.673	27.827	35.439	27.754	793	33.97	216.35
NERS6	162	35.667	27.797	35.443	27.753	353	32.59	216.09
NERS6	163	35.630	27.777	35.439	27.754	414	25.97	216.35
NERS6	164	35.558	27.774	35.444	27.753	154	15.21	216.09
NERS6	165	35.623	27.862	35.444	27.754	246	30.88	215.00
NERS6	166	35.627	27.816	35.443	27.753	257	27.62	216.10
NERS6	167	35.555	27.870	35.441	27.754	203	26.12	216.33
NERS6	168	35.675	27.856	35.443	27.753	777	34.75	216.93
NERS7	169	35.686	27.683	35.475	27.680	772	30.57	567.43
NERS7	170	35.697	27.663	35.477	27.680	678	35.32	567.37
NERS7	171	35.654	27.743	35.476	27.680	204	30.71	567.42
NERS7	172	35.563	27.716	35.477	27.680	138	12.46	567.37
NERS7	173	35.580	27.702	35.476	27.680	133	14.71	567.37
NERS7	174	35.661	27.639	35.474	27.681	200	26.56	567.45
NERS7	175	35.671	27.669	35.477	27.680	347	27.94	567.37
NERS7	176	35.854	27.603	35.477	27.680	515	57.46	567.37
NERS7	177	35.812	27.686	35.474	27.681	588	45.20	567.45
NERS7	178	35.880	27.675	35.477	27.680	521	57.60	567.37
NERS7	179	35.771	27.840	35.475	27.680	1431	64.14	567.44
NERS7	180	35.761	27.842	35.474	27.681	1554	61.53	567.45
NERS7	181	35.764	27.806	35.477	27.680	788	51.90	567.37
NERS7	182	35.686	27.834	35.473	27.681	1259	55.98	567.46
NERS7	183	35.851	27.743	35.478	27.680	527	55.45	567.36
NERS7	184	35.838	27.817	35.473	27.681	996	59.64	567.46
NERS7	185	35.892	27.777	35.472	27.684	554	60.36	556.83
NERS7	186	35.703	27.789	35.474	27.680	355	48.65	0.04
NERS8	187	35.739	27.635	35.574	27.490	916	33.21	247.08
NERS8	188	35.734	27.613	35.574	27.490	302	31.61	247.08
NERS8	189	35.750	27.629	35.573	27.490	870	35.46	247.09
NERS8	190	35.759	27.620	35.571	27.490	656	35.69	247.29
NERS8	191	35.775	27.611	35.570	27.489	725	34.61	247.29
NERS8	192	35.797	27.613	35.569	27.489	832	42.67	247.31
NERS8	193	35.842	27.597	35.574	27.490	416	41.94	247.08
NERS8	194	35.725	27.593	35.573	27.490	208	30.36	247.09
NERS8	195	35.670	27.580	35.574	27.490	152	21.54	247.08

Catchment name	Stream no.	Head		Mouth		Max. elevation (m)	Length (km)	Catchment area (km^2)
		Long.	Lat.	Long.	Lat.			
NERS8	196	35.571	27.530	35.574	27.490	15	6.33	247.08
NERS8	197	35.644	27.552	35.572	27.489	160	14.57	247.10
NERS8	198	35.597	27.522	35.572	27.489	60	6.62	247.10
NERS8	199	35.786	27.575	35.571	27.490	240	30.99	247.29
NERS9	200	35.913	27.547	35.676	27.354	286	45.00	323.35
NERS9	201	35.821	27.499	35.677	27.354	184	26.96	323.35
NERS9	202	35.949	27.457	35.676	27.354	626	40.97	323.35
NERS9	203	35.958	27.445	35.678	27.355	729	41.02	323.34
NERS9	204	35.818	27.439	35.676	27.354	174	24.59	323.36
NERS9	205	35.721	27.445	35.679	27.354	146	14.67	322.45
NERS9	206	35.856	27.502	35.677	27.354	198	32.83	323.34
NERS9	207	35.750	27.476	35.679	27.354	135	20.24	322.45
NERS9	208	35.827	27.452	35.681	27.354	181	29.14	322.42
NERS9	209	35.880	27.555	35.679	27.354	405	41.78	322.45
NERS9	210	35.854	27.584	35.676	27.354	413	44.87	323.35
NERS9	211	35.939	27.477	35.678	27.355	421	42.92	323.34
NERS9	212	35.879	27.534	35.678	27.354	283	39.59	323.26
NERS9	213	35.891	27.527	35.676	27.354	274	40.13	323.36
NERS9	214	35.890	27.471	35.682	27.354	263	35.73	322.42
NERS10	215	35.988	27.315	35.813	27.202	174	34.18	289.57
NERS11	216	36.386	27.786	35.792	27.169	1229	162.92	4259.55
NERS11	217	36.263	27.725	35.789	27.170	1257	167.39	4273.23
NERS11	218	36.677	27.683	35.794	27.169	1444	170.68	4254.81
NERS12	219	36.702	27.208	35.918	27.000	917	139.89	1703.79
NERS12	220	36.324	27.250	35.919	26.999	354	70.32	1703.74
NERS12	221	36.356	27.167	35.915	27.002	286	82.37	0.12
NERS13	222	36.691	27.108	36.183	26.667	540	101.69	4920.83
NERS13	223	37.161	26.759	36.184	26.668	932	150.93	4920.81
NERS13	224	37.084	26.966	36.185	26.670	912	156.46	4920.41
NERS13	225	36.535	27.133	36.181	26.665	406	91.39	4920.91
NERS13	226	36.731	27.146	36.183	26.667	952	139.06	4920.84
NERS13	227	36.866	27.043	36.184	26.668	928	142.70	5881.87
NERS13	228	36.187	26.780	36.183	26.666	111	19.36	4920.88
NERS13	229	36.208	26.811	36.183	26.670	149	22.44	4919.74
NERS13	230	36.218	26.830	36.183	26.667	172	28.48	4920.34
NERS13	231	36.188	26.952	36.184	26.669	114	51.56	4919.74
NERS14	232	36.430	26.374	36.367	26.372	34	8.89	445.17
NERS14	233	36.471	26.604	36.369	26.373	210	54.39	444.39
NERS14	234	36.430	26.612	36.367	26.372	255	59.07	445.18
NERS14	235	36.449	26.570	36.366	26.372	542	56.63	445.19
NERS14	236	36.559	26.579	36.369	26.373	184	47.22	445.09
NERS14	237	36.547	26.429	36.369	26.372	158	27.09	444.55
NERS14	238	36.610	26.505	36.367	26.372	240	46.26	445.17
NERS14	239	36.492	26.567	36.369	26.372	196	38.43	444.55
NERS14	240	36.606	26.491	36.366	26.372	226	45.55	445.19
NERS14	241	36.504	26.428	36.369	26.373	138	22.00	445.09
NERS14	242	36.548	26.436	36.365	26.372	162	33.91	445.19
NERS14	243	36.572	26.455	36.370	26.373	172	38.19	444.46
NERS14	244	36.454	26.553	36.367	26.372	285	35.34	445.17
NERS14	245	36.417	26.505	36.367	26.372	127	25.96	445.17
NERS14	246	36.490	26.427	36.367	26.372	123	22.20	445.17
NERS15	247	36.716	26.413	36.421	26.279	234	52.04	313.23
NERS15	248	36.499	26.364	36.422	26.280	93	19.71	313.11
NERS15	249	36.615	26.463	36.421	26.280	205	39.64	313.22
NERS15	250	36.693	26.418	36.421	26.280	222	43.58	313.22
NERS15	251	36.625	26.376	36.424	26.282	168	33.81	264.07
NERS15	252	36.496	26.292	36.420	26.278	51	10.76	313.25
NERS15	253	36.561	26.433	36.420	26.278	161	34.01	313.26
NERS15	254	36.695	26.456	36.423	26.282	198	46.66	299.69
NERS15	255	36.634	26.495	36.420	26.278	217	47.76	313.25
NERS16	256	36.703	26.412	36.463	26.229	220	44.25	326.51
NERS16	257	36.602	26.349	36.464	26.229	160	26.88	326.49
NERS16	258	36.676	26.387	36.465	26.230	197	38.17	246.86
NERS16	259	36.654	26.336	36.463	26.228	177	29.18	326.52
NERS16	260	36.604	26.245	36.465	26.230	126	18.86	246.83

Catchment name	Stream no.	Head		Mouth		Max. elevation (m)	Length (km)	Catchment area (km^2)
		Long.	Lat.	Long.	Lat.			
NERS16	261	36.607	26.235	36.464	26.229	120	27.36	326.50
NERS16	262	36.469	26.268	36.465	26.230	21	7.51	246.83
NERS16	263	36.537	26.215	36.464	26.229	60	9.84	326.49
NERS17	264	37.067	26.708	36.513	26.106	843	132.38	1325.63
NERS18	265	36.854	26.271	36.656	26.055	195	42.90	314.73
NERS19	266	37.208	26.179	36.707	26.008	303	77.84	1998.52
NERS19	267	37.167	26.463	36.705	26.007	750	115.85	2001.08
NERS20	268	36.749	27.235	36.705	25.961	1346	591.94	102908.77
NERS20	269	36.790	27.518	36.699	25.964	1707	625.39	102911.41
NERS20	270	36.988	27.107	36.703	25.962	1203	555.76	102910.87
NERS20	*271*	*37.319*	*26.370*	*36.703*	*25.962*	*822*	*172.18*	*102910.87*
NERS20	272	37.140	26.657	36.702	25.963	1120	491.43	102911.17
NERS20	*273*	*37.226*	*26.440*	*36.702*	*25.965*	*1500*	*451.87*	*98616.33*
NERS20	*274*	*38.037*	*26.620*	*36.678*	*25.892*	*760*	*416.73*	*7.45*
NERS20	*275*	*38.523*	*26.572*	*36.678*	*25.892*	*1095*	*454.64*	*7.45*
NERS20	*276*	*37.966*	*26.118*	*36.678*	*25.892*	*566*	*342.30*	*7.45*
NERS20	*277*	*37.781*	*25.665*	*36.678*	*25.892*	*282*	*170.32*	*7.45*
NERS20	278	38.188	25.166	36.678	25.892	540	323.16	7.45
NERS20	*279*	*40.681*	*24.465*	*36.678*	*25.892*	*806*	*634.60*	*7.45*
NERS20	*280*	*40.225*	*24.101*	*36.678*	*25.892*	*772*	*599.50*	*7.45*
NERS20	*281*	*40.189*	*23.819*	*36.678*	*25.892*	*947*	*658.11*	*7.45*
NERS30	*282*	*37.721*	*24.833*	*37.367*	*24.563*	*990*	*73.67*	*0.05*
NERS30	283	37.668	24.740	37.362	24.577	386	46.46	623.89
NERS33	*284*	*37.850*	*24.238*	*37.815*	*24.188*	*10*	*10.23*	*0.06*
NERS35	285	38.193	24.526	37.951	24.157	1743	83.95	954.30
NERS37	286	38.836	24.432	38.153	24.022	510	126.32	6468.07
NERS37	287	38.173	24.529	38.152	24.022	1321	184.65	6469.47
NERS42	*288*	*39.001*	*24.212*	*38.596*	*23.573*	*664*	*161.57*	*0.20*
NERS42	*289*	*39.065*	*24.014*	*38.596*	*23.573*	*376*	*130.53*	*0.20*
NERS42	*290*	*39.186*	*24.038*	*38.596*	*23.573*	*634*	*156.60*	*0.20*
EGA1	*291*	*36.814*	*27.570*	*34.971*	*29.546*	*1632*	*644.45*	*58175.56*
EGA1	292	36.758	27.675	34.971	29.550	1511	574.38	58175.10
EGA1	293	36.466	27.816	34.971	29.549	1451	508.94	58175.10
EGA1	294	36.316	27.930	34.971	29.551	1365	489.40	58175.09
EGA1	295	35.438	28.471	34.971	29.547	1233	428.48	58175.46
EGA1	*296*	*36.379*	*30.359*	*34.971*	*29.545*	*909*	*269.11*	*4.15*
EGA1	*297*	*36.457*	*30.374*	*34.971*	*29.545*	*909*	*270.60*	*4.15*
EGA1	*298*	*36.495*	*30.324*	*34.971*	*29.545*	*909*	*266.10*	*4.15*
EGA1	*299*	*36.624*	*30.234*	*34.971*	*29.545*	*909*	*263.79*	*4.15*
EGA1	*300*	*36.363*	*29.675*	*34.971*	*29.545*	*878*	*198.49*	*4.15*
EGA1	*301*	*36.653*	*29.707*	*34.971*	*29.545*	*908*	*229.12*	*4.15*
EGA1	*302*	*36.299*	*29.454*	*34.971*	*29.545*	*878*	*185.36*	*4.15*
EGA1	303	36.189	29.065	34.971	29.545	878	207.21	4.15
EGA1	304	36.400	28.918	34.971	29.545	878	231.44	4.15
EGA1	*305*	*36.686*	*28.859*	*34.971*	*29.545*	*878*	*258.93*	*4.15*
EGA1	*306*	*36.564*	*28.701*	*34.971*	*29.545*	*878*	*264.27*	*4.15*
EGA1	*307*	*36.804*	*28.673*	*34.971*	*29.545*	*878*	*282.12*	*4.15*
EGA1	308	36.637	28.290	34.971	29.545	878	313.79	4.15
EGA1	309	36.785	28.250	34.971	29.545	878	321.72	4.15
EGA1	*310*	*36.806*	*28.116*	*34.971*	*29.545*	*878*	*340.06*	*4.15*
EGA8	311	35.456	29.156	34.950	29.297	1242	65.92	818.45
EGA12	312	35.065	28.948	34.937	29.237	1314	51.95	553.02
EGA16	313	35.030	28.904	34.831	28.906	1114	25.09	81.43
EGA17	314	34.962	28.813	34.842	28.850	1057	16.29	49.07
EGA19	315	34.888	28.744	34.785	28.661	1120	20.84	47.75
EGA21	316	34.973	28.748	34.802	28.559	890	39.80	262.57
EGA23	317	34.936	28.413	34.744	28.398	275	36.03	323.07
EGA23	318	34.841	28.365	34.742	28.401	214	20.58	323.78
WGA1	319	34.791	29.572	34.894	29.495	693	18.96	91.05
WGA2	320	34.774	29.545	34.853	29.455	685	18.94	52.52
WGA3	321	34.736	29.510	34.842	29.439	819	19.15	38.73
WGA4	322	34.748	29.469	34.802	29.382	801	15.42	50.91
WGA5	323	34.716	29.392	34.768	29.341	936	12.66	32.37
WGA5	324	34.704	29.361	34.768	29.341	656	11.38	32.36
WGA6	325	34.679	29.311	34.739	29.283	744	10.54	32.51

Catchment name	Stream no.	Head		Mouth		Max. elevation (m)	Length (km)	Catchment area (km^2)
		Long.	Lat.	Long.	Lat.			
WGA6	326	34.701	29.333	34.738	29.283	717	9.83	32.50
WGA7	327	34.666	29.274	34.735	29.260	653	11.10	24.16
WGA8	328	34.645	29.253	34.706	29.171	749	19.36	49.58
WGA9	329	34.617	29.211	34.688	29.148	775	14.18	53.24
WGA10	330	34.591	29.178	34.682	29.134	742	20.68	52.56
WGA11	331	34.058	29.056	34.683	28.999	1058	109.63	3648.76
WGA11	332	34.256	29.196	34.686	28.998	1024	77.01	3648.82
WGA11	333	34.443	29.509	34.690	28.998	898	108.04	3648.83
WGA11	334	33.988	28.803	34.684	28.999	1219	133.08	3648.77
WGA12	335	34.568	28.908	34.658	28.972	788	18.78	34.87
WGA13	336	34.576	28.901	34.643	28.965	750	14.32	22.25
WGA14	337	34.599	28.877	34.645	28.932	551	10.25	22.32
WGA15	338	34.573	28.884	34.644	28.861	738	15.85	64.84
WGA15	339	34.523	28.801	34.642	28.862	795	19.57	64.79
WGA16	340	34.518	28.796	34.622	28.765	791	18.18	41.18
WGA17	341	34.498	28.782	34.581	28.662	756	23.95	78.11
WGA18	342	34.511	28.710	34.567	28.626	655	19.52	72.11
WGA18	343	34.517	28.607	34.566	28.627	455	13.03	72.02
WGA19	344	34.030	28.611	34.499	28.481	1398	81.74	2141.09
WGA19	345	34.427	28.853	34.499	28.482	698	56.22	2141.09
WGA19	346	34.037	28.768	34.499	28.484	1312	93.52	2140.42
WGA19	347	33.966	28.396	34.500	28.484	1800	103.77	2140.39
WGA20	348	34.370	28.466	34.469	28.448	586	19.44	101.91
WGA20	349	34.349	28.394	34.466	28.449	718	22.61	101.84
WGA21	350	34.347	28.295	34.405	28.301	316	8.39	24.06
WGA22	351	34.319	28.264	34.406	28.269	396	13.23	29.60
WGA23	352	34.335	28.234	34.409	28.229	280	12.27	25.28
WGA24	353	34.083	28.197	34.435	28.139	1219	54.53	1089.05
WGA24	354	34.332	28.499	34.438	28.140	1114	72.85	1089.18
WGA24	355	34.035	28.365	34.435	28.139	1350	73.23	1089.04
WGA25	356	34.341	28.126	34.434	28.094	288	15.93	23.22
WGA26	357	34.093	28.108	34.425	28.076	1131	58.32	372.60
WGA26	358	34.088	28.151	34.427	28.074	1235	48.27	372.74
WGA27	359	34.326	28.049	34.430	27.990	214	19.00	55.46
WGA29	360	34.223	28.036	34.333	27.917	421	27.71	70.69
WGA30	361	34.169	27.996	34.328	27.914	694	27.20	112.40
WGA30	362	34.190	27.955	34.329	27.913	547	28.70	112.45
EGS1	363	33.094	29.891	32.585	29.951	642	86.33	627.86
EGS1	364	33.114	30.177	32.582	29.954	588	95.77	3240.55
EGS2	365	32.912	29.870	32.627	29.871	550	47.66	246.72
EGS2	366	32.912	29.870	32.627	29.871	550	47.66	246.72
EGS3	367	33.265	29.680	32.699	29.716	726	96.23	1097.50
EGS4	368	33.298	29.659	32.724	29.534	766	89.86	1283.96
EGS4	369	33.341	29.427	32.722	29.532	724	91.11	1284.30
EGS5	370	33.417	29.215	32.928	29.210	1089	88.90	921.82
EGS5	371	33.414	29.309	32.928	29.209	872	93.59	1081.05
EGS6	372	33.340	29.197	33.074	29.071	614	55.33	379.84
EGS7	373	33.716	29.044	33.175	28.964	985	87.05	763.80
EGS8	374	33.942	29.039	33.180	28.892	1280	118.45	1111.88
EGS9	375	33.921	28.897	33.206	28.688	1371	129.57	1845.10
EGS10	376	33.711	28.607	33.595	28.255	938	69.97	1988.63
EGS10	377	33.929	28.392	33.592	28.254	1803	76.01	1988.77
EGS10	378	33.941	28.481	33.592	28.254	1877	71.14	1988.69
EGS10	379	33.843	28.565	33.588	28.253	1380	79.86	1989.41
EGS10	380	33.711	28.449	33.593	28.252	314	51.23	0.14
EGS10	381	33.678	28.330	33.612	28.239	83	20.40	1896.34
EGS11	382	34.013	28.401	33.759	28.053	1614	71.48	652.59
EGS12	383	34.023	28.241	33.901	27.941	1565	48.12	259.00
EGS12	384	34.084	28.132	33.901	27.940	907	41.66	259.13
EGS13	385	34.076	28.070	33.910	27.941	814	34.12	283.73
EGS13	386	34.053	28.096	33.910	27.941	748	36.01	283.74
EGS13	387	34.100	28.005	33.908	27.939	750	32.51	283.91
WGS2	388	31.901	29.845	32.355	29.675	360	64.18	1053.93
WGS3	389	31.743	29.872	32.345	29.610	404	99.30	3171.40
WGS3	390	32.253	29.252	32.347	29.605	994	140.67	3172.16

Catchment name	Stream no.	Head		Mouth		Max. elevation (m)	Length (km)	Catchment area (km^2)
		Long.	Lat.	Long.	Lat.			
WGS5	391	32.021	29.239	32.663	29.112	720	126.68	4326.22
WGS5	392	32.362	28.656	32.662	29.112	1124	193.47	4326.20
WGS6	393	32.410	28.888	32.860	28.604	1243	86.92	1182.19
WGS7	394	32.312	28.021	32.937	28.534	771	130.10	1438.35
WGS10	395	32.757	28.036	33.106	28.328	851	99.86	819.59
WGS11	396	32.809	28.068	33.139	28.279	829	66.48	961.26
WGS13	397	32.784	28.023	33.369	28.036	822	97.10	1207.13
WGS14	398	32.936	27.550	33.485	27.836	676	114.00	1217.20
WGS15	399	33.033	27.591	33.507	27.761	675	73.88	339.87
WGS16	400	33.014	27.412	33.564	27.563	730	89.39	1661.80
WGS17	401	33.464	27.018	33.680	27.382	744	85.17	903.11
WGS19	402	33.491	27.047	33.827	27.120	701	55.30	583.91
WGS20	403	33.495	26.996	33.853	27.099	987	60.49	317.15
WGS21	404	33.527	26.900	33.904	26.989	838	59.35	358.71
SWRS1	405	33.575	26.775	33.944	26.749	587	55.68	507.37
SWRS2	406	33.512	26.699	34.001	26.625	682	77.61	753.27
SWRS3	407	33.537	26.558	34.155	26.346	645	96.00	1871.08
SWRS3	408	33.496	26.328	34.155	26.348	625	95.24	1871.10
SWRS3	409	33.782	26.103	34.154	26.346	516	72.98	1845.69
SWRS4	410	33.745	26.086	34.281	26.099	562	95.13	1569.50
SWRS4	411	34.059	25.699	34.280	26.099	636	96.97	1569.43
SWRS5	412	34.158	25.625	34.383	25.944	574	71.22	724.94
SWRS6	413	34.231	25.768	34.431	25.840	319	36.12	222.02
SWRS7	414	34.270	25.336	34.548	25.725	595	74.69	871.33
SWRS7	415	34.192	25.636	34.543	25.723	478	54.10	863.08
SWRS8	416	34.306	25.188	34.652	25.507	601	84.81	847.12
SWRS8	417	34.290	25.352	34.651	25.505	523	60.14	846.86
SWRS9	418	34.557	24.981	34.740	25.321	553	68.29	754.57
SWRS9	419	34.406	25.187	34.740	25.322	475	54.30	754.79
SWRS9	420	34.574	25.154	34.744	25.321	286	37.66	748.86
SWRS10	421	34.623	24.867	34.892	25.078	769	61.55	335.84
SWRS11	422	34.666	24.909	34.999	24.823	565	56.47	518.27
SWRS11	423	34.780	24.706	34.997	24.823	433	41.54	518.27
SWRS12	424	34.816	24.715	35.079	24.695	353	38.88	197.96
SWRS13	425	34.506	24.797	35.094	24.644	564	101.94	2018.47
SWRS13	426	35.014	24.173	35.095	24.643	1078	150.01	2018.70
SWRS14	427	34.928	24.444	35.132	24.523	321	37.70	270.99
SWRS15	428	34.919	24.425	35.202	24.449	397	45.53	385.29
SWRS15	429	35.024	24.271	35.201	24.449	372	43.47	385.25
SWRS16	430	35.029	24.231	35.240	24.396	660	44.56	248.34
SWRS17	431	35.210	23.886	35.486	23.941	566	87.27	920.62
SWRS17	432	35.068	24.128	35.483	23.943	684	73.44	917.25
SWRS18	433	35.066	23.751	35.491	23.654	495	71.40	876.65
SWRS20	434	35.213	23.592	35.573	23.224	496	99.52	1113.90
SWRS21	435	35.034	23.855	35.622	23.139	522	221.64	11425.93
SWRS21	436	35.178	22.210	35.624	23.141	648	290.16	11425.99
SWRS21	437	34.591	22.649	35.621	23.139	521	223.09	11425.68
SWRS21	438	34.556	23.229	35.622	23.139	460	176.94	11425.68
SWRS22	439	35.411	22.872	35.676	22.957	189	42.66	303.86
SWRS23	440	35.265	22.783	35.727	22.923	419	85.76	3410.37
SWRS23	441	35.467	22.144	35.726	22.925	714	142.21	3410.47
SWRS23	442	35.435	22.388	35.823	22.786	337	93.65	1905.23
SWRS24	443	35.575	22.270	35.951	22.709	519	103.45	41900.65
SWRS25	444	36.260	20.762	35.987	22.691	491	380.80	42212.50
-	*445*	*34.885*	*28.347*	*34.746*	*28.100*	*179*	*43.94*	*335.86*
-	*446*	*36.670*	*26.176*	*36.575*	*26.071*	*89*	*22.09*	*56.52*
-	*447*	*36.624*	*26.130*	*36.578*	*26.075*	*44*	*11.23*	*51.06*
-	*448*	*36.599*	*26.128*	*36.576*	*26.074*	*38*	*10.05*	*54.87*
-	*449*	*35.497*	*27.823*	*35.435*	*27.773*	*141*	*13.22*	*77.63*
-	*450*	*35.508*	*27.834*	*35.433*	*27.771*	*174*	*17.68*	*77.67*
-	*451*	*35.456*	*27.842*	*35.434*	*27.772*	*126*	*12.32*	*77.65*
-	*452*	*35.475*	*27.779*	*35.435*	*27.774*	*67*	*5.78*	*77.60*
-	*453*	*35.708*	*27.754*	*35.478*	*27.697*	*768*	*32.59*	*99.95*
-	*454*	*35.660*	*27.774*	*35.474*	*27.694*	*665*	*29.35*	*100.37*
-	*455*	*35.597*	*27.767*	*35.475*	*27.694*	*189*	*21.59*	*100.34*

Catchment name	Stream no.	Head		Mouth		Max. elevation (m)	Length (km)	Catchment area (km^2)
		Long.	Lat.	Long.	Lat.			
-	456	35.625	27.773	35.473	27.694	292	27.70	100.39
-	457	35.533	27.755	35.475	27.695	105	13.04	100.36
-	458	35.684	27.774	35.474	27.694	553	32.02	100.37
-	459	35.980	27.412	35.764	27.283	388	36.55	180.40
-	460	35.968	27.432	35.764	27.283	753	37.17	180.80
-	461	35.911	27.398	35.762	27.282	235	27.41	180.86
-	462	35.879	27.403	35.762	27.282	215	25.68	180.86
-	463	35.837	27.396	35.761	27.281	176	22.18	180.87
-	464	35.848	27.410	35.762	27.282	202	24.45	180.86
-	465	35.825	27.382	35.762	27.282	161	20.19	180.87
-	466	35.912	27.336	35.766	27.284	192	25.46	180.38
-	467	35.983	27.379	35.763	27.283	330	32.83	180.83
-	468	35.974	27.357	35.765	27.284	260	31.45	180.38
-	469	35.851	27.316	35.762	27.282	140	13.48	180.86
-	470	35.880	27.345	35.761	27.281	182	20.85	180.87
-	471	35.805	27.338	35.763	27.283	129	12.99	180.83
-	472	35.956	27.390	35.762	27.282	257	30.81	180.86
-	473	35.807	27.326	35.761	27.281	110	8.94	180.87
-	474	35.904	27.331	35.802	27.233	206	24.00	74.50
-	475	35.906	27.311	35.801	27.231	214	22.07	74.96
-	476	35.887	27.283	35.800	27.231	142	15.02	75.00
-	477	35.861	27.262	35.801	27.230	57	10.04	75.01
-	478	35.868	27.278	35.801	27.231	108	13.10	74.96
-	479	35.903	27.298	35.801	27.230	213	20.66	75.01
-	480	35.836	27.291	35.803	27.233	71	11.03	74.51
-	481	35.850	27.244	35.805	27.229	40	6.60	8.87
-	482	35.861	27.284	35.802	27.233	106	11.71	74.50
-	483	36.098	26.893	36.052	26.849	137	10.84	23.28
-	484	35.908	27.129	35.807	27.126	43	13.08	21.19
-	485	35.867	27.107	35.804	27.126	20	8.90	21.63
-	486	35.854	27.136	35.805	27.127	16	8.16	21.63
-	487	35.926	27.114	35.853	27.065	58	13.31	25.17
-	488	35.882	27.090	35.857	27.068	20	5.16	24.88
-	489	35.883	27.075	35.853	27.065	17	5.26	25.18
-	490	35.842	27.094	35.842	27.080	11	2.94	2.79
-	491	35.827	27.108	35.824	27.099	11	2.20	1.21
-	492	35.934	27.078	35.884	27.031	51	9.93	6.61
-	493	35.939	27.100	35.879	27.042	67	12.35	23.21
-	494	35.926	27.098	35.880	27.039	59	12.56	23.34
-	495	35.894	27.050	35.880	27.038	11	2.95	1.05
-	496	35.925	27.062	35.887	27.027	27	7.53	12.26
-	497	35.918	27.025	35.887	27.027	15	4.32	12.26
-	498	35.945	27.014	35.940	26.983	15	5.16	7.32
-	499	35.986	26.986	35.949	26.986	70	5.19	7.96
-	500	35.967	27.004	35.946	26.984	50	5.19	8.47
-	501	36.041	26.981	35.971	26.960	149	13.87	26.96
-	502	36.021	26.974	35.970	26.960	122	8.93	26.97
-	503	36.003	26.955	35.987	26.943	40	3.64	2.11
-	504	36.031	26.967	36.010	26.929	123	7.10	9.27
-	505	36.077	26.916	36.037	26.902	144	6.51	6.35
-	506	36.083	26.898	36.042	26.898	149	6.79	5.96
-	507	36.073	26.886	36.048	26.880	86	5.68	5.45
-	508	36.133	26.904	36.012	26.922	162	19.42	65.32
-	509	36.106	26.938	36.010	26.922	146	14.80	65.38
-	510	36.089	26.961	36.008	26.923	129	14.66	65.48
-	511	36.056	26.987	36.010	26.922	115	13.79	65.38
-	512	36.059	26.989	36.007	26.924	116	14.64	65.49
-	513	36.091	26.947	36.012	26.922	127	11.84	65.36
-	514	36.029	26.912	36.010	26.920	8	3.76	4.72
-	515	36.058	26.923	36.012	26.922	83	7.51	65.32
-	516	36.067	26.927	36.007	26.924	98	10.18	65.49
-	517	36.121	26.882	36.046	26.851	161	12.26	23.88
-	518	36.083	26.842	36.062	26.831	97	4.35	6.56
-	519	36.078	26.829	36.061	26.830	30	3.10	6.57
-	520	35.566	27.604	35.530	27.604	78	4.98	6.53

Catchment name	Stream no.	Head		Mouth		Max. elevation (m)	Length (km)	Catchment area (km^2)
		Long.	Lat.	Long.	Lat.			
-	521	35.561	27.614	35.528	27.605	45	5.05	6.92
-	522	35.716	27.649	35.536	27.588	859	25.54	75.39
-	523	35.678	27.638	35.532	27.587	266	21.48	76.87
-	524	35.604	27.574	35.531	27.587	142	10.93	76.89
-	525	35.634	27.577	35.552	27.558	162	13.38	37.43
-	526	35.591	27.569	35.546	27.567	99	6.60	5.44
-	527	35.630	27.548	35.552	27.558	144	11.75	36.67
-	528	35.582	27.565	35.552	27.558	80	4.36	37.43
-	529	35.554	27.529	35.543	27.524	28	2.29	2.55
-	530	35.542	27.530	35.536	27.528	13	1.46	0.73
-	531	35.641	27.482	35.582	27.477	104	8.95	3.59
-	532	35.635	27.477	35.584	27.475	92	7.41	7.98
-	533	35.623	27.426	35.611	27.424	11	2.15	1.31
-	534	35.679	27.424	35.623	27.405	104	8.89	17.42
-	535	35.624	27.471	35.587	27.471	63	5.07	3.72
-	536	35.595	27.460	35.589	27.461	15	1.40	1.20
-	537	35.597	27.456	35.591	27.455	13	1.50	0.51
-	538	35.675	27.397	35.625	27.406	68	8.36	17.39
-	539	35.644	27.391	35.624	27.405	19	3.78	17.39
-	540	35.628	27.417	35.610	27.423	10	2.98	3.82
-	541	35.651	27.384	35.645	27.384	19	1.47	1.05
-	542	35.703	27.424	35.671	27.360	139	12.44	19.67
-	543	35.685	27.385	35.669	27.357	39	5.12	19.73
-	544	35.828	27.551	35.604	27.430	259	35.87	125.72
-	545	35.822	27.508	35.605	27.430	207	32.06	125.71
-	546	35.740	27.464	35.603	27.429	140	19.61	125.73
-	547	35.699	27.434	35.601	27.429	149	12.96	125.74
-	548	35.702	27.452	35.604	27.430	138	14.21	125.72
-	549	35.642	27.468	35.604	27.430	86	8.28	125.72
-	550	35.636	27.472	35.605	27.430	90	8.68	12.04
-	551	35.789	27.399	35.700	27.351	166	14.57	25.05
-	552	35.763	27.396	35.698	27.349	145	11.81	26.05
-	553	35.739	27.361	35.698	27.349	67	6.49	26.05
-	554	35.664	27.407	35.625	27.406	69	5.95	17.37
-	555	35.729	27.353	35.724	27.333	56	3.71	3.45
-	556	35.794	27.333	35.746	27.322	115	8.16	8.45
-	557	35.768	27.322	35.748	27.319	20	5.95	9.02
-	558	35.838	27.407	35.738	27.325	192	17.66	41.72
-	559	35.827	27.373	35.763	27.283	151	18.69	180.83
-	560	35.802	27.359	35.738	27.327	190	12.75	40.29
-	561	35.721	27.623	35.571	27.490	343	31.08	247.29
-	562	35.349	27.875	35.348	27.856	19	3.69	2.92
-	563	35.366	27.873	35.354	27.854	27	3.62	5.22
-	564	35.407	27.837	35.356	27.838	41	7.13	32.34
-	565	35.379	27.871	35.351	27.839	40	8.15	33.30
-	566	35.380	27.829	35.356	27.833	19	3.57	3.07
-	567	35.358	27.818	35.352	27.819	8	1.51	0.92
-	568	35.388	27.796	35.386	27.791	10	1.46	1.66
-	569	35.414	27.811	35.403	27.785	31	5.11	7.60
-	570	35.420	27.789	35.410	27.782	9	2.16	2.56
-	571	35.416	27.802	35.403	27.788	22	4.27	7.13
-	572	35.489	27.867	35.358	27.804	200	21.92	21.01
-	573	35.518	27.857	35.436	27.774	197	19.16	77.47
-	574	35.520	27.827	35.436	27.774	155	14.89	77.47
-	575	35.512	27.795	35.435	27.773	122	11.85	77.63
-	576	35.485	27.779	35.432	27.771	89	9.02	77.74
-	577	35.444	27.844	35.433	27.771	118	11.66	77.65
-	578	35.495	27.862	35.435	27.773	195	17.28	77.63
-	579	35.429	27.816	35.434	27.772	36	7.36	77.65
-	580	35.514	27.746	35.453	27.734	72	7.74	10.40
-	581	35.530	27.809	35.433	27.771	161	15.66	77.67
-	582	35.474	27.770	35.438	27.763	52	5.06	5.28
-	583	35.528	27.749	35.466	27.712	86	10.71	12.76
-	584	35.499	27.732	35.468	27.714	42	5.71	4.14
-	585	35.468	27.727	35.462	27.725	8	1.55	0.66

Catchment name	Stream no.	Head		Mouth		Max. elevation (m)	Length (km)	Catchment area (km^2)
		Long.	Lat.	Long.	Lat.			
-	586	35.451	27.747	35.444	27.747	9	1.37	0.79
-	587	35.440	27.770	35.439	27.764	7	1.45	1.03
-	588	35.497	27.710	35.472	27.710	20	3.53	2.89
-	589	35.488	27.715	35.471	27.710	14	2.86	3.00
-	590	35.458	27.773	35.439	27.764	28	3.56	4.22
-	591	35.504	27.684	35.476	27.677	25	4.19	3.68
-	592	35.516	27.669	35.478	27.667	35	5.12	4.78
-	593	35.535	27.665	35.501	27.639	51	5.95	6.62
-	594	35.511	27.653	35.496	27.646	19	2.87	2.90
-	595	35.509	27.663	35.485	27.660	35	3.58	1.53
-	596	35.511	27.637	35.504	27.636	7	1.41	0.66
-	597	35.517	27.637	35.506	27.634	9	2.17	1.02
-	598	35.605	27.630	35.529	27.622	132	11.76	39.20
-	599	35.606	27.638	35.528	27.622	163	10.96	39.28
-	600	35.573	27.655	35.529	27.622	157	8.75	39.20
-	601	35.546	27.657	35.525	27.623	76	6.61	40.71
-	602	35.528	27.637	35.528	27.622	11	3.08	39.28
-	603	36.194	26.865	36.067	26.809	186	20.56	63.22
-	604	36.142	26.899	36.069	26.810	176	19.71	63.02
-	605	36.102	26.851	36.070	26.810	106	8.90	63.01
-	606	36.131	26.820	36.068	26.810	119	10.31	63.18
-	607	36.119	26.890	36.009	26.923	162	18.69	65.43
-	608	36.170	26.890	36.070	26.811	187	20.34	62.94
-	609	36.126	26.807	36.074	26.795	118	7.21	10.40
-	610	36.164	26.848	36.070	26.811	151	15.21	62.93
-	611	36.131	26.866	36.067	26.809	138	14.51	63.22
-	612	36.142	26.827	36.092	26.759	129	14.62	53.58
-	613	36.183	26.803	36.096	26.759	129	14.73	48.69
-	614	36.108	26.780	36.091	26.760	62	5.08	53.62
-	615	36.200	26.854	36.095	26.759	181	21.36	48.69
-	616	36.423	26.515	36.343	26.436	149	22.75	45.88
-	617	36.403	26.482	36.346	26.438	117	16.12	44.36
-	618	36.398	26.456	36.341	26.436	89	8.58	45.90
-	619	36.383	26.426	36.346	26.418	38	4.89	5.99
-	620	36.380	26.411	36.348	26.401	34	5.03	5.96
-	621	34.727	29.330	34.755	29.310	371	5.97	8.10
-	622	34.740	24.897	34.933	24.959	402	29.80	74.62
-	623	34.345	28.205	34.421	28.209	225	12.25	19.34
-	624	35.454	22.952	35.674	22.979	109	35.54	135.64
-	625	34.500	25.286	34.739	25.337	330	34.19	187.73
-	626	34.182	27.931	34.134	27.794	528	27.69	60.95
-	627	34.122	27.999	34.003	27.861	941	30.74	68.26
-	628	34.781	29.442	34.820	29.420	516	7.63	7.24
-	629	34.754	29.386	34.780	29.361	642	5.73	5.44
-	630	34.627	29.084	34.668	29.066	462	9.39	19.80
-	631	34.510	28.584	34.523	28.559	346	4.92	7.96
-	632	34.392	28.377	34.426	28.351	436	8.13	14.79
-	633	34.383	28.352	34.426	28.351	438	6.89	14.80
-	634	33.970	28.179	33.769	28.034	956	39.77	97.01
-	635	34.701	29.255	34.734	29.248	314	7.31	11.91
-	636	34.605	28.799	34.623	28.813	262	4.30	6.56
-	637	32.093	29.731	32.357	29.665	329	41.64	137.14
-	638	34.622	25.052	34.838	25.178	530	41.47	198.17
-	639	35.068	24.170	35.408	24.254	779	51.10	134.49
-	640	34.621	28.880	34.642	28.873	485	4.27	5.30
-	641	34.416	28.401	34.445	28.377	554	7.11	9.39
-	642	33.833	26.667	33.946	26.653	253	17.67	53.99
-	643	34.442	25.496	34.611	25.603	390	33.23	97.98
-	644	34.914	24.719	35.068	24.753	243	23.71	76.44
-	645	47.039	24.627	51.715	24.210	586	661.16	9.85
-	646	52.027	21.162	51.917	23.975	122	530.75	44.77
-	647	49.770	20.093	51.917	23.975	280	888.26	44.77
-	648	49.821	20.053	51.917	23.975	280	891.61	44.77
-	649	42.931	16.571	42.734	16.514	47	30.29	0.10
-	650	42.962	16.547	42.734	16.514	56	35.34	0.10

Catchment name	Stream no.	Head		Mouth		Max. elevation (m)	Length (km)	Catchment area (km^2)
		Long.	Lat.	Long.	Lat.			
-	651	55.592	22.243	51.917	23.975	108	873.73	44.77
-	652	55.757	22.255	51.917	23.975	108	887.28	44.77
-	653	55.733	22.191	51.917	23.975	108	879.77	44.77
-	654	55.831	22.173	51.917	23.975	108	885.59	44.77
-	655	50.070	25.887	50.115	25.944	0	15.86	0.02
-	656	57.563	22.663	58.532	20.469	365	388.95	1.73
-	657	57.035	22.474	51.917	23.975	282	1063.50	44.77
-	658	58.722	23.025	58.927	23.257	514	55.43	0.14
-	659	56.942	22.319	51.917	23.975	211	1033.28	44.77
-	660	55.994	21.954	51.917	23.975	108	886.26	44.77
-	661	54.519	21.401	51.917	23.975	108	726.06	44.77
-	662	50.832	19.814	51.917	23.975	235	860.26	44.77
-	663	55.725	21.710	51.917	23.975	108	855.91	44.77
-	664	57.980	22.410	58.532	20.469	314	330.66	1.73
-	665	39.891	20.934	39.501	20.732	213	77.95	0.04
-	666	53.740	20.802	51.917	23.975	108	817.08	44.77
-	667	43.639	16.071	42.780	15.837	1024	184.94	0.60
-	668	51.563	19.912	51.917	23.975	197	803.04	44.77
-	669	58.152	22.313	58.532	20.469	289	330.69	1.73
-	670	48.058	18.224	51.917	23.975	545	1295.06	44.77
-	671	49.359	18.773	51.917	23.975	357	1122.78	44.77
-	672	54.777	21.107	51.917	23.975	108	764.60	44.77
-	673	56.712	21.655	51.917	23.975	108	963.85	44.77
-	674	42.957	15.375	42.804	15.289	40	28.03	0.23
-	675	49.411	18.636	51.917	23.975	362	1175.20	44.77
-	676	56.560	21.527	51.917	23.975	108	945.72	44.77
-	677	56.601	21.489	51.917	23.975	108	951.72	44.77
-	678	56.564	21.448	51.917	23.975	108	952.10	44.77
-	679	52.859	19.961	51.917	23.975	159	1239.25	44.77
-	680	55.529	21.009	51.917	23.975	108	837.56	44.77
-	681	58.490	21.930	58.532	20.469	172	250.26	1.73
-	682	45.279	16.255	51.133	15.184	1201	1036.69	9.81
-	683	50.065	18.577	51.917	23.975	336	1173.42	44.77
-	684	56.956	21.242	57.995	20.432	120	244.54	1.97
-	685	49.883	25.675	50.170	25.782	69	54.48	0.69
-	686	57.004	21.225	57.995	20.432	120	239.52	1.97
-	687	57.010	21.219	57.995	20.432	120	238.45	1.97
-	688	56.997	21.219	57.995	20.432	120	237.68	1.97
-	689	58.337	21.629	58.532	20.469	120	201.47	1.73
-	690	57.025	21.159	57.995	20.432	120	234.98	1.97
-	691	47.182	16.982	51.917	23.975	864	1537.03	44.77
-	692	46.633	16.620	51.917	23.975	958	1628.02	44.77
-	693	59.353	21.854	59.455	21.656	52	42.07	0.09
-	694	56.119	20.672	51.917	23.975	108	999.18	44.77
-	695	45.316	15.783	51.133	15.184	1022	992.68	9.81
-	696	41.942	21.947	51.857	23.981	1029	1923.91	34.33
-	697	51.637	18.829	51.917	23.975	283	1443.26	44.77
-	698	57.905	21.104	57.995	20.432	52	116.64	1.97
-	699	50.089	18.058	51.917	23.975	412	1213.51	44.77
-	700	46.862	16.337	51.133	15.184	930	836.31	9.81
-	701	50.301	18.081	51.917	23.975	426	1209.58	44.77
-	702	50.792	18.235	51.917	23.975	449	1144.84	44.77
-	703	57.063	20.675	57.995	20.432	129	238.49	1.97
-	704	50.138	17.865	51.917	23.975	478	1246.45	44.77
-	705	43.219	14.194	43.081	14.170	59	20.90	0.01
-	706	48.936	25.027	49.134	27.427	327	390.82	2.25
-	707	55.122	19.789	51.917	23.975	108	970.61	44.77
-	708	55.233	19.782	51.917	23.975	108	990.41	44.77
-	709	46.758	15.914	51.133	15.184	816	778.55	9.81
-	710	54.521	19.434	51.917	23.975	128	1039.43	44.77
-	711	50.784	17.783	51.917	23.975	617	1235.19	44.77
-	712	43.329	13.943	43.225	13.892	81	17.16	0.04
-	713	56.320	20.039	51.917	23.975	144	1139.37	44.77
-	714	56.300	19.977	51.917	23.975	144	1146.77	44.77
-	715	52.009	18.144	51.917	23.975	456	1529.43	44.77

Catchment name	Stream no.	Head		Mouth		Max. elevation (m)	Length (km)	Catchment area (km^2)
		Long.	Lat.	Long.	Lat.			
-	716	44.096	22.730	51.715	24.210	941	1187.43	9.85
-	717	52.842	18.443	51.917	23.975	317	1349.96	44.77
-	718	55.345	19.435	51.917	23.975	138	1089.41	44.77
-	719	46.207	15.178	51.133	15.184	927	836.03	9.81
-	720	51.518	17.736	51.917	23.975	594	1644.56	44.77
-	721	54.761	19.016	51.917	23.975	179	1074.90	44.77
-	722	55.285	19.191	51.917	23.975	176	1126.85	44.77
-	723	47.378	15.582	51.133	15.184	772	633.63	9.81
-	724	47.752	15.681	51.133	15.184	727	567.71	9.81
-	725	50.253	16.808	51.917	23.975	931	1401.79	44.77
-	726	49.072	24.995	49.134	27.427	279	387.77	2.25
-	727	57.507	19.690	57.681	19.681	46	37.91	0.09
-	728	51.254	17.175	51.917	23.975	876	1734.67	44.77
-	729	45.895	14.371	51.133	15.184	1456	955.07	9.81
-	730	51.602	17.150	51.917	23.975	875	1697.57	44.77
-	731	46.388	14.507	51.133	15.184	1113	886.71	9.81
-	732	54.836	18.379	51.917	23.975	263	1179.88	44.77
-	733	46.417	14.486	51.133	15.184	1107	883.61	9.81
-	734	53.892	17.932	51.917	23.975	351	1236.61	44.77
-	735	55.730	18.600	56.755	18.705	212	164.12	0.37
-	736	43.377	22.295	51.857	23.981	930	1635.32	34.33
-	737	52.322	17.087	51.917	23.975	813	1605.77	44.77
-	738	55.964	18.574	56.755	18.705	201	130.00	0.37
-	739	52.308	16.992	51.917	23.975	874	1620.10	44.77
-	740	45.115	13.257	45.330	13.046	182	49.47	0.11
-	741	44.907	13.057	45.086	12.921	113	38.15	0.42
-	742	54.747	17.810	51.917	23.975	399	1345.38	44.77
-	743	55.377	17.917	55.599	17.880	351	41.42	0.03
-	744	52.257	16.499	52.356	16.344	97	28.76	0.22
-	745	48.643	24.615	51.715	24.210	343	509.21	9.85
-	746	51.062	15.712	51.133	15.184	651	116.13	9.81
-	747	54.407	17.114	54.334	17.032	423	18.83	0.01
-	748	48.412	14.174	48.348	14.023	333	28.18	0.02
-	749	43.660	22.297	51.857	23.981	1003	1683.75	34.33
-	750	51.478	25.644	51.534	25.617	4	11.63	0.01
-	751	46.652	23.521	51.715	24.210	710	755.83	9.85
-	752	43.328	21.910	51.857	23.981	884	1581.86	34.33
-	753	43.576	22.014	51.857	23.981	948	1622.42	34.33
-	754	45.725	22.881	51.715	24.210	636	905.11	9.85
-	755	46.272	23.146	51.715	24.210	624	828.62	9.85
-	756	41.934	20.994	51.857	23.981	1367	1951.06	34.33
-	757	42.585	22.994	51.857	23.981	944	1753.72	34.33
-	758	46.120	22.932	51.715	24.210	624	859.17	9.85
-	759	38.835	34.853	48.689	30.015	478	1670.01	88.52
-	760	37.696	34.337	48.689	30.015	609	1823.20	88.52
-	761	46.083	22.865	51.715	24.210	624	868.66	9.85
-	762	38.124	34.359	48.689	30.015	462	1761.25	88.52
-	763	39.841	34.960	48.689	30.015	251	1542.03	88.52
-	764	38.511	34.227	48.689	30.015	469	1762.14	88.52
-	765	46.035	22.819	51.715	24.210	624	878.40	9.85
-	766	37.898	33.646	35.028	32.808	742	417.20	17.94
-	767	39.045	34.241	48.689	30.015	576	1718.97	88.52
-	768	37.577	33.430	35.028	32.808	638	351.73	17.94
-	769	35.496	32.438	35.028	32.808	57	77.56	17.94
-	770	43.347	21.310	51.857	23.981	848	1484.81	34.33
-	771	41.159	34.825	48.689	30.015	183	1432.08	88.52
-	772	37.585	33.270	35.028	32.808	638	341.42	17.94
-	773	35.547	32.304	35.028	32.808	57	97.07	17.94
-	774	36.241	32.547	35.028	32.808	581	177.95	17.94
-	775	37.195	33.008	35.028	32.808	638	306.97	17.94
-	776	41.096	34.603	48.689	30.015	183	1405.11	88.52
-	777	50.002	24.308	50.856	24.763	193	164.51	0.86
-	778	37.616	32.798	35.028	32.808	673	362.54	17.94
-	779	39.616	33.525	48.689	30.015	717	1667.80	88.52
-	780	35.430	31.477	35.028	32.808	57	200.27	17.94

Catchment name	Stream no.	Head		Mouth		Max. elevation (m)	Length (km)	Catchment area (km^2)
		Long.	Lat.	Long.	Lat.			
-	781	39.011	33.147	48.689	30.015	746	1817.07	88.52
-	782	35.519	31.397	35.028	32.808	57	212.75	17.94
-	783	39.017	32.995	48.689	30.015	769	1840.63	88.52
-	784	33.413	30.079	33.805	31.145	396	250.84	1.69
-	785	45.125	22.018	51.715	24.210	786	1077.89	9.85
-	786	38.947	32.810	35.028	32.808	782	519.11	17.94
-	787	43.099	34.435	48.689	30.015	62	1032.87	88.52
-	788	40.403	33.203	48.689	30.015	619	1403.23	88.52
-	789	35.923	31.166	35.028	32.808	778	279.77	17.94
-	790	34.509	30.326	33.805	31.145	506	213.77	1.69
-	791	37.084	31.665	35.028	32.808	592	299.21	17.94
-	792	35.206	30.595	35.028	32.808	57	343.96	17.94
-	793	35.181	30.542	35.028	32.808	57	346.20	17.94
-	794	45.125	21.929	51.715	24.210	785	1057.69	9.85
-	795	43.066	34.090	48.689	30.015	62	1001.22	88.52
-	796	44.092	34.457	48.689	30.015	55	1022.69	88.52
-	797	40.214	32.896	48.689	30.015	659	1450.22	88.52
-	798	38.857	32.066	35.028	32.808	854	802.13	17.94
-	799	37.099	31.328	35.028	32.808	592	335.51	17.94
-	800	43.420	33.966	48.689	30.015	62	965.32	88.52
-	801	40.421	32.711	48.689	30.015	716	1132.14	88.52
-	802	38.171	31.695	35.028	32.808	704	549.06	17.94
-	803	43.428	33.816	48.689	30.015	62	960.39	88.52
-	804	41.234	19.850	40.846	19.560	468	93.21	0.10
-	805	38.284	31.622	35.028	32.808	709	562.35	17.94
-	806	43.787	33.881	48.689	30.015	60	935.19	88.52
-	807	34.049	29.349	33.805	31.145	905	319.26	1.69
-	808	37.390	31.044	35.028	32.808	592	378.87	17.94
-	809	36.985	30.643	35.028	32.808	790	469.93	17.94
-	810	48.541	23.441	51.857	23.981	313	552.65	34.33
-	811	47.054	34.955	48.689	30.015	1484	1170.38	88.52
-	812	40.443	32.110	48.689	30.015	713	1202.38	88.52
-	813	44.171	33.544	48.689	30.015	37	858.98	88.52
-	814	39.084	31.298	35.028	32.808	828	689.51	17.94
-	815	44.239	33.468	48.689	30.015	37	849.24	88.52
-	816	38.305	30.886	35.028	32.808	592	453.06	17.94
-	817	42.150	22.813	51.857	23.981	944	1783.91	34.33
-	818	46.620	22.348	51.857	23.981	568	905.57	34.33
-	819	42.706	32.770	48.689	30.015	207	846.16	88.52
-	820	46.103	34.169	48.689	30.015	1042	1002.55	88.52
-	821	42.173	32.396	48.689	30.015	330	983.15	88.52
-	822	38.317	30.651	35.028	32.808	592	473.01	17.94
-	823	40.437	31.506	48.689	30.015	698	1193.12	88.52
-	824	43.578	32.843	48.689	30.015	31	749.24	88.52
-	825	43.183	32.667	48.689	30.015	105	791.54	88.52
-	826	43.961	20.974	51.857	23.981	769	1359.48	34.33
-	827	42.702	32.396	48.689	30.015	276	894.84	88.52
-	828	37.910	30.141	35.028	32.808	646	536.99	17.94
-	829	43.708	32.682	48.689	30.015	31	732.40	88.52
-	830	38.586	30.335	35.028	32.808	592	570.27	17.94
-	831	40.374	31.119	48.689	30.015	732	1318.02	88.52
-	832	43.429	32.389	48.689	30.015	97	783.92	88.52
-	833	41.344	19.541	41.046	19.254	177	62.69	0.03
-	834	40.051	30.749	48.689	30.015	796	1388.82	88.52
-	835	43.853	32.375	48.689	30.015	99	734.24	88.52
-	836	45.764	33.069	48.689	30.015	32	615.81	88.52
-	837	40.074	30.479	35.028	32.808	784	884.91	17.94
-	838	38.823	29.906	35.028	32.808	592	667.52	17.94
-	839	38.824	29.810	35.028	32.808	592	684.19	17.94
-	840	45.568	21.691	51.715	24.210	701	1050.56	9.85
-	841	42.387	31.437	48.689	30.015	304	993.93	88.52
-	842	40.395	30.333	48.689	30.015	693	1430.31	88.52
-	843	42.390	31.093	48.689	30.015	308	1041.58	88.52
-	844	40.183	30.054	35.028	32.808	664	823.81	17.94
-	845	44.538	31.901	48.689	30.015	21	568.65	88.52

Catchment name	Stream no.	Head		Mouth		Max. elevation (m)	Length (km)	Catchment area (km^2)
		Long.	Lat.	Long.	Lat.			
-	846	42.014	19.785	51.857	23.981	1685	1798.87	34.33
-	847	45.873	32.359	48.689	30.015	15	534.51	88.52
-	848	41.701	30.622	48.689	30.015	457	1153.64	88.52
-	849	46.413	32.429	48.689	30.015	9	458.46	88.52
-	850	43.107	30.857	48.689	30.015	310	847.96	88.52
-	851	46.618	32.215	48.689	30.015	9	425.98	88.52
-	852	49.664	23.308	51.857	23.981	187	361.16	34.33
-	853	38.857	28.800	35.028	32.808	767	839.47	17.94
-	854	36.328	27.365	35.802	27.124	310	92.34	0.31
-	855	42.824	30.452	48.689	30.015	354	919.36	88.52
-	856	44.799	31.174	48.689	30.015	76	508.25	88.52
-	857	43.099	30.391	48.689	30.015	332	923.51	88.52
-	858	43.085	30.334	48.689	30.015	332	928.56	88.52
-	859	46.569	31.545	48.689	30.015	8	338.61	88.52
-	860	44.935	30.838	48.689	30.015	136	504.32	88.52
-	861	45.371	30.975	48.689	30.015	30	449.77	88.52
-	862	44.034	30.374	48.689	30.015	338	671.03	88.52
-	863	39.880	28.386	48.689	30.015	942	1591.52	88.52
-	864	38.159	27.410	35.028	32.808	1018	1110.66	17.94
-	865	42.019	29.154	48.689	30.015	654	1144.01	88.52
-	866	40.478	28.392	48.689	30.015	904	1507.57	88.52
-	867	44.056	20.712	51.857	23.981	754	1324.65	34.33
-	868	45.533	30.582	48.689	30.015	109	431.58	88.52
-	869	42.301	29.125	48.689	30.015	628	1145.96	88.52
-	870	42.031	28.944	48.689	30.015	695	1220.48	88.52
-	871	38.717	27.296	35.028	32.808	958	1142.43	17.94
-	872	43.636	29.493	48.689	30.015	456	1100.20	88.52
-	873	43.371	29.241	48.689	30.015	522	1147.81	88.52
-	874	41.122	28.037	48.689	30.015	861	1456.82	88.52
-	875	43.144	29.084	48.689	30.015	554	1157.83	88.52
-	876	56.130	25.719	55.952	25.778	313	33.90	0.08
-	877	40.346	27.513	48.689	30.015	918	1579.31	88.52
-	878	46.885	30.537	48.689	30.015	27	269.90	88.52
-	879	40.644	27.660	48.689	30.015	914	1532.55	88.52
-	880	40.237	27.435	48.689	30.015	918	1590.28	88.52
-	881	39.214	26.687	35.028	32.808	1113	1277.00	17.94
-	882	40.440	27.324	48.689	30.015	914	1581.18	88.52
-	883	41.551	27.795	48.689	30.015	869	1408.27	88.52
-	884	43.317	20.228	51.857	23.981	1019	1462.05	34.33
-	885	47.804	30.223	47.959	30.052	4	32.33	0.36
-	886	39.049	26.278	35.028	32.808	1261	1335.35	17.94
-	887	47.079	29.859	48.689	30.015	107	294.04	88.52
-	888	42.341	27.744	48.689	30.015	730	1308.51	88.52
-	889	45.338	28.893	48.689	30.015	350	734.29	88.52
-	890	44.661	28.578	48.689	30.015	448	886.72	88.52
-	891	39.521	26.134	36.678	25.892	920	444.23	7.45
-	892	45.556	28.868	48.689	30.015	329	706.55	88.52
-	893	41.610	22.459	51.857	23.981	944	1852.93	34.33
-	894	56.257	25.625	56.267	25.630	4	1.40	0.01
-	895	40.117	26.042	48.689	30.015	1237	1581.13	88.52
-	896	47.024	29.158	47.713	29.387	251	107.65	0.40
-	897	40.459	25.999	48.689	30.015	1049	1518.41	88.52
-	898	47.277	29.081	47.713	29.387	230	91.65	0.40
-	899	40.167	25.698	48.689	30.015	1287	1575.16	88.52
-	900	42.393	26.821	48.689	30.015	948	1345.27	88.52
-	901	42.654	26.725	48.689	30.015	874	1298.17	88.52
-	902	47.646	22.094	51.857	23.981	400	814.14	34.33
-	903	45.096	27.764	48.689	30.015	411	664.32	88.52
-	904	47.850	28.803	47.908	29.340	124	97.51	0.62
-	905	43.553	26.969	48.689	30.015	694	1121.30	88.52
-	906	42.965	26.610	48.689	30.015	835	1286.36	88.52
-	907	44.131	26.910	48.689	30.015	584	944.28	88.52
-	908	41.742	25.715	48.689	30.015	884	1336.61	88.52
-	909	42.062	25.769	48.689	30.015	803	1292.83	88.52
-	910	52.013	23.940	52.043	23.970	5	5.66	0.34

Catchment name	Stream no.	Head		Mouth		Max. elevation (m)	Length (km)	Catchment area (km^2)
		Long.	Lat.	Long.	Lat.			
-	911	45.363	27.227	48.608	28.131	519	496.51	4.49
-	912	44.409	26.702	48.689	30.015	579	937.70	88.52
-	913	43.088	25.836	48.689	30.015	727	1152.05	88.52
-	914	42.166	25.303	48.689	30.015	799	1303.91	88.52
-	915	45.332	26.698	48.608	28.131	578	719.40	4.49
-	916	55.210	25.077	55.186	25.138	4	14.01	0.09
-	917	42.539	25.182	48.689	30.015	818	1277.68	88.52
-	918	45.308	26.310	48.608	28.131	662	791.20	4.49
-	919	44.933	26.013	48.689	30.015	651	991.65	88.52
-	920	43.985	25.559	48.689	30.015	726	1144.49	88.52
-	921	47.600	26.965	48.814	27.822	277	245.52	1.82
-	922	39.017	22.826	38.968	22.859	-1	9.01	0.37
-	923	40.296	23.416	51.857	23.981	944	2177.41	34.33
-	924	39.070	22.686	39.025	22.677	2	7.26	0.00
-	925	51.566	23.605	51.857	23.981	30	77.45	34.33
-	926	39.247	22.726	39.053	22.621	54	40.20	0.05
-	927	45.412	25.708	48.608	28.131	778	882.01	4.49
-	928	39.770	22.923	38.968	22.859	646	155.82	0.37
-	929	39.553	22.663	39.139	22.412	298	86.47	0.07
-	930	46.421	25.992	48.608	28.131	583	720.03	4.49
-	931	40.672	23.122	51.857	23.981	944	2052.47	34.33
-	932	45.467	25.321	48.608	28.131	665	872.41	4.49
-	933	43.799	24.484	48.689	30.015	886	1331.85	88.52
-	934	42.729	24.029	48.689	30.015	976	1516.89	88.52
-	935	50.914	23.277	51.857	23.981	96	200.43	34.33
-	936	48.363	26.540	48.914	27.568	250	180.87	0.96
-	937	38.985	21.918	38.978	21.974	1	8.88	0.20
-	938	47.494	26.073	48.814	27.822	423	386.29	1.82
-	939	40.736	22.671	51.857	23.981	944	1947.97	34.33
-	940	40.829	22.667	51.857	23.981	944	1941.87	34.33
-	941	41.798	23.111	51.857	23.981	944	1816.32	34.33
-	942	49.467	26.561	49.962	26.839	50	93.76	0.15
-	943	43.734	24.124	48.689	30.015	945	1379.07	88.52
-	944	41.793	23.026	51.857	23.981	944	1814.05	34.33
-	945	45.533	20.757	51.857	23.981	681	1146.59	34.33
-	946	41.829	22.982	51.857	23.981	944	1811.02	34.33
-	947	42.122	23.007	51.857	23.981	944	1783.04	34.33
-	948	48.824	26.172	49.134	27.427	187	241.28	2.25
-	949	42.508	23.184	51.857	23.981	944	1777.09	34.33
-	950	41.485	22.641	51.857	23.981	944	1856.73	34.33
-	951	48.318	25.803	49.134	27.427	339	341.45	2.25
-	952	41.922	22.765	51.857	23.981	944	1805.26	34.33
-	953	41.872	18.822	41.310	18.584	258	114.82	0.37
-	954	55.206	24.756	54.666	24.702	72	77.73	0.05
-	955	45.979	24.455	51.715	24.210	705	1013.57	9.85
-	956	49.302	22.334	51.857	23.981	209	465.01	34.33
-	957	54.818	24.478	54.610	24.534	44	31.46	0.10
-	958	50.080	22.591	51.857	23.981	167	376.14	34.33
-	959	50.774	22.773	51.857	23.981	128	264.53	34.33
-	960	43.130	19.172	51.857	23.981	1389	1571.93	34.33
-	961	52.157	23.247	52.043	23.970	56	149.89	0.34
-	962	45.096	20.035	51.857	23.981	698	1209.71	34.33
-	963	42.185	18.439	41.310	18.584	739	173.12	0.37
-	964	51.578	22.800	51.857	23.981	78	200.62	34.33
-	965	47.936	21.141	51.857	23.981	347	725.96	34.33
-	966	47.227	24.997	49.134	27.427	624	621.73	2.25
-	967	51.794	22.774	51.857	23.981	70	196.47	34.33
-	968	52.084	22.838	51.917	23.975	69	210.31	44.77
-	969	44.785	19.427	51.857	23.981	869	1281.97	34.33
-	970	54.323	23.569	53.982	24.109	111	132.28	0.25
-	971	44.170	18.955	51.857	23.981	1230	1389.66	34.33
-	972	51.830	22.431	51.917	23.975	85	262.82	44.77
-	973	52.257	22.473	51.917	23.975	94	305.01	44.77
-	974	47.583	20.376	51.857	23.981	399	857.60	34.33
-	975	43.342	18.181	51.857	23.981	2048	1718.64	34.33

Catchment name	Stream no.	Head		Mouth		Max. elevation (m)	Length (km)	Catchment area (km^2)
		Long.	Lat.	Long.	Lat.			
-	976	49.600	25.947	50.016	26.176	61	111.93	0.29
-	977	56.807	24.024	56.918	24.137	112	24.67	0.03
-	978	52.928	22.497	51.917	23.975	110	647.32	44.77
-	979	48.659	20.663	51.857	23.981	302	707.65	34.33
-	980	52.767	22.394	51.917	23.975	111	384.83	44.77
-	981	54.788	23.037	51.917	23.975	108	1153.83	44.77
-	982	54.715	22.962	51.917	23.975	108	1140.44	44.77
-	983	54.749	22.912	51.917	23.975	108	1135.87	44.77
-	984	55.387	23.083	51.917	23.975	115	1166.07	44.77
-	985	55.399	23.067	51.917	23.975	117	1169.29	44.77
-	986	44.153	23.368	51.715	24.210	807	1139.64	9.85
-	987	45.231	18.681	51.857	23.981	890	1348.96	34.33
-	988	49.519	20.585	51.857	23.981	280	675.05	34.33
-	989	47.712	19.668	51.857	23.981	458	931.54	34.33
-	990	56.040	23.035	51.917	23.975	198	1086.52	44.77
-	991	46.589	18.999	51.857	23.981	690	1079.20	34.33
-	992	51.033	20.933	51.917	23.975	170	673.32	44.77
-	993	55.291	22.605	51.917	23.975	108	985.73	44.77
-	994	55.417	22.598	51.917	23.975	108	980.46	44.77
-	995	55.714	22.647	51.917	23.975	120	999.79	44.77
-	996	55.960	22.635	51.917	23.975	144	950.51	44.77
-	997	27.526	25.971	30.513	31.458	251	2892.43	3982567.50
-	998	27.642	25.873	30.513	31.458	280	2919.66	3982567.50
-	999	27.945	25.808	30.513	31.458	209	2750.32	3982567.50
-	1000	28.027	24.953	30.513	31.458	356	2832.09	3982567.50
-	1001	28.128	23.569	30.513	31.458	344	2239.22	3982567.50
-	1002	25.969	22.358	30.513	31.458	589	2544.59	3982567.50
-	1003	26.733	22.563	30.513	31.458	465	2427.14	3982567.50
-	1004	36.724	21.484	36.941	21.559	255	34.95	399.39
-	1005	32.080	21.309	30.513	31.458	409	1938.63	3982567.50
-	1006	30.507	20.825	30.513	31.458	185	1999.85	3982567.50
-	1007	34.564	20.497	30.513	31.458	471	1945.99	3982567.50
-	1008	33.306	20.495	30.513	31.458	309	1737.00	3982567.50
-	1009	31.474	20.041	30.513	31.458	319	2231.13	3982567.50
-	1010	34.629	19.800	30.513	31.458	411	3129.45	3982567.50
-	1011	33.960	19.548	30.513	31.458	348	2951.21	3982567.50
-	1012	35.552	19.412	30.513	31.458	509	3217.85	3982567.50
-	1013	30.485	19.489	30.513	31.458	224	2240.38	3982567.50
-	1014	32.545	19.125	30.513	31.458	287	2697.26	3982567.50
-	1015	29.528	19.028	30.513	31.458	246	2381.65	3982567.50
-	1016	34.239	18.536	30.513	31.458	370	3039.97	3982567.50
-	1017	37.293	18.541	37.541	18.719	294	52.77	657.67
-	1018	32.627	18.495	30.513	31.458	417	2686.69	3982567.50
-	1019	35.147	17.875	30.513	31.458	422	3342.84	3982567.50
-	1020	38.206	17.907	38.275	18.200	272	47.09	573.21
-	1021	35.106	17.457	30.513	31.458	385	3287.04	3982567.50
-	1022	37.481	17.617	37.680	18.722	131	176.32	63528.62
-	1023	38.352	17.315	38.852	17.544	731	100.35	1752.35
-	1024	36.422	17.055	37.680	18.722	414	388.68	63528.62
-	1025	37.969	16.954	37.680	18.722	510	377.92	63528.62
-	1026	31.614	17.111	30.513	31.458	315	2642.49	3982567.50
-	1027	37.642	16.746	37.680	18.722	368	331.30	63528.62
-	1028	31.722	16.847	30.513	31.458	322	2684.04	3982567.50
-	1029	36.398	16.389	30.513	31.458	418	3503.36	3982567.50
-	1030	32.874	16.505	30.513	31.458	361	3291.85	3982567.50
-	1031	34.810	16.212	30.513	31.458	392	3351.89	3982567.50
-	1032	34.011	16.036	30.513	31.458	425	3328.91	3982567.50
-	1033	37.721	15.556	37.680	18.722	547	521.29	63528.62
-	1034	37.482	15.735	37.680	18.722	472	476.27	63528.62
-	1035	32.479	15.573	30.513	31.458	373	3418.67	3982567.50
-	1036	29.834	15.427	30.513	31.458	440	2910.83	3982567.50
-	1037	30.793	31.384	30.568	31.469	0	31.85	1586.29
-	1038	31.187	30.917	30.938	31.571	6	116.79	5570.87
-	1039	30.423	30.630	30.107	31.276	21	131.22	15025.58
-	1040	31.346	30.291	32.321	31.263	13	194.96	15313.21

Catchment name	Stream no.	Head		Mouth		Max. elevation (m)	Length (km)	Catchment area (km^2)
		Long.	Lat.	Long.	Lat.			
-	1041	31.303	29.600	30.513	31.458	23	342.40	3982567.50
-	1042	33.534	29.371	33.808	31.146	648	313.12	23389.72
-	1043	31.468	28.776	30.513	31.458	213	503.90	3982567.50
-	1044	30.764	28.683	30.513	31.458	31	480.84	3982567.50
-	1045	31.613	27.767	30.513	31.458	314	648.83	3982567.50
-	1046	29.961	27.636	30.513	31.458	126	739.78	3982567.50
-	1047	29.250	27.399	30.513	31.458	246	851.50	3982567.50
-	1048	29.039	27.022	30.513	31.458	250	902.82	3982567.50
-	1049	29.883	26.560	30.513	31.458	289	1020.03	3982567.50
-	1050	32.691	26.152	30.513	31.458	65	953.38	3982567.50
-	1051	33.629	25.710	30.513	31.458	328	1112.79	3982567.50
-	1052	31.640	25.108	30.513	31.458	452	2663.25	3982567.50
-	1053	30.173	24.419	30.513	31.458	180	2214.70	3982567.50
-	1054	30.372	24.117	30.513	31.458	180	2106.22	3982567.50
-	1055	35.231	23.867	35.483	23.898	654	39.09	99.44
-	1056	29.964	23.393	30.513	31.458	180	1887.09	3982567.50
-	1057	35.511	23.238	35.567	23.248	16	11.95	124.86
-	1058	32.161	22.705	30.513	31.458	180	1469.95	3982567.50
-	1059	33.460	22.658	30.513	31.458	235	1460.05	3982567.50
-	1060	33.693	22.377	30.513	31.458	246	1499.64	3982567.50
-	1061	34.498	22.005	30.513	31.458	364	1623.09	3982567.50
-	1062	27.497	21.717	30.513	31.458	373	2374.03	3982567.50
-	1063	28.983	21.684	30.513	31.458	293	2087.00	3982567.50
-	1064	27.280	21.256	30.513	31.458	421	2445.67	3982567.50
-	1065	26.659	20.864	30.513	31.458	505	2569.01	3982567.50
-	1066	28.190	19.857	30.513	31.458	363	2514.73	3982567.50
-	1067	24.384	19.437	30.513	31.458	666	3000.82	3982567.50
-	1068	28.236	19.723	30.513	31.458	364	2579.54	3982567.50
-	1069	24.297	19.318	30.513	31.458	716	3058.10	3982567.50
-	1070	24.872	18.694	30.513	31.458	574	2992.57	3982567.50
-	1071	28.882	17.348	30.513	31.458	357	2672.48	3982567.50
-	1072	25.805	17.160	30.513	31.458	576	3132.65	3982567.50
-	1073	25.844	16.287	30.513	31.458	703	3232.51	3982567.50
-	1074	23.012	15.817	30.513	31.458	781	3630.29	3982567.50
-	1075	24.949	15.976	30.513	31.458	691	3373.73	3982567.50
-	1076	27.722	15.944	30.513	31.458	599	2998.78	3982567.50
-	1077	24.321	15.796	30.513	31.458	718	3459.78	3982567.50
-	1078	26.002	15.366	30.513	31.458	815	3365.21	3982567.50
-	1079	26.090	15.418	30.513	31.458	791	3350.04	3982567.50